Predictive Control Strategies for Safe Payload Handling in Crane-Based Offshore Operations

Prädiktive Regelungsstrategien zur sicheren Lastführung in kranbasierten Offshore-Operationen

Von der Fakultät für Maschinenwesen der Rheinisch-Westfälischen Technischen Hochschule Aachen zur Erlangung des akademischen Grades eines Doktors der Ingenieurwissenschaften genehmigte Dissertation

vorgelegt von

Philipp Schubert

Berichter: Univ.-Prof. Dr.-Ing. Dirk Abel
Univ.-Prof. Dr.-Ing. Dr. h. c. (UPT) Burkhard Corves

Tag der mündlichen Prüfung: 28. Januar 2025

Diese Dissertation ist auf den Internetseiten der Universitätsbibliothek online verfügbar.

To Franzi, Ava and Carina, who are more essential to this work than any LaTeX distribution or controller topology.

Abstract

Crane-based loading operations present an integral part of today's ocean economy, an industry that is projected to become even more vital due to the emergence of offshore windparks as part of a more sustainable future. At the same time, offshore operations are getting increasingly challenging as drilling platforms and wind parks move from shallow waters to open sea, where more severe sea states are common. So-called knuckle boom cranes (KBC) are deployed e.g. on supply vessels and offer increased flexibility during payload handling thanks to an additional articulated boom. To this day, most loading operations are controlled manually requiring highly trained crane operators and additional personnel overseeing operation. Increasing the level of automatization promises a simplified handling task, reduced costs and improved operational safety. Yet, only solutions for vertical payload stabilization are established in industrial practice. The objective of sway control attracted interest from academia, while an holistic approach to spatial payload stabilization through automated control remains an open gap.

In context of this thesis project, predictive control strategies directed towards more efficient and safe offshore operations are researched. After reviewing common modeling approaches, a control-oriented model of vessel, crane and payload is derived, which forms the basis of the investigated model predictive payload controller. Different formulations of the underlying optimal control problem are assessed for control performance and real-time feasibility. In particular, a control scheme is put forward leveraging the differential flatness of the crane-payload system in order to invert the system equations. It further motivates a payload-centric approach to payload stabilization and trajectory tracking. The flatness-based model predictive controller (FMPC) is compared to established linear as well as nonlinear versions of MPC. The considered predictive control topology is complemented by an target selector yielding optimized crane configurations and a receding horizon observer providing estimates of the system state alongside short-time predictions of the vessel motions.

The controller designs are studied in simulation for different sea states. The control performance is shown to be directly linked to the available capacity of the crane's hydraulic actuators. Also, the added benefit of optimizing the crane configuration based on the crane's manipulability index is demonstrated. Last, first validation trials of a model predictive payload controller in a robot-based test bench are presented suggesting that MPC can be used to induce damping and reduce payload oscillations. The thesis concludes with a discussion of operational safety from an automated control perspective.

Kurzfassung

Kranbasierte Verladevorgänge sind heute ein integraler Bestandteil des maritimen Sektors, einer Branche, die aufgrund der Zunahme an Offshore-Windparks im Kontext einer nachhaltigeren Zukunft noch an Bedeutung gewinnen wird. Allerdings wird der Offshore-Betrieb gleichzeitig immer schwieriger, da sich Bohrinseln und Windparks von flachen Gewässern zunehmend in die offene See verlagern, wo stärkerer Seegang herrscht. Sogenannte Knickgelenkauslegerkrane werden etwa auf Versorgungsschiffen eingesetzt und bieten dank eines zusätzlichen Gelenkauslegers mehr Flexibilität beim Lastumschlag. Bis heute werden die meisten Ladevorgänge weiterhin manuell gesteuert, was gut ausgebildete Kranführer sowie zusätzliches Überwachungspersonal erfordert. Ein höherer Automatisierungsgrad verspricht eine vereinfachte Lasthandhabung, geringere Kosten und eine höhere Betriebssicherheit. In der industriellen Praxis haben sich bisher jedoch nur Lösungen zur vertikalen Laststabilisierung durchgesetzt, während die ebene Schwingungsdämpfung in der Forschung adressiert wird. Ein ganzheitlicher Regleransatz zur räumlichen Laststabilisierung stellt jedoch noch eine Forschungslücke dar. Im Rahmen dieser Dissertation werden prädiktive Regelungsstrategien untersucht, die auf einen effizienteren und sichereren Offshore-Betrieb abzielen. Nach einer Betrachtung gängiger Modellierungsansätze wird ein regelungsorientiertes Modell von Schiff, Kran und Last abgeleitet, das die Grundlage für den untersuchten prädiktiven Lastregler bildet. Verschiedene Formulierungen des zugrundeliegenden Regelungsproblems werden auf Regelgüte und Echtzeitfähigkeit hin untersucht. Insbesondere wird ein Regelerschema vorgeschlagen, das die differentielle Flachheit des Kran-Last-Systems ausnutzt, um die Systemgleichungen zu invertieren. Es motiviert zudem einen lastzentrierten Ansatz zur Stabilisierung und Trajektorienfolgeregelung. Der flachheitsbasierte modellprädiktive Regler (engl. model predictive controller - MPC) wird mit etablierten linearen und nichtlinearen Versionen der MPC verglichen. Die betrachtete prädiktive Reglertopologie wird ergänzt durch einen Target Selektor, der optimierte Krankonfigurationen bestimmt, sowie einen Beobachter mit weichendem Horizont, der Zustandschätzung und Kurzzeitvorhersagen der Schiffsbewegungen liefert. Die Reglerentwürfe werden simulativ für verschiedene Seegänge untersucht. Es zeigt sich, dass die Regelgüte direkt von der Kapazität der hydraulischen Aktuatoren des Krans abhängt. Außerdem wird der zusätzliche Nutzen einer Optimierung der Krankonfiguration anhand der Manipulierbarkeitsellipse des Krans aufgezeigt. Schließlich werden erste Validierungsversuche eines modellprädiktiven Lastreglers an einem roboterbasierten Prüfstand vorgestellt, die zeigen, dass MPC zur Dämpfung und Reduzierung von Lastschwingungen eingesetzt werden können. Die Arbeit schließt mit einer Diskussion operativer Sicherheit aus regelungstechnischer Perspektive.

Acknowledgements

This dissertation was compiled during my time as a research associate at the Institute of Automatic Control at RWTH Aachen University. The presented research was conducted under the *SFI Offshore Mechatronics* initiative funded by the Norwegian Research Council under project number 237896.

I would like to express my candid thanks to Univ.-Prof. Dr.-Ing. Dirk Abel for his supervision of my work as well as his continuous support as a person. Furthermore, my gratitude goes to Univ.-Prof. Dr.-Ing. Dr. h. c. (UPT) Burkhard Corves, for assuming the co-referee role. I would also like to thank Univ.-Prof. Dr.-Ing. Christian Hopmann for taking on the role of the examination chair as well as Prof. em. Dr.-Ing. Heinrich Rake for participating as a member of the examination committee.

In context of the SFI Offshore Mechatronics, I like to thank Prof. Geir Hovland, Rachel Funderud Syrtveit, Prof. Geir Grasmo, Asle Pedersen, Anne-Line Aagedal, Prof. Olav Egeland and Sondre Sanden Tørdal for their input, project management and above all for providing an always welcoming environment for my studies.

On a personal note, I would like to express my cordial gratitude to all my colleagues at IRT – especially to all current and former members of G-Ind, G-Prod and G-Med, as well as the non-scientific staff – with whom I enjoyed working every day and who have shaped a workplace that I will always remember fondly. The same holds for the collaborators across multiple institutes and entities that I had the pleasure of cooperating with on various projects and project proposals. I would like to give special mention to Jens Ahlers and Robert Göllinger for their tireless support of the work that shaped the final presentation of my oral examination.

In particular, I would like to acknowledge a group of dear peers and friends – Markus Zimmer, Tobias Salesch, Verena Neisen, and Nuria Peña-Perez – for their continuous input, their company, as well as their support during everyday work and while writing up this thesis. Thank you ever so much!

Above all else, I dedicate this work to my wife, who had to bear a lot to make this doctorate possible yet whose support I could always count on.

Contents

1 Introduction **1**
- 1.1 Challenges in Crane-based Offshore Operations . . . 3
- 1.2 Motivation for Automated Payload Control . . . 4
- 1.3 State of the Art . . . 6
  - 1.3.1 Crane Control Onshore . . . 6
  - 1.3.2 Crane Control Offshore . . . 8
- 1.4 Deficit . . . 12
- 1.5 Scientific Contribution . . . 14
- 1.6 Scope and Outline of this Thesis . . . 16

2 Fundamentals **19**
- 2.1 Coordinate Transformations . . . 19
- 2.2 Spline Curves and Trajectories . . . 25
- 2.3 Dynamic Systems . . . 31
- 2.4 Differential Flatness . . . 36
- 2.5 Predictive Control . . . 37
- 2.6 State Estimation . . . 41
- 2.7 Numerical Optimization . . . 55

3 Modeling **65**
- 3.1 System Overview and Relevant Coordinate Frames . . . 65
- 3.2 Vessel Dynamics and Environmental Loads . . . 67
- 3.3 Knuckle Boom Crane . . . 75
  - 3.3.1 Review of Crane Models . . . 77
  - 3.3.2 Kinematics . . . 79
  - 3.3.3 Dynamics . . . 86
  - 3.3.4 System Constraints . . . 90
  - 3.3.5 Sensors . . . 92
- 3.4 Control-Oriented Model . . . 94
- 3.5 Differential Flatness of the Crane System . . . 96
- 3.6 Simulation Environment . . . 99
- 3.7 Robot-based Test Bench . . . 101

4 Control **103**
4.1 Definition of the Control Task . . . 104
4.1.1 Control Objective . . . 105
4.1.2 Performance Indicators . . . 108
4.2 Estimation of Vessel and Crane State . . . 111
4.2.1 Parameterization of the Vessel Motions . . . 111
4.2.2 Observer Design . . . 113
4.2.3 State Reconstruction . . . 118
4.2.4 Short-time Prediction of the Vessel Motions . . . 120
4.2.5 Discussion of the observer designs . . . 123
4.3 Target Selection . . . 124
4.3.1 Optimization Problem . . . 124
4.3.2 Crane Manipulability . . . 125
4.3.3 Simulative Validation . . . 126
4.4 Predictive Payload Controller . . . 128
4.4.1 Preliminaries to Predictive Payload Control . . . 129
4.4.2 Linear Model Predictive Control . . . 131
4.4.3 Nonlinear Model Predictive Control . . . 132
4.4.4 Flatness-Based Model Predictive Control . . . 133
4.5 Simulative Controller Evaluation . . . 136
4.5.1 Controller Parameterization . . . 137
4.5.2 Stabilization Performance of LMPC, NMPC and FMPC . . . 137
4.5.3 Influence of the Sea State and Actuator Capacity . . . 139
4.5.4 Trajectory Tracking with FMPC . . . 141
4.6 Experimental Controller Validation . . . 143
4.6.1 Test Scenario . . . 143
4.6.2 Results and Discussion . . . 144
4.7 Perspectives on Safe Offshore Operations . . . 146
4.7.1 Notions of Safety . . . 146
4.7.2 Safety Functions in Crane-Based Offshore Operations . . . 149
4.7.3 Model-Based Emergency Braking . . . 150
4.7.4 Predictive Safety Filter . . . 155

5 Revisiting the Research Questions **161**

6 Potentials of Predictive Control in Offshore Payload Handling **165**
6.1 Research Context and Relevance . . . 165
6.2 Research Summary and Conclusion . . . 167
6.3 Outlook . . . 170

A Supplementary Information **173**

Bibliography **175**

Own Publications

This thesis is based in parts on the following own publications:

[S1] Schubert, P. ; Abel, D.: Flatness-based Model Predictive Payload Control for Offshore Cranes, in *2023 European Control Conference (ECC)*, Bucharest, Romania: IEEE, Jun. 2023, pp. 1–8. DOI: 10.23919/ECC57647.2023.10178159.

[S2] Schubert, P. ; Abel, D., Payload Stabilization for Offshore Cranes: A Unified Controller Based on Flatness, *IFAC-PapersOnLine*, vol. 56, no. 2, pp. 7886–7892, 2023. DOI: 10.1016/j.ifacol.2023.10.024.

[S3] Schubert, P. ; Stemmler, S. ; Abel, D.: Roboterbasierter Teststand zur assistierten Teleoperation teilautonomer Offshore Kräne, in *VDI Automation*, 2018.

[S4] Schubert, P. ; Stemmler, S. ; Abel, D.: Development of a Human Machine Interface for Crane-based Load Handling using a Lightweight Robot, in *2019 27th Mediterranean Conference on Control and Automation (MED)*, Akko, Israel: IEEE, Jul. 2019, pp. 292–298. DOI: 10.1109/MED.2019.8798578.

[S5] Schubert, P. ; Stemmler, S. ; Abel, D.: Towards Predictive Anti-Sway Control of Hanging Loads: Model-based Controller Design for a Knuckle Boom Crane, in *2019 18th European Control Conference (ECC)*, Naples, Italy: IEEE, Jun. 2019, pp. 2276–2282. DOI: 10.23919/ECC.2019.8795871.

List of Figures

1.1 Knuckle boom crane . . . 2
1.2 Payload oscillations in crane-based offshore operations . . . 3
1.3 Considered control topology . . . 17

2.1 Pose of a rigid body . . . 19
2.2 Euler angles: roll-pitch-yaw convention . . . 21
2.3 Coordinate transformation between two frames . . . 22
2.4 Denavit-Hartenberg convention . . . 24
2.5 Polynomial path planning . . . 26
2.6 Properties of the B-spline basis . . . 30
2.7 Block diagram of a feedback linearization . . . 33
2.8 Trajectories considered during finite-horizon predictive control . . . 40
2.9 Block diagram of a state estimator . . . 43
2.10 Full information estimation . . . 48
2.11 Update scheme during Kalman filtering . . . 51
2.12 State estimation based on a moving horizon . . . 54

3.1 Coordinate frames in crane-based offshore operations . . . 66
3.2 Vessel motions during seakeeping . . . 68
3.3 Vessel dynamics informed by force RAOs . . . 70
3.4 Exemplary wave spectra . . . 73
3.5 Exemplary vessel trajectories . . . 74
3.6 Exemplary configurations of a knuckle boom crane . . . 75
3.7 Schematics of a knuckle boom crane . . . 76
3.8 Kinematics of a knuckle boom crane . . . 80
3.9 Exemplary geometry involved in determining the stored cable length . . . 85
3.10 Simplified body assignment for a KBC . . . 87
3.11 Radial workspace of the KBC . . . 91
3.12 Maximum payload sway angle during frequency sweep of the wave disturbance . . . 100
3.13 Robot-based test bench . . . 101

4.1 Predictive control topology . . . 103
4.2 Schematic of an error envelope . . . 109
4.3 Performance measures of exemplary closed loop trajectories . . . 110
4.4 Initial guess of vessel motion . . . 113

4.5 Observer designs 115
4.6 Spectrograms of exemplary vessel motions 118
4.7 Observer performance during JONSWAP excitation 119
4.8 Observer performance during Torsethaugen excitation 120
4.9 Observer-based prediction of the vessel motions 122
4.10 Prediction performance of the MHE 123
4.11 Ambiguity of the payload actuation 125
4.12 Depiction of the manipulability index 127
4.13 Error trajectories for control with and without target selection 128
4.14 Spline approximation of input trajectory 130
4.15 Scheduling in receding horizon estimation and control 130
4.16 Payload stabilization with a LMPC at moderate seas 138
4.17 Payload stabilization with a NMPC at moderate seas 138
4.18 Payload stabilization with a FMPC at moderate seas 139
4.19 Performance map of LMPC 140
4.20 Tracking performance of FMPC at moderate seas 142
4.21 Computation times of FMPC during trajectory tracking 142
4.22 Predictive control topology used in laboratory tests 144
4.23 Experimental Validation of a MPC 145
4.24 Flow chart of a simple model-based AEB function 150
4.25 Exemplary behavior of model-based emergency braking 154
4.26 Schematics of a Safety Filter 155

List of Tables

1.1 Levels of automation according to [48] 5

3.1 Definition of sea state codes and corresponding wave parameters 73
3.2 DH-parameters of the knuckle boom crane 81
3.3 Maximum response times for crane-based offshore operations 89
3.4 Kinematic constraints of the considered KBC 90
3.5 Dynamic constraints of the considered KBC 91

4.1 Computational times of the different observer designs 120
4.2 Performance measures of control with and without target selection . . . 127
4.3 Computational times of the different MPC designs 139
4.4 Sea state parameterization 140
4.5 Euclidean error during trajectory tracking 141

List of Abbreviations

AD	algorithmic differentiation
AHC	active heave compensation
ASC	anti-sway control
BO	Bayesian optimization
COM	center of mass
DH	Denavit-Hartenberg
DoF	degrees of freedom
DP	dynamic positioning
EKF	extended Kalman filter
ERK4	explicit Runge-Kutta of 4^{th} order
FMPC	flatness-based model predictive controller
GP	Gaussian random process
GPR	Gaussian process regression
HPU	hydraulic power unit
IMU	inertial measurement unit
IRK2	implicit Runge-Kutta of 2^{nd} order
KBC	knuckle boom crane
KKT	Karush–Kuhn–Tucker
LMPC	linear model predictive controller
LoA	level of automation
LTI	linear time-invariant
MHE	moving horizon estimator
MIMO	multiple-input, multiple-output
MPC	model predictive controller
MRU	motion reference unit
ned	north-east-down

NLP	nonlinear program
NMPC	nonlinear model predictive controller
OCP	optimal control problem
p.d	positive definite
p.s.d	positive semidefinite
PDF	probability density function
QP	quadratic program
RAO	response amplitude operator
rpy	roll-pitch-yaw
SCS	safety-related control system
SE	squared-exponential
SISO	single-input, single-output
SQP	sequential quadratic programming
SSC	Sea State Code
SWL	safe working load
TCP	tool center point
UKF	unscented Kalman filter
ZOH	zero-order hold

List of Symbols

Symbol	Description
Automatic Control	
d	dimension of the disturbance vector $\boldsymbol{d}$
m	dimension of the input vector $\boldsymbol{u}$
n	dimension of the state vector $\boldsymbol{x}$
q	dimension of the measured output vector $\boldsymbol{y}_\mathrm{m}$
p	dimension of the output vector $\boldsymbol{y}$
$\boldsymbol{x}$	vector of system states, $\boldsymbol{x} \in \mathbb{R}^n$
$\boldsymbol{x}_0$	initial respective current state, which represents the left boundary condition at t_0 during predictive control
$\boldsymbol{u}$	vector of system inputs, $\boldsymbol{u} \in \mathbb{R}^m$
$\boldsymbol{d}$	vector of system disturbances, $\boldsymbol{d} \in \mathbb{R}^d$
$\boldsymbol{y}$	vector of system outputs, $\boldsymbol{y} \in \mathbb{R}^p$
$\boldsymbol{y}_\mathrm{m}$	vector of measured system outputs, $\boldsymbol{y}_\mathrm{m} \in \mathbb{R}^q$
$\boldsymbol{\upsilon}$	random vector representing measurement noise, $\boldsymbol{\upsilon} \in \mathbb{R}^q$
$\boldsymbol{\varepsilon}$	random vector representing process noise, $\boldsymbol{\varepsilon} \in \mathbb{R}^n$
$\mathcal{X}$	admissible set of states $\boldsymbol{x}$, where $\mathcal{X} \subseteq \mathbb{R}^n$
$\boldsymbol{\delta}$	vector of slack variables with $\boldsymbol{\delta} \geq \boldsymbol{0}$
$\mathcal{X}_{T_\mathrm{p}}$	subset of $\mathcal{X}$ constraining the terminal state $\boldsymbol{x}(T_\mathrm{p})$ within the predictive controller, i.e. $\mathcal{X}_{T_\mathrm{p}} \subseteq \mathcal{X}$
$\mathcal{U}$	admissible set of inputs $\boldsymbol{u}$, where $\mathcal{U} \subseteq \mathbb{R}^m$
$\mathcal{D}$	set of psossible disturbances $\boldsymbol{d}$, where $\mathcal{D} \subseteq \mathbb{R}^d$
$\mathcal{Y}$	admissible set of outputs $\boldsymbol{y}$, where $\mathcal{Y} \subseteq \mathbb{R}^p$
f_c	execution rate of the control algorithm on a discrete computing hardware
f_e	execution rate of the estimator algorithm on a discrete computing hardware
f_s	generic sample rate

T_s	generic sample time, i.e. the reciprocal of the sample rate f_s
T_f	moving horizon considered during filtering in seconds, $[T_\mathrm{f}] = \mathrm{s}$
T_p	prediction horizon in seconds, $[T_\mathrm{p}] = \mathrm{s}$
T_c	cycle time of the control algorithm on a discrete computing hardware, i.e. the reciprocal of its execution rate f_c
T_e	cycle time of the estimator algorithm on a discrete computing hardware, i.e. the reciprocal of its execution rate f_e
k	running index used for time discretization, i.e. $t = t_\mathrm{init} + kT_c$ with $k = \{0, 1, 2, \ldots\}$
t_init	time instance at which the controller is activated
L	cost function for rating the system trajectories over the prediction horizon T_p, where $L : \mathcal{X} \times \mathcal{U} \times \mathcal{Y} \times \mathbb{R} \to \mathbb{R}_{\geq 0}$
L_{T_p}	cost function for rating the terminal state $\boldsymbol{x}(T_\mathrm{p})$, where $L_{T_\mathrm{p}} : \mathcal{X}_{T_\mathrm{p}} \to \mathbb{R}_{\geq 0}$
$\boldsymbol{x}(t\|t_0)$	predicted trajectories of states $\boldsymbol{x}$ calculated at t_0
$\hat{\boldsymbol{x}}(k\|k \pm i)$	state estimate at instance k based on measurements up to $k \pm i$, $i \in \mathbb{N}$
$\boldsymbol{x}^*(t\|t_0)$	optimal trajectories of states $\boldsymbol{x}$ calculated at t_0
$\boldsymbol{x}(\cdot\|k)$	discrete trajectories (series of weighted pulses) of states $\boldsymbol{x}$ predicted at $t = t_\mathrm{init} + kT_c$
$\boldsymbol{u}(t\|t_0)$	predicted trajectories of inputs $\boldsymbol{u}$ calculated at t_0
$\boldsymbol{u}^*(t\|t_0)$	optimal trajectories of inputs $\boldsymbol{u}$ calculated at t_0
$\boldsymbol{u}(\cdot\|k)$	discrete trajectories (series of weighted pulses) of inputs $\boldsymbol{u}$ predicted at $t = t_\mathrm{init} + kT_c$
$\boldsymbol{y}(t\|t_0)$	predicted trajectories of outputs $\boldsymbol{y}$ calculated at t_0
$\boldsymbol{y}^*(t\|t_0)$	optimal trajectories of outputs $\boldsymbol{y}$ calculated at t_0
$\boldsymbol{y}(\cdot\|k)$	discrete trajectories (series of weighted pulses) of outputs $\boldsymbol{y}$ predicted at $t = t_\mathrm{init} + kT_c$

Offshore Applications

$\boldsymbol{p}_\mathrm{load}$	Cartesian position of the payload, e.g. $\boldsymbol{p}_\mathrm{load}^{ned} = (n_\mathrm{load} \quad e_\mathrm{load} \quad d_\mathrm{load})^\mathrm{T} \in \mathbb{R}^3$
$\boldsymbol{p}_\mathrm{tip}$	Cartesian position of the crane tip, e.g. $\boldsymbol{p}_\mathrm{tip}^{root} = (x_\mathrm{tip} \quad y_\mathrm{tip} \quad z_\mathrm{tip})^\mathrm{T} \in \mathbb{R}^3$
$\boldsymbol{\rho}$	vector of crane actuator variables, i.e. $\boldsymbol{\rho} \in \mathcal{P} \subset \mathbb{R}^4$
$\boldsymbol{q}$	vector of crane joint variables, i.e. $\boldsymbol{q} \in \mathcal{Q} \subset \mathbb{R}^4$
$\boldsymbol{\xi}$	vector of vessel variables mapping its pose resp. deflection, i.e. $\boldsymbol{\xi} \in \mathbb{R}^6$
$\mathcal{P}$	admissible set of actuator variables $\mathcal{P} \subset \mathbb{R}^4$
$\mathcal{Q}$	admissible set of joint variables with $\mathcal{Q} \subset \mathbb{R}^4$

H_s	significant wave height, $[H_\mathrm{s}] = \mathrm{m}$
ω_p	wave spectrum's peak frequency, $[\omega_\mathrm{p}] = {}^{\mathrm{rad}}/_{\mathrm{s}}$
ves	identifier indicating quantities referring to the vessel
$\boldsymbol{O}-\boldsymbol{e}_1\boldsymbol{e}_2\boldsymbol{e}_3$	reference frame defined by its origin $\boldsymbol{O}$ and three unit vectors $\boldsymbol{e}_i \in \mathbb{R}^3,\ i = 1, 2, 3$ representing the frame axes
$\boldsymbol{p}_\mathrm{b}^{cs}$	position of a point or body b with respect to frame cs, i.e. $\boldsymbol{p}_\mathrm{b}^{cs} \in \mathbb{R}^3$
$\boldsymbol{o}_\mathrm{b}^{cs}$	orientation of a body b with respect to frame cs, i.e. $\boldsymbol{o}_\mathrm{b}^{cs} \in \mathbb{R}^q$ where $q \in \{3, 4\}$ depending on whether Euler-angles or quaternions are utilized
$\boldsymbol{\eta}_\mathrm{b}^{cs}$	pose (position + orientation) of a body b with respect to frame cs, i.e. $\boldsymbol{\eta}_\mathrm{b}^{cs} = ((\boldsymbol{p}_\mathrm{b}^{cs})^\mathrm{T}\ (\boldsymbol{o}_\mathrm{b}^{cs})^\mathrm{T})^\mathrm{T} \in \mathbb{R}^{3+q}$ where $q \in \{3, 4\}$ depending on $\boldsymbol{o}_\mathrm{b}^{cs}$
$\mathbf{R}_{cs_2}^{cs_1}$	rotation matrix between two frames cs_1 and cs_2, i.e. $\mathbf{R}_{cs_2}^{cs_1} \in SO(3)$
$\mathbf{T}_{cs_2}^{cs_1}$	homogeneous transformation matrix between two frames cs_1 and cs_2, i.e. $\mathbf{T}_{cs_2}^{cs_1} \in \mathbb{R}^{4\times4}$ and $((\boldsymbol{p}_O^{cs_1})^\mathrm{T}\ 1)^\mathrm{T} = \mathbf{T}_{cs_2}^{cs_1}((\boldsymbol{p}_O^{cs_2})^\mathrm{T}\ 1)^\mathrm{T}$ for any point $\boldsymbol{O} \in \mathbb{R}^3$
$\boldsymbol{\theta}_{rpy}$	Euler angles (roll-pitch-yaw), i.e. $\boldsymbol{\theta}_{rpy} = (\phi \quad \theta \quad \psi)^\mathrm{T} \in \mathbb{R}^3$
$\boldsymbol{\zeta}_{DH,i}$	Denavit-Hartenberg (DH) parameters associated with link L_i of a serial manipulator, i.e. $\boldsymbol{\zeta}_{DH,i} = (d_i \quad \vartheta_i \quad r_i \quad \alpha_i)^\mathrm{T} \in \mathbb{R}^4$

Mathematical Notation

x	scalar $x \in \mathbb{R}$
$\boldsymbol{x}$	vector $\boldsymbol{x} = (x_1\ \dots\ x_u)^\mathrm{T} \in \mathbb{R}^u$
$\mathbf{X}$	matrix $\mathbf{X} = (x_{i,j})_{1\le i\le u, 1\le j\le v} = \begin{bmatrix} x_{1,1} & \dots & x_{1,v} \\ \vdots & \ddots & \vdots \\ x_{u,1} & \dots & x_{u,v} \end{bmatrix} \in \mathbb{R}^{u\times v}$
x_i	element x_i of vector $\boldsymbol{x} \in \mathbb{R}^u$ with $i \in [1, u]$
$x_{i,j}$	element $x_{i,j}$ of matrix $\mathbf{X} \in \mathbb{R}^{u\times v}$ with $i \in [1, u]$, $j \in [1, v]$
$\dot{\boldsymbol{x}}$	first derivative of a variable $\boldsymbol{x}$ with respect to time t, i.e. $\dot{\boldsymbol{x}} = \frac{\mathrm{d}}{\mathrm{d}t}\boldsymbol{x}$
$\ddot{\boldsymbol{x}}$	second time derivative of variable $\boldsymbol{x}$, i.e. $\ddot{\boldsymbol{x}} = \frac{\mathrm{d}^2}{\mathrm{d}t^2}\boldsymbol{x}$
$\boldsymbol{x}^{(k)}$	k-th time derivative of variable $\boldsymbol{x}$, i.e. $\boldsymbol{x}^{(k)} = \frac{\mathrm{d}^\mathrm{k}}{\mathrm{d}t^k}\boldsymbol{x}$
$\boldsymbol{x}^{(\boldsymbol{k})}$	vectorial time derivative of order $\boldsymbol{k} = (k_1\ \dots\ k_u)^\mathrm{T}$, i.e. $\boldsymbol{x}^{(\boldsymbol{k})} := \left(x_1^{(k_1)}\ \dots\ x_u^{(k_u)}\right)^\mathrm{T} = \left(\frac{\mathrm{d}^{k_1}}{\mathrm{d}t^{k_1}}x_1\ \dots\ \frac{\mathrm{d}^{k_u}}{\mathrm{d}t^{k_u}}x_u\right)^\mathrm{T}$
$\|\boldsymbol{x}\|_1$	1 norm of vector $\boldsymbol{x}$, i.e. $\|\boldsymbol{x}\|_1 = \sum_{i=1}^u \lvert x_i\rvert$
$\|\boldsymbol{x}\|_2$	Euclidean norm of vector $\boldsymbol{x}$, i.e. $\|\boldsymbol{x}\|_2 = \sqrt{\sum_{i=1}^u x_i^2}$
$\|\boldsymbol{x}\|_\mathbf{A}$	Matrix norm of vector $\boldsymbol{x}$, i.e. $\|\boldsymbol{x}\|_\mathbf{A} = \boldsymbol{x}^\mathrm{T}\mathbf{A}\boldsymbol{x}$

$L_{\boldsymbol{f}}h(\boldsymbol{x})$	first Lie derivative of a real-valued function $h(\boldsymbol{x})$ along a vector field $\boldsymbol{f}(\boldsymbol{x})$, i.e. $L_{\boldsymbol{f}}h_j(\boldsymbol{x}) = \frac{\partial h_j(\boldsymbol{x})}{\partial \boldsymbol{x}}\boldsymbol{f}(\boldsymbol{x})$
$L_{\boldsymbol{f}}^k h(\boldsymbol{x})$	k-th Lie derivative of a real-valued function $h(\boldsymbol{x})$ along a vector field $\boldsymbol{f}(\boldsymbol{x})$, which satisfies the recursion $L_{\boldsymbol{f}}^k h(\boldsymbol{x}) = \frac{\partial\left(L_{\boldsymbol{f}}^{k-1}h(\boldsymbol{x})\right)}{\partial \boldsymbol{x}}\boldsymbol{f}(\boldsymbol{x})$ with $L_{\boldsymbol{f}}^0 h(\boldsymbol{x}) = h(\boldsymbol{x})$
$L_{\boldsymbol{g}}L_{\boldsymbol{f}}h(\boldsymbol{x})$	nested Lie derivative of a real-valued function $h(\boldsymbol{x})$ along two vector fields $\boldsymbol{f}(\boldsymbol{x})$ and $\boldsymbol{g}(\boldsymbol{x})$, i.e. $L_{\boldsymbol{g}}L_{\boldsymbol{f}}h(\boldsymbol{x}) = \frac{\partial\left(L_{\boldsymbol{f}}h(\boldsymbol{x})\right)}{\partial \boldsymbol{x}}\boldsymbol{g}(\boldsymbol{x})$
C^k	class of all differentiable functions whose derivatives exist and are continuous up to order k
Π_n	space of all polynomials $P(x)$ of degree n, i.e. $\Pi_n = \{\sum_{i=0}^{n} a_i x^i \,\vert\, a_i \in \mathbb{R},\, a_n \neq 0\}$
$\boldsymbol{\chi}$	vector of free variables during optimization, $\boldsymbol{\chi} \in \mathbb{R}^{n_{\text{opt}}}$
ϕ_{acq}	acquisition function $\phi_{\text{acq}} : \mathbb{R}^{n_{\text{opt}}} \to \mathbb{R}$ used during Bayesian optimization

Chapter 1

Introduction

The maritime sector plays an important role in global economic output as well as employment. Regarding the year 2010, the Organisation for Economic Co-operation and Development (OECD) reports a gross added value (GAV) of USD 1.5 trillion worldwide and jobs amounting to 1 % of global work force for ocean-based industries [46]. In the same study, the importance of the maritime sector is projected to remain unchanged through 2030; a fact reflected in the national *maritime agenda 2025* [28]. Traditionally, the offshore oil and gas industry has been the area recording the highest revenues among maritime branches, making up for 34 % of its total GAV [46]. With the public as well as statutory focus on a more environmentally friendly and sustainable energy system, this may change in the near future. While the latest *world energy outlook* published by the International Energy Agency (IEA) sees the demand in all fossil energy sources peeking before 2050 [81], the offshore oil and gas industry is expected to take on a major bridging role such that overall consumption will only fall gradually. In fact, the demand in oil and gas is predicted to be at comparable levels in 2022 and 2050 according to the Stated Policies Scenario (STEPS) [81]. Taking into account that oil fields at shallow sea are slowly depleting, continued investments and technical advancements will be necessary to upheld supply and harness resources at deeper waters. At the same time, most studies suggest that offshore wind energy will emerge as an important contributor to the energy mix of the future. This applies in particular to regions where photovoltaics or onshore wind energy are less profitable, e.g. in Japan. By 2030, the offshore wind energy's share on the total GAV of the ocean economy is predicted to increase up to 8 % [46]. Furthermore, projections in [81] indicate that around the same time 30 % of the annually added wind capacity will be offshore. According trends can already been observed today. Until 2022, an offshore wind capacity of 64 GW was installed, with more than half of it added over the last three years (2020-2022) [71]. Another 130 GW are expected to be commissioned by 2027 [71]. Yet, in most markets offshore wind energy remains among the least competitive sources of energy (cf. value-adjusted levelized cost of electricity (VALCOE) in [81, p. 301]), due to high costs both during installation and operation. The latter mainly stems from the increased service and maintenance costs offshore. Technical challenges arise from wind farms at deeper seas, which often operate in harsher weather conditions and will increasingly be reliant on floating plants. In this context, synergies

between the offshore wind as well as offshore oil and gas industries are pointed out in [78], e.g. in relation to maintenance and inspection practices for offshore platforms.

Cranes have been long used across various industry sectors like transportation, manufacturing or construction. Offshore lifting and handling applications include but are not limited to maintenance of offshore energy plants, installation of drilling sites and ship-to-ship cargo transfer. Depending on the working environment and task, the employed cranes differ in structure, operational space, lift capacity, actuator technology or degrees of freedom (DoF). Trolley jib tower cranes commonly found at construction sites possess a large slender structure with three electric actuated DoF, namely cargo hoisting/lowering, jib slew, and trolley translation [49]. In contrast, shipboard cranes installed at vessels or floaters are traditionally built more compact and feature hydraulic actuators, as to prevent losses in payload capacity due to the moving (tilting) crane base. A definition of different shipboard cranes is included in e.g. [48]. In scope of this thesis, a so-called knuckle boom crane (KBC) is considered, an example of which is depicted in Fig. 1.1. Due to its additional DoF (knuckle jib), the KBC provides increased flexibility during payload handling and allows for minimal working radii. Main boom and knuckle jib are driven by hydraulic cylinders, i.e. the luffing resp. the folding cylinder(s), which enable manipulation of the vertical and radial tip position. The crane's angular orientation is adjusted by means of the hydraulically actuated slewing bearing. Finally, the suspended payload can be hoisted/ lowered using a hydraulic winch, usually installed on the crane frame. Modern designs furthermore incorporate assistant systems like active heave compensation (AHC) or automated tensioning solutions, cf. section 1.3. Established manufacturers of KBC include Liebherr-MCCtec (Liebherr-International Deutschland GmbH, Biberach, Germany), MacGregor (Cargotec Oyj, Helsinki, Finland), NOV (National Oilwell Varco, Houston, USA) and Palfinger Marine (Palfinger AG, Bergheim, Austria) among others.

Fig. 1.1: Knuckle boom crane onboard a supply vessel – image kindly provided by MacGregor

1.1 Challenges in Crane-based Offshore Operations

The feasibility of offshore crane operations is generally dependent on the handling task as well as a variety of parameters such as the transferred payload or the expected weather conditions. For instance, the safety requirements for personnel transportation are higher than for the transfer of equipment or general cargo. Also, the available clearance as well as the target location (which itself may float, e.g. in a ship-to-ship scenario) play an important role during risk assessment. An extensive list of significant parameters has been compiled by the DNV[1] in its DNV-ST-N001: *Marine operations and marine warranty* standard [50]. Wind has a direct impact on the safety of the lifting operation. Similar, the sea swell continuously excites the vessel and thus the crane base. As a result of the vessel's wave-induced motions, the suspended payload oscillates, see Fig. 1.2. While lifting off or unloading on a floating vessel, the hosting speed has to be adapted

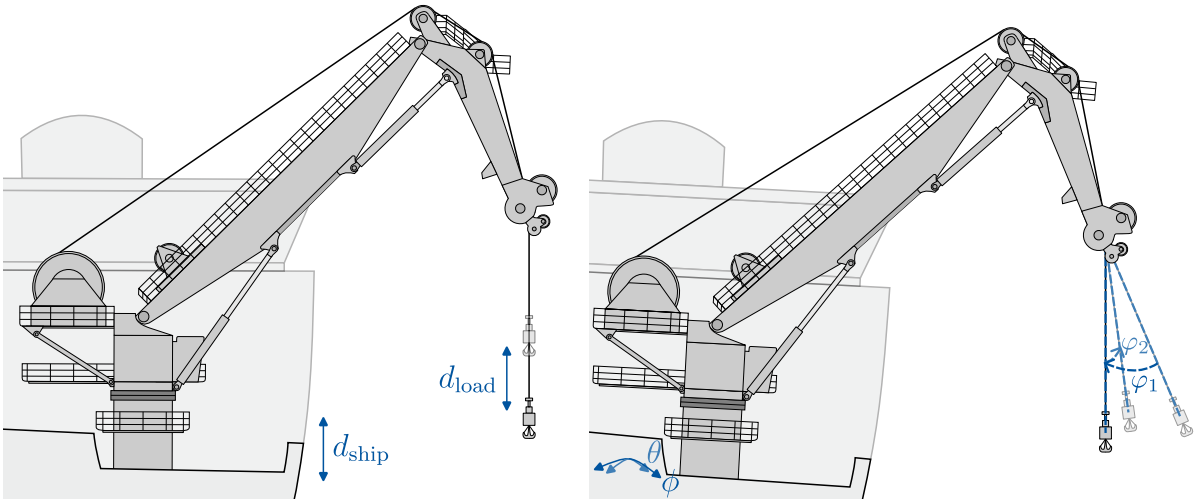

(a) Vertical payload oscillation **(b)** Spatial payload oscillations

Fig. 1.2: Payload oscillations due to the vessel's heave (a) as well as rolling and pitching (b) motions. For a definition of the depicted variables, please refer to chapter 3.

in order to account for the vertical movement of the vessel, i.e. its *heave* motion. If ignored, the payload may otherwise crash onto the deck repeatedly, cf. Fig. 1.2a. Heave disturbances are also of primary concern when lifting subsea, as they load and can damage the hosting rope. Spatial payload oscillations have a detrimental effect on both the safety and efficiency of crane operations, too. These oscillations, also known as payload sway, stem from the crane vessel's *rolling* and *pitching* motions, actuation of the

[1]The DNV (DNV, Høvik, Norway) is an international accredited registrar and classification society, providing services across the maritime sector. It was established as a merger between Det Norske Veritas (Norway) and Germanischer Lloyd (Germany) in 2013, which was then known as DNV GL.

crane or an initial payload deflection during lift-off, cf. Fig. 1.2b. Maximum admissible sway angles therefore constitute an exemplary limiting condition for crane operations, which should be assessed during planning [50]. Since the vessel acts as a low pass filter with regards to the wave excitation, the effect of the sea swell on the crane operation is furthermore dependent on the vessel type and its hydrodynamic characteristics. Moreover, it is common practice to derate the crane's lifting capacity given by its safe working load (SWL) as a function of not only the lifting radius but also the sea state [52]. The above considerations can be aggregated in a so-called *weather window*, which specifies the environmental conditions under which a safe crane operation is feasible. For example, the installation of a wind turbine may be restricted to times with gust speeds less than $8\,\mathrm{m/s}$ and significant wave heights (H_s, cf. section 3.2) not exceeding $1.5\,\mathrm{m}$ [186]. For the transport of personnel via shipboard cranes, the DNV stipulates average wind speeds below $10\,\mathrm{m/s}$ and significant wave heights under $2\,\mathrm{m}$ [55]. Adverse weather is indicated for $H_\mathrm{s} \geq 2.5\,\mathrm{m} - 3.5\,\mathrm{m}$ depending on the scenario[2] [50]. The sensitivity of offshore crane operations to weather is directly linked to the high costs associated with installation, maintenance or cargo transfer at sea.

Adding to overall costs is the fact that today's crane operations are still controlled manually. Besides the crane operator, who performs the lift from a cabin mounted on the crane tower, additional personnel (slingers, signallers) are usually required to ensure proper crane operation [85]. The crane operator handles the payload via a joystick-based interface, allowing to directly manipulate the crane's (hydraulic) actuators. The crane operator is furthermore responsible for adhering to the relevant capacity charts, dynamic limitations or any operating instructions issued by the manufacturer. Most importantly, the crane operator must ensure the safety of persons and equipment not involved in the crane operation. For offshore lifts, this involves taking into account and continuously compensating for environmental loads like wind or wave disturbances. Hence, the safety and efficiency of crane operations is largely dependent on both the operator's ability and experience. As a consequence, the offshore sector is reliant on highly trained personnel, see also [86]. Yet, the shortage of skilled workforce observed across industries has also impacted the offshore sector, a situation that will probably be highlighted by the projected increase in labor demand both in the offshore oil and gas industry (126 %) as well as the offshore wind industry (1257 %) [46].

1.2 Motivation for Automated Payload Control

Increasing the level of automation (LoA) [158] offers the possibility of a simplified lifting operation. Adding automated safety or assistance functions relieves the operator during payload handling and, in the long term, will allow extending the operating window. Similar

[2]The specification assumes a monohull vessel with length $\geq 80\,\mathrm{m}$ and a static hook load $\leq 100 \times 10^3\,\mathrm{kg}$.

effects are already observable for today's AHC systems, which enable operations during more adverse sea states [52]. Just as in assisted car driving, automated functionalities are believed to add to the efficiency and safety of offshore crane operations. It is for this reason, that the latest revision of DIN EN 13852-1:2021 *Cranes – Offshore cranes – Part 1: General-purpose offshore cranes* [48] saw an increase in listed assistance functionalities, reflecting current efforts in both industry and academia. The norm specifies five LoA as given in Tab. 1.1, which are based on the classification of autonomous driving functions in [151]. While perception systems for deck motion detection, hook position detection

Table 1.1: Levels of automation according to [48]

Level 0	**Level 1**	**Level 2**	**Level 3**	**Level 4**
Fully operator controlled	Operator assisted	Partly automated	Highly automated	Fully automated

or people detection may be rated as Level 0 functionalities, approaches for automated payload stabilization by means of active heave compensation (AHC) or anti-sway control (ASC) systems are examples of Level 1 - Level 2 solutions. Advanced functions of higher LoA further include handsfree slinging or automatic collision prevention [48]. Automated slinging offers the possibility of removing personnel from hazardous areas and ultimately reducing the workforce. Automatic collision prevention would represent a major step towards safe handling operations. Yet, precise payload control in the face of harsh weather conditions remains a key enabling factor for both functionalities. With both oil and gas rigs as well as offshore wind farms moving to deeper seas, the impact of wind and waves on crane operations will intensify. This is especially true for the increasing number of floating installations. Extending the weather window through automation is thus a major concern resp. enabler for most maritime industries.

As a side effect of the accompanying increase in sensor and perception systems, it may furthermore become feasible to implement decentralized handling concepts, i.e. controlling the crane system from a remote location (teleoperation). While the technical prerequisites are multifaceted, corresponding solutions approaching LoA 3 possess the potential to greatly reduce the costs of offshore operations, since on site personnel can be pared down and crane operators can be used more effectively by eliminating standby times between lifts. Cutting costs would further promote economic operation of e.g. offshore wind turbines, whose erection and maintenance costs are currently hampering large-scale expansion of the installed capacity [81].

Considering that accidents at sea result in high damage, costs or danger to human life, automatization solutions are required to be fail-safe and robust. Accordingly, specialized assistance systems supporting a human operator during specific tasks (LoA 1-3) may shape advancements in crane technology for the foreseeable future. They are, nonetheless,

an opportunity to not only increase safety during offshore operations, but also to improve the attractiveness of the crane operator profession. The latter gains importance in light of the aforementioned shortage of skilled workers. Besides technological progress, further automation will also depend on regulatory changes.

In line with the above reasoning, the presented work aims at supporting the crane operator through layered control loops for payload stabilization and improved handling. In this context, a payload-centric approach to controller synthesis is proposed. Next, the state of the art with regard to crane automatization is outlined, before specific research questions are formulated in section 1.5.

1.3 State of the Art

The task of moving a suspended payload from one point to another forms the basis of any crane operation, irresp. of the crane type or its area of application. Accordingly, there is a vast amount of literature on crane control as well as related products. While the focus of this thesis is on offshore lifting and handling operations, it is sensible to also consider automation concepts for onshore cranes as a reference. A non-exhaustive overview of popular control approaches is included in section 1.3.1. Relevant work for the offshore sector is summarized in section 1.3.2. Contributions to the field of (partially) automated offshore cranes can be broken down into three categories: the automation of low-level crane functionalities, disturbance rejection and high-level operational procedures. The objective of payload stabilization is usually subdivided into two problems: active heave compensation (AHC) and anti-sway control (ASC). Strategies for AHC aim to decouple the vertical payload position from the vessel's heave motion (cf. Fig. 1.2a), whereas approaches of ASC try to reduce payload sway induced by the vessel's rolling and pitching motions (cf. Fig. 1.2b). Since the addressed scenarios, i.e. the combination of crane type, set of manipulated variables and environmental disturbances vary across sources, most findings can not be compared quantitatively. Instead, these sections serve as an overview over existing and proposed solutions to improve the handling task with a focus on automatic control. An assessment in the context of the shipboard KBC considered hereafter is provided in section 1.4.

1.3.1 Crane Control Onshore

Tower-, gantry- and boom cranes have been applied throughout various economies for decades. Although differing in structure or DoF, the typically underdamped dynamics of the suspended payload present similar challenges during crane operation. Payload oscillations constitute a primary concern as they reduce both efficiency and safety of

the handling task. While payload sway is already induced by inertia forces during crane actuation, oscillations may be aggravated by exogenous disturbances like wind loads. An early review of approaches for payload control is given in [1]. For an updated list the reader is referred to [142]. The following overview is limited to the most popular control schemes in land-based crane operations. Many more are referenced in [1], [141], [142].

If the handling task is subject to only minimal disturbances, open-loop control approaches can be assessed to compensate for motion-induced payload sway. Since most cranes are operated manually, a considerable amount of contributions is devoted to *input shaping* techniques. The original control signal is convolved with a pulse sequence so that the resulting input excites less payload oscillations. An overview for different crane types is included in [23]. While incorporation of the crane operator is straightforward, challenges arise due to the nonlinear payload dynamics, which require extension of the originally linear theory. Characteristic of all open-loop solutions is the drawback that neither disturbances nor residual oscillations due to imperfect modeling can be tackled. In this context, closed-loop control may improve handling efficiency considerably. Nonlinear concepts include but are not limited to LYAPUNOV-designs [25], [135], [184] or *sliding mode* control [6], [19], [187]. The latter offers increased robustness against uncertain parameters, e.g. with respect to payload or free cable length. However, actuator stress due to the switching characteristic of the control law should be monitored if applied on a real crane. Another class of controllers is based on the *differential flatness* of many crane systems [102]. For this purpose, a set of virtual input and output variables is introduced for which the system dynamics are linear. The system can then be controlled by means of a simple linear state feedback. Solving for the original system inputs results in a non-linear feedback law that can be extended to yield a two-degree-of-freedom structure. Examples of corresponding control concepts can be found in [103], [185] for gantry cranes respectively [11], [128] for boom cranes. Depending on the considered system topology, forces acting on the suspension point, control voltages or commanded velocities for the crane actuators are calculated. *Optimization-based* approaches for ASC are researched in [10], [30]. In both contributions, a model predictive controller (MPC) is implemented that allows to explicitly account for actuator limitations while damping payload oscillations. In [30] the crane system is linearized about the pendulum's lower equilibrium point, whereas the authors in [10] expand around a prescribed reference trajectory. By this means, linear MPC are obtained, which at the expense of prediction accuracy enable real-time implementation. A combined approach for tracking and anti-sway control is proposed in [130]. The scheme incorporates a flatness-based controller alongside an optimal (MPC-like) trajectory generator, which is subsequently tested on a mobile harbor crane.

1.3.2 Crane Control Offshore

Shipboard cranes differ from their onshore counterparts particularly in the increased level of exogenous disturbances. Most importantly, the persistent excitation of the crane base resulting from the vessel's wave-induced motions entails additional payload oscillations that can greatly afffect operational safety and efficiency. It is for this reason that open-loop control approaches have seen less interest in the automatization of offshore cranes. Yet, various closed-loop topologies have been proposed for different objectives, scenarios or crane types. An overview is included hereafter, where some effort has been made to categorize the relevant literature.

Low-Level Automatization: With most offshore cranes being driven hydraulically, a considerable amount of work has focused on either performance or energy efficiency of the hydraulic system. For example, algorithms for controlling the hydraulic actuators are described in [104], [133]. In [133], sequential control of the balancing valves is proposed to improve power transmission in the hydraulic path of the slew drive. In contrast, the authors in [104] present a virtual decomposition control for decoupling load pressure and load force in hydraulic cylinders, which leads to a reduction in the required energy. The energy saving potential when utilizing pump controlled cylinder drives is analyzed in [99]. Recently, a comparative study of energy efficiency in motor-controlled and vale-controlled cylinders was published in [188]. Digital hydraulics are evaluated for both control performance and energy consumption in [56], where the authors research a novel multi-chamber cylinder and compare it to a differential cylinder traditionally found in KBCs. Advanced control schemes (linear model predictive controller) are then applied in [57] to operate the discrete displacement cylinders. The more general task of motion control in a hydraulic KBC is addressed by e.g. [15], [165], [167]. Further research towards automated tool point resp. crane tip control is presented in [14], [90], [166]. In industry, additional low-level functionalities have been automatized to increase safety during crane operations. Among others, common features are automatic overload protection systems (AOPS) [127] or constant tension control of the winch [121].

Active Heave Compensation: Systems for vertical payload stabilization have been the subject of numerous publications and are usually subdivided into *active* and *passive* approaches [183]. While passive solutions rely on constructive extensions of the crane kinematics, active concepts are based on feedback of the vessel's measured heave motion and consequent actuation of e.g. the crane's main winch [3]. Passive systems integrate a spring-damper element (usually in form of a hydraulic cylinder with hydropneumatic accumulator) between vessel and payload [89]. If the resonant frequency is selected carefully, a mechanical decoupling of the payload movement from the exciting wave motion is achieved. The spring-damper element therefore acts as a low-pass filter [147]. The hydraulic cylinder system can be installed directly on the winch, via pulleys in the hoist line or close to the payload on the crane hook [58]. The comparatively simple

design of passive solutions offers a cost-effective option for heave compensation. Yet, the authors in [77] found that compensation efficiency of related systems is limited to 65 % at most. In the case of active approaches, four topologies can be distinguished depending on the part of the crane actuated for heave compensation, refer to e.g. [3] for an overview. In *Winch Drive* AHC and *Flying Sheave* AHC systems the crane's main winch is used to directly control the vertical payload position, see e.g. [129]. The winch is continuously actuated contrary to the ship's heave motion. Whilst the compensatable payload displacement is unlimited in theory, increased power consumption [148] and cable stress [155] are associated with according AHC concepts. Furthermore, the winch's dynamic behavior is key for the achievable compensation performance. A different approach is adopted by *Nodding Boom* AHC and *Sub-A Frame* AHC systems, in which the crane boom(s) or additional kinematic structures are moved to compensate for wave-induced deviations in the vertical payload position [3], [140]. As a result, the winch drives are utilized less. On the downside, the maximum compensatable heave amplitude is limited by the crane's kinematic constraints. Moreover, such systems require actuation of the remaining crane actuators, which are usually governed by slower dynamics. In comparison to passive approaches, AHC techniques are suitable for a wider range of applications. For example, active solutions may be adopted to compensate for relative heave motions during a ship-to-ship scenario [122], [157]. The same is not viable with passive compensation systems. Besides conventional control methods, higher control concepts such as model predictive controller (MPC) are increasingly being implemented to derive suitable signals for winch actuation as well as to realize feedback of the measured sea state [108], [148], [183], [189]. An estimation of the vertical vessel motion is derived based on inertial measurement units (IMU) [107] or motion reference units (MRU) [72], usually in conjunction with digital signal processing [72] or model-based observers like the Kalman filter [109]. Feasibility of MPC-based AHC was demonstrated in [147], where the control performance is verified in actual deep-sea lifts. In fact, AHC systems of varying complexity are now established in industrial practice and are offered by various manufacturers [106], [118], [122], [153]. Common to most commercial products is a direct actuation of the main winch, a prescribed weather window as well as a derated load capacity during AHC operation.

Anti-Sway Control: Approaches to AHC are focused on the vertical payload position, thus neglecting spatial payload oscillations caused by the vessel's rolling and pitching motions. In this context, techniques for anti-sway control (ASC) are researched. Due to the increase in system complexity, e.g. in the required perception and control topology, no solution to ASC is established in today's offshore operations. However, various strategies for ASC are reported in literature, where the topic has seen increased interest over the last years. Recently, three commercial products for ASC have been introduced as well, each relying on structural extensions of the crane system and additional actuators [18], [126], [163]. In contrast, concepts assessed in academia typically consider the crane actuators for ASC. The two approaches are not mutually exclusive and are thus described hereafter.

In [177] sway energy is dissipated by actuating both crane tip and cable length depending on the relative position between payload and crane tip. Modeling both crane and payload as a pendulum system with moving suspension point, an algorithm computing basic acceleration trajectories is derived and verified for initial payload deflections as well as simple disturbances. Vertical payload oscillations are neglected within the simulations, as is the tilting of the crane base during wave excitation. Due to the actuation of the cable, integration of AHC techniques is not straightforward. A simple method incorporating both ASC and AHC capabilities is presented in [32], where both objectives are addressed separately. The crane tip is constantly moved in direction of the deflected payload, thereby dissipating energy from the payload oscillation. As a simplifying assumption, the crane tip is controlled in its Cartesian workspace while operating at a constant (maximum) velocity. The proposed control scheme is thus independent of the specific crane type. Yet, dynamic effects of the crane actuators as well as kinematic constraints can not be mapped. In [174], a cascaded topology of two linear controllers is proposed for payload stabilization with a KBC. While the outer control loop is designed to damp out payload oscillations, the layered controller tracks the commanded crane tip accelerations. For control synthesis, the crane system is linearized and transformed to a second-order system with prescribed damping characteristics by virtue of a static state feedback. The angular position and velocity of the deflected payload as well as the effective (free) cable length are derived via a marker-based camera system and an EKF. The Cartesian tip accelerations calculated by the payload controller are filtered and transformed to the actuator space. Tracking of the reference signals is realized with the help of propotional-derivative (PD) controllers. Although not covered, the winch actuator could be used for AHC, as only planar motions of the crane tip are considered for ASC. In this case, the coupling with the outer control loop would have to be investigated. Transferability of the control scheme to continuous swell excitations or tuning of the damping factor remain unanswered. To guarantee asymptotic stability also in the case of persistent rolling motions of the vessel, the authors in [119] derive a nonlinear control law based on a LYAPUNOV design. The system is simplified to the two-dimensional case with a single roll disturbance. Furthermore, the examined crane features only one main boom. As manipulated variables a torque acting on the boom as well as an additional cable force are utilized, which in a demonstrator setup are then applied via servo motors. Besides the reduced number of DoF, the coupled nature of a three-dimensional payload oscillation as well as actuator constraints are neglected. A similar albeit three-dimensional scenario is assessed in [83], where a (second-order) sliding mode controller is proposed for a wire luffing boom crane. The controller is tested in simulation for simplified sine-wave disturbances of small amplitude[3] and varying payloads. A depiction of the actuator signals (joint torques) is not included, nor is information on the required sensor signals. An optimization-based approach to ASC is assessed in [101], where a MPC is implemented

[3]The contribution specifies heave amplitudes of less than 2 cm and vessel deflections smaller 0.5° at periods of approximately 5 s, which in context of a real-world crane system seems questionable.

alongside a feedforward controller. Interaction of the two strategies remains unclear, as does the disturbance trajectory used for prediction. Furthermore, the boom angle of the ship crane is used as manipulated variable. Dynamic effects are thus neglected.

Alongside contributions from the scientific community, the increased demand for spatial payload stabilization has spawned related products from several crane manufacturers. At the time of writing, NOV has presented its *Anti-Sway Rotator* (*ASR*) [126], a cone-shaped device mounted to the crane tip that includes additional vision and actuators between tip and payload in order to reduce payload deflections. In addition, the payload can be rotated 360°, which should increase efficiency during deck operations, e.g. during vessel loading or unloading. While no information on the applied control scheme are public, commissioning requires tuning and function testing in order to adapt the solution to the vessel's dynamic characteristics. Compensation performance is likely limited by the built-in actuators both in terms of disturbance dynamics and admissible payload. Similar, MacGregor has introduced the *Colibri™* crane series in 2023, which adds a lightweight articulation on the folding jib of the traditional KBC. The hydraulic tool handles compensation in the horizontal plane only, while heave compensation is realized by classical AHC winches. The *Colibri™* system is market for a reduced SWL of 3 T to 5 T, while the operational weather window is not specified. A different approach is taken by Barge Master (Barge Master B.V., Rotterdam, Netherlands) with the *T40* ship crane, which features a motion-compensated crane base [18]. The hydraulic pedestal directly inverts the vessel's roll, pitch and heave motion based on measurements from an MRU. As a result, the crane tip is deflected less, which reduces payload sway. While the manufacturer specifies a maximum SWL of 20 T and a SWL of 5 T at sea elevations up to $H_\mathrm{s} = 3\,\mathrm{m}$, it should be noted that the compensation approach is open-loop, i.e. swaying of the payload caused by residual excitations of the crane or gust cannot be damped.

High-Level Automatization: In the context of offshore cranes, there are only a few contributions related to the automation of operational tasks, with the tracking of planned payload trajectories being the most common example for a LoA 2 and above functionality. In [84] a tracking controller based on a sliding mode design is proposed for a gantry type crane on board a supply vessel. The authors assess a two-dimensional scenario with simplified swell disturbance and uncertain parameters in form of the payload mass resp. cable length. The control topology requires transforming the reference trajectories in the actuator space first. Furthermore, the system model is linearized about an operating point in order to derive the control law. Tracking performance may therefore vary depending on the system state. Furthermore, implications of actuator constraints as well as the actuator stress arising from the switching behavior of the utilized first-order sliding mode controller would have to be investigated in practice. Applying the same cascaded control topology as for ASC (cf. [174]), a controller for payload positioning is presented in [176]. Here, the outer control loop is closed with a nonlinear MPC (NMPC) to account for actuator limitations and facilitate trajectory tracking. The control scheme is based on the idea that a sway-free payload can be handled safely through positioning

the crane tip, i.e. the positions of crane tip and payload will only differ by a vertical offset equal to the free cable length as long as the bandwidth of the layered damping controller is fast enough. Noteworthy, this quasi-static approach to payload handling favors safety over operational efficiency. With respect to implementation, tuning of the layered damping characteristics remains challenging as is the real-time feasibility of the model predictive controller. The control scheme was tested in simulation for initial payload deflections. Aside from automatic control, the vision of autonomous crane operations does also require advances in automated planning. While related topics are heavily researched e.g. in context of autonomous driving, almost no approaches tailored to ship cranes are reported. An exception is [29], where the authors explore the problem of finding time optimal trajectories for an offshore luffing boom crane. For the considered planar problem, two reference polynomials of 9^{th} order are computed for the payload trajectory based on a flat analysis of the crane system. Adherence to actuator constraints (limited velocity and acceleration of both crane boom and cable) as well as operational constraints (bounded payload deflection) is addressed through time scaling, postulating that slower payload trajectories correlate with less dynamic actuator signals. While this is intuitive for the disturbance-free case, it does not generally hold for a crane system subject to wave disturbances, cf. chapter 3 and chapter 4, respectively.

1.4 Deficit

Automatization of crane systems is addressed extensively both in industry and academia. While cranes may differ in structure, lift capacity, actuator technology or degrees of freedom (DoF), swinging motions of the suspended payload are detrimental to handling efficiency as well as operational safety across applications. Yet, the authors in [1] found a discrepancy between the vast body of scientific work and the amount of solutions established in industrial practice. Arguably, the lack in technology readiness level of many proposed control schemes stems from oversimplifying assumptions during controller synthesis, intransparent transient controller behavior, ignored actuator constraints or improper LoA. Furthermore, the sensor and actuator technology required for more sophisticated controllers may not be readily available. Counterexamples are open-loop ASC in gantry-type cranes and AHC systems for offshore cranes, both of which are widely adopted. Remaining deficits ($\mathtt{D}_1$-$\mathtt{D}_4$) are highlighted hereafter.

($\mathtt{D}_1$) Applicability of previous findings in crane control to offshore KBC is limited.

Offshore crane operations are exposed to persistent wave disturbances that excite the vessel and crane base. As a result of the increase in exogenous disturbances, open-loop approaches like input shaping are not applicable offshore. Due to their fundamentally different actuator concept, transferability of closed-loop topologies proposed for onshore tower or overhead cranes to shipboard cranes is also limited. Compared to general boom

cranes, only a few control strategies for knuckle boom cranes have been proposed in literature, none of which explicitly took advantage of the additional knuckle boom. Hence, further research towards optimal utilization of the KBC's actuators is advisable, e.g. to promote operational efficiency or controller performance.

($\mathtt{D}_2$) Modular controller designs addressing either vertical or horizontal payload oscillations are predominant, whereby the coupling between both motions is ignored.

Currently, the problems of AHC and ASC are tackled separately, which is reflected in the commercial products available today. However, the payload dynamics are highly coupled. Therefore, a unified control topology should be investigated to align the individual crane actuations and boost the damping behavior. Despite reducing the effect of wave disturbances, the introduction of a motion-compensated crane base does not solve the problem of residual, inertia- or wind-induced payload oscillations. Effectiveness and market acceptance of added articulations at the end of the crane kinematics have yet to be evaluated, too. While bypassing limitations of the central hydraulic power unit (HPU) is advantageous, higher costs as well as a reduction in SWL might mitigate benefits. Hence, an automatization solution using only existing actuators may be favorable as long as the sea state does not supersede the dynamic capacities of the crane's hydraulic system. In such case, combining the larger stroke of conventional actuators with the faster response of the referenced compensation units could be assessed to further extend the weather window. On the other hand, this would increase system complexity considerably. Both scenarios suggest that there is a continued need for more capable controllers providing complete payload stabilization.

($\mathtt{D}_3$) Explicit consideration of the sea swell is missing from current control topologies addressing spatial payload stabilization.

The authors in [142] suggest that most contributions in the field lack an adequate representation of the exogenous disturbances, e.g. of the vessel motion. Presumably, an explicit consideration of the wave disturbance is necessary in order to achieve satisfactory control performance during severe sea states. In this context, relying solely on the robustness of, e.g., a sliding mode controller may prove insufficient. Most commonly, the controlled payload response to initial deflections is analyzed. However, this might not be descriptive of the damping behavior during persistent wave excitation. Frequently, harmonic disturbances in form of simple sine-trajectories are investigated, which does also not capture the complex payload motions resulting from realistic wave profiles. Controller performance will always be a function of the sea state, the crane's actuator and kinematic limitations as well as the vessel's hydrodynamic characteristics. Yet, a discussion of related effects is missing from most contributions. Accordingly, no systematic way to indicate controller performance depending on a set of key parameters exists.

($\mathtt{D}_4$) Controller design has focused almost exclusively on damping performance. In contrast, operational safety has seen less attention in the related literature.

Compensating for wave-induced payload sway is a crucial step towards safe handling operations at sea. However, further constraining crane actuation might be necessary depending on the task. For example, limiting the movement of the crane tip or defining maximum payload sway angles is essential when servicing an offshore wind platform in close proximity. Of course, this is in addition to the actuator constraints that any control topology must comply with at all times. In this context, the problem of finding proper, i.e. safe and feasible reference trajectories for both crane and payload has been largely unanswered. Also, the notion of safety has not been addressed from a control perspective. In fact, safety usually requires a holistic approach to both planning and control.

Model predictive control has proven effective both in automated handling tasks on land and in heave compensation during subsea lifts. Implementation in real-world crane systems is facilitated by the ability to consider arbitrary constraints in the optimization-based algorithms. Moreover, MPC naturally extends to the tracking problem. Yet, the nonlinear dynamics of payload and crane hamper real-time feasibility. Linearizing the system equations reduces computational complexity but decreases prediction accuracy at the same time. Furthermore, application of predictive control requires a (short-term) prediction of the sea swell resp. the vessel motion, which to the best knowledge of the author was only attempted for AHC.

1.5 Scientific Contribution

The aim of this thesis is to support the crane operator by means of layered control loops for payload positioning including tailored techniques for state estimation and target selection. In this context, a load-centered approach is explored that transforms the task of payload handling from an indirect manipulation via the crane's actuator space to a direct control in the Cartesian working space. For this purpose, a combined controller design for AHC and ASC is developed to decouple the payload position from the ship and crane motions as efficiently as possible. Predictive controller designs are evaluated both for their proven performance and the possibility to include operational constraints, thus contributing towards safe loading operations.

Research hypothesis: The use of predictive control strategies enables safe payload handling during crane-based offshore operations. Hereby, the payload trajectory is decoupled from both crane and vessel motions, thus mitigating effects of the sea state.

An automatization solution in the above sense holds the potential for more efficient and safer crane operations at sea. In contrast to the hypothesis, however, it is to be expected that the obtainable control performance will decrease with an increase in wave excitation, i.e. at rougher sea states. Any control scheme thus should be assessed in light of the current computing hardware, available sensor technology as well as limitations in

crane kinematics and actuation. In order to explore the working hypothesis and under consideration of the aforementioned deficits, the following research questions ($\mathtt{Q}_1$-$\mathtt{Q}_4$) are covered within the scope of this thesis:

($\mathtt{Q}_1$) How should the control task be formulated within a predictive controller to obtain a real-time capable algorithm while ensuring precise payload handling?

To address $\mathtt{D}_2$, the task of payload stabilization and handling is encoded as an optimal control problem (OCP), which has to be compiled to a real-time feasible code. Three approximations to the OCP are investigated that then yield three MPC. The derived controllers are evaluated with respect to control performance and computational complexity. Because of the model-based nature of the MPC, mapping the characteristics of the KBC is straightforward, cf. $\mathtt{D}_1$. Also, actuator as well as operational constraints can be directly integrated in the control algorithms. By contrast, handling the nonlinear dynamics of crane and payload is challenging, especially in terms of computational times. An elegant way to resolve the model complexity is the crane's differential flatness, which allows to invert the system equations. Difficulties arise from the high relative degree of the crane system and the restriction of flatness-based approaches to square plants, i.e. systems with the same number of inputs and outputs. In this context, the presented work constitutes one of few contributions reflecting on the combination of differential flatness and MPC. Moreover, the differential flatness offers a unique perspective on the effects of swell disturbances on the crane operation. In line with $\mathtt{D}_3$, explicit predictions of the vessel motion along the control horizon are required for all MPC. Extending the signal-oriented approach of [109] to three dimensions, a simple disturbance model is investigated to describe the vessel's heave, pitching and rolling motions. For this purpose, an optimization-based method (moving horizon estimator) is adopted that yields estimates of the current system state.

($\mathtt{Q}_2$) Is it possible to leverage the redundancy of the KBC's kinematics in context of a control system?

A total of four actuators (slew drive, main resp. knuckle boom cylinders and hydraulic winch) may be utilized in order to control the payload in its three translational DoF. The additional knuckle boom does not only add to the crane's flexibility but also allows to realize the same outreach at different crane tip heights. The question which tip height is optimal depends on factors such as the payload to SWL ratio or the handling task. With respect to $\mathtt{D}_1$, a fourth output variable is introduced to solve the overdeterminedness during controller synthesis. Doing so becomes particularly important in the context of a flat controller design. An optimization-based target selector is implemented, by which secondary control objectives can be incorporated in the control topology. An exemplary objective targeting improvements in ASC performance is established based on a manipulation index known from robotics. Closed-loop operation under target selection is compared to the case of a constant tip height.

($\mathtt{Q}_3$) Up to which sea state is it feasible to decouple the payload from the wave excitation?

The compensation of wave-induced disturbances is limited by the accuracy of available sensor technology and the dynamics of the crane actuators respectively the maximum capacity of the crane's hydraulic system. Similar to current AHC solutions, the question up to which sea state payload oscillations can be reliably eliminated is to be answered. For this purpose, simulation series are carried out for different wave spectra. Thereafter, the maximum Cartesian position error of the payload during steady state oscillation is determined as a function of both wave and crane parameters. The results are checked in a robot-based laboratory setup.

($\mathtt{Q}_4$) How can safety be defined and subsequently addressed during planning and control?

In $\mathtt{D}_4$ the notion of operational safety is brought up, which in connection with offshore automatization has not yet been fully standardized. Some effort has been made to avoid loading of the crane cable during subsea lifts or to automatically detect overloading of the crane structure. Apart from some guidelines, the safety of both man and machinery falls under the responsibility of the crane operator. An exposition to safety from a control perspective is included at the end of this thesis. It is argued that the controller performance during payload stabilization is a key measure, which should be reflected in planning as an upper confidence bound. The differential flatness of the considered crane system gives further insights into the relation of tip and payload movements, thus facilitating the consideration of operational safety constraints.

1.6 Scope and Outline of this Thesis

Ambitions to increase the LoA of crane-based offshore operations necessitate advances in various areas of engineering, e.g. in sensor technology, hydraulics, automatic control or human-machine interaction. Furthermore, the versatility of shipboard cranes naturally entails a multitude of application-specific challenges. For example, subsea lifts (compensation of swell and ocean currents) differ from ship-to-ship loading (compensation of relative motions), while payloads varying in size, shape, mass or mounting technique may affect the payload motion. Other parameters influencing the operation range from the hydrodynamic characteristics of the vessel to geographic differences in sea behavior. To limit the scope of this thesis, some assumptions will be made throughout, i.e. the investigations are restricted to

- hydraulic knuckle boom cranes, during
- handling of light payloads above sea level, in
- a static scenario.

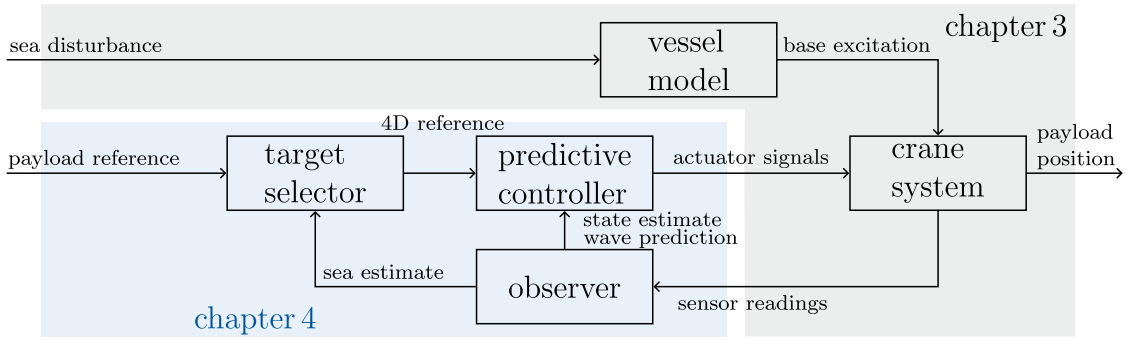

Fig. 1.3: Considered control topology for safe payload handling in crane-based offshore operations – Payload trajectories are tracked by virtue of a model predictive controller (blue). In order to integrate secondary control objectives, an optimization-based target selector is included. Estimates of the current sea and crane state are provided by an observer. The crane system is subject to persistent disturbances in form of the wave-induced vessel motions (gray).

The latter is with the exception of wave-induced motions. Complex interactions between vessel, crane and sea are not covered, but approximated as a reactionless exogenous disturbance. For an analysis of the system's coupled hydrodynamics the interested reader is referred to e.g. [34], [38], [175] and the references therein. Noteworthy, neglecting the coupled dynamics is often reasonable unless special cases as the transfer of heavy payloads on small ships are studied. As a rule of thumb, separate modeling of crane vessel and payload is valid as long as the lifted object weighs less than 2 % (usually a few hundred tons) of the vessel's tonnage displacement [51]. Since modern ships are typically equipped with systems for dynamic positioning (DP), the analysis of wave disturbances will mainly focus on the vessel's heave, rolling and pitching motions. In practice, the limited performance of DP solutions may also affect crane operation. Yet, the effects are believed to be neglectable as much as they are highly specific for a particular vessel and automatization system. The consideration of moving objects in the crane's drop zone is of high relevance for operational safety, but constitutes a research topic on its own. While the presented work may serve as an entry point into related discussions, the reader is pointed towards e.g. the fundamental research in [60] for a more throughout treatment of offshore perception and detection algorithms in dynamic environments.

In scope of this thesis, an automatization solution is developed, which comprises (i) a controller for payload positioning resp. stabilization, (ii) an observer design to estimate the current system state as well as to predict the future wave disturbance, (iii) a target selector for deriving optimal crane tip heights. The relation between the individual modules is illustrated in Fig. 1.3. The main body of this thesis is structured as follows: In chapter 2 the theoretic fundamentals and the utilized notation is introduced. Based on a review of the related literature, a control-oriented model of the crane system along

a description of the exogenous disturbances is derived in chapter 3. Furthermore, an analysis of the crane's differential flatness is included, which subsequently motivates the researched control algorithms. Chapter 4 deals with the controller design and validation, before the concept of operational safety is discussed. The research questions are then revisited in chapter 5. The thesis concludes with an outlook (chapter 6) to future research directions in the field of crane-based offshore operations.

Chapter 2

Fundamentals

In the context of this chapter, the underlying concepts used throughout this thesis are introduced. Furthermore, the utilized notation is established, which is also summarized in the glossary. References to the main part of this work are included where appropriate and vice versa. The chapter is organized in separate sections reflecting the topics of *modeling*, *planning*, and *control*. They are thus intended as a preliminary reading. The experienced reader may skip this chapter and refer to the relevant sections as required.

2.1 Coordinate Transformations

A crane might generally be regarded as a manipulator acting on the pose (position $\boldsymbol{p} \in \mathbb{R}^3$ and orientation $\boldsymbol{o} \in \mathbb{R}^q$) of the appended payload. The dimensionality $q \in \{3, 4\}$ of the orientation is depending on the chosen representation, e.g. Euler-angles or quaternions [159]. In the Euclidean space, the pose of a rigid body is hence given (at least) by a six-dimensional vector $\boldsymbol{\eta} = (\boldsymbol{p}^\mathrm{T}\, \boldsymbol{o}^\mathrm{T})^\mathrm{T} \in \mathbb{R}^6$ describing the body's degrees of freedom (DoF) with regard to a reference frame $ref : \boldsymbol{O}_\mathrm{r} - \boldsymbol{e}_{\mathrm{r},1}\boldsymbol{e}_{\mathrm{r},2}\boldsymbol{e}_{\mathrm{r},3}$. The latter is defined by its origin $\boldsymbol{O}_\mathrm{r}$ along with its axes, which are given by three (orthonormal) unit vectors $\boldsymbol{e}_{\mathrm{r},i} \in \mathbb{R}^3,\ i \in \{1, 2, 3\}$, cf. Fig. 2.1.

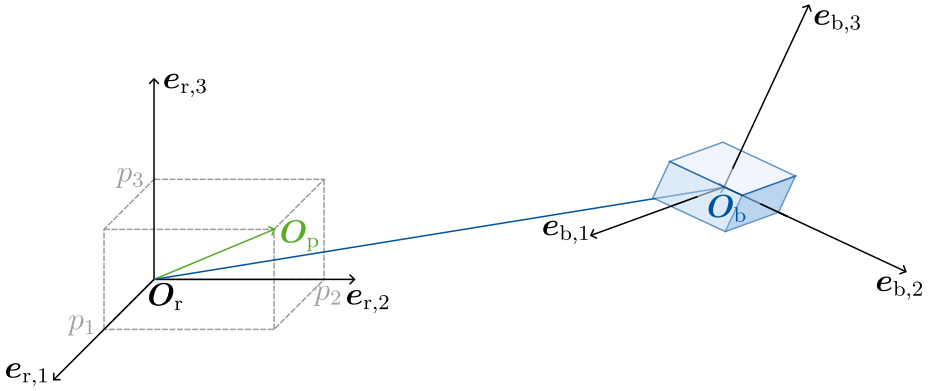

Fig. 2.1: Pose of a rigid body – Cartesian position of a point $\boldsymbol{O}_\mathrm{p}$ (left) and orientation of a rigid body (right)

The positional vector between the reference frame's origin $\boldsymbol{O}_\mathrm{r}$ and any point $\boldsymbol{O}_\mathrm{p}$ may then be expressed as a linear combination of the unit vectors $\boldsymbol{e}_{\mathrm{r},i}$, $i \in \{1,2,3\}$

$$\boldsymbol{p}_\mathrm{p}^{ref} = p_1\boldsymbol{e}_{\mathrm{r},1} + p_2\boldsymbol{e}_{\mathrm{r},2} + p_3\boldsymbol{e}_{\mathrm{r},3}$$

or equivalent, by its Cartesian coordinates $p_i \in \mathbb{R}$ written in vector form

$$\boldsymbol{p}_\mathrm{p}^{ref} = \begin{pmatrix} p_1 & p_2 & p_3 \end{pmatrix}^\mathrm{T} .$$

Here, a superscript was added in order to make the dependence on the considered reference frame explicit. Likewise, a subindex is introduced to specify which point or body is referenced. The same notation is used throughout this thesis to indicate frame-dependent quantities. When describing the pose of a rigid body, it is reasonable to define a second frame $body : \boldsymbol{O}_\mathrm{b} - \boldsymbol{e}_{\mathrm{b},1}\boldsymbol{e}_{\mathrm{b},2}\boldsymbol{e}_{\mathrm{b},3}$ attached to the same, see Fig. 2.1. The body's orientation is then related to the orthonormal body axes $\boldsymbol{e}_{\mathrm{b},i} \in \mathbb{R}^3$, $i \in \{1,2,3\}$ expressed in the reference frame

$$\begin{aligned}
\boldsymbol{e}_{\mathrm{b},1} &= r_{1,1}\boldsymbol{e}_{\mathrm{r},1} + r_{1,2}\boldsymbol{e}_{\mathrm{r},2} + r_{1,3}\boldsymbol{e}_{\mathrm{r},3} \\
\boldsymbol{e}_{\mathrm{b},2} &= r_{2,1}\boldsymbol{e}_{\mathrm{r},1} + r_{2,2}\boldsymbol{e}_{\mathrm{r},2} + r_{2,3}\boldsymbol{e}_{\mathrm{r},3} \\
\boldsymbol{e}_{\mathrm{b},3} &= r_{3,1}\boldsymbol{e}_{\mathrm{r},1} + r_{3,2}\boldsymbol{e}_{\mathrm{r},2} + r_{3,3}\boldsymbol{e}_{\mathrm{r},3}
\end{aligned}$$

where the individual components $r_{i,j} \in \mathbb{R}$ with $i,j \in \{1,2,3\}$ may be collected in the so-called *rotation matrix* $\mathbf{R}_{ref}^{body} \in SO(3)$

$$\mathbf{R}_{ref}^{body} = \begin{bmatrix} r_{1,1} & r_{1,2} & r_{1,3} \\ r_{2,1} & r_{2,2} & r_{2,3} \\ r_{3,1} & r_{3,2} & r_{3,3} \end{bmatrix} .$$

The *special orthogonal group of order three* $SO(3)$ is defined by $SO(3) \coloneqq \{\mathbf{R} | \mathbf{R} \in \mathbb{R}^{3\times3}$, $\mathbf{R}$ is orthogonal and $\det(\mathbf{R}) = 1\}$. A useful observation can be drawn from $\mathbf{R}_{ref}^{body}$ being orthogonal, which means that its inverse is in fact its transpose, i.e.

$$(\mathbf{R}_{ref}^{body})^{-1} = (\mathbf{R}_{ref}^{body})^\mathrm{T} = \mathbf{R}_{body}^{ref} . \tag{2.1}$$

The rotation matrix between two frames can be derived through different means. One possibility is the utilization of elementary rotations about a given set of axes, which leads to the notion of Euler-angles. The latter provide a minimal representation of the body's orientation based on three angles of rotation. While different definitions exist, here the *zyx*-convention (*roll-pitch-yaw* model) is adopted, which yields three intrinsic rotations illustrated in Fig. 2.2. Noteworthy, the order of elementary rotations is not arbitrary but fixed. The convention originated in the field of (aero)nautics, where it is used to this day.

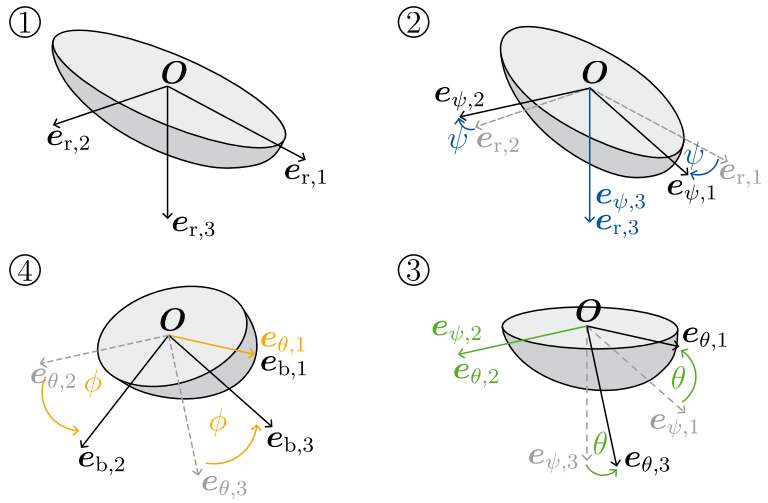

Fig. 2.2: The *roll-pitch-yaw* convention – The reference frame *ref* : $\boldsymbol{O}_\mathrm{r}$–$\boldsymbol{e}_{\mathrm{r},1}\boldsymbol{e}_{\mathrm{r},2}\boldsymbol{e}_{\mathrm{r},3}$ is translated to the fixed body frame *body* : $\boldsymbol{O}_\mathrm{b}$–$\boldsymbol{e}_{\mathrm{b},1}\boldsymbol{e}_{\mathrm{b},2}\boldsymbol{e}_{\mathrm{b},3}$ by three intrinsic rotations defined in order by the yaw angle ψ, pitch angle θ and roll angle ϕ. Without loss of generality, the origins of both frames are chosen to coincide, i.e. $\boldsymbol{O}_\mathrm{r} = \boldsymbol{O}_\mathrm{b} = \boldsymbol{O}$.

Assuming that there is no translational offset between the origins of both frames, the global reference frame *ref* is first rotated a *yaw* angle $\psi \in (-\pi, \pi]$ about the $\boldsymbol{e}_{\mathrm{r},3}$-axis, yielding the rotated frame cs_ψ : $\boldsymbol{O}_\mathrm{r} - \boldsymbol{e}_{\psi,1}\boldsymbol{e}_{\psi,2}\boldsymbol{e}_{\psi,3}$. Note that Fig. 2.2 defines a yaw-axis ($\boldsymbol{e}_{\mathrm{r},3} = \boldsymbol{e}_{\psi,3}$) pointing downwards, reflecting common practice in the maritime sector where the *north-east-down* (ned) coordinate system is usually considered as global reference frame [68]. The intermediate frame cs_ψ is then rotated about the new axis $\boldsymbol{e}_{\psi,2}$ according to the *pitch* angle $\theta \in [-\frac{\pi}{2}, \frac{\pi}{2}]$. Doing so results in a second auxiliary frame cs_θ : $\boldsymbol{O}_\mathrm{r} - \boldsymbol{e}_{\theta,1}\boldsymbol{e}_{\theta,2}\boldsymbol{e}_{\theta,3}$, which shares an axis with both the former frame ($\boldsymbol{e}_{\psi,2} = \boldsymbol{e}_{\theta,2}$) and the body fixed frame ($\boldsymbol{e}_{\theta,1} = \boldsymbol{e}_{\mathrm{b},1}$). Finally, the body frame is obtained by rotating frame cs_θ about the body's longitudinal axis $\boldsymbol{e}_{\mathrm{b},1}$ as a function of the *roll* angle $\phi \in (-\pi, \pi]$. The sequence of rotations might then be equivalently described by a single rotation matrix[1]

$$\mathbf{R}_{body}^{ref}(\boldsymbol{\theta}_{rpy}) = \begin{bmatrix} \mathrm{c}\psi\,\mathrm{c}\theta & -\mathrm{s}\psi\,\mathrm{c}\phi + \mathrm{c}\psi\,\mathrm{s}\theta\,\mathrm{s}\phi & \mathrm{s}\psi\,\mathrm{s}\phi + \mathrm{c}\psi\,\mathrm{s}\theta\,\mathrm{c}\phi \\ \mathrm{s}\psi\,\mathrm{c}\theta & \mathrm{c}\psi\,\mathrm{c}\phi + \mathrm{s}\psi\,\mathrm{s}\theta\,\mathrm{s}\phi & -\mathrm{c}\psi\,\mathrm{s}\phi + \mathrm{s}\psi\,\mathrm{s}\theta\,\mathrm{c}\phi \\ -\mathrm{s}\theta & \mathrm{c}\theta\,\mathrm{s}\phi & \mathrm{c}\theta\,\mathrm{c}\phi \end{bmatrix} \tag{2.2}$$

that depends on the vector of roll-pitch-yaw angles $\boldsymbol{\theta}_{rpy} = (\phi \quad \theta \quad \psi)^\mathrm{T}$. Conversely, given a rotation matrix $\tilde{\mathbf{R}} = (\tilde{r}_{i,j})_{1\leq i,j\leq 3}$, the set of Euler angles is calculated according to

$$\phi = \mathrm{atan2}(\tilde{r}_{3,2}, \tilde{r}_{3,3}) \tag{2.3a}$$

$$\theta = \mathrm{atan2}(-\tilde{r}_{3,1}, \sqrt{\tilde{r}_{3,2}^2 + \tilde{r}_{3,3}^2}) \tag{2.3b}$$

$$\psi = \mathrm{atan2}(\tilde{r}_{2,1}, \tilde{r}_{1,1}) \tag{2.3c}$$

[1]The shorthand notations $\mathrm{c}\alpha$, $\mathrm{s}\alpha$ denote the cosine ($\cos\alpha$) resp. sine ($\sin\alpha$) of a given angle α.

where atan2(·) is the four-quadrant inverse of the tangent function. Noteworthy, the roll-pitch-yaw representation of a body's orientation becomes singular if $\theta = \pm\frac{\pi}{2}$, which is also known as *gimbal lock*. This property may be detrimental if the angle convention is used e.g. in a controller topology incorporating some inverse calculations. In this case, quaternions offer a more robust though non-minimal representation of orientation. However, as will be argued in chapter 3, the gimbal lock is nonrestrictive for the system of ship, crane and payload since the corresponding configurations are implausible under normal operation conditions.

When analyzing the motion of a dynamic multi-body system, multiple reference frames may be defined depending on the task at hand. For example, the cargo transfer is best described in a common (i.e. global) reference frame, while the crane configuration might be conveniently referenced locally to the crane base. Similar, measurements from sensors such as cameras or inertial measurement units (IMU) are usually given in a local (potentially moving) reference frame. In this context, coordinate vectors have to be transformed between different reference frames in order to facilitate not only modeling but also planing and control of crane operations.

Consider two reference frames $cs_1 : \boldsymbol{O}_1 - \boldsymbol{e}_{1,1}\boldsymbol{e}_{1,2}\boldsymbol{e}_{1,3}$ resp. $cs_2 : \boldsymbol{O}_2 - \boldsymbol{e}_{2,1}\boldsymbol{e}_{2,2}\boldsymbol{e}_{2,3}$ with differing origins $\boldsymbol{O}_1 \neq \boldsymbol{O}_2$. Furthermore, let the frames' axes be rotated against each other, i.e. $\mathbf{R}_{cs_2}^{cs_1} \neq \mathbf{I}_{3\times3}$ with $\mathbf{I}_{3\times3} \in \mathbb{R}^{3\times3}$ the identity matrix. By geometric considerations [159], the positional vectors $\boldsymbol{p}_\mathrm{p}^{cs_1}$, $\boldsymbol{p}_\mathrm{p}^{cs_2}$ describing the same point $\boldsymbol{O}_\mathrm{p}$ in the two frames may then be mapped according to

$$\boldsymbol{p}_\mathrm{p}^{cs_1} = \boldsymbol{p}_{\boldsymbol{O}_2}^{cs_1} + \mathbf{R}_{cs_2}^{cs_1}\,\boldsymbol{p}_\mathrm{p}^{cs_2} \tag{2.4}$$

where $\boldsymbol{p}_{\boldsymbol{O}_2}^{cs_1}$ describes the translational offset between the frames' origins and $\mathbf{R}_{cs_2}^{cs_1}$ is a rotation matrix as defined above, cf. Fig. 2.3.

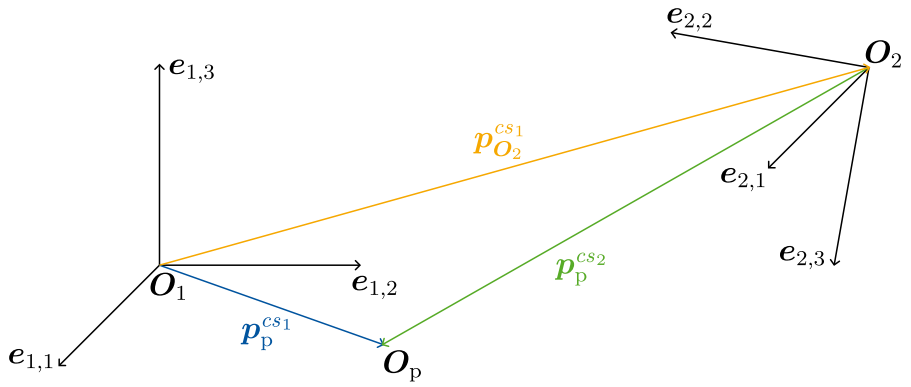

Fig. 2.3: Coordinate transformation – The point $\boldsymbol{O}_\mathrm{p}$ may be expressed in either frame $cs_1 : \boldsymbol{O}_1 - \boldsymbol{e}_{1,1}\boldsymbol{e}_{1,2}\boldsymbol{e}_{1,3}$ or $cs_2 : \boldsymbol{O}_2 - \boldsymbol{e}_{2,1}\boldsymbol{e}_{2,2}\boldsymbol{e}_{2,3}$. Both representations $\boldsymbol{p}_\mathrm{p}^{cs_1}$, $\boldsymbol{p}_\mathrm{p}^{cs_2}$ are related by a coordinate transformation $\mathbf{T}_{cs_2}^{cs_1}$, which accounts for the translation $\boldsymbol{p}_{\boldsymbol{O}_2}^{cs_1}$ between the frames' origins as well as the rotation $\mathbf{R}_{cs_2}^{cs_1}$ between the frames' axes.

A result that will be used frequently in chapter 3, chapter 4 is the inverse mapping obtained by solving (2.4) for the position $\boldsymbol{p}_{\mathrm{p}}^{cs_2}$ using property (2.1):

$$\boldsymbol{p}_{\mathrm{p}}^{cs_2} = -(\mathbf{R}_{cs_2}^{cs_1})^{\mathrm{T}}\boldsymbol{p}_{\boldsymbol{O}_2}^{cs_1} + (\mathbf{R}_{cs_2}^{cs_1})^{\mathrm{T}}\boldsymbol{p}_{\mathrm{p}}^{cs_1} = -\mathbf{R}_{cs_1}^{cs_2}\,\boldsymbol{p}_{\boldsymbol{O}_2}^{cs_1} + \mathbf{R}_{cs_1}^{cs_2}\,\boldsymbol{p}_{\mathrm{p}}^{cs_1}\,. \tag{2.5}$$

Equations (2.4) and (2.5) give rise to the concept of *homogeneous transformations*, which are defined by extending the positional vectors and using matrix notation, i.e.

$$\begin{pmatrix}\boldsymbol{p}_{\mathrm{p}}^{cs_1}\\ 1\end{pmatrix} = \mathbf{T}_{cs_2}^{cs_1}\begin{pmatrix}\boldsymbol{p}_{\mathrm{p}}^{cs_2}\\ 1\end{pmatrix},\ \text{resp.}\ \begin{pmatrix}\boldsymbol{p}_{\mathrm{p}}^{cs_2}\\ 1\end{pmatrix} = \mathbf{T}_{cs_1}^{cs_2}\begin{pmatrix}\boldsymbol{p}_{\mathrm{p}}^{cs_1}\\ 1\end{pmatrix} \tag{2.6a}$$

with the homogeneous transformation matrices $\mathbf{T}_{cs_1}^{cs_2}$, $\mathbf{T}_{cs_2}^{cs_1}$ defined according to

$$\mathbf{T}_{cs_2}^{cs_1} = \begin{bmatrix}\mathbf{R}_{cs_2}^{cs_1} & \boldsymbol{p}_{\boldsymbol{O}_2}^{cs_1}\\ \mathbf{0}_{1\times 3} & 1\end{bmatrix} \tag{2.6b}$$

$$\mathbf{T}_{cs_1}^{cs_2} = \begin{bmatrix}\mathbf{R}_{cs_1}^{cs_2} & \boldsymbol{p}_{\boldsymbol{O}_1}^{cs_2}\\ \mathbf{0}_{1\times 3} & 1\end{bmatrix} = \begin{bmatrix}(\mathbf{R}_{cs_2}^{cs_1})^{\mathrm{T}} & -(\mathbf{R}_{cs_2}^{cs_1})^{\mathrm{T}}\boldsymbol{p}_{\boldsymbol{O}_2}^{cs_1}\\ \mathbf{0}_{1\times 3} & 1\end{bmatrix} = (\mathbf{T}_{cs_2}^{cs_1})^{-1} \tag{2.6c}$$

where $\mathbf{0}_{1\times 3} \in \mathbb{R}^{1\times 3}$ denotes a matrix with all elements equal to zero. A particularly helpful feature of homogeneous transformation matrices is that they can be concatenated in order to summarize a sequence of $n \in \mathbb{N}_{>0}$ coordinate transformations, i.e.

$$\mathbf{T}_{cs_n}^{cs_1} = \mathbf{T}_{cs_2}^{cs_1}\mathbf{T}_{cs_3}^{cs_2}\dots\mathbf{T}_{cs_n}^{cs_{n-1}} = \prod_{i=1}^{n-1}\mathbf{T}_{cs_{i+1}}^{cs_i}\,.$$

This facilitates modeling of manipulators with multiple moving parts such as the crane. Since the knuckle boom crane furthermore resembles an open kinematic chain, the Denavit-Hartenberg convention [45] will be used in chapter 3 to systematically assign reference frames to the crane system. The approach is illustrated in Fig. 2.4 for a kinematic section consisting of three joints J_{i-1}, J_i, J_{i+1} connected by two links L_{i-1}, L_i where i is a running index [159].

For each link L_i, a reference frame $cs_i : \boldsymbol{O}_i - \boldsymbol{e}_{i,1}\boldsymbol{e}_{i,2}\boldsymbol{e}_{i,3}$ is defined applying the following procedure:

i) The axis $\boldsymbol{e}_{i,3}$ is chosen in direction of joint J_{i+1}.

ii) The origin $\boldsymbol{O}_i$ is placed at the intersection of axis $\boldsymbol{e}_{i,3}$ with the common normal (line of minimal length) between the joint axes defined by $\boldsymbol{e}_{i-1,3}$ resp. $\boldsymbol{e}_{i,3}$.

iii) The axis $\boldsymbol{e}_{i,1}$ is chosen perpendicular to $\boldsymbol{e}_{i-1,3}$ and $\boldsymbol{e}_{i,3}$, i.e. $\boldsymbol{e}_{i,1} = \boldsymbol{e}_{i-1,3} \times \boldsymbol{e}_{i,3}$.

iv) The axis $\boldsymbol{e}_{i,2}$ is chosen such that frame cs_i is a right-handed coordinate system.

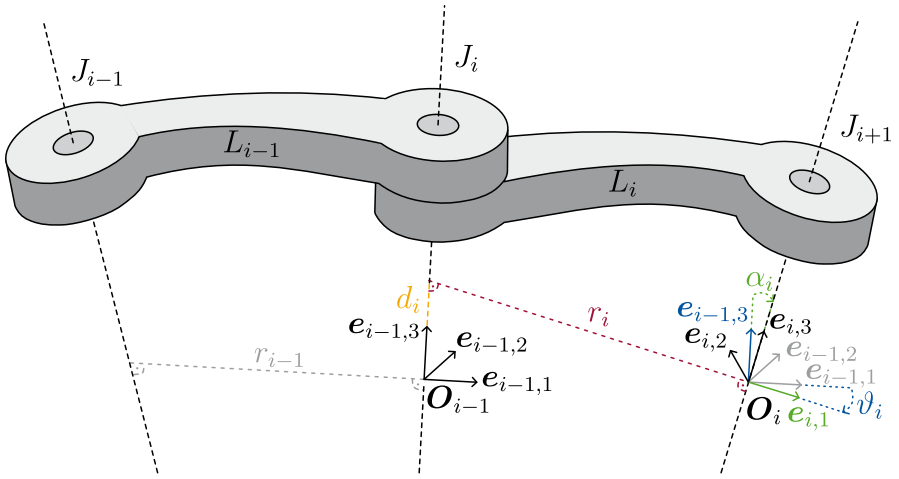

Fig. 2.4: Denavit-Hartenberg convention – Reference frames are defined for each link following a systematic methodology. The frames are related by a homogeneous transformation matrix $\mathbf{T}_{cs_i}^{cs_{i-1}}$, which depends on the DH-parameters $\boldsymbol{\zeta}_{DH,i} = (d_i\, \vartheta_i\, r_i\, \alpha_i)^{\mathrm{T}}$; figure adopted from [159].

The approach is ambiguous, e.g. if two consecutive joint axes are parallel or intersect. In these cases, the axis $\boldsymbol{e}_{i,1}$ might be chosen such that the overall kinematic model is simplified. Additional design choices arise for the first and last frame. The coordinate transformation between two consecutive links is then given by a homogeneous transformation matrix $\mathbf{T}_{cs_i}^{cs_{i-1}}$ which depends on the so-called Denavit-Hartenberg (DH) parameters $\boldsymbol{\zeta}_{DH,i} = (d_i \quad \vartheta_i \quad r_i \quad \alpha_i)^{\mathrm{T}}$:

$$\mathbf{T}_{cs_i}^{cs_{i-1}}(\boldsymbol{\zeta}_{DH,i}) = \begin{bmatrix} \mathrm{c}\vartheta_i & -\mathrm{s}\vartheta_i \mathrm{c}\alpha_i & \mathrm{s}\vartheta_i \mathrm{s}\alpha_i & r_i \mathrm{c}\vartheta_i \\ \mathrm{s}\vartheta_i & \mathrm{c}\vartheta_i \mathrm{c}\alpha_i & -\mathrm{c}\vartheta_i \mathrm{s}\alpha_i & r_i \mathrm{s}\vartheta_i \\ 0 & \mathrm{s}\alpha_i & \mathrm{c}\alpha_i & d_i \\ 0 & 0 & 0 & 1 \end{bmatrix} = \begin{bmatrix} \mathbf{R}_{cs_i}^{cs_{i-1}} & \boldsymbol{p}_{\boldsymbol{O}_i}^{cs_{i-1}} \\ \mathbf{0}_{1\times 3} & 1 \end{bmatrix} . \tag{2.7}$$

The DH-parameters are derived from four single operations, illustrated in Fig. 2.4. The frame cs_{i-1} is first translated an offset d_i (yellow) along $\boldsymbol{e}_{i-1,3}$ from $\boldsymbol{O}_{i-1}$ to the common normal (red). It is then rotated by an angle ϑ_i (blue) about $\boldsymbol{e}_{i-1,3}$ such that $\boldsymbol{e}_{i-1,1}$ and $\boldsymbol{e}_{i,1}$ point in the same direction. Hereafter, the frame is translated a length r_i along the common normal, i.e. in direction of $\boldsymbol{e}_{i,1}$. Last, the axes $\boldsymbol{e}_{i-1,3}$ and $\boldsymbol{e}_{i,3}$ are aligned by rotating an angle α_i (green) with respect to $\boldsymbol{e}_{i,1}$. For joints with a single DoF, either d_i or ϑ_i is variable based on whether joint J_i is *prismatic* or *revolute*. In contrast, both r_i and α_i only depend on the geometry of the connecting link L_i.

For a detailed introduction to coordinate transformations and kinematics in general, the reader is referred to e.g. [159].

2.2 Spline Curves and Trajectories

The computation of trajectories occurs in both motion planning and (predictive) control, cf. section 2.5. In the context of this thesis, a trajectory is considered a parametric function of time t on a finite[2] interval $t \in [t_\mathrm{l}, t_\mathrm{u}]$. Depending on the domain, trajectories map to different spaces. For example, in motion planing the trajectory $\boldsymbol{p}(t)$ describes the Cartesian position of an object in the operational space over time, i.e. $t \mapsto \boldsymbol{p}(t) \in \mathbb{R}^3$. In contrast, the state trajectories $\boldsymbol{x}(t)$ represent the time evolution of a dynamic system (see section 2.3) and therefore live on the state space, i.e. $t \mapsto \boldsymbol{x}(t) \in \mathbb{R}^n$. In either case, the explicit dependence on time is central to the definition of a trajectory.

The objective of transferring the payload from one point to another will naturally yield a Cartesian payload trajectory in the crane's operational space. Additional trajectories will be introduced to specify the crane's motion profile in its joint resp. actuator space, which reflects the subsequent control task. With respect to ship, crane and payload moving in (the three-dimensional) space and time, the following distinction will be made, see e.g. [22]:

- A geometric *path* $\sigma \mapsto \mathtt{p}(\sigma) \in \mathbb{R}^3$ describes a parametric curve in space as a function of the scalar path variable $\sigma \in [\sigma_\mathrm{l}, \sigma_\mathrm{u}]$.
- A geometric *trajectory* $t \mapsto \boldsymbol{p}(t) \in \mathbb{R}^3$ describes a parametric curve in space as a function of time $t \in [t_\mathrm{l}, t_\mathrm{u}]$.

Hence, a path only holds geometric information (locus), whereas a trajectory further relates space and time (motion). Both path and trajectory are linked by the monotonic *timing law* $\sigma = \varsigma(t)$ where $\varsigma : [t_\mathrm{l}, t_\mathrm{u}] \to [\sigma_\mathrm{l}, \sigma_\mathrm{u}]$, i.e.

$$\boldsymbol{p}(t) = (\mathtt{p} \circ \varsigma)(t) = \mathtt{p}(\varsigma(t)) \; . \tag{2.8}$$

The velocity and acceleration profiles associated with the trajectory $\boldsymbol{p}(t)$ are derived by applying the chain rule to (2.8), yielding

$$\dot{\boldsymbol{p}}(t) = \left.\frac{\mathrm{d}\mathtt{p}}{\mathrm{d}\sigma}\right|_{\sigma=\varsigma(t)} \dot{\varsigma}(t) \tag{2.9}$$

$$\ddot{\boldsymbol{p}}(t) = \left.\frac{\mathrm{d}\mathtt{p}}{\mathrm{d}\sigma}\right|_{\sigma=\varsigma(t)} \ddot{\varsigma}(t) + \left.\frac{\mathrm{d}^2\mathtt{p}}{\mathrm{d}\sigma^2}\right|_{\sigma=\varsigma(t)} \dot{\varsigma}^2(t) \tag{2.10}$$

[2]While the restriction to a finite interval seems arbitrary, the case $t_\mathrm{u} \to \infty$ usually has no practical implications. Although concepts as e.g. asymptotic stability are frequently used in control theory, the trajectories of a physical process are ultimately analyzed over a finite (albeit potentially large) horizon. On the other hand, a finite interval $t_\mathrm{u} < \infty$ proves useful from a computational viewpoint.

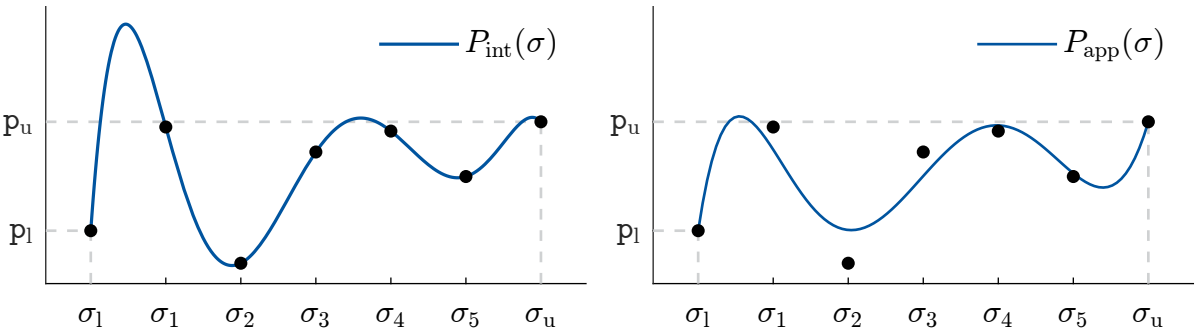

(a) Interpolation $\mathrm{p}(\sigma) = P_{\mathrm{int}}(\sigma) \in \Pi_6$ **(b)** Approximation $\mathrm{p}(\sigma) = P_{\mathrm{app}}(\sigma) \in \Pi_6$

Fig. 2.5: Polynomial path planning – Two polynomials of degree six are fitted to a sequence of five via-points $\mathrm{p}_1, \ldots, \mathrm{p}_5$ located at $\sigma_1, \ldots, \sigma_5$. The interpolating polynomial $P_{\mathrm{int}}(\sigma)$ (left) passes through all via-points as well as the initial and final waypoints $(\sigma_\mathrm{l}, \mathrm{p}_\mathrm{l})$ resp. $(\sigma_\mathrm{u}, \mathrm{p}_\mathrm{u})$. The approximating polynomial $P_{\mathrm{app}}(\sigma)$ (right) minimizes the path curvature, therefore only the initial and final waypoints are attained exactly.

where the dot-notation is used to indicate the trajectories' first derivative with respect to time, i.e. $\dot{\boldsymbol{p}}(t) = \frac{\mathrm{d}}{\mathrm{d}t}\boldsymbol{p}(t)$. Following common conventions, the second time derivative $\ddot{\boldsymbol{p}}(t)$ is defined accordingly, while higher-order derivatives will be denoted $\boldsymbol{p}^{(k)}(t)$, $k \geq 3$.

In view of (2.8), devising a trajectory is usually divided into finding a suitable path and then specifying an adequate timing law. This two-step approach is sometimes referred to as *path-velocity decomposition* [97]. Following the definition above, a path can take any shape parameterizable by the path variable σ. In practice, additional constraints such as continuity or smoothness are typically imposed. In the simplest case (*point-to-point* scenario), only the initial and final points $\mathrm{p}_\mathrm{l} = \mathrm{p}(\sigma_\mathrm{l})$ resp. $\mathrm{p}_\mathrm{u} = \mathrm{p}(\sigma_\mathrm{u})$ are specified, which renders the design space in path planning infinite. The same is true for *multipoint* paths, where an N-tuple of intermediate via-points $\mathcal{V} = (\mathrm{p}_1, \ldots, \mathrm{p}_N)$ with matching path parameters $\mathcal{O} = (\sigma_1, \ldots, \sigma_N)$ is defined. As a solution, path primitives might be adopted, see e.g. [22], [59]. Another possibility is to restrict the path synthesis to analytic functions, such as polynomials $P(\cdot)$ of degree[3] n, i.e.

$$\mathrm{p}_i(\sigma) = P_i(\sigma) \in \Pi_n = \{\sum_{j=0}^{n} a_j \sigma^j \,|\, a_0, \ldots, a_n \in \mathbb{R},\ a_n \neq 0\}, \qquad i = 1, \ldots, 3$$

which are characterized by a limited number of free parameters a_j. The task of path planning then reverts to the problem of *interpolation* or function *approximation*, depending on the posed constraints.

[3]The *degree* of a polynomial refers to the highest exponent in any of its monomials with non-zero coefficients. The term is preferred here over the notion of *order* to avoid ambiguity with the *order of a spline* introduced below.

In Fig. 2.5 a one-dimensional example including a sequence of five via-points $\{(\sigma_1, \mathtt{p}_1), \ldots, (\sigma_5, \mathtt{p}_5)\}$ is given along with both an interpolating (left) and an approximating (right) polynomial of degree six. While the interpolating polynomial $P_{\text{int}}(\sigma)$ passes through all via-points, the approximating polynomial $P_{\text{app}}(\sigma)$ is optimized for a smaller path curvature therefore only adhering to the initial and final waypoints. A derivation of both polynomials is included in A. The choice of behavior during path planning depends on the prioritization of different design criteria, e.g. an interpolating polynomial might be favorable to realize collision-free paths if the via-points are chosen accordingly. In contrast, an approximating curve allows for smoother paths yielding less actuator stress for a given timing law. In practice, an interpolating curve may be obtained as the limit of an approximating polynomial by means of a predefined tolerance, which constrains the maximum (Euclidean) deviation from the via-points.

Using a single polynomial usually proves impractical for either path or trajectory planning. For more complex curves (shape, number of via-points, etc.), the required polynomial degree increases, giving rise to numerical issues like e.g. RUNGE's phenomenon [149]. The most popular workaround is to apply piecewise defined polynomials of lower degree, i.e. polynomial *splines*. A function $S : [\kappa_\text{l}, \kappa_\text{u}] \to \mathbb{R}$ is called polynomial spline of order $l \geq 2$ with respect to the *knot* sequence $\mathcal{K} = (\kappa_1, \ldots, \kappa_m)$, $m > l$ where

$$\kappa_\text{l} = \kappa_1 < \kappa_2 < \ldots < \kappa_{m-1} < \kappa_m = \kappa_\text{u}$$

if the following conditions are true [42]:

i) $S(\kappa) \in \Pi_{l-1}$ for $\kappa_i \leq \kappa < \kappa_{i+1}, \quad i = 1, \ldots, m-1$

ii) $S(\kappa) \in C^{l-2}$ for $\kappa \in [\kappa_\text{l}, \kappa_\text{u}]$.

Here, C^{l-2} denotes the class of all differentiable functions whose derivatives exist and are continuous up to order $l-2$. While the first property states that the spline takes the form of a polynomial of degree $k = l-1$ on each knot interval $[\kappa_i, \kappa_{i+1})$, the second characteristic requires continuity of the spline function and its derivatives at the interior interval boundaries, i.e.

$$\lim_{h \to 0} S^{(k)}(\kappa_i + h) = \lim_{h \to 0} S^{(k)}(\kappa_i - h) \qquad \forall\, i = 2, \ldots, m-1 \text{ and } k = 0, \ldots, l-2 \,.$$

Note, that differentiability outside the knots (breakpoints) is already guaranteed by the polynomial form. For notational convenience, the space of all splines of order l belonging to a given knot sequence $\mathcal{K}$ is represented by $\Sigma_{l,\mathcal{K}}$. Depending on the number of knots m, a spline then possess $d = m + l - 2$ DoF, which is relevant in regards to the computational complexity associated with spline optimization, cf. chapter 4.

Several representations of splines exist, all of which can be written in terms of

$$S(\kappa) = \sum_{j=1}^{m+l-2} \alpha_j N_j(\kappa)$$

with some basis functions $N_j : [\kappa_\mathrm{l}, \kappa_\mathrm{u}] \to \mathbb{R}$ spanning $\Sigma_{l,\mathcal{K}}$ and corresponding coefficients $\alpha_j \in \mathbb{R}$. The question thus becomes which basis is best suited to describe splines in technical applications. While the truncated power basis is a direct generalization of the monomial basis $1, \kappa, \ldots, \kappa^n$ of Π_n and therefore straightforward to implement, its numerical instability renders this particular representation unfavorable in most cases [42], [61]. A better conditioned basis is established by the so-called *basis splines* (B-splines) yielding polynomial splines of the form

$$S_B(\kappa) = \sum_{j=1}^{m+l-2} \alpha_j B_{j,l}(\kappa) \tag{2.11}$$

where the basis functions $B_{j,l} : \mathbb{R} \to \mathbb{R}$ are defined recursively

$$l = 1: \qquad B_{j,1}(\kappa) = \begin{cases} 1 & \text{for} \quad \bar{\kappa}_j \leq \kappa < \bar{\kappa}_{j+1} \\ 0 & \text{for} \quad \bar{\kappa}_j > \kappa \quad \text{and} \quad \kappa \geq \bar{\kappa}_{j+1} \end{cases} \tag{2.12a}$$

$$l \geq 2: \qquad B_{j,l}(\kappa) = \frac{\kappa - \bar{\kappa}_j}{\bar{\kappa}_{j+l-1} - \bar{\kappa}_j} B_{j,l-1}(\kappa) + \frac{\bar{\kappa}_{j+l} - \kappa}{\bar{\kappa}_{j+l} - \bar{\kappa}_{j+1}} B_{j+1,l-1}(\kappa) \tag{2.12b}$$

with respect to an extended knot sequence $\mathcal{K}_B$, which satisfies

$$\mathcal{K}_B = (\bar{\kappa}_1, \ldots, \bar{\kappa}_{l-1}, \underbrace{\bar{\kappa}_l, \ldots, \bar{\kappa}_{l+m-1}}_{=(\kappa_1,\ldots,\kappa_m)=\mathcal{K}}, \bar{\kappa}_{m+l}, \ldots, \bar{\kappa}_{2l+m-2}) \; . \tag{2.13}$$

The basis functions are defined exactly such that the spline S_B meets the prescribed smoothness over the entire interval $[\kappa_\mathrm{l}, \kappa_\mathrm{u}]$. With reference to (2.12), this requires a knot sequence comprising $2(l-1)$ additional knots, which are appended to the left and right of the original knot sequence $\mathcal{K}$. Depending on the choice of convention, the added knot sequences will no longer be strictly increasing, so that in general only $\bar{\kappa}_1 \leq \ldots \leq \bar{\kappa}_{l-1} \leq \kappa_1$ resp. $\kappa_m \leq \bar{\kappa}_{m+l} \leq \ldots \leq \bar{\kappa}_{2l+m-2}$ hold. In the special case where the inner knots $\mathcal{K}$ are chosen equidistant with step size $\Delta\kappa \coloneqq \frac{\kappa_\mathrm{u} - \kappa_\mathrm{l}}{m-1}$, the knot sequence can be simply extended by placing the additional knots according to the same spacing, i.e.

$$\begin{aligned} \bar{\kappa}_{l+i} &= \kappa_\mathrm{l} + i\Delta\kappa && \text{for} \quad i = 0, \ldots, m-1 \\ \bar{\kappa}_{l-k} = \kappa_\mathrm{l} - k\Delta\kappa, \quad \bar{\kappa}_{l+m-1+k} &= \kappa_\mathrm{u} + k\Delta\kappa && \text{for} \quad k = 1, \ldots, l-1 \; . \end{aligned}$$

If the inner knots are spaced unevenly, the distance between two consecutive knots at the resp. interval boundary may be used to augment the knot sequence. Another possibility is to choose all outside knots equal to the interval boundaries, i.e. $\bar{\kappa}_{l-k} = \kappa_\mathrm{l}$ and $\bar{\kappa}_{l+m-1+k} = \kappa_\mathrm{u}$ for all $k \in [1, l-1]$.

The B-spline basis possesses several advantages over the truncated power basis, some of which are illustrated in Fig. 2.6. First, the basis functions $B_{j,l}$, $j = 1, \ldots, m+l+2$ form

a *partition of unity* on the spline's domain, that is, at any point $\kappa_* \in [\kappa_\mathrm{l}, \kappa_\mathrm{u}]$ the sum over all basis functions is equal to one

$$\sum_{j=1}^{m+l-2} B_{j,l}(\kappa_*) = 1 \ . \tag{2.14}$$

As a result, the magnitude of the spline function is directly related to the spline coefficients α_j. In fact, the spline is guaranteed to lie within the convex hull associated with the coefficients, which in the multidimensional case are therefore also referred to as *control points*. In Fig. 2.6a, four basis functions are non-zero at κ_* (red line). As stated in (2.14), their function values add up to one. Second, the B-spline basis defines a *local basis* in the sense that each basis function $B_{j,l}$ vanishes outside of $[\bar{\kappa}_j, \bar{\kappa}_{j+l})$, compare $B_{6,4}(\kappa)$ (Fig. 2.6a, green). Consequently, changing α_j only affects the spline on a limited interval. As an example, the fifth spline coefficient α_5 is varied in Fig. 2.6b, confirming its local influence on the spline curve. Noticing that on each interval $[\bar{\kappa}_j, \bar{\kappa}_{j+1})$ a maximum of l basis functions is unequal to zero, calculating the spline function can be simplified to

$$S_B(\kappa) = \sum_{i=j-l+1}^{j} \alpha_i B_{i,l}(\kappa) \qquad \text{for} \quad \bar{\kappa}_j \leq \kappa < \bar{\kappa}_{j+1} \ . \tag{2.15}$$

An even more efficient way to evaluate the spline function is given by De Boor's algorithm [43]. Last, B-splines admit a straightforward way to describe derivatives of arbitrary order $p \leq l-2$, which will be exploited in chapter 4. The pth derivative of the spline (2.11) with respect to κ is given by [42]

$$S_B^{(p)}(\kappa) = \sum_{j=1+p}^{m+l-2} \alpha_j^{(p)} B_{j,l-p}(\kappa) \tag{2.16a}$$

where the pth differences[4] of the B-spline coefficients $\alpha_j^{(p)}$ are determined recursively

$$\alpha_j^{(p)} = \begin{cases} \alpha_j, & p = 0 \\ (l-p)\frac{\alpha_j^{(p-1)} - \alpha_{j-1}^{(p-1)}}{\bar{\kappa}_{j+l-p} - \bar{\kappa}_j}, & 0 < p \leq l-2 \end{cases} \ . \tag{2.16b}$$

Hence, the derivative of a B-spline function is again a linear combination of B-splines of lower order and smaller support, which is reflected by the index shift in (2.16a). For a thorough discussion of B-splines and their properties please refer to [43].

[4] Although not indicating the derivative of a function, the abuse of notation $\alpha_j^{(p)}$ is in line with most literature on B-splines.

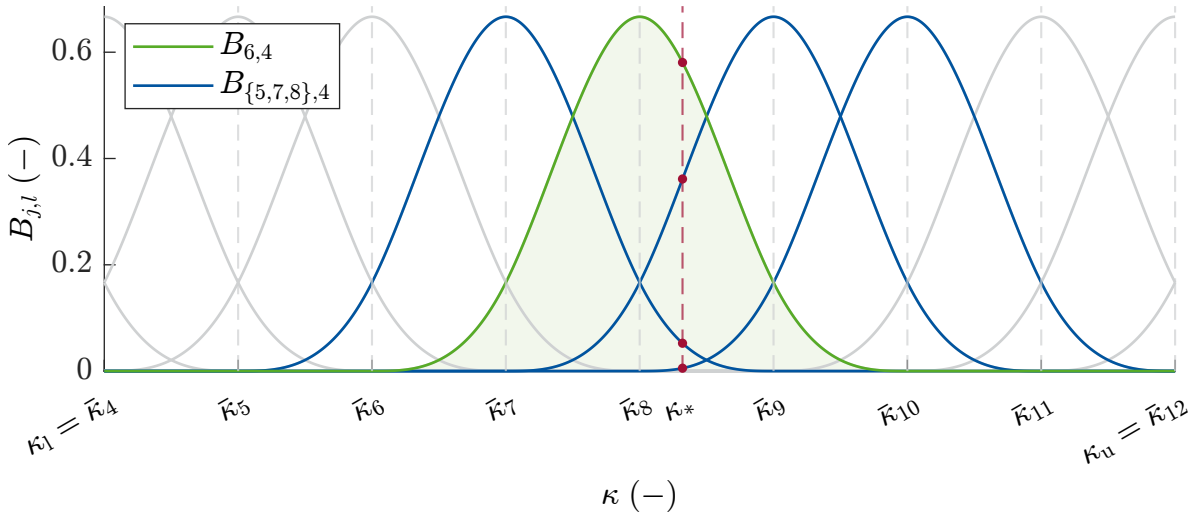

(a) B-spline basis of order 4 to an equidistant knot sequence with 9 inner knots

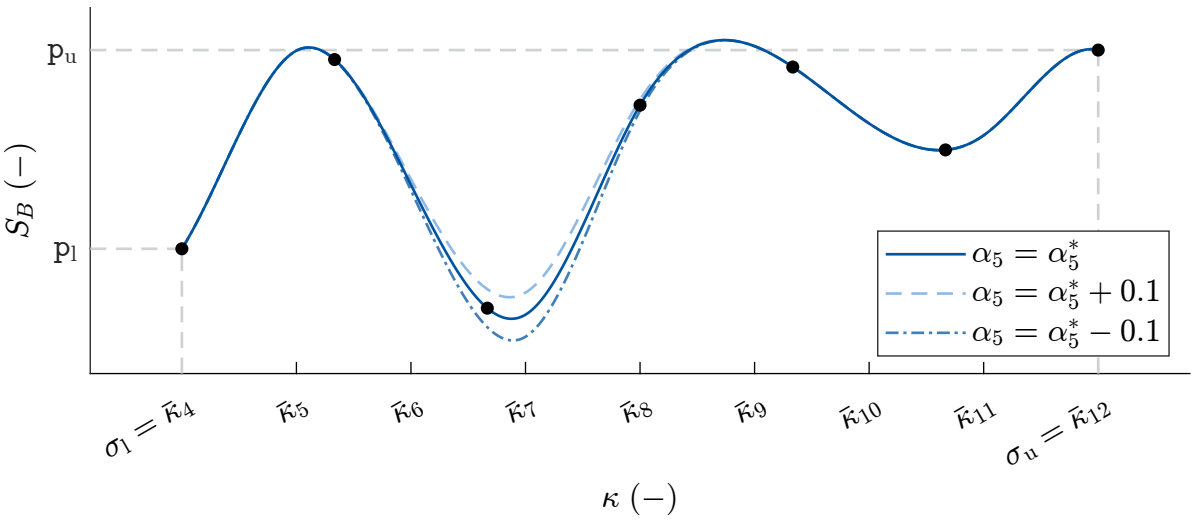

(b) Approximation $\mathrm{p}(\kappa) = S_B(\kappa) \in \Sigma_{4,\mathcal{K}}$ for varying coefficients α_5

Fig. 2.6: Properties of the B-spline basis – Exemplary depiction of a B-spline basis of order 4 (top) and according spline curve (bottom) fitted to the scenario of Fig. 2.5. The B-splines are defined with respect to an equidistant inner knot sequence $\kappa_i = \sigma_1 + i\frac{\sigma_u - \sigma_1}{8}$ with $i = 0, \dots, 8$. The extended knot sequence $\bar{\kappa}_j$, $j = 1, \dots, 15$ is formed by appending $l - 1 = 3$ knots both before κ_1 and after κ_9, keeping the same knot distance. The B-spline basis yields a partition of unity, as illustrated at κ_* (red line), where the basis functions add up to one. The limited support of individual basis functions may be checked with regard to $B_{6,4}$ (highlighted in green), which is zero outside of $[\bar{\kappa}_{j=6}, \bar{\kappa}_{j+l=10})$. On each interval $[\bar{\kappa}_j, \bar{\kappa}_{j+1}]$ exactly $l = 4$ basis functions are positive, compare $B_{5,4}$ to $B_{8,4}$ (marked in blue) for $\bar{\kappa}_8 \leq \kappa \leq \bar{\kappa}_9$. The spline curve (bottom) is shown for different coefficients α_5 chosen around a nominal value α_5^*. In accordance with the associated basis function $B_{5,4}$ taking its maximum at $\bar{\kappa}_7$ and vanishing outside of $[\bar{\kappa}_5, \bar{\kappa}_9)$, the family of spline curves only differs locally around $\bar{\kappa}_7$, i.e. small variations in the spline coefficients yield bounded deviations in the spline curve.

2.3 Dynamic Systems

Following IEC 60050-351, a *system* is defined as a "*set of interrelated elements considered in a defined context as a whole and separated from their environment*" [79]. In contrast to static systems, which in general can be described by a nonlinear mapping $\boldsymbol{y} = \boldsymbol{f}(\boldsymbol{u})$ between inputs $\boldsymbol{u} \in \mathbb{R}^m$ and outputs $\boldsymbol{y} \in \mathbb{R}^p$, dynamic systems are further characterized by internal states $\boldsymbol{x} \in \mathbb{R}^n$ and are thus time-dependent. As a result, the mathematical model of a dynamic system is given by a set of (differential) equations[5]

$$\dot{\boldsymbol{x}} = \boldsymbol{f}\left(\boldsymbol{x}, \boldsymbol{u}, t\right) \qquad \text{(state equation)} \tag{2.17a}$$

$$\boldsymbol{y} = \boldsymbol{h}\left(\boldsymbol{x}, \boldsymbol{u}, t\right) \qquad \text{(output equation)} \tag{2.17b}$$

describing the evolution of the system trajectories over time t. Here, the mappings $\boldsymbol{f} : \mathbb{R}^n \times \mathbb{R}^m \times \mathbb{R} \to \mathbb{R}^n$, $\boldsymbol{h} : \mathbb{R}^n \times \mathbb{R}^m \times \mathbb{R} \to \mathbb{R}^p$ constitute a so-called (nonlinear) *state space* model. If the system is time-invariant, i.e. its dynamics do not depend explicitly on time, the argument t is usually dropped in (2.17).

As will be shown in chapter 3, the crane dynamics belong to a special subclass of (2.17a) also referred to as *affine input* systems, for which the (time-invariant) state equation reads

$$\dot{\boldsymbol{x}} = \boldsymbol{f}\left(\boldsymbol{x}\right) + \sum_{i=1}^{m} \boldsymbol{g}_i(\boldsymbol{x}) u_i \; . \tag{2.18}$$

Here, the relation between inputs $\boldsymbol{u} = \left(u_1 \; \ldots \; u_m\right)^{\mathrm{T}}$ and state change $\dot{\boldsymbol{x}}$ is characterized by the input mappings $\boldsymbol{g}_i : \mathbb{R}^n \to \mathbb{R}^n$, $i = 1, \ldots, m$.

An important parameter for control is given by the system's relative degree $\boldsymbol{r} = \left(r_1 \; \ldots \; r_m\right)^{\mathrm{T}} \in \mathbb{N}^m$, i.e. the order for which the time derivatives $y_i^{(r_i)}$ first depend on (at least one of) the inputs $\boldsymbol{u}$. A formal definition is established in [82]: The affine input system (2.18), (2.17b) with $\dim(\boldsymbol{y}) = \dim(\boldsymbol{u})$ and no direct feedthrough has a vector relative degree $\boldsymbol{r}$ at a given point $\boldsymbol{x}_0 \in \mathbb{R}^n$ if

i) $L_{\boldsymbol{g}_i} L_{\boldsymbol{f}}^k h_j(\boldsymbol{x}) = 0 \qquad \forall\, i = 1, \ldots, m \;, \forall\, j = 1, \ldots, m \;, \; \forall\, k = 1, \ldots, r_i - 1 \;,$
$\forall\, \boldsymbol{x} \in \mathcal{U}(\boldsymbol{x}_0) \coloneqq \left\{ \boldsymbol{x} \in \mathbb{R}^n \;\middle|\; \left\| \boldsymbol{x} - \boldsymbol{x}_0 \right\|_2 < \epsilon \right\} \text{ with } \epsilon > 0$

ii) $\operatorname{rank}\left(\mathbf{D}(\boldsymbol{x}_0)\right) = m$

$$\text{where } \mathbf{D}(\boldsymbol{x}) \;=\; \begin{bmatrix} L_{\boldsymbol{g}_1} L_{\boldsymbol{f}}^{r_1 - 1} h_1(\boldsymbol{x}) & \ldots & L_{\boldsymbol{g}_m} L_{\boldsymbol{f}}^{r_1 - 1} h_1(\boldsymbol{x}) \\ L_{\boldsymbol{g}_1} L_{\boldsymbol{f}}^{r_2 - 1} h_2(\boldsymbol{x}) & \ldots & L_{\boldsymbol{g}_m} L_{\boldsymbol{f}}^{r_2 - 1} h_2(\boldsymbol{x}) \\ \vdots & \ddots & \vdots \\ L_{\boldsymbol{g}_1} L_{\boldsymbol{f}}^{r_m - 1} h_m(\boldsymbol{x}) & \ldots & L_{\boldsymbol{g}_m} L_{\boldsymbol{f}}^{r_m - 1} h_m(\boldsymbol{x}) \end{bmatrix} \in \mathbb{R}^{m \times m} \; .$$

[5] In fact, differential equations only present a particular approach to describe dynamic systems. Other representations may be derived, e.g. from data.

Following the notation in [82], the first LIE derivative $L_{\boldsymbol{f}} h_j(\boldsymbol{x})$ of a real-valued function $h_j(\boldsymbol{x})$ along the vector field $\boldsymbol{f}(\boldsymbol{x})$ is defined as $L_{\boldsymbol{f}} h_j(\boldsymbol{x}) \coloneqq \frac{\partial h_j(\boldsymbol{x})}{\partial \boldsymbol{x}} \boldsymbol{f}(\boldsymbol{x})$. Nested derivatives along two vector fields $\boldsymbol{f}(\boldsymbol{x})$ and $\boldsymbol{g}_i(\boldsymbol{x})$ may be written

$$L_{\boldsymbol{g}_i} L_{\boldsymbol{f}} h_j(\boldsymbol{x}) = \frac{\partial \left(L_{\boldsymbol{f}} h_j(\boldsymbol{x}) \right)}{\partial \boldsymbol{x}} \boldsymbol{g}_i(\boldsymbol{x}) \, .$$

Finally, the superscript k is used to indicate higher order Lie derivatives $L_{\boldsymbol{f}}^k h_j(\boldsymbol{x})$, which satisfy the recursion

$$L_{\boldsymbol{f}}^k h_j(\boldsymbol{x}) = \frac{\partial \left(L_{\boldsymbol{f}}^{k-1} h_j(\boldsymbol{x}) \right)}{\partial \boldsymbol{x}} \boldsymbol{f}(\boldsymbol{x}), \qquad\qquad L_{\boldsymbol{f}}^0 h_j(\boldsymbol{x}) = h_j(\boldsymbol{x}) \, .$$

Significance of the decoupling matrix $\mathbf{D}(\boldsymbol{x})$ becomes apparent, noting that the above definition of the vector relative degree implies

$$\begin{pmatrix} y_1^{(r_1)} \\ y_2^{(r_2)} \\ \vdots \\ y_m^{(r_m)} \end{pmatrix} = \underbrace{\begin{pmatrix} L_{\boldsymbol{f}}^{r_1} h_1(\boldsymbol{x}) \\ L_{\boldsymbol{f}}^{r_2} h_2(\boldsymbol{x}) \\ \vdots \\ L_{\boldsymbol{f}}^{m} h_m(\boldsymbol{x}) \end{pmatrix}}_{=:\boldsymbol{\beta}(\boldsymbol{x})} + \mathbf{D}(\boldsymbol{x}) \begin{pmatrix} u_1 \\ u_2 \\ \vdots \\ u_m \end{pmatrix} \, . \tag{2.19}$$

If the $(m \times m)$-matrix $\mathbf{D}(\boldsymbol{x})$ is regular on $\mathcal{U}(\boldsymbol{x}_0)$, equation (2.19) can be solved for $\boldsymbol{u}$ at least locally. Applying control according to

$$\boldsymbol{u} = \mathbf{D}^{-1}(\boldsymbol{x}) \left(-\boldsymbol{\beta}(\boldsymbol{x}) + \boldsymbol{v} \right) \tag{2.20}$$

then yields m non-interacting integrator chains of length r_i, $i = 1, \ldots, m$ relating the output $\boldsymbol{y}$ to a new set of (virtual) inputs $\boldsymbol{v} \in \mathbb{R}^m$

$$\begin{pmatrix} y_1^{(r_1)} \\ y_2^{(r_2)} \\ \vdots \\ y_m^{(r_m)} \end{pmatrix} = \begin{pmatrix} v_1 \\ v_2 \\ \vdots \\ v_m \end{pmatrix} \, . \tag{2.21}$$

Using state space notation results in the BRUNOVSKY canonical form, which comprises m single-input, single-output systems $(\boldsymbol{z}_i, v_i, y_i)$, $i = 1, \ldots, m$ of the form

$$\dot{\boldsymbol{z}}_i = \frac{\mathrm{d}}{\mathrm{d}t} \begin{pmatrix} z_{i,1} \\ z_{i,2} \\ \vdots \\ z_{i,r_i-1} \\ z_{i,r_i} \end{pmatrix} = \begin{pmatrix} z_{i,2} \\ z_{i,3} \\ \vdots \\ z_{i,r_i} \\ 0 \end{pmatrix} + \begin{pmatrix} 0 \\ 0 \\ \vdots \\ 0 \\ 1 \end{pmatrix} v_i \tag{2.22a}$$

$$y_i = z_{i,1} \, . \tag{2.22b}$$

Here, the two subscripts do not reference the elements of a matrix but are used to indicate both the resp. subsystem and the individual state. Aggregating all state variables $\boldsymbol{z}_i$ yields a single state vector $\boldsymbol{z} = (\boldsymbol{z}_1, \ldots, \boldsymbol{z}_m)^{\mathrm{T}}$ with $\dim(\boldsymbol{z}) = \sum_{i=1}^{m} r_i$. In the special case where $\dim(\boldsymbol{z}) = \dim(\boldsymbol{x})$, i.e. $\sum_{i=1}^{m} r_i = n$, the original (nonlinear) system (2.18), (2.17b) and the Brunovsky canonical form (2.22) are fully related by the static feedback (2.20) and a state transformation $\boldsymbol{\phi}_{\mathrm{B}} : \mathbb{R}^n \to \mathbb{R}^n$ given by

$$\boldsymbol{z} = \begin{pmatrix} z_{1,1} \\ z_{1,2} \\ \vdots \\ z_{1,r_1} \\ z_{2,1} \\ \vdots \\ z_{m-1,r_{m-1}} \\ z_{m,1} \\ z_{m,2} \\ \vdots \\ z_{m,r_m} \end{pmatrix} = \boldsymbol{\phi}_{\mathrm{B}}(\boldsymbol{x}) = \begin{pmatrix} h_1(\boldsymbol{x}) \\ L_{\boldsymbol{f}} h_1(\boldsymbol{x}) \\ \vdots \\ L_{\boldsymbol{f}}^{r_1-1} h_1(\boldsymbol{x}) \\ h_2(\boldsymbol{x}) \\ \vdots \\ L_{\boldsymbol{f}}^{r_{m-1}-1} h_{m-1}(\boldsymbol{x}) \\ h_m(\boldsymbol{x}) \\ L_{\boldsymbol{f}} h_1(\boldsymbol{x}) \\ \vdots \\ L_{\boldsymbol{f}}^{r_m-1} h_m(\boldsymbol{x}) \end{pmatrix}. \tag{2.23}$$

Noteworthy, the mapping $\boldsymbol{\phi}_{\mathrm{B}}(\boldsymbol{x})$ is invertible on $\mathcal{U}(\boldsymbol{x}_0)$, i.e. the inverse $\boldsymbol{x} = \boldsymbol{\phi}_{\mathrm{B}}^{-1}(\boldsymbol{z})$ exists. Since the controlled system (2.22) is linear, the control law (2.20) solves the so-called *exact linearization* problem [82]. Hence, (2.20) is also referred to as *linearizing* feedback. Controller synthesis is then carried out by means of a cascaded design, see

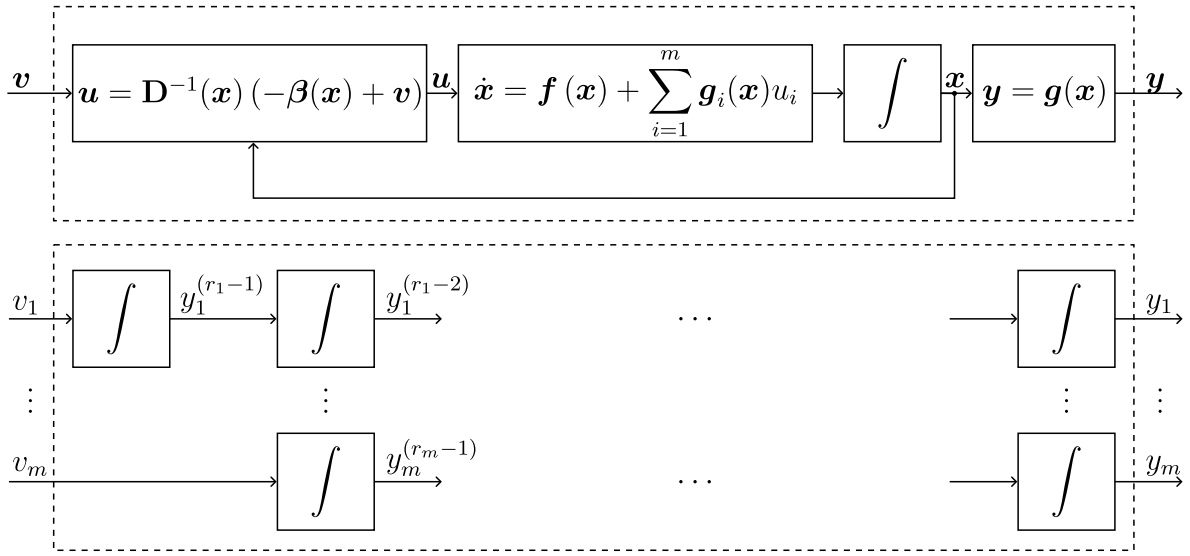

Fig. 2.7: Block diagram of a feedback linearization – Nonlinear system under feedback linearization (top) and linear auxiliary system (bottom)

Fig. 2.7. While the linearizing feedback is used in an inner loop to render the system linear, the task of stabilization or reference tracking is realized in the new coordinates $(\boldsymbol{z}, \boldsymbol{v}, \boldsymbol{y})$. The latter is straightforward due to the linearity of (2.22). As a result, high controller performances may be achieved albeit the application of linear design methods. Furthermore, stability of the linear auxiliary system (2.22) implies stability of the original (nonlinear) system, as long as there is minimal model mismatch. Regarding the crane system a useful observation is given by the fact, that the above restriction on the system's vector relative degree is always satisfied if the system is *flat*, cf. section 2.4. In contrast, if $\sum_{i=1}^{m} r_i < n$ the nonlinear system (2.18), (2.17b) under control (2.20) is characterized by a linear input-output behavior (Brunovsky part) along with an uncontrollable mode also referred to as *internal dynamics*, see [82, p. 310]. The internal dynamics are critical for the stability of the closed-loop system. Therefore, additional tests, e.g. analysis of the zero dynamics, are necessary to guarantee that all system trajectories remain bounded.

Today almost all controllers are implemented on discrete computation hardware. Suppose the cycle times and the system's time constants are of the same order. In that case, it is usually sensible to perform the controller synthesis in the discrete-time domain to also account for dynamic effects stemming from the sampling or the hold element interfacing e.g. the actuators. Accordingly, consider a discretized time axis $t \in \{t_k = t_0 + kT_\mathrm{s}\}$ with an initial time instance t_0, a running index $k = 0, 1, 2, \ldots$ and the sampling time T_s. A discrete version of the system dynamics (2.17) is then given by

$$\boldsymbol{x}_{k+1} = \boldsymbol{f}_\mathrm{d}\left(\boldsymbol{x}_k, \boldsymbol{u}_k, k\right) \qquad \text{(state equation)} \tag{2.24a}$$

$$\boldsymbol{y}_k = \boldsymbol{h}_\mathrm{d}\left(\boldsymbol{x}_k, \boldsymbol{u}_k, k\right) \qquad \text{(output equation)} \tag{2.24b}$$

where the evaluated point in time is indicated by an index, i.e. $\boldsymbol{x}_{k+1} = \boldsymbol{x}\left(t_0 + (k+1)T_\mathrm{s}\right)$ and $\boldsymbol{x}_k = \boldsymbol{x}\left(t_0 + kT_\mathrm{s}\right)$. Noteworthy, the state evolution is now given by a difference equation. While the mappings $\boldsymbol{h}$, $\boldsymbol{h}_\mathrm{d}$ in (2.17b) resp. (2.24b) are the same, relating the state equations (2.17a) and (2.24a) is in general not straightforward. An exact transformation exists for the special case of multiple-input, multiple-output (MIMO) linear time-invariant (LTI) systems, for which (2.17a) takes the form

$$\dot{\boldsymbol{x}}(t) = \mathbf{A}\boldsymbol{x}(t) + \mathbf{B}\boldsymbol{u}(t) \tag{2.25}$$

with the system matrix $\mathbf{A} \in \mathbb{R}^{n \times n}$ as well as the input matrix $\mathbf{B} \in \mathbb{R}^{n \times m}$. Similarly, the discrete system dynamics are described by

$$\boldsymbol{x}_{k+1} = \mathbf{A}_\mathrm{d}\boldsymbol{x}_k + \mathbf{B}_\mathrm{d}\boldsymbol{u}_k \,. \tag{2.26}$$

The continuous as well as discrete model matrices are then related according to

$$\mathbf{A}_\mathrm{d} = \mathrm{e}^{\mathbf{A}T_\mathrm{s}}, \qquad \mathbf{B}_\mathrm{d} = \int_0^{T_\mathrm{s}} \mathrm{e}^{\mathbf{A}\tau}\mathrm{d}\tau \tag{2.27}$$

where the matrix exponential function is used [2]. For the general nonlinear case, the discrete equivalent of (2.17a) is approximated by applying numerical integration schemes between two consecutive time steps, i.e. on the time interval $t \in [t_k, t_{k+1}]$. Among the most common techniques are different versions of the RUNGE-KUTTA method [112], [150]. Depending on the order $s \in \mathbb{N}$ of the iterative scheme, the system trajectories are evaluated at a finite grid of time instances t_i, $i \in \{1, \dots, s\}$. For the state equation, this yields

$$\boldsymbol{x}_{k+1} \approx \boldsymbol{x}_k + h \sum_{i=1}^{s} b_i \boldsymbol{k}_i \tag{2.28a}$$

$$\boldsymbol{k}_i = \boldsymbol{f}\left(\boldsymbol{x}_i, \boldsymbol{u}_i, t_k + c_i h\right) \tag{2.28b}$$

$$\boldsymbol{x}_i = \boldsymbol{x}_k + h \sum_{j=1}^{s} a_{ij} \boldsymbol{k}_j, \qquad \boldsymbol{u}_i = \boldsymbol{u}(t_k + c_i h) \tag{2.28c}$$

with the step size $h > 0 \in \mathbb{R}$, which is often equal to the sample time T_s or (in case of multistage formulations) a multiple of the same. The weights $b_i \in [0, 1]$, nodes $c_i \in [0, 1]$ and Runge-Kutta coefficients $a_{ij} \in [0, 1]$ vary depending on the applied version of the algorithm and are thus often summarized in the so-called BUTCHER tableau:

$$\begin{array}{c|cccc} c_1 & a_{11} & a_{12} & \dots & a_{1s} \\ c_2 & a_{21} & a_{22} & \dots & a_{2s} \\ \vdots & \vdots & \vdots & \ddots & \vdots \\ c_s & a_{s1} & a_{s2} & \dots & a_{ss} \\ \hline & b_1 & b_2 & \dots & b_s \end{array}$$

In the context of this thesis, both the explicit Runge-Kutta of fourth order (ERK4) and the implicit Runge-Kutta of second order (IRK2) are utilized, which are defined by the following Butcher tableaus:

ERK4 :

$$\begin{array}{c|cccc} 0 & 0 & 0 & 0 & 0 \\ 1/2 & 1/2 & 0 & 0 & 0 \\ 1/2 & 0 & 1/2 & 0 & 0 \\ 1 & 0 & 0 & 1 & 0 \\ \hline & 1/6 & 1/3 & 1/3 & 1/6 \end{array}$$

IRK2 :

$$\begin{array}{c|cc} 0 & 0 & 0 \\ 1/2 & 1/2 & 1/2 \\ \hline & 1/2 & 1/2 \end{array}$$

In the context of automated control, two observations may be exploited to speed up calculation of the integration schemes. Noting that the output of a discrete control algorithm is usually converted back to a continuous-time signal by use of a zero-order hold (ZOH), the intermediate inputs in (2.28c) simplify to $\boldsymbol{u}_i = \boldsymbol{u}_k$, $\forall i$. Moreover, when using a single-stage formulation, the IRK2 algorithm admits eliminating the intermediate variables $\boldsymbol{k}_1$, $\boldsymbol{k}_2$, yielding

$$\boldsymbol{x}_{k+1} \approx \boldsymbol{x}_k + \frac{h}{2}\left(\boldsymbol{f}\left(\boldsymbol{x}_k, \boldsymbol{u}_k, t_k\right) + \boldsymbol{f}\left(\boldsymbol{x}_{k+1}, \boldsymbol{u}_{k+1}, t_{k+1}\right)\right) \ .$$

2.4 Differential Flatness

The notion of *flatness* was first introduced by Fliess et al. [65], who used differential geometry to link the existence of a linearizing feedback (cf. section 2.3) to certain structural characteristics of the underlying system. In fact, such systems are parameterizable by means of a (specific) output vector and its time derivatives, which facilitates both open- and closed-loop controller design. Since the considered crane system presents a multiple-input, multiple-output (MIMO) system, the following definition will be used for notational brevity: Given an n-dimensional vector $\boldsymbol{a} = (a_1 \ \dots \ a_n)^{\mathrm{T}} \in \mathbb{R}^n$, define the vectorial time derivative of order $\boldsymbol{k} = (k_1 \ \dots \ k_n)^{\mathrm{T}}$ as

$$\boldsymbol{a}^{(\boldsymbol{k})} \coloneqq \left(a_1^{(k_1)} \ \dots \ a_n^{(k_n)}\right)^{\mathrm{T}} = \left(\frac{\mathrm{d}^{k_1}}{\mathrm{d}t^{k_1}} a_1 \ \dots \ \frac{\mathrm{d}^{k_n}}{\mathrm{d}t^{k_n}} a_n\right)^{\mathrm{T}} .$$

A dynamic system (2.17a) is called *flat*, if a (fictive) output $\boldsymbol{\gamma} \in \mathbb{R}^m$ exists with $\dim(\boldsymbol{\gamma}) = \dim(\boldsymbol{u})$ for which the following conditions hold [4]:

i) The flat output $\boldsymbol{\gamma}$ only depends on the states $\boldsymbol{x}$, inputs $\boldsymbol{u}$ as well as a finite number $\boldsymbol{\varepsilon} = (\varepsilon_1 \ \dots \ \varepsilon_m)^{\mathrm{T}}$ of time derivatives per input:

$$\boldsymbol{\gamma} = \boldsymbol{\psi}_{\gamma}\left(\boldsymbol{x}, \boldsymbol{u}, \dot{\boldsymbol{u}}, \dots, \boldsymbol{u}^{(\boldsymbol{\varepsilon})}\right). \tag{2.29a}$$

ii) All states $\boldsymbol{x}$ are parameterizable by means of the flat output $\boldsymbol{\gamma}$ and its first $\boldsymbol{\delta} = (\delta_1 \ \dots \ \delta_m)^{\mathrm{T}}$ time derivatives, yielding the flat state mapping $\boldsymbol{\psi}_{\boldsymbol{x}}(\cdot)$:

$$\boldsymbol{x} = \boldsymbol{\psi}_{\boldsymbol{x}}\left(\boldsymbol{\gamma}, \dot{\boldsymbol{\gamma}}, \dots, \boldsymbol{\gamma}^{(\boldsymbol{\delta})}\right). \tag{2.29b}$$

iii) Similar, the input vector $\boldsymbol{u}$ may be expressed as a function of the flat output $\boldsymbol{\gamma}$ and its first $\boldsymbol{\delta} + 1$ time derivatives, where the flat input mapping $\boldsymbol{\psi}_{\boldsymbol{u}}(\cdot)$ is well-defined:

$$\boldsymbol{u} = \boldsymbol{\psi}_{\boldsymbol{u}}\left(\boldsymbol{\gamma}, \dot{\boldsymbol{\gamma}}, \dots, \boldsymbol{\gamma}^{(\boldsymbol{\delta}+1)}\right). \tag{2.29c}$$

iv) The elements of $\boldsymbol{\gamma}$ are differentially independent, i.e. no mapping $\boldsymbol{\psi}_{\boldsymbol{a}}$ exists for which holds:

$$0 = \boldsymbol{\psi}_{\boldsymbol{a}}\left(\boldsymbol{\gamma}, \dot{\boldsymbol{\gamma}}, \dots, \boldsymbol{\gamma}^{(\boldsymbol{\alpha})}\right) . \tag{2.29d}$$

The (fictive) output $\boldsymbol{\gamma}$ is referred to as *linearizing* or *flat output*. If the conditions (2.29a)-(2.29d) hold only on a subspace of $\boldsymbol{x} \in \mathcal{X}$, the system is considered *locally flat*.

The system's relative degree $\boldsymbol{r}_{\boldsymbol{\gamma}} = (r_{\gamma_1} \ \dots \ r_{\gamma_m})^{\mathrm{T}} \in \mathbb{N}^m$ with respect to the flat output $\boldsymbol{\gamma}$ is well-defined on the entire (resp. relevant) state space and satisfies $\sum_{i=1}^{m} r_{\gamma_i} = n$. Hence, no internal dynamics occur when transforming the system to its BRUNOVSKY canonical form (2.22), see section 2.3. For a detailed introduction to the theory of flatness the reader is referred to e.g. [66], [82].

A key correlation can be established by means of (2.29b)-(2.29c): Noting that the system state $\boldsymbol{x}$ is fully determined by the flat output $\boldsymbol{\gamma}$ and its time derivatives, it is easy to show that any flat system is also *controllable*, which is paramount for control. In order to steer the system trajectories from an arbitrary initial state $\boldsymbol{x}(t_0) = \boldsymbol{x}_1$ to any given final state $\boldsymbol{x}(T) = \boldsymbol{x}_2$, it is sufficient to find a trajectory $\boldsymbol{\gamma}_d(t)$, which is continuously differentiable at least $\boldsymbol{\delta} + 1$ times and satisfies

$$\begin{aligned} \boldsymbol{x}_1 &= \boldsymbol{\psi}_{\boldsymbol{x}} \left(\boldsymbol{\gamma}_d(t_0), \dot{\boldsymbol{\gamma}}_d(t_0), \dots, \boldsymbol{\gamma}_d^{(\boldsymbol{\delta})}(t_0) \right) \\ \boldsymbol{x}_2 &= \boldsymbol{\psi}_{\boldsymbol{x}} \left(\boldsymbol{\gamma}_d(T), \dot{\boldsymbol{\gamma}}_d(T), \dots, \boldsymbol{\gamma}_d^{(\boldsymbol{\delta})}(T) \right) \ . \end{aligned}$$

The corresponding input trajectory is then given by

$$\boldsymbol{u}(t) = \boldsymbol{\psi}_{\boldsymbol{u}} \left(\boldsymbol{\gamma}_d(t), \dot{\boldsymbol{\gamma}}_d(t), \dots, \boldsymbol{\gamma}_d^{(\boldsymbol{\delta}+1)}(t) \right), \qquad t \in [t_0, T] \ .$$

The fact that (2.29c) allows calculating suitable input trajectories $\boldsymbol{u}(t)$ without the need to integrate the system dynamics (2.17a), will be exploited in section 4.4.4 to derive a computationally efficient controller formulation.

2.5 Predictive Control

As reflected in the thesis title, the concept of predictive control is central to the investigated automation solution, cf. chapter 1. The following is an introduction to the fundamental notions which apply to most predictive controllers. In this context, the associated open-loop optimal control problem (OCP) is introduced, which also forms the basis of the control algorithms proposed in chapter 4.

In classical control, sensor feedback is used to derive suitable control actions that stabilize the system around a given operating point (*regulation*) or steer it along a predefined trajectory (*tracking*). Depending on the application, system characteristics and available computational resources, different control strategies are applied ranging from conventional PID-control to robust formulations, e.g. H_∞-control. The aforementioned control topologies rely on the current (as well as past) values of the controlled variables in order to calculate appropriate inputs to the system. The same holds true for the large class of controllers based on state feedback. In contrast, *predictive control* further takes into account the future system behavior, which is anticipated based on some system model.

As a result, predictive policies often yield higher control performance when compared to topologies only integrating current and past system information. A simple example is the Smith predictor [162] known from linear control theory, which compensates for a delay in the process by using the (predicted) delay-free system response for feedback. The latter is calculated based on the system's transfer function neglecting the delay. Although not typically considered a predictive control scheme, the authors in [123] argue that the gain in controller bandwidth stems from the internal system model, which is essential to any predictive control. In fact, the authors identify three fundamental principles characteristic to predictive control:

i) an internal model that is used to predict future system trajectories (given some input trajectory),

ii) the receding horizon concept and

iii) solving of the control problem by means of numerical optimization

Furthermore, the importance of an appropriate reference trajectory representing the desired closed-loop behavior is stressed, along with the necessity to limit the free variables during optimization, e.g. by restricting the input trajectory, cf. [123]. A similar conception can already be found in [40], where the authors used linear, discrete-time transfer functions to formulate what they called *generalized predictive control*.

In order to translate the above principles into a predictive control algorithm, most textbooks resort to a discrete representation of the control task. This naturally results in finite problems, such that online computation is (in theory) straightforward. Yet, since the first predictive controllers emerged from industrial process control in the 1970s, various techniques have been developed to derive real-time feasible algorithms. Therefore, consider the more general time-continuous OCP

$$\boldsymbol{u}^*(t|t_0) = \arg\min_{\boldsymbol{u}(t)} \int_{t_0}^{t_0+T_\mathrm{p}} L\left(\boldsymbol{x}(t), \boldsymbol{u}(t), \boldsymbol{w}(t), t\right) \mathrm{d}t + L_{T_\mathrm{p}}(\boldsymbol{x}(T_\mathrm{p})) \tag{2.30}$$

$$\begin{aligned}
\text{s.t.} \quad \dot{\boldsymbol{x}}(t) &= \boldsymbol{f}\left(\boldsymbol{x}(t), \boldsymbol{u}(t)\right) && \forall\, t \in [t_0, t_0 + T_\mathrm{p}] && \text{(system dynamics)} \\
\boldsymbol{x}(t_0) &= \boldsymbol{x}_0 && && \text{(initial state constraint)} \\
\boldsymbol{x}(t) &\in \mathcal{X} && \forall\, t \in [t_0, t_0 + T_\mathrm{p}] && \text{(state constraints)} \\
\boldsymbol{u}(t) &\in \mathcal{U} && \forall\, t \in [t_0, t_0 + T_\mathrm{p}] && \text{(input constraints)} \\
\boldsymbol{x}(T_\mathrm{p}) &\in \mathcal{X}_{T_\mathrm{p}} \subset \mathcal{X} && && \text{(terminal state constraint)}
\end{aligned}$$

with the optimal input trajectory $\boldsymbol{u}^*(t|t_0)$, an arbitrary starting time t_0, the evaluated time horizon T_p, the reference trajectory $\boldsymbol{w}(t)$ and two cost functionals $L : \mathcal{X} \times \mathcal{U} \times \mathcal{Y} \times \mathbb{R} \to \mathbb{R}_{\geq 0}$, $L_{T_\mathrm{p}} : \mathcal{X}_{T_\mathrm{p}} \to \mathbb{R}_{\geq 0}$ rating the system trajectories resp. the final state. Here, the $(t|t_0)$-notation is used to indicate the variable's predicted trajectory over $t \in [t_0, t_0 + T_\mathrm{p}]$ calculated at time instance t_0, i.e. only information available at t_0 are considered for

prediction. Also, three sets $\mathcal{X} \subseteq \mathbb{R}^n$, $\mathcal{U} \subseteq \mathbb{R}^m$, $\mathcal{Y} \subseteq \mathbb{R}^p$ are introduced which denote the admissible sets of states, inputs and outputs. The system model is included by means of the system dynamics $\boldsymbol{f}$, which restrict the state evolution $\boldsymbol{x}^*(t|t_0)$ for a given initial state $\boldsymbol{x}_0$. In other words, $\boldsymbol{x}^*(t|t_0)$ solves the following initial value problem

$$\begin{aligned} \dot{\boldsymbol{x}}^*(t\ |t_0) &= \boldsymbol{f}\left(\boldsymbol{x}^*(t|t_0), \boldsymbol{u}^*(t|t_0)\right) \\ \boldsymbol{x}^*(t_0|t_0) &= \boldsymbol{x}_0\ . \end{aligned} \tag{2.31}$$

Since minimizing (2.30) for an infinite prediction horizon $T_\mathrm{p} \to \infty$ or arbitrary input trajectories $\boldsymbol{u}(t)$ is computationally intractable, the OCP is usually restricted to a finite horizon $0 < T_\mathrm{p} < \infty$ and approximated thereafter. Different techniques exist for the latter: While collocation methods parameterize the solution space based on spline interpolation, shooting methods apply time-discretization along with numerical integration to obtain finite problems [146]. Implementations of the aforementioned approaches are included in chapter 4, where different controller formulations for predictive payload stabilization are discussed.

At first instance, the OCP (2.30) informs an open-loop control law. For the simple case of a SISO system, the predictive control problem of tracking a given reference trajectory $w(t)$ is illustrated in Fig. 2.8. While the system's past input trajectory $u(t)$ and output trajectory $y(t)$ establish the initial boundary condition at t_0, the output trajectory $y(t|t_0)$ is predicted as a function of the (free) input trajectory $u(t|t_0)$ by means of the system model. Noteworthy, the system's time evolution beyond the finite horizon $t \in [t_0, t_0 + T_\mathrm{p}]$ is neglected. The optimal trajectories $u^*(t|t_0)$, $y^*(t|t_0)$ are then precisely those that minimize the cost function in (2.30). In order to close the control loop, the open-loop OCP is solved repeatedly at each sampling instance $t_0 = t_\mathrm{init} + kT_\mathrm{c}$ whilst updating the initial state $\boldsymbol{x}_0$. Here, t_init denotes the point in time at which the controller is activated, T_c is the controller cycle time and $k = 0, 1, 2, \ldots$ is a running index. The initial state $\boldsymbol{x}_0$ therefore constitutes the feedback component characteristic for closed-loop control. In accordance, only the first part of the optimal input trajectory $u^*(t|t_\mathrm{init} + kT_\mathrm{c})$ with $kT_\mathrm{c} \leq t - t_\mathrm{init} \leq (k+1)T_\mathrm{c}$ is applied between consecutive time steps, before a new optimum $u^*(t|t_\mathrm{init} + (k+1)T_\mathrm{c})$ is calculated. Since the evaluated time horizon shifts by increments of T_c, the control strategy is also known as *receding horizon control*. In this context, an additional subset $\mathcal{X}_{T_\mathrm{p}}$ may be defined to constrain the terminal state, i.e. the predicted state at $t = t_0 + T_\mathrm{p}$, which is usually included to improve stability of the finite-horizon controller [146].

Taking into account the discrete execution nature of modern computing hardware, the following shortened form of the above $(t|t_0)$-notation is commonly accepted: Without loss of generality, the time of controller initialization is set to zero, i.e. $t_\mathrm{init} = 0$. The time axis is then fully defined by the running index k along with the controller's constant execution rate $f_\mathrm{c} = \frac{1}{T_\mathrm{c}}$. Hence, when referring to a predicted trajectory, the time of prediction is simply indicated by k. For example, the output evolution predicted at

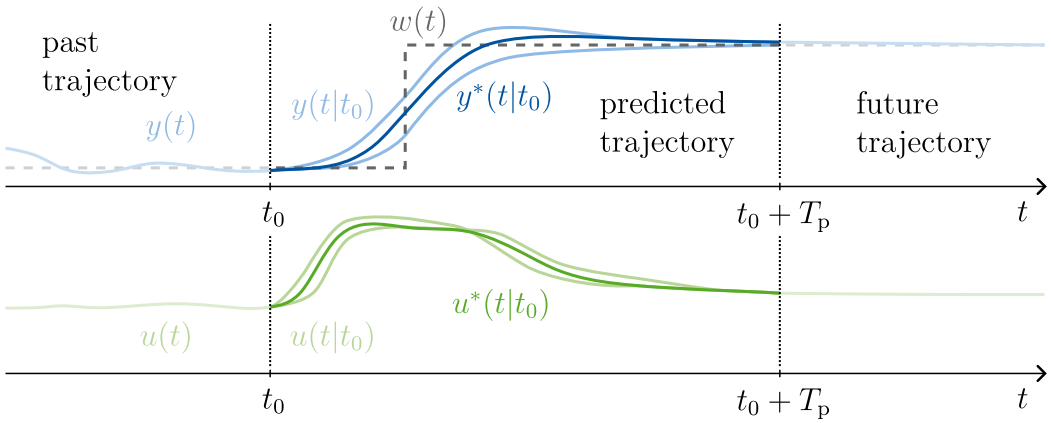

Fig. 2.8: Trajectories considered during finite-horizon predictive control of a SISO system – The initial boundary condition is determined by the system's past evolution $y(t)$, $u(t)$. The system response $y(t|t_0)$ over the finite horizon $t \in [t_0, t_0 + T_\mathrm{p}]$ is predicted on basis of the underlying system model and the free input trajectory $u(t|t_0)$. An optimal input trajectory $u^*(t|t_0)$ is calculated by solving the OCP (2.30) for a given reference trajectory $w(t)$. During optimization, the system's future trajectories from $t > t_0 + T_\mathrm{p}$ are neglected.

$t_0 = t_\mathrm{init} + kT_\mathrm{c}$ is denoted $\boldsymbol{y}(t|k)$. If the system variables are also discretized in time, i.e., their time evolution is represented by a series of weighted pulses, then a dot notation will be used to reference the entire trajectory over the prediction horizon T_p, e.g. $\boldsymbol{y}(\cdot|k)$.

In order to highlight the model-based nature of the control approaches based on a finite-version of the OCP (2.30), most related controllers are referred to as model predictive controller (MPC). Due to the extensive application of MPC both in academia and industry, the terms *predictive control* and *model-based predictive control* are used synonymously today. Predictive control strategies perform best when high accuracy models are available. Otherwise, robust formulations like *tube-based* MPC, adaptive schemes based on online system identification or disturbance observers may be applied to handle uncertainties [146]. Distinctive advantages over conventional controller designs stem from the inherent ability to address MIMO problems as well as to account for system limitations by means of the state and input constraints imposed in (2.30). On the downside, MPC is associated with an increase in computational complexity, such that real-time feasibility is a central challenge during controller synthesis. While a detailed introduction to the theory of MPC can be found in [123], advanced topics in predictive control are discussed e.g. in [146].

2.6 State Estimation

The behavior of a dynamical system (2.17) is determined by both its exogenous[6] inputs $\boldsymbol{u} \in \mathcal{U} \subseteq \mathbb{R}^m$ and inner states $\boldsymbol{x} \in \mathcal{X} \subseteq \mathbb{R}^n$, see section 2.3. Therefore, knowledge of the latter is crucial in a wide variety of technical applications. This holds particularly true for control topologies such as MPC, which rely on full state feedback. However, in most cases some states cannot be measured directly for either technical or economic reasons. In such instances, the state must be inferred from the known inputs $\boldsymbol{u}$ and measured outputs $\boldsymbol{y}_\mathrm{m} \in \mathbb{R}^q$, which is possible if the system is *observable*.

Observability

Formally, a nonlinear dynamic MIMO-system

$$\dot{\boldsymbol{x}} = \boldsymbol{f}\left(\boldsymbol{x}, \boldsymbol{u}\right) \qquad \text{(state equation)} \tag{2.32a}$$

$$\boldsymbol{y} = \boldsymbol{h}\left(\boldsymbol{x}, \boldsymbol{u}\right) \qquad \text{(performance outputs)} \tag{2.32b}$$

$$\boldsymbol{y}_\mathrm{m} = \bar{\boldsymbol{h}}\left(\boldsymbol{x}, \boldsymbol{u}\right) \qquad \text{(measured outputs)} \tag{2.32c}$$

with $\boldsymbol{f} : \mathcal{X} \times \mathcal{U} \to \mathbb{R}^n$, $\boldsymbol{h} : \mathcal{X} \times \mathcal{U} \to \mathbb{R}^p$, $\bar{\boldsymbol{h}} : \mathcal{X} \times \mathcal{U} \to \mathbb{R}^q$ is observable as long as every two system states $\boldsymbol{x}_1$, $\boldsymbol{x}_2 \in \mathcal{X}$, $\boldsymbol{x}_1 \neq \boldsymbol{x}_2$ are *distinguishable* for some input trajectory [76]. An input trajectory is said to distinguish between two states if it yields different outputs when the system is initialized at the resp. state, i.e.

$$\exists\, t \in [t_0, t_\mathrm{e}] : \quad \boldsymbol{y}_\mathrm{m}(t)\big|_{\boldsymbol{x}(t_0)=\boldsymbol{x}_1} \neq \boldsymbol{y}_\mathrm{m}(t)\big|_{\boldsymbol{x}(t_0)=\boldsymbol{x}_2} \ .$$

The system is observable in time $T = t_\mathrm{e} - t_0$ given that any two distinct states are distinguishable in time at most T and $t_\mathrm{e} < \infty$ is finite. Loosely speaking, a system is therefore observable if the states can be determined (distinguished) based on input/output data [164]. Note that in (2.32) two output equations are included in order to differentiate between *controlled* and *measured* outputs denoted $\boldsymbol{y}$ and $\boldsymbol{y}_\mathrm{m}$, respectively[7]. In practice, both outputs may overlap.

[6] The exogenous inputs to a system are in general not limited to the manipulated variables specified by the operator or controller, but may also include unknown disturbances. This leads to the class of *disturbance observers* or *unknown input observers*, not covered here. For related topics the interested reader is referred to e.g. [30], [110], [117]. Whenever necessary, the distinction between known and unknown inputs is emphasized by introducing an additional disturbance signal $\boldsymbol{d} \in \mathcal{D} \subseteq \times\mathbb{R}^d$ in (2.17) resp. (2.24), representing all inputs not available to the state estimator.

[7] Some textbooks adopt the more general concept of *performance outputs* instead of controlled outputs. These are typically labeled $\boldsymbol{z}$, which is avoided here to preclude ambiguity with the flat state introduced in section 2.4.

Due to the dependency on the applied input trajectories, proving the observability of a driven nonlinear system is often impractical. Yet, different approaches exist to check observability for special classes of systems, e.g. the KALMAN criterion for LTI systems [96]. In the context of the crane system, a more useful corollary follows from the observation that the nonlinear system (2.17) with measurements (2.32c) is observable if for some $k_i \in \mathbb{N}$ such that $\sum_{i=1}^{q} k_i = n$ the mapping

$$\begin{pmatrix} y_{\mathrm{m},1} \\ y_{\mathrm{m},1}^{(1)} \\ \vdots \\ y_{\mathrm{m},1}^{(k_1-1)} \\ y_{\mathrm{m},2} \\ \vdots \\ y_{\mathrm{m},q-1}^{(k_{q-1}-1)} \\ y_{\mathrm{m},q} \\ y_{\mathrm{m},q}^{(1)} \\ \vdots \\ y_{\mathrm{m},q}^{(k_q-1)} \end{pmatrix} = \boldsymbol{\varphi}_{\mathcal{O}}\left(\boldsymbol{x}, \boldsymbol{u}, \ldots, \boldsymbol{u}^{(\max\{k_1,\ldots,k_q\}-1)}\right) = \begin{pmatrix} \varphi_{\mathcal{O},1}^{0}(\boldsymbol{x}, \boldsymbol{u}) \\ \varphi_{\mathcal{O},1}^{1}(\boldsymbol{x}, \boldsymbol{u}, \dot{\boldsymbol{u}}) \\ \vdots \\ \varphi_{\mathcal{O},1}^{k_1-1}(\boldsymbol{x}, \boldsymbol{u}, \ldots, \boldsymbol{u}^{(k_1-1)}) \\ \varphi_{\mathcal{O},2}^{0}(\boldsymbol{x}, \boldsymbol{u}) \\ \vdots \\ \varphi_{\mathcal{O},q-1}^{k_{q-1}-1}(\boldsymbol{x}, \boldsymbol{u}, \ldots, \boldsymbol{u}^{(k_{q-1}-1)}) \\ \varphi_{\mathcal{O},q}^{0}(\boldsymbol{x}, \boldsymbol{u}) \\ \varphi_{\mathcal{O},q}^{1}(\boldsymbol{x}, \boldsymbol{u}, \dot{\boldsymbol{u}}) \\ \vdots \\ \varphi_{\mathcal{O},q}^{k_q-1}(\boldsymbol{x}, \boldsymbol{u}, \ldots, \boldsymbol{u}^{(k_q-1)}) \end{pmatrix} \tag{2.33}$$

is invertible[8] with respect to $\boldsymbol{x}$ and its inverse is sufficiently smooth [44]. The auxiliary functions $\varphi_{\mathcal{O},i}^{j}$ are defined recursively

$$\begin{aligned} \varphi_{\mathcal{O},i}^{0}(\boldsymbol{x}, \boldsymbol{u}) &:= \bar{h}_i(\boldsymbol{x}, \boldsymbol{u}) && i = 1, \ldots, q\,, \\ \varphi_{\mathcal{O},i}^{j}(\boldsymbol{x}, \boldsymbol{u}, \ldots, \boldsymbol{u}^{(j)}) &:= \frac{\partial \varphi_{\mathcal{O},i}^{j-1}}{\partial \boldsymbol{x}} \boldsymbol{f}(\boldsymbol{x}, \boldsymbol{u}) + \sum_{k=0}^{j-1} \frac{\partial \varphi_{\mathcal{O},i}^{j-1}}{\partial \boldsymbol{u}^{(k)}} \boldsymbol{u}^{(k+1)} && i = 1, \ldots, q\,,\ j = 1, \ldots, k_i - 1\,. \end{aligned}$$

Comparing (2.33), (2.23) and (2.29b) then implies that if a system is flat and the associated flat output $\boldsymbol{\gamma}$ is measurable, the system is indeed completely observable. The states are hence given as a function of the flat output and its derivatives irresp. of the input. Similar to the definition of flatness in section 2.4, observability of a system may be extended to a local notion, cf. [44], [76].

Given that the system under consideration is observable, the system states can be estimated by means of a *state estimator*, also commonly referred to as *observer* or *soft sensor*. The general concept of a state estimator is depicted in Fig. 2.9. In order to reconstruct the system state $\boldsymbol{x}$, a system model is computed in parallel to the physical system. The state estimator takes the known manipulated variables $\boldsymbol{u}$ and measured outputs $\boldsymbol{y}_{\mathrm{m}}$ as an input, while providing estimates of the state $\hat{\boldsymbol{x}}$ and measured outputs $\hat{\boldsymbol{y}}_{\mathrm{m}}$. In order to account for model mismatch as well as erroneous measurements, two

[8] A simple test for (local) observability is therefore to check whether the matrix $\boldsymbol{\Phi}_{\mathcal{O}} = \frac{\partial \boldsymbol{\varphi}_{\mathcal{O}}}{\partial \boldsymbol{x}}$ has full rank [44].

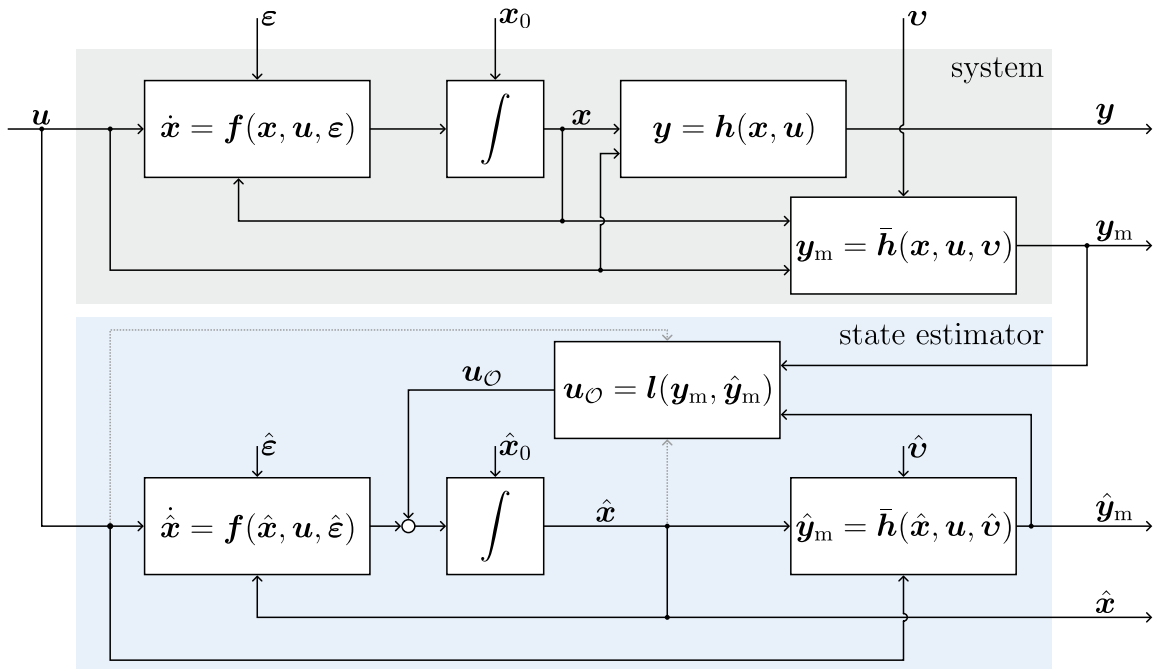

Fig. 2.9: Block diagram of a state estimator – Estimates $\hat{\boldsymbol{x}}$ of the system state $\boldsymbol{x}$ are derived on basis of a system model, which is simulated in open loop parallel to the physical system. Despite applying the same inputs $\boldsymbol{u}$, deviations in the state estimates remain due to different initial values $\boldsymbol{x}_0$ resp. $\hat{\boldsymbol{x}}_0$. Furthermore, the system is subject to both process noise $\boldsymbol{\varepsilon}$ and measurement noise $\boldsymbol{v}$. In the context of state estimation, the noise signals are approximated by their (uncertain) nominal values $\hat{\boldsymbol{\varepsilon}}$ and $\hat{\boldsymbol{v}}$. To correct the state estimates, feedback $\boldsymbol{u}_\mathcal{O}$ based on the measured and calculated outputs $\boldsymbol{y}_\mathrm{m}$ resp. $\hat{\boldsymbol{y}}_\mathrm{m}$ is incorporated.

additional inputs to the system – the process noise $\boldsymbol{\varepsilon} \in \mathbb{R}^n$ resp. the measurement noise $\boldsymbol{v} \in \mathbb{R}^q$ – are introduced. Usually, both signals are considered to be realizations of (continuous) *random processes*, which are characterized by time-dependent statistics, e.g. a mean and covariance function. The noise signals have to be approximated within the state estimator. If both system and measurements are unbiased, the estimates $\hat{\boldsymbol{\varepsilon}}$ and $\hat{\boldsymbol{v}}$ are fixed to zero. By definition, the initial state $\boldsymbol{x}(t_0) = \boldsymbol{x}_0$ is unknown. Hence, the estimator model is simulated starting at an inaccurate state $\hat{\boldsymbol{x}}_0$. Referring back to the notion of local observability, a good initial guess $\hat{\boldsymbol{x}}_0$ is often paramount in order to obtain viable estimates. Whether an initial guess is "good" depends on the system's nonlinearity. Assuming continuity of the system equations up to some degree, a common measure is the Euclidean distance $\|\boldsymbol{x}_0 - \hat{\boldsymbol{x}}_0\|$ between both states. To ensure convergence of the estimates, i.e. $\hat{\boldsymbol{x}} \to \boldsymbol{x}$ for $t \to t_\mathrm{e} \leq \infty$, an additional feedback $\boldsymbol{u}_\mathcal{O}$ is added to the state estimator. Commonly, the feedback law $\boldsymbol{l}(\cdot)$ is designed as a weighted function of the output error $\boldsymbol{e}_{\boldsymbol{y}_\mathrm{m}} = \boldsymbol{y}_\mathrm{m} - \hat{\boldsymbol{y}}_\mathrm{m}$, see for example the original work of Luenberger [120] or the more general results in [39].

Since most sensor readings are distorted by noise, the problem of state estimation is best conceived in a stochastic sense. As a result of modeling the noise signals $\boldsymbol{\epsilon}(t)$, $\boldsymbol{\upsilon}(t)$ as sampled multidimensional random processes, the system state itself becomes probabilistically distributed. Hereafter, a brief summary of the characteristics of random processes is included, which subsequently motivates the KALMAN filter covered below. In addition, two kinds of random processes that recur throughout this work are explained in more detail, namely *white* and GAUSSIAN processes. A thorough introduction to the stochastics of random processes can be found e.g. in [26], [137].

Random Processes

A random process $\{X(t)\}_{t\in[0,\infty)}$ is simply a random variable X that changes with time t [160]. In other words, two random variables $X^{'} = X(t_1)$ resp. $X^{''} = X(t_2)$ are observed at distinct times $t_1 \neq t_2$. As before, bold notation is adopted to indicate a vector-valued (i.e. multivariate) random process $\{\boldsymbol{X}(t)\}_{t\in[0,\infty)}$ whose components are themselves random processes. If the index t only takes discrete values $t = t_0 + kT$ with $k \in \mathbb{N}_0$, the random process reverts to a *random sequence* $\{X_k\}_{k\in\mathbb{N}_0}$. Sampling a random process or sequence yields particular realizations $x(t)$ resp. x_k, which can be evaluated explicitly. They are therefore indicated by lowercase identifiers, just as deterministic signals were before. The following descriptions refer to multivariate random processes [137]. Define the time-dependent (first-order) probability density function of an n-dimensional random process according to $f_{\boldsymbol{X}}(\boldsymbol{x},t) = \frac{\partial^n P(X_1(t)\leq x_1 \wedge \ldots \wedge X_n(t)\leq x_n)}{\partial x_1 \cdots \partial x_n}$, where $P(\cdot)$ denotes the probability measure. The PDF then allows calculating the process's *mean* function

$$\boldsymbol{\mu}_{\boldsymbol{X}}(t) = \int \cdots \int_{\mathbb{R}^n} \boldsymbol{x} f_{\boldsymbol{X}}(\boldsymbol{x},t)\,\mathrm{d}x_1 \ldots \mathrm{d}x_n \tag{2.34}$$

which gives its expected value $\boldsymbol{\mu}_{\boldsymbol{X}}(t_*) = E[\boldsymbol{X}(t_*)]$ for any given instant $t_* \in [0,\infty)$. Since in general the statistics of the process change with time, a supplementary characteristic is given by the correlation between different time instances. This gives rise to the second-order PDF $f_{\boldsymbol{X}_{t_1},\boldsymbol{X}_{t_2}}(\boldsymbol{x}_{t_1},\boldsymbol{x}_{t_2},t_1,t_2) = \frac{\partial^{2n} P\left(\bigwedge_{i=1}^{n} X_i(t_1)\leq x_{t_1,i} \wedge X_i(t_2)\leq x_{t_2,i}\right)}{\partial x_{t_1,1}\cdots\partial x_{t_1,n}\partial x_{t_2,1}\cdots\partial x_{t_2,n}}$, which is equal to the *joint* PDF of two random vectors $\boldsymbol{X}_{t_1} = \boldsymbol{X}(t_1)$ and $\boldsymbol{X}_{t_2} = \boldsymbol{X}(t_2)$ associated with the process at instants t_1, $t_2 \in [0,\infty)$. The relation between any two time instances is then described by the process's *autocorrelation*

$$\begin{aligned}\mathbf{R}_{\boldsymbol{X}\boldsymbol{X}}(t_1,t_2) &= E[\boldsymbol{X}(t_1)\boldsymbol{X}^{\mathrm{T}}(t_2)] \\ &= \int \cdots \int_{\mathbb{R}^{2n}} \boldsymbol{x}_{t_1}\boldsymbol{x}_{t_2}^{\mathrm{T}} f_{\boldsymbol{X}_{t_1},\boldsymbol{X}_{t_2}}(\boldsymbol{x}_{t_1},\boldsymbol{x}_{t_2},t_1,t_2)\,\mathrm{d}x_{t_1,1}\ldots\mathrm{d}x_{t_1,n}\mathrm{d}x_{t_2,1}\ldots\mathrm{d}x_{t_2,n}\end{aligned}$$

resp. its *autocovariance*

$$\begin{aligned}\boldsymbol{\Sigma}_{\boldsymbol{X}\boldsymbol{X}}(t_1,t_2) &= E[(\boldsymbol{X}(t_1) - E[\boldsymbol{X}(t_1)])\,(\boldsymbol{X}(t_2) - E[\boldsymbol{X}(t_2)])^{\mathrm{T}}] \\ &= \mathbf{R}_{\boldsymbol{X}\boldsymbol{X}}(t_1,t_2) - \boldsymbol{\mu}_{\boldsymbol{X}}(t_1)\boldsymbol{\mu}_{\boldsymbol{X}}^{\mathrm{T}}(t_2)\end{aligned} \tag{2.35}$$

which both are matrix-valued functions of the considered times t_1, t_2. If the random process $\{\boldsymbol{X}(t)\}_{t\in[0,\infty)}$ is *stationary* its statistics do not change with time. More precisely, the process is called *first-order stationary* if its first-order PDF is invariant with respect to time, i.e. $f_{\boldsymbol{X}}(\boldsymbol{x},t) = f_{\boldsymbol{X}}(\boldsymbol{x},t+\tau)$ for all t, $\tau \in [0,\infty)$. By implication, such a process has a constant mean $\boldsymbol{\mu}_{\boldsymbol{X}}(t) = \boldsymbol{\mu}_{\boldsymbol{X}}$. Similar, the process is called *second-order stationary* if its second-order PDF is invariant with respect to time, i.e. $f_{\boldsymbol{X}_{t_1},\boldsymbol{X}_{t_2}}(\boldsymbol{x}_{t_1},\boldsymbol{x}_{t_2},t_1,t_2) = f_{\boldsymbol{X}_{t_1+\tau},\boldsymbol{X}_{t_2+\tau}}(\boldsymbol{x}_{t_1+\tau},\boldsymbol{x}_{t_2+\tau},t_1+\tau,t_2+\tau)$ for all t, $\tau \in [0,\infty)$. As a result, the process's autocorrelation and autocovariance only depend on the time difference $\Delta t = t_2 - t_1$ irresp. of the absolute times t_1, t_2

$$\begin{aligned}\mathbf{R}_{\boldsymbol{X}\boldsymbol{X}}(t_1,t_2) &= \mathbf{R}_{\boldsymbol{X}\boldsymbol{X}}(t,t+\Delta t) \qquad \forall\, t,t_1,t_2 \in [0,\infty),\\ \boldsymbol{\Sigma}_{\boldsymbol{X}\boldsymbol{X}}(t_1,t_2) &= \boldsymbol{\Sigma}_{\boldsymbol{X}\boldsymbol{X}}(t,t+\Delta t) \qquad \forall\, t,t_1,t_2 \in [0,\infty)\end{aligned}$$

in which case it is common to use the abbreviated notations $\mathbf{R}_{\boldsymbol{X}\boldsymbol{X}}(\Delta t)$ and $\boldsymbol{\Sigma}_{\boldsymbol{X}\boldsymbol{X}}(\Delta t)$, respectivley. The process is *stationary*[9] if it is not only first or second-order stationary but the above reasoning holds for all PDFs up to arbitrary order, i.e. number of considered time instances. See [137] for a complete treatment of random processes and their statistics.

White Random Processes

A stochastic process is called *white* if it has zero mean, finite covariance and the two random vectors $\boldsymbol{X}(t_1)$ and $\boldsymbol{X}(t_2)$ are uncorrelated for all $t_1 \neq t_2$, i.e. $\mathbf{R}_{\boldsymbol{X}\boldsymbol{X}}(t_1, t_2 \neq t_1) = \mathbf{0}$. More formally, the autocorrelation of a white (and thus stationary) process is given by

$$\mathbf{R}_{\boldsymbol{X}\boldsymbol{X}}(t_1,t_2) = \mathbf{R}_{\boldsymbol{X}\boldsymbol{X}}(0)\delta(t_2 - t_1)$$

where $\delta(\Delta t)$ denotes the delta distribution or Dirac-impulse, which is zero outside of $\Delta t = t_2 - t_1 = 0$ and whose integral over $\mathbb{R}$ is equal to one. Accordingly, the autocorrelation of a white random sequence $\{\boldsymbol{X}_k\}_{k\in\mathbb{N}_0}$ is obtained as $\mathbf{R}_{\boldsymbol{X}\boldsymbol{X}}(k_1,k_2) = \mathbf{R}_{\boldsymbol{X}\boldsymbol{X}}(0)\delta_{k_2-k_1}$, where $\delta_{\Delta k}$ is the Kronecker delta function. Again, for any fixed point in time, the random sequence is correlated only with itself. In view of (2.35), the autocovariance of a white and therefore mean-free process is equal to its autocorrelation. Given that a multivariate random process is white but has correlated elements, define the covariance matrix

$$\mathbf{Q}_{\boldsymbol{X}} \coloneqq \begin{bmatrix} E[X_1^2(t)] & \dots & E[X_1(t)X_n(t)] \\ \vdots & \ddots & \vdots \\ E[X_n(t)X_1(t)] & \dots & E[X_n^2(t)] \end{bmatrix} = \begin{bmatrix} \sigma_1^2 & \dots & \sigma_{1,n} \\ \vdots & \ddots & \vdots \\ \sigma_{n,1}^2 & \dots & \sigma_n^2 \end{bmatrix} = \boldsymbol{\Sigma}_{\boldsymbol{X}\boldsymbol{X}}(0) = \text{const.}$$

[9] A stationary process is also called *strict sense stationary*. In contrast, the weaker notion of *wide sense stationarity* is implied by second-order stationarity alone, although the converse is not true [137].

where the diagonal elements equate to the variances associated with the resp. (scalar-valued) random process $\{X_i(t)\}_{t\in[0,\infty)}$, $i = 1, \ldots, n$. Noteworthy, whiteness does not suggest any particular distribution. Its definition rather draws from the fact that realizations of the process have equal intensity over all frequencies. Accordingly, a white process features a constant power spectrum, which is the FOURIER transform of its autocorrelation [100].

Gaussian Random Processes

For a Gaussian random process (GP), statistical characterization is possible solely in terms of normal distributions. By definition, a random process is Gaussian if for every finite set of time instances $\mathcal{T} = \{t_1, \ldots, t_m\}$ with arbitrary size m the associated mth-order PDF is normal, i.e.

$$f_{X_1,\ldots,X_m}(x_1, \ldots, x_m, t_1, \ldots, t_m) = \frac{1}{\sqrt{(2\pi)^m \det \boldsymbol{\Sigma}_{\boldsymbol{ZZ}}}} \exp\left(-\frac{1}{2}(\boldsymbol{Z} - \boldsymbol{\mu}_{\boldsymbol{Z}})^{\mathrm{T}} \boldsymbol{\Sigma}_{\boldsymbol{ZZ}}^{-1} (\boldsymbol{Z} - \boldsymbol{\mu}_{\boldsymbol{Z}})\right) \tag{2.36}$$

where for notational brevity all random variables $X_i = X(t_i)$ with $i = 1, \ldots, m$ are concatenated to yield a single m-dimensional random vector $\boldsymbol{Z} = (X_1 \ \ldots \ X_m)^{\mathrm{T}}$ with mean $\boldsymbol{\mu}_{\boldsymbol{Z}}$ and covariance $\boldsymbol{\Sigma}_{\boldsymbol{ZZ}}$, both of which may depend on $\mathcal{T}$. The concept directly extends to random sequences.

Similar to the definition above, a multivariate random process with $n \in \mathbb{N}$ elements is jointly Gaussian, if the $\bar{m} = \sum_{i=1}^{n} m_i$-dimensional random vector

$$\bar{\boldsymbol{Z}} = (X_1(t_1) \ \ldots \ X_1(t_{m_1}) \, X_2(t_{m_1+1}) \ \ldots \ X_{n-1}(t_{\bar{m}-m_n}) \, X_n(t_{\bar{m}-m_n+1}) \ \ldots \ X_n(t_{\bar{m}}))^{\mathrm{T}}$$

based on the superset

$$\bar{\mathcal{T}} = \{\underbrace{t_1, \ldots, t_{m_1}}_{=\mathcal{T}_1}, t_{m_1+1}, \ldots, t_{\bar{m}-m_n}, \underbrace{t_{\bar{m}-m_n+1}, \ldots, t_{\bar{m}}}_{=\mathcal{T}_n}\}$$

informs a multivariate normal distribution resp. PDF for all possible sets $\mathcal{T}_i$ (arbitrary time instances $t_j \in [0, \infty)$, $j \in [1, \bar{m}]$ and finite sizes $m_i \in \mathbb{N}_0$). Therefore, Gaussianity of the individual random processes $\{X_i(t)\}_{t\in[0,\infty)}$, $i = 1, \ldots, n$ does not suffice to render the multivariate process $\{\boldsymbol{X}(t)\}_{t\in[0,\infty)}$ Gaussian.

The prevalence of Gaussian processes in practice stems from the underlying normal distributions, which facilitate computations considerably. First, a GP is completely determined by specifying its mean and autocorrelation functions. Furthermore, any GP with constant mean and shift-invariant autocorrelation (wide sense stationarity) can be shown to be stationary. As a result, PDF of arbitrary order may be expressed by simple identities. Another property that carries over from normal distributions is the equivalence

of uncorrelatedness and mutual independence. If two GPs are uncorrelated, they are also mutually independent, and vice versa. Clearly, the same holds true for two random variables resp. vectors associated with a single GP at two instants. Last, an important system-theoretic characteristic of GPs follows from the fact that any linear combination of jointly Gaussian random variables is again normally distributed. Accordingly, if a linear (potentially time-variant) dynamic system is driven by a GP, the output process is also Gaussian. Additional identities can be proven if the system is LTI or if the input process is at least wide sense stationary. Refer to [137] for a derivation of the aforementioned properties.

Following common conventions, a normally distributed random vector $\boldsymbol{X}$ will be denoted $\boldsymbol{X} \sim \mathcal{N}(\boldsymbol{\mu}_{\boldsymbol{X}}, \boldsymbol{\Sigma}_{\boldsymbol{X}\boldsymbol{X}})$. With a slight abuse of notation, a similar expression is used to indicate that the vector-valued random process $\{\boldsymbol{X}(t)\}_{t\in[0,\infty)}$ corresponds to a GP, i.e. $\boldsymbol{X}(t) \sim \mathcal{GP}(\boldsymbol{\mu}_{\boldsymbol{X}}(t), \boldsymbol{\Sigma}_{\boldsymbol{X}\boldsymbol{X}}(t_1, t_2))$. It should be noted, that Gaussian processes are widely adopted in regression, too. There, the index set – or more generally the *input domain* – is typically not characterized by a time parameterization, but rather by one or more independent variables referred to as *predictors*, cf. section 2.7. Yet, analogous definitions apply.

Types of Estimation

Since today, the majority of state estimators is implemented on discrete computing hardware and most sensors are processed digitally, hereafter a time-discrete system of the form

$$\boldsymbol{x}_{k+1} = \boldsymbol{f}_{\mathrm{d}}\left(\boldsymbol{x}_k, \boldsymbol{u}_k, \boldsymbol{\varepsilon}_k\right) \tag{2.37a}$$

$$\boldsymbol{y}_k = \boldsymbol{h}_{\mathrm{d}}\left(\boldsymbol{x}_k, \boldsymbol{u}_k\right) \tag{2.37b}$$

$$\boldsymbol{y}_{\mathrm{m},k} = \bar{\boldsymbol{h}}_{\mathrm{d}}\left(\boldsymbol{x}_k, \boldsymbol{u}_k, \boldsymbol{\upsilon}_k\right) \tag{2.37c}$$

will be considered. In accordance with Fig. 2.9, two additional inputs $\boldsymbol{\varepsilon}_k$ and $\boldsymbol{\upsilon}_k$ are included, reflecting process and measurement noise, respectively. If not stated otherwise, both signals are assumed to be realizations of independent random sequences. In the case where (2.37) is a discrete approximation to a continuous-time system – such as the union of ship, crane and payload in chapter 3 – the process noise $\boldsymbol{\varepsilon}_k$ might be thought of as the cumulative contribution of the continuous-time noise process $\{\boldsymbol{\mathcal{E}}(t)\}_{t\in[0,\infty)}$ to the state vector $\boldsymbol{x}$ over one sampling interval $[t_k, t_{k+1}]$. Relating the statistics of the random process $\{\boldsymbol{\mathcal{E}}(t)\}_{t\in[0,\infty)}$ and sequence $\{\boldsymbol{\mathcal{E}}_k\}_{k\in\mathbb{N}_0}$ is difficult in general, however equivalence with respect to the state evolution can be attained for some problems, see [26]. In the context of this thesis, an identity of particular interest may be derived for the special case of an LTI-system driven by a white noise process with covariance $\mathbf{Q}_{\boldsymbol{\mathcal{E}}}$. The discrete analogous is then given by a white sequence with covariance $\mathbf{Q}_{\boldsymbol{\mathcal{E}},\mathrm{d}} = \frac{1}{T_{\mathrm{s}}}\mathbf{Q}_{\boldsymbol{\mathcal{E}}}$ [160].

Following [160], four types of estimation will be distinguished depending on the data that is used for state estimation. Adopting the same notation introduced in section 2.5, define

- the *smoothed* estimate $\hat{\boldsymbol{x}}(k|k+N) = E[\boldsymbol{X}_k|\boldsymbol{y}_{\mathrm{m},1}, \boldsymbol{y}_{\mathrm{m},2}, \ldots, \boldsymbol{y}_{\mathrm{m},k}, \ldots, \boldsymbol{y}_{\mathrm{m},k+N}]$ as the expected value of $\boldsymbol{X}_k$ conditioned on all measurements up to some time instance $t_{k+N} = t_0 + (k+N)T_\mathrm{s}$, which include $N \in \mathbb{N}$ sensor readings after time instance t_k,
- the *a priori* estimate $\hat{\boldsymbol{x}}(k|k-1) = E[\boldsymbol{X}_k|\boldsymbol{y}_{\mathrm{m},1}, \boldsymbol{y}_{\mathrm{m},2}, \ldots, \boldsymbol{y}_{\mathrm{m},k-1}]$ as the expected value of $\boldsymbol{X}_k$ conditioned on all measurements up to but not including time instance t_k, which is also referred to as $\hat{\boldsymbol{x}}_k^-$,
- the *a posterior* estimate $\hat{\boldsymbol{x}}(k|k) = E[\boldsymbol{X}_k|\boldsymbol{y}_{\mathrm{m},1}, \boldsymbol{y}_{\mathrm{m},2}, \ldots, \boldsymbol{y}_{\mathrm{m},k}]$ as the expected value of $\boldsymbol{X}_k$ conditioned on all measurements up to and including time instance t_k, which is also referred to as $\hat{\boldsymbol{x}}_k^+$,
- the *predicted* estimate $\hat{\boldsymbol{x}}(k|k-M) = E[\boldsymbol{X}_k|\boldsymbol{y}_{\mathrm{m},1}, \boldsymbol{y}_{\mathrm{m},2}, \ldots, \boldsymbol{y}_{\mathrm{m},k-M}]$ as the expected value of $\boldsymbol{X}_k$ conditioned on all measurements up to some time instance $t_{k-M} = t_0 + (k-M)T_\mathrm{s}$ located $M \in \mathbb{N}$ sample intervals T_s before time instance t_k.

The different estimates are illustrated in Fig. 2.10. In the definitions above, all measurements from initialization up to the current time step are used for state estimation. Hence, the considered data basis grows with each sampling interval T_s. In this case, a conforming estimator solves the so-called *full information problem*. In theory, the full information

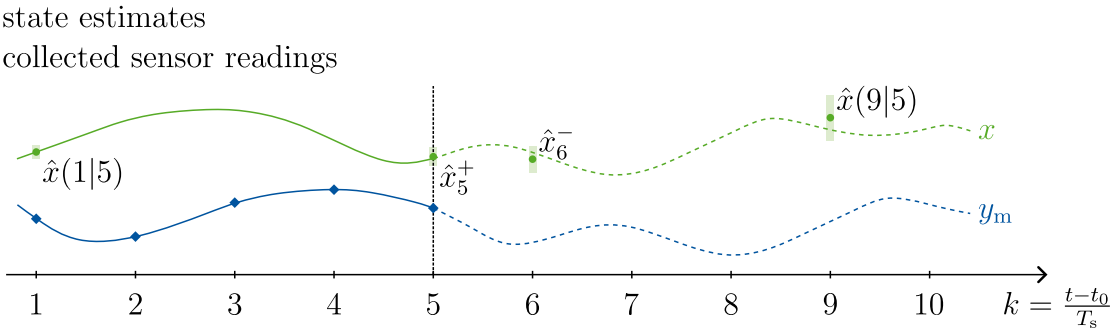

Fig. 2.10: Full information estimation – Exemplary trajectories of a system with one state x (green) and measured output y_m (blue). At the current time step $t_5 = t_0 + 5T_\mathrm{s}$ five measurements (rhombs) have been processed, on which basis four state estimates (circles) are derived. In particular, the smoothed estimate $\hat{x}(1|5)$, the a posterior estimate $\hat{x}_5^+$, the a priori estimate $\hat{x}_6^-$ as well as the predicted estimate $\hat{x}(9|5)$ are computed. If the underlying model is inaccurate, the state estimates are erroneous and thus deviate from the state trajectory. Furthermore, the uncertainty in the state estimates (shaded areas) increases from left to right, as less relevant sensor data is available.

estimations can be calculated similar to (2.34), i.e. the conditional expectation of $\boldsymbol{X}_k$ given $l \in \mathbb{N}$ measurements satisfies

$$E[\boldsymbol{X}_k|\boldsymbol{y}_{\mathrm{m},1},\ldots,\boldsymbol{y}_{\mathrm{m},l}] = \int \cdots \int_{\mathbb{R}^n} \boldsymbol{x} \frac{f_{\boldsymbol{X}_k,\boldsymbol{Y}_{\mathrm{m},1},\ldots,\boldsymbol{Y}_{\mathrm{m},l}}(\boldsymbol{x},\boldsymbol{y}_{\mathrm{m},1},\ldots,\boldsymbol{y}_{\mathrm{m},l})}{f_{\boldsymbol{Y}_{\mathrm{m},1},\ldots,\boldsymbol{Y}_{\mathrm{m},l}}(\boldsymbol{y}_{\mathrm{m},1},\ldots,\boldsymbol{y}_{\mathrm{m},l})} \,\mathrm{d}x_1 \ldots \mathrm{d}x_n \quad (2.38)$$

where the fact has been used that the conditional PDF may be expressed as the quotient of two joint PDFs. However, the use of iterative schemes renders the explicit evaluation of (2.38) obsolete in practice. Two iterative state estimators are described in the following.

Kalman Filtering

First proposed in 1960, the Kalman filter [95] provides state estimates of minimal variance under the following assumptions:

(A_1) The system under consideration is linear but not necessarily LTI.

(A_2) A perfect system model is available, that is there is no model mismatch.

(A_3) Process and measurement noise coincide with uncorrelated random sequences, which are both Gaussian and white.

If the assumptions (A_1)-(A_3) are fulfilled, the Kalman filter is optimal with regard to a (weighted) two-norm of the expected estimation error, i.e. the estimates $\hat{\boldsymbol{x}}_k = E[\hat{\boldsymbol{X}}_k]$ minimize the quadratic loss function $E[\boldsymbol{E}_{\boldsymbol{x}}^{\mathrm{T}}(k)\mathbf{S}_k\boldsymbol{E}_{\boldsymbol{x}}(k)]$, where the random[10] estimation error $\boldsymbol{E}_{\boldsymbol{x}}$ is given by $\boldsymbol{E}_{\boldsymbol{x}}(k) = \boldsymbol{X}_k - \hat{\boldsymbol{X}}_k$ and $\mathbf{S}_k$ is a positive definite weighting matrix [160]. As hinted in [95], the Kalman filter is still the optimal linear estimator even if the noise sequences are not Gaussian but otherwise meet (A_3).

In practice, none of the preceding assumptions is likely to be valid. While the original filter can be extended in order to handle correlated or colored noise [160], modifying the estimation problem may be considered to account for e.g. uncertain parameters. In the latter case, the state vector $\boldsymbol{x}$ is augmented by the unknown parameters $\boldsymbol{\theta}$ so that states and parameters are estimated jointly [70]. However, maintaining observability of the augmented system with state vector $\tilde{\boldsymbol{x}} = (\boldsymbol{x}^{\mathrm{T}}\ \boldsymbol{\theta}^{\mathrm{T}})^{\mathrm{T}}$ limits the number of parameters that can be estimated at the same time. Therefore, sufficient (non-redundant) sensor data must be available to render the joint estimation problem feasible. A similar approach is adopted in section 4 to determine calibration offsets during experimental controller validation. Regarding the crane system, applying the Kalman filter is impractical due to the nonlinearity of the system, which contradicts (A_1). Since nonlinear dynamics are

[10] As argued before, the state $\boldsymbol{x}_k$ becomes statistically distributed as a result of the random process noise $\{\boldsymbol{\mathcal{E}}_k\}_{k\in\mathbb{N}}$. The same holds true for the estimates $\hat{\boldsymbol{x}}_k$, which by virtue of the measured outputs $\boldsymbol{y}_{\mathrm{m},k}$ are a function of the random sequence $\{\boldsymbol{\mathcal{V}}_k\}_{k\in\mathbb{N}}$. Therefore, it is reasonable to evaluate the estimation error $\boldsymbol{e}_{\boldsymbol{x}}(k) = \boldsymbol{x}_k - \hat{\boldsymbol{x}}_k$ in a statistical setting as done above.

widely encountered in real-world applications, there are several approaches to generalize the linear filter. The most commonly used approximation is to linearize the system equations (2.37) about the current state estimate and input, which is also known as the *extended Kalman filter* (EKF) [70]. While the EKF no longer enjoys the theoretical optimal properties of the linear Kalman filter, it allows propagating the conditional mean of the state and its covariance matrix in a similar way, which greatly facilitates computation in practice. Yet, rigorous estimator validation is imperative since the filter performance can be poor depending on the severity of the system's nonlinearity. In the worst case, the state estimates may diverge. The iterative filter equations of the EKF are illustrated in Fig. 2.11 and summarized hereafter. The presentation follows that in [160].

Extended Kalman filter: Consider a nonlinear system of form (2.37), whose state and measurement equations are given by

$$\begin{aligned} \boldsymbol{x}_{k+1} &= \boldsymbol{f}_{\mathrm{d}}\left(\boldsymbol{x}_k, \boldsymbol{u}_k, \boldsymbol{\varepsilon}_k\right) \\ \boldsymbol{y}_{\mathrm{m},k} &= \bar{\boldsymbol{h}}_{\mathrm{d}}\left(\boldsymbol{x}_k, \boldsymbol{u}_k, \boldsymbol{\upsilon}_k\right) \ . \end{aligned}$$

The process noise $\boldsymbol{\varepsilon}_k$ and measurement noise $\boldsymbol{\upsilon}_k$ are determined by uncorrelated, white and Gaussian noise sequences

$$\boldsymbol{\mathcal{E}}_k \sim \mathcal{GP}(\mathbf{0}, \mathbf{Q}_{\boldsymbol{\mathcal{E}},\mathrm{d}}\delta_{k-j}), \qquad \boldsymbol{\mathcal{V}}_k \sim \mathcal{GP}(\mathbf{0}, \mathbf{Q}_{\boldsymbol{\mathcal{V}},\mathrm{d}}\delta_{k-j}), \qquad E[\boldsymbol{\mathcal{E}}_k \boldsymbol{\mathcal{V}}_j^{\mathrm{T}}] = \mathbf{0} \quad \forall\, k, j \in \mathbb{N}_0$$

with covariance matrices $\mathbf{Q}_{\boldsymbol{\mathcal{E}},\mathrm{d}} \in \mathbb{R}^{n\times n}$ and $\mathbf{Q}_{\boldsymbol{\mathcal{V}},\mathrm{d}} \in \mathbb{R}^{q\times q}$. Assume that at initialization the system state is normally distributed according to $\boldsymbol{x}_0 \sim \mathcal{N}(\hat{\boldsymbol{x}}_0^+, \mathbf{P}_0^+)$, such that the initial estimates of state $\hat{\boldsymbol{x}}_0^+ \in \mathbb{R}^n$ and (error) covariance $\mathbf{P}_0^+ \in \mathbb{R}^{n\times n}$ satisfy

$$\hat{\boldsymbol{x}}_0^+ = E[\boldsymbol{X}_0], \qquad \mathbf{P}_0^+ = E[(\boldsymbol{X}_0 - \hat{\boldsymbol{x}}_0^+)(\boldsymbol{X}_0 - \hat{\boldsymbol{x}}_0^+)^{\mathrm{T}}] \ .$$

In practice, the quantities $\hat{\boldsymbol{x}}_0^+$, $\mathbf{P}_0^+$ present tuning factors for the estimator, which have to be provided based on expert knowledge. A priori as well as a posterior state estimates are then obtained iteratively by computing the EKF's *time update* (TU) resp. *measurement update* (MU) for $k \geq 1$:

$$\text{TU}: \begin{cases} \hat{\boldsymbol{x}}_k^- = \boldsymbol{f}_{\mathrm{d}}(\hat{\boldsymbol{x}}_{k-1}^+, \boldsymbol{u}_{k-1}, \mathbf{0}) \\ \mathbf{P}_k^- = \mathbf{A}_{k-1}\mathbf{P}_{k-1}^+\mathbf{A}_{k-1}^{\mathrm{T}} + \mathbf{B}_{\boldsymbol{\varepsilon},k-1}\mathbf{Q}_{\boldsymbol{\mathcal{E}},\mathrm{d}}\mathbf{B}_{\boldsymbol{\varepsilon},k-1}^{\mathrm{T}} \end{cases} \tag{2.39}$$

$$\text{MU}: \begin{cases} \mathbf{K}_k = \mathbf{P}_k^-\bar{\mathbf{C}}_k^{\mathrm{T}}(\bar{\mathbf{C}}_k\mathbf{P}_k^-\bar{\mathbf{C}}_k^{\mathrm{T}} + \bar{\mathbf{D}}_{\boldsymbol{\upsilon},k}\mathbf{Q}_{\boldsymbol{\mathcal{V}},\mathrm{d}}\bar{\mathbf{D}}_{\boldsymbol{\upsilon},k}^{\mathrm{T}})^{-1} \\ \hat{\boldsymbol{x}}_k^+ = \hat{\boldsymbol{x}}_k^- + \mathbf{K}_k(\boldsymbol{y}_{\mathrm{m},k} - \bar{\boldsymbol{h}}_{\mathrm{d}}\left(\hat{\boldsymbol{x}}_k^-, \boldsymbol{u}_k, \mathbf{0}\right)) \\ \mathbf{P}_k^+ = (\mathbf{I}_{n\times n} - \mathbf{K}_k\bar{\mathbf{C}}_k)\mathbf{P}_k^-(\mathbf{I}_{n\times n} - \mathbf{K}_k\bar{\mathbf{C}}_k)^{\mathrm{T}} + \mathbf{K}_k\bar{\mathbf{D}}_{\boldsymbol{\upsilon},k}\mathbf{Q}_{\boldsymbol{\mathcal{V}},\mathrm{d}}\bar{\mathbf{D}}_{\boldsymbol{\upsilon},k}^{\mathrm{T}}\mathbf{K}_k^{\mathrm{T}} \ . \end{cases} \tag{2.40}$$

In order to propagate the state's covariance matrix the following Jacobians are calculated at each sampling instance

$$\begin{aligned} \mathbf{A}_{k-1} &= \left.\frac{\partial \boldsymbol{f}_\mathrm{d}}{\partial \boldsymbol{x}_k}\right|_{\hat{\boldsymbol{x}}_{k-1}^+,\boldsymbol{u}_{k-1},\mathbf{0}}, & \mathbf{B}_{\boldsymbol{\varepsilon},k-1} &= \left.\frac{\partial \boldsymbol{f}_\mathrm{d}}{\partial \boldsymbol{\varepsilon}_k}\right|_{\hat{\boldsymbol{x}}_{k-1}^+,\boldsymbol{u}_{k-1},\mathbf{0}}, \\ \bar{\mathbf{C}}_k &= \left.\frac{\partial \bar{\boldsymbol{h}}_\mathrm{d}}{\partial \boldsymbol{x}_k}\right|_{\hat{\boldsymbol{x}}_k^-,\boldsymbol{u}_k,\mathbf{0}}, & \bar{\mathbf{D}}_{\boldsymbol{v},k} &= \left.\frac{\partial \bar{\boldsymbol{h}}_\mathrm{d}}{\partial \boldsymbol{v}_k}\right|_{\hat{\boldsymbol{x}}_k^-,\boldsymbol{u}_k,\mathbf{0}}. \end{aligned} \tag{2.41}$$

The MU uses Joseph's covariance update, which is numerically more stable [27].

Implementing an EKF usually involves finding a discrete approximation to a dynamical model in continuous time, which for example was derived based on first-principles. For this purpose techniques like the Runge-Kutta method may be adopted, see section 2.3. Doing so allows to symbolically calculate the required Jacobians (2.41) and storing them as functions of the estimated state and applied inputs, hence facilitating online calculation. Due to its simple structure, the EKF presents the de facto standard in many fields of engineering. Yet, other variants such as the unscented Kalman filter (UKF) [93], [94] may yield superior performance when dealing with severe nonlinearities as it removes the Taylor series expansion used to propagate the covariance, cf. (2.39)-(2.41). For an extensive introduction to applied Kalman filtering and different nonlinear extensions of the classical filter the reader is referred to e.g. [26].

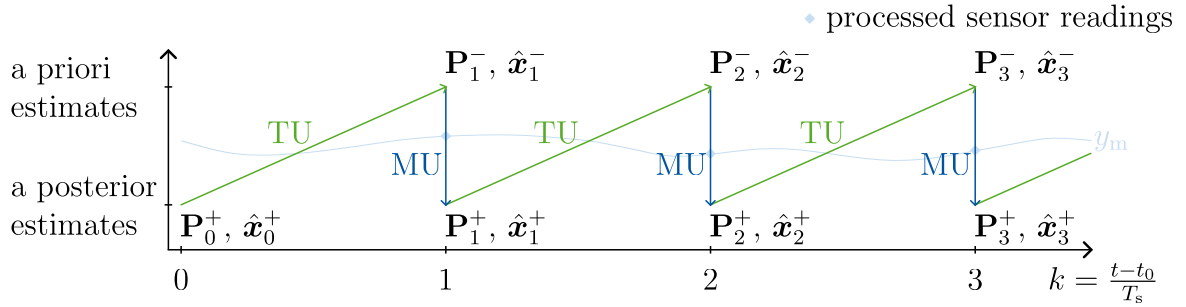

Fig. 2.11: Update scheme during Kalman filtering – State estimation is initialized at $k = 0$ with user-defined guesses for the (a posterior) state $\hat{\boldsymbol{x}}_0^+$ and the error covariance $\mathbf{P}_0^+$. Subsequently, the filter is iterated by performing time updates (TU) and measurement updates (MU), which are illustrated in green resp. blue. While time updates are computed "between" sample instances, i.e. when no new sensor data $\boldsymbol{y}_{\mathrm{m},k}$ is available, measurement updates are triggered whenever new sensor readings have been processed. Following the EKF algorithm, the a priori estimates $\hat{\boldsymbol{x}}_k^-$ constitute one-step ahead predictions from the previous estimates $\hat{\boldsymbol{x}}_{k-1}^+$. In contrast, the a posterior estimates $\hat{\boldsymbol{x}}_k^+$ are corrected based on the obtained measurements, which include sensor readings at time k. Figure adapted from [115].

Moving Horizon Estimation

With the exception of trivial systems, the full information problem becomes computational intractable with time. The KALMAN filter – as well as nonlinear variants such as the EKF – retains a fixed complexity due to its iterative scheme, which processes the sensor readings one at a time. Yet, estimation performance might be poor if the system is nonlinear. The authors in [146] argue that this quality is in fact representative of any one-step recursive estimator. In contrast, the moving horizon estimator (MHE) accounts for multiple past measurements taken over a receding horizon of length $N_\mathrm{f} = \lfloor \frac{T_\mathrm{f}}{T_\mathrm{e}} \rfloor$. As with MPC, the estimator design is based on numerical optimization. To fix the size of the resulting optimization problem, all information gathered up to the current time window is aggregated in a single a priori estimate and an according confidence measure, i.e. a covariance matrix, which are included via the so-called *arrival costs*. The MHE algorithm is summarized below. An illustration of the moving horizon is given in Fig. 2.12. The formulation of the optimization problem follows [144], while the reader is referred to e.g. [143] for a discussion of the MHE's theoretic properties.

Moving horizon estimator: Consider a nonlinear system (2.37) with additive measurement noise $\boldsymbol{\upsilon}_k$, whose state and measurement equations equate to

$$\begin{aligned} \boldsymbol{x}_{k+1} &= \boldsymbol{f}_\mathrm{d}\left(\boldsymbol{x}_k, \boldsymbol{u}_k, \boldsymbol{\varepsilon}_k\right) \\ \boldsymbol{y}_{\mathrm{m},k} &= \bar{\boldsymbol{h}}_\mathrm{d}\left(\boldsymbol{x}_k, \boldsymbol{u}_k\right) + \boldsymbol{\upsilon}_k \ . \end{aligned}$$

Given measurements $\{\boldsymbol{y}_{\mathrm{m},i}\}_{k-N_\mathrm{f} \le i \le k-1}$, the MHE problem at time instance k with horizon length N_f is defined by

$$\min_{\boldsymbol{x}_{k-N_\mathrm{f}}, \boldsymbol{\varepsilon}_{k-N_\mathrm{f}}, \ldots, \boldsymbol{\varepsilon}_{k-1}} \ L_0(\boldsymbol{x}_{k-N_\mathrm{f}}) + \sum_{i=k-N_\mathrm{f}}^{k-1} L\left(\boldsymbol{\varepsilon}_i, \boldsymbol{\upsilon}_i\right) \tag{2.42}$$

$$\begin{aligned} \text{s.t.} \quad \mathbf{0} &= \boldsymbol{x}_{i+1} - \boldsymbol{f}_\mathrm{d}\left(\boldsymbol{x}_i, \boldsymbol{u}_i, \boldsymbol{\varepsilon}_i\right) && i = k-N_\mathrm{f}, \ldots, k-1 \\ \boldsymbol{\upsilon}_i &= \boldsymbol{y}_{\mathrm{m},i} - \bar{\boldsymbol{h}}_\mathrm{d}\left(\boldsymbol{x}_i, \boldsymbol{u}_i\right) && i = k-N_\mathrm{f}, \ldots, k-1 \\ \boldsymbol{x}_i &\in \mathcal{X} && i = k-N_\mathrm{f}, \ldots, k \\ \boldsymbol{\varepsilon}_\mathrm{min} &\le \mathbf{E}\,\boldsymbol{\varepsilon}_i \le \boldsymbol{\varepsilon}_\mathrm{max} && i = k-N_\mathrm{f}, \ldots, k-1 \end{aligned}$$

where the *arrival cost* $L_0(\cdot)$ and *stage cost* $L(\cdot)$ are chosen according to

$$L_0(\boldsymbol{x}_{k-N_\mathrm{f}}) = \left\| \boldsymbol{x}_{k-N_\mathrm{f}} - \bar{\boldsymbol{x}}_{k-N_\mathrm{f}} \right\|^2_{\mathbf{Q}^{-1}_{\boldsymbol{x}_{k-N_\mathrm{f}}}} \tag{2.43}$$

$$L\left(\boldsymbol{\varepsilon}_i, \boldsymbol{\upsilon}_i\right) = \left\| \boldsymbol{\varepsilon}_i \right\|^2_{\mathbf{Q}^{-1}_{\boldsymbol{\varepsilon}}} + \left\| \boldsymbol{\upsilon}_i \right\|^2_{\mathbf{Q}^{-1}_{\boldsymbol{\upsilon}}} \tag{2.44}$$

with positive definite weighting matrices $\mathbf{Q}_{\boldsymbol{x}_{k-N_\mathrm{f}}} \in \mathbb{R}^{n \times n}$, $\mathbf{Q}_{\boldsymbol{\varepsilon}} \in \mathbb{R}^{n \times n}$, $\mathbf{Q}_{\boldsymbol{\upsilon}} \in \mathbb{R}^{q \times q}$, as

well as an initial guess $\bar{\boldsymbol{x}}_{k-N_\mathrm{f}}$ of the system state at the horizon's left boundary. In (2.43) and (2.44), the individual costs are specified using the shorthand notation $\|\boldsymbol{x}\|^2_{\mathbf{Q}} = \boldsymbol{x}^\mathrm{T}\mathbf{Q}\boldsymbol{x}$, which is also frequently utilized hereafter. With regard to (2.42), the state disturbance $\boldsymbol{\varepsilon}_i$ is constrained to a polyhedral convex set, established by linear inequalities $\mathbf{E}\,\boldsymbol{\varepsilon}_i \leq \boldsymbol{\varepsilon}_\mathrm{max}$ resp. $-\mathbf{E}\,\boldsymbol{\varepsilon}_i \leq -\boldsymbol{\varepsilon}_\mathrm{min}$. This choice is arbitrary but reflects common practice. Noteworthy, the noise variables $\boldsymbol{\upsilon}_i$ are usually not constrained to allow for outliers in the sensor signals. Solving the nonlinear program (2.42) yields estimates of the state $\hat{\boldsymbol{x}}(k-N_\mathrm{f}|k-1)$ and disturbance sequence $\{\hat{\boldsymbol{\varepsilon}}(i|k-1)\}_{k-N_\mathrm{f}\leq i\leq k-1}$. An a priori estimate of the current state $\hat{\boldsymbol{x}}_k^- = \hat{\boldsymbol{x}}(k|k-1)$ may then be derived by iterating the state equation.

When implementing the MHE, the open loop simulation required to derive $\hat{\boldsymbol{x}}_k^-$ might be avoided if the state equation can be solved explicitly for $\boldsymbol{\varepsilon}_i$. In such case, a simple change in the free variables of (2.42), namely from $(\boldsymbol{x}_{k-N_\mathrm{f}}, \boldsymbol{\varepsilon}_{k-N_\mathrm{f}}, \ldots, \boldsymbol{\varepsilon}_{k-1})$ to $(\boldsymbol{x}_{k-N_\mathrm{f}}, \ldots, \boldsymbol{x}_k)$, allows to directly derive the entire state sequence as part of the optimization problem. The substitution is straightforward if the process noise enters the system additive. The weighting matrices in (2.43)-(2.44) reflect one's confidence in the system model, the sensor signal or the previous estimate of the system state at the horizon's left boundary.

In practice, the noise signals $\boldsymbol{\varepsilon}_k$ and $\boldsymbol{\upsilon}_k$ are typically considered in a stochastic setting just as in case of the Kalman filter, which then admits a statistical interpretation of the MHE parameterization. Assuming that both noise sequences are uncorrelated, white and Gaussian the weighting matrices in (2.44) equate to the resp. covariance matrices

$$\mathbf{Q}_\varepsilon = \mathbf{Q}_{\boldsymbol{\mathcal{E}},\mathbf{d}}, \qquad \mathbf{Q}_\upsilon = \mathbf{Q}_{\boldsymbol{\mathcal{V}},\mathbf{d}} \tag{2.45}$$

which are positive definite by definition. Hence, their square root matrices satisfying $\mathbf{Q}_\varepsilon = (\mathbf{Q}_\varepsilon^{1/2})^\mathrm{T}\mathbf{Q}_\varepsilon^{1/2}$ and $\mathbf{Q}_\upsilon = (\mathbf{Q}_\upsilon^{1/2})^\mathrm{T}\mathbf{Q}_\upsilon^{1/2}$ are well-defined, which will be exploited during numerical optimization in section 2.7. Following [143], the arrival cost $L_0(\cdot)$ represents an *equivalent statistic* subsuming the full information problem up to the evaluated horizon. However, unless the system is unconstrained and linear, an exact equivalent does not exist. Thus, the ideal arrival cost has to be approximated. Applying a Kalman-like approach yields the *filtering update*, for which

$$\bar{\boldsymbol{x}}_{k-N_\mathrm{f}} = \hat{\boldsymbol{x}}_{k-N_\mathrm{f}}^-, \qquad \mathbf{Q}_{\boldsymbol{x}_{k-N_\mathrm{f}}} = \mathbf{P}_{k-N_\mathrm{f}}^- \tag{2.46}$$

where the a priori estimate $\hat{\boldsymbol{x}}_{k-N_\mathrm{f}}^- = \hat{\boldsymbol{x}}(k-N_\mathrm{f}|k-N_\mathrm{f}-1)$ was determined at time instance $k-N_\mathrm{f}$, i.e. with knowledge of $k-N_\mathrm{f}-1$ measurements. To simplify notation, the first time index of the current horizon is denoted by $k_0 = k-N_\mathrm{f}$. The above error covariance matrix $\mathbf{P}_{k_0}^-$ is then determined recursively according to

$$\begin{aligned}\mathbf{P}_{k_0}^- = {}& \mathbf{B}_{\boldsymbol{\varepsilon},k_0-1}\mathbf{Q}_{\boldsymbol{\mathcal{E}},\mathbf{d}}\mathbf{B}_{\boldsymbol{\varepsilon},k_0-1}^\mathrm{T} + \mathbf{A}_{k_0-1}\mathbf{P}_{k_0-1}^-\mathbf{A}_{k_0-1}^\mathrm{T} \\ & - \mathbf{A}_{k_0-1}\mathbf{P}_{k_0-1}^-\bar{\mathbf{C}}_{k_0-1}^\mathrm{T}\left(\bar{\mathbf{C}}_{k_0-1}\mathbf{P}_{k_0-1}^-\bar{\mathbf{C}}_{k_0-1}^\mathrm{T} + \mathbf{Q}_{\boldsymbol{\mathcal{V}},\mathbf{d}}\right)^{-1}\bar{\mathbf{C}}_{k_0-1}\mathbf{P}_{k_0-1}^-\mathbf{A}_{k_0-1}^\mathrm{T}\end{aligned}$$

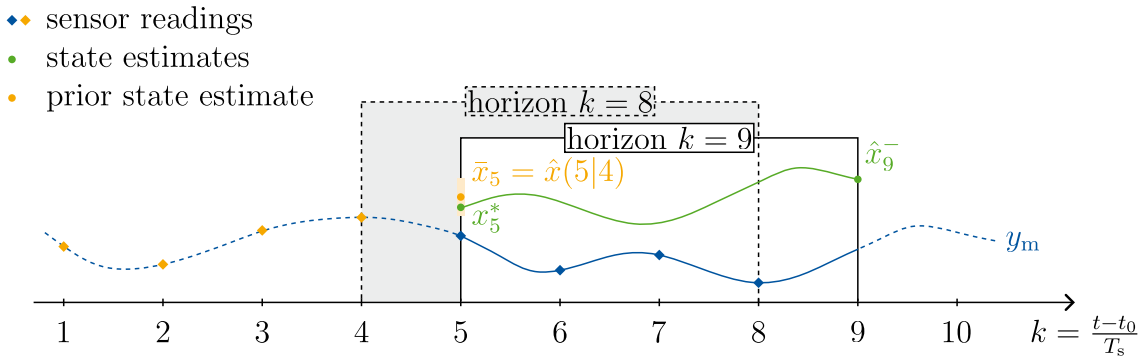

(a) Filtering update

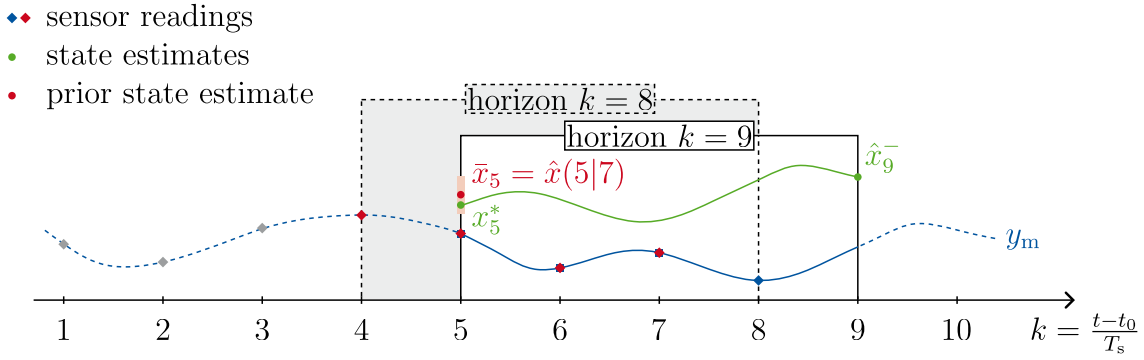

(b) Smoothing update

Fig. 2.12: State estimation based on a moving horizon – At each sampling instance, a sequence of $N_\mathrm{f} = 4$ measurements (blue rhombs) is considered to infer a state sequence (green) by numerical optimization, cf. (2.42). Two update strategies for determining the arrival cost are shown, namely the filtering update (top) and the smoothing update (bottom). In both cases, a set of sensor readings (yellow resp. red rhombs) is used to compute prior estimates (in matching colors) of the left-boundary state $\bar{x}_5$ and its associated covariance matrix (shaded areas). While the filtering update only accounts for past measurements, the smoothing update incorporates sensor readings processed after $k = 5$. After optimization, an a priori estimate of the current state $\hat{x}_9^-$ is derived by an open loop simulation starting at x_5^*.

wherein the Jacobians are derived analogously to the case of the EKF in (2.41), i.e.

$$\mathbf{A}_{k_0-1} = \left.\frac{\partial \boldsymbol{f}_\mathrm{d}}{\partial \boldsymbol{x}_k}\right|_{\hat{\boldsymbol{x}}_{k_0-1}^-, \boldsymbol{u}_{k_0-1}, \mathbf{0}}, \quad \mathbf{B}_{\boldsymbol{\varepsilon},k_0-1} = \left.\frac{\partial \boldsymbol{f}_\mathrm{d}}{\partial \boldsymbol{\varepsilon}_k}\right|_{\hat{\boldsymbol{x}}_{k_0-1}^-, \boldsymbol{u}_{k_0-1}, \mathbf{0}}, \quad \bar{\mathbf{C}}_{k_0-1} = \left.\frac{\partial \bar{\boldsymbol{h}}_\mathrm{d}}{\partial \boldsymbol{x}_k}\right|_{\hat{\boldsymbol{x}}_{k_0-1}^-, \boldsymbol{u}_{k_0-1}, \mathbf{0}}.$$

The filtering update is straightforward to implement but requires storage of N_f past state estimates in order to calculate (2.46). Utilizing the a priori estimate $\hat{\boldsymbol{x}}(k - N_\mathrm{f}|k - N_\mathrm{f} - 1)$ furthermore ignores the fact that at time $k-1$ more recent measurements have already been processed. It is therefore desirable to make use of the estimate $\hat{\boldsymbol{x}}(k-N_\mathrm{f}|k-2)$ instead.

This leads to the so-called *smoothing update*, which may provide better approximations to the arrival cost, albeit being more computational involved. See [171] for a derivation of the smoothing update for nonlinear discrete systems. An illustration of the scheme is included in Fig. 2.12. In practice, choosing the update strategy is dependent on the system, as both the computational overhead and the resulting convergence behavior of the estimator must be taken into account. Noteworthy, even a zero prior weighting $L_0 = 0$ may give satisfactory results if the computational resources allow optimizing over large horizons and the system is observable [146].

2.7 Numerical Optimization

Thanks to the increase in computational resources, numerical optimization has become a viable tool for solving many technical problems. The availability of tailored software packages, commonly known as *solvers*, furthermore enables optimizing some problems in real time and on embedded hardware. In the context of this thesis, numerical optimization is used for target selection (section 4.3), state estimation (section 4.2), predictive control (section 4.4) or controller tuning. Consider a generic optimization problem of form

$$\begin{aligned} \boldsymbol{\chi}^* = \ & \arg\min_{\boldsymbol{\chi}} l(\boldsymbol{\chi}) && (2.47)\\ \text{s.t.} \quad & \boldsymbol{c}_{\text{eq}}(\boldsymbol{\chi}) = \mathbf{0} && \text{(equality constraints)}\\ & \boldsymbol{c}_{\text{ieq}}(\boldsymbol{\chi}) \leq \mathbf{0} && \text{(inequality constraints)} \end{aligned}$$

with free variables $\boldsymbol{\chi} \in \mathbb{R}^{n_{\text{opt}}}$, objective function $l : \mathbb{R}^{n_{\text{opt}}} \to \mathbb{R}$, equality constraint function $\boldsymbol{c}_{\text{eq}} : \mathbb{R}^{n_{\text{opt}}} \to \mathbb{R}^{n_{\text{eq}}}$ and inequality constraint function $\boldsymbol{c}_{\text{ieq}} : \mathbb{R}^{n_{\text{opt}}} \to \mathbb{R}^{n_{\text{ieq}}}$. As before, an asterisk (*) is used to denote optimal values. In the following, a distinction is made between *white box* and *black box* optimization, depending on whether or not analytical representations of the objective and constraint functions are available. As the literature on related algorithms is vast, the following overview is non-exhaustive but restricted to two techniques applied in this work. With both MPC and MHE, optimization is based on an underlying system model, compare (2.30) resp. (2.42). Since the crane model in section 3 is derived from first principles, the objective function along with its derivative information can be calculated explicitly, thus enabling white box optimization. Below a *line search* algorithm utilizing *sequential quadratic programming* (SQP) is detailed. For alternative approaches, the reader is referred to [132]. By contrast, the functional dependency between e.g. closed-loop performance and controller parameterization is usually unknown. Optimization is thus reliant on repeated evaluation of the objective and constraint functions at candidate solutions. In section 4, Bayesian optimization (BO) is adopted to solve the black box optimization problem associated with controller tuning. An introduction to BO is included hereafter, whereas a detailed presentation can be found in [69].

White Box Optimization

An optimization problem described by (2.47) is referred to as *nonlinear program* (NLP). While there are multiple approaches to solve such problem, the solution $\boldsymbol{\chi}^*$ is known to necessarily satisfy the KARUSH–KUHN–TUCKER (KKT) conditions [98], [111]

$$\nabla_{\chi}\mathcal{L}(\boldsymbol{\chi}^*, \boldsymbol{\lambda}^*, \boldsymbol{\mu}^*) = \mathbf{0} \tag{2.48a}$$
$$\boldsymbol{c}_{\mathrm{eq}}(\boldsymbol{\chi}^*) = \mathbf{0} \tag{2.48b}$$
$$\boldsymbol{c}_{\mathrm{ieq}}(\boldsymbol{\chi}^*) \leq \mathbf{0} \tag{2.48c}$$
$$\boldsymbol{\mu}^* \geq \mathbf{0} \tag{2.48d}$$
$$(\boldsymbol{\mu}^*)^{\mathrm{T}}\boldsymbol{c}_{\mathrm{ieq}}(\boldsymbol{\chi}^*) = 0 \tag{2.48e}$$

which under consideration of the Lagrangian $\mathcal{L}(\boldsymbol{\chi}, \boldsymbol{\lambda}, \boldsymbol{\mu}) = l(\boldsymbol{\chi}) + \boldsymbol{\lambda}^{\mathrm{T}}\boldsymbol{c}_{\mathrm{eq}}(\boldsymbol{\chi}) + \boldsymbol{\mu}^{\mathrm{T}}\boldsymbol{c}_{\mathrm{ieq}}(\boldsymbol{\chi})$ with multipliers[11] $\boldsymbol{\lambda} \in \mathbb{R}^{n_{\mathrm{eq}}}$ and $\boldsymbol{\mu} \in \mathbb{R}^{n_{\mathrm{ieq}}}$ provide a simple test for optimality. Equation (2.48a) is also referred to as *first-order optimality* condition, which requires the gradient of the Lagrangian $\nabla_{\boldsymbol{\chi}}\mathcal{L} = (\partial\mathcal{L}/\partial_{\chi_1} \ \dots \ \partial\mathcal{L}/\partial_{\chi_{n_{\mathrm{opt}}}})^{\mathrm{T}}$ to vanish for any (local) minimizer $\boldsymbol{\chi}^*$ and according multipliers $\boldsymbol{\lambda}^*$, $\boldsymbol{\mu}^*$. Conditions (2.48b)-(2.48c) guarantee *primal* feasibility of the solution, while (2.48d) enforces feasibility of the so-called *dual problem*, see [132]. The *complementary slackness* (2.48e) requires either μ_i or $c_{\mathrm{ieq},i}(\boldsymbol{\chi}^*)$ to be zero for each $i = 1, \dots, n_{\mathrm{ieq}}$. The set of indexes i for which $\mu_i \neq 0$ further defines the *active set* $\mathcal{A}(\boldsymbol{\chi})$ at $\boldsymbol{\chi} = \boldsymbol{\chi}^*$, which in addition to the equality constraints $\boldsymbol{c}_{\mathrm{eq}}(\boldsymbol{\chi})$ thus determines all inequality constraints $c_{\mathrm{ieq},i}(\boldsymbol{\chi})$ equating to zero.

In practice, NLPs are solved iteratively. Starting at some initial guess $\boldsymbol{\chi}_0$, a sequence of solutions $\{\boldsymbol{\chi}_i\}_{i\in\mathbb{N}_0}$ is computed via local approximation of the objective and constraint functions about the current iterate. Each candidate solution may be checked for (2.48). Following [9], the iteration law $\boldsymbol{\chi}_i \mapsto \boldsymbol{\chi}_{i+1}$ is determined by four design choices, namely

- the *approximation scheme* used to derive the local subproblems,
- the *refining mechanism* limiting the optimal step to mitigate approximation errors,
- the *globalization strategy* promoting convergence in case of poor initializations,
- the *convergence criterion* required to terminate the iterative algorithm.

Arguably the most significant difference between particular algorithms stems from the way the NLP is approximated in each iteration. Among the most popular approaches are variations of *sequential linear programming*, *sequential quadratic programming* and *interior point methods*. The latter may be seen as evolution of the more classical *barrier* method, which is why both terms have been used in the literature. Solving the NLP iteratively in terms of local subproblems inevitable entails approximation errors, such that the difference or *step* between consecutive solutions $\Delta\boldsymbol{\chi}_{i+1} = \boldsymbol{\chi}_{i+1} - \boldsymbol{\chi}_i$ is constrained

[11] Here, $\boldsymbol{\lambda}$ are the LAGRANGE multipliers. Accordingly, the pair $(\boldsymbol{\lambda}, \boldsymbol{\mu})$ is known as the KKT multipliers.

by either *line search* or *trust region* techniques [132]. The resulting solvers differ in computational complexity, convergence behavior or accuracy of the solutions. Choosing an appropriate algorithm is thus application dependent. For a thorough treatment of NLPs arising in optimal control see [21]. While real-time feasibility is critical in order to implement the MPC in chapter 4 online, problems arising in trajectory planning are less restrictive. If not stated otherwise, white box NLPs are solved via the SQP algorithm below, which can be parameterized for different timing requirements.

In sequential quadratic programming the NLP is approximated by a sequence of quadratic subproblems derived via TAYLOR series expansion of the Lagrangian and constraint functions up to second resp. first order, i.e.

$$\begin{aligned}
\mathcal{L}(\boldsymbol{\chi}, \boldsymbol{\lambda}, \boldsymbol{\mu}) &\approx \mathcal{L}(\boldsymbol{\chi}_\mathrm{e}, \boldsymbol{\lambda}_\mathrm{e}, \boldsymbol{\mu}_\mathrm{e}) + (\nabla_{\boldsymbol{\chi}} \mathcal{L}(\boldsymbol{\chi}_\mathrm{e}, \boldsymbol{\lambda}_\mathrm{e}, \boldsymbol{\mu}_\mathrm{e}))^\mathrm{T} \boldsymbol{d}_{\boldsymbol{\chi}_\mathrm{e}} + \frac{1}{2} \boldsymbol{d}_{\boldsymbol{\chi}_\mathrm{e}}^\mathrm{T} (\nabla_{\boldsymbol{\chi}\boldsymbol{\chi}}^2 \mathcal{L}(\boldsymbol{\chi}_\mathrm{e}, \boldsymbol{\lambda}_\mathrm{e}, \boldsymbol{\mu}_\mathrm{e})) \boldsymbol{d}_{\boldsymbol{\chi}_\mathrm{e}} \\
\boldsymbol{c}_\mathrm{eq}(\boldsymbol{\chi}) &\approx \boldsymbol{c}_\mathrm{eq}(\boldsymbol{\chi}_\mathrm{e}) \qquad + (\nabla_{\boldsymbol{\chi}} \boldsymbol{c}_\mathrm{eq}(\boldsymbol{\chi}_\mathrm{e}))\, \boldsymbol{d}_{\boldsymbol{\chi}_\mathrm{e}} \\
\boldsymbol{c}_\mathrm{ieq}(\boldsymbol{\chi}) &\approx \boldsymbol{c}_\mathrm{ieq}(\boldsymbol{\chi}_\mathrm{e}) \qquad + (\nabla_{\boldsymbol{\chi}} \boldsymbol{c}_\mathrm{ieq}(\boldsymbol{\chi}_\mathrm{e})) \boldsymbol{d}_{\boldsymbol{\chi}_\mathrm{e}}
\end{aligned}$$

with general expansion point $\boldsymbol{\chi}_\mathrm{e}$ and deviation $\boldsymbol{d}_{\boldsymbol{\chi}_\mathrm{e}} = \boldsymbol{\chi} - \boldsymbol{\chi}_\mathrm{e}$ thereof. Analogous to the gradient of a scalar function, e.g. $\nabla_{\boldsymbol{\chi}} \mathcal{L}(\cdot)$, the first-order derivative information of the vector-valued constraint functions are indicated using the nabla operator. The JACOBIAN matrices $\nabla_{\boldsymbol{\chi}} \boldsymbol{c}_\mathrm{eq} \in \mathbb{R}^{n_\mathrm{eq} \times n_\mathrm{opt}}$ and $\nabla_{\boldsymbol{\chi}} \boldsymbol{c}_\mathrm{ieq} \in \mathbb{R}^{n_\mathrm{ieq} \times n_\mathrm{opt}}$ are then defined by

$$\nabla_{\boldsymbol{\chi}} \boldsymbol{c}_\mathrm{eq}(\boldsymbol{\chi}_\mathrm{e}) = \left[\begin{matrix} \frac{\partial c_{\mathrm{eq},1}}{\partial \chi_1} & \cdots & \frac{\partial c_{\mathrm{eq},1}}{\partial \chi_{n_\mathrm{opt}}} \\ \vdots & \ddots & \vdots \\ \frac{\partial c_{\mathrm{eq},n_\mathrm{eq}}}{\partial \chi_1} & \cdots & \frac{\partial c_{\mathrm{eq},n_\mathrm{eq}}}{\partial \chi_{n_\mathrm{opt}}} \end{matrix} \right] \Bigg|_{\boldsymbol{\chi}=\boldsymbol{\chi}_\mathrm{e}}, \quad \nabla_{\boldsymbol{\chi}} \boldsymbol{c}_\mathrm{ieq}(\boldsymbol{\chi}_\mathrm{e}) = \left[\begin{matrix} \frac{\partial c_{\mathrm{ieq},1}}{\partial \chi_1} & \cdots & \frac{\partial c_{\mathrm{ieq},1}}{\partial \chi_{n_\mathrm{opt}}} \\ \vdots & \ddots & \vdots \\ \frac{\partial c_{\mathrm{ieq},n_\mathrm{ieq}}}{\partial \chi_1} & \cdots & \frac{\partial c_{\mathrm{ieq},n_\mathrm{ieq}}}{\partial \chi_{n_\mathrm{opt}}} \end{matrix} \right] \Bigg|_{\boldsymbol{\chi}=\boldsymbol{\chi}_\mathrm{e}}. \tag{2.49}$$

The matrix of second partial derivatives of $\mathcal{L} : \mathbb{R}^{n_\mathrm{opt}} \times \mathbb{R}^{n_\mathrm{eq}} \times \mathbb{R}^{n_\mathrm{ieq}} \to \mathbb{R}$ with respect to $\boldsymbol{\chi}$ is referred to as HESSIAN and denoted by

$$\nabla_{\boldsymbol{\chi}\boldsymbol{\chi}}^2 \mathcal{L}(\boldsymbol{\chi}_\mathrm{e}, \boldsymbol{\lambda}_\mathrm{e}, \boldsymbol{\mu}_\mathrm{e}) = \left[\begin{matrix} \frac{\partial^2 \mathcal{L}}{\partial \chi_1 \partial \chi_1} & \cdots & \frac{\partial^2 \mathcal{L}}{\partial \chi_1 \partial \chi_{n_\mathrm{opt}}} \\ \vdots & \ddots & \vdots \\ \frac{\partial^2 \mathcal{L}}{\partial \chi_{n_\mathrm{opt}} \partial \chi_1} & \cdots & \frac{\partial^2 \mathcal{L}}{\partial \chi_{n_\mathrm{opt}} \partial \chi_{n_\mathrm{opt}}} \end{matrix} \right] \Bigg|_{\boldsymbol{\chi}=\boldsymbol{\chi}_\mathrm{e},\, \boldsymbol{\lambda}=\boldsymbol{\lambda}_\mathrm{e},\, \boldsymbol{\mu}=\boldsymbol{\mu}_\mathrm{e}} \tag{2.50}$$

using again the nabla operator. By definition, the HESSIAN matrix is symmetric. Furthermore, its eigenvalues are (strictly) positive if the underlying function is (strictly) *convex*. Since a strictly convex function is guaranteed to possess no more than one minimum, definiteness of the HESSIAN matrix is key in quadratic programming, where the objective is quadratic, and the constraints are linear. The quadratic program (QP) informed by the above expansions gives rise to the following SQP algorithm.

Sequential quadratic programming: Given an initial triple $(\boldsymbol{\chi}_0, \boldsymbol{\lambda}_0, \boldsymbol{\mu}_0)$ of minimizer $\boldsymbol{\chi}_0$ and KKT multipliers $(\boldsymbol{\lambda}_0, \boldsymbol{\mu}_0)$, the NLP (2.47) is solved iteratively by solving a sequence of local QPs.

In each iteration i the current solution is checked for optimality, e.g. by evaluating $\|\nabla_{\boldsymbol{\chi}} \mathcal{L}(\boldsymbol{\chi}_i, \boldsymbol{\lambda}_i, \boldsymbol{\mu}_i)\| > \epsilon$. Here, the parameter $\epsilon \in \mathbb{R}^+$ is a predefined tolerance upper bounding the permissible violation of (2.48a). If the iterates have not yet converged to a KKT point, the Lagrangian and constraint functions are expanded around $(\boldsymbol{\chi}_i, \boldsymbol{\lambda}_i, \boldsymbol{\mu}_i)$ to obtain a local QP of form

$$\boldsymbol{d}^*_{\boldsymbol{\chi}_i} = \arg\min_{\boldsymbol{d}_{\boldsymbol{\chi}_i}} \frac{1}{2} \boldsymbol{d}^{\mathrm{T}}_{\boldsymbol{\chi}_i} (\nabla^2_{\boldsymbol{\chi}\boldsymbol{\chi}} \mathcal{L}(\boldsymbol{\chi}_i, \boldsymbol{\lambda}_i, \boldsymbol{\mu}_i)) \boldsymbol{d}_{\boldsymbol{\chi}_i} + (\nabla_{\boldsymbol{\chi}} \mathcal{L}(\boldsymbol{\chi}_i, \boldsymbol{\lambda}_i, \boldsymbol{\mu}_i))^{\mathrm{T}} \boldsymbol{d}_{\boldsymbol{\chi}_i} \tag{2.51a}$$

$$\text{s.t.} \quad \nabla_{\boldsymbol{\chi}} \boldsymbol{c}_{\mathrm{eq}}(\boldsymbol{\chi}_i) \boldsymbol{d}_{\boldsymbol{\chi}_i} + \boldsymbol{c}_{\mathrm{eq}}(\boldsymbol{\chi}_i) = \boldsymbol{0} \tag{2.51b}$$

$$\nabla_{\boldsymbol{\chi}} \boldsymbol{c}_{\mathrm{ieq}}(\boldsymbol{\chi}_i) \boldsymbol{d}_{\boldsymbol{\chi}_i} + \boldsymbol{c}_{\mathrm{ieq}}(\boldsymbol{\chi}_i) \leq \boldsymbol{0} \tag{2.51c}$$

which is solved for the optimal step $\boldsymbol{d}^*_{\boldsymbol{\chi}_i}$ and local KKT multipliers $\boldsymbol{\lambda}^*_{\mathrm{QP},i}$, $\boldsymbol{\mu}^*_{\mathrm{QP},i}$. Steps in the NLP's KKT multipliers are then calculated according to

$$\boldsymbol{d}^*_{\boldsymbol{\lambda}_i} = \boldsymbol{\lambda}^*_{\mathrm{QP},i} - \boldsymbol{\lambda}_i \tag{2.52a}$$

$$\boldsymbol{d}^*_{\boldsymbol{\mu}_i} = \boldsymbol{\mu}^*_{\mathrm{QP},i} - \boldsymbol{\mu}_i \ . \tag{2.52b}$$

Due to the approximating nature of (2.51), the optimal steps $(\boldsymbol{d}^*_{\boldsymbol{\chi}_i}, \boldsymbol{d}^*_{\boldsymbol{\lambda}_i}, \boldsymbol{d}^*_{\boldsymbol{\mu}_i})$ are usually refined by means of a scaling factor $\alpha_i \in (0, 1]$. While large values of α_i may accelerate convergence, smaller values render the scheme more robust to approximation errors. In order to balance both requirements, an optimal scaling α^*_i is determined by means of a backtracking line search. Starting at e.g. $\alpha_i = 1$ the scaling is reduced systematically, while rating the resulting steps by some merit function. Prominent stopping criteria are the Armijo-, Wolf- or Goldstein-conditions resp. their constrained equivalents [132].

Given the optimized steps $(\boldsymbol{d}^*_{\boldsymbol{\chi}_i}, \boldsymbol{d}^*_{\boldsymbol{\lambda}_i}, \boldsymbol{d}^*_{\boldsymbol{\mu}_i})$ and the refined step length α^*_i, new iterates are derived according to

$$\boldsymbol{\chi}_{i+1} = \boldsymbol{\chi}_i + \alpha_i \boldsymbol{d}^*_{\boldsymbol{\chi}_i}, \qquad \boldsymbol{\lambda}_{i+1} = \boldsymbol{\lambda}_i + \alpha_i \boldsymbol{d}^*_{\boldsymbol{\lambda}_i}, \qquad \boldsymbol{\mu}_{i+1} = \boldsymbol{\mu}_i + \alpha_i \boldsymbol{d}^*_{\boldsymbol{\mu}_i} \tag{2.53}$$

before the procedure is repeated for $i \leftarrow i + 1$.

When implementing a SQP procedure in practice, special attention must be paid to its convergence behavior. The linearized constraints (2.51b), (2.51c) may contradict, thus rendering the sub-QP (2.51) infeasible even if the original NLP (2.47) is well-defined. For this reason, additional optimization variables are usually added to the constraint functions. While being heavily penalized, such *slack variables* $\boldsymbol{\delta}$ effectively remove the

strictness of the constraints, which ensures consistency during the sequential optimization [9]. An example is (4.52) in section 4.7.3. As mentioned briefly above, positive definiteness of the HESSIAN matrix is key in obtaining proper descent directions by means of (2.51). However, $\nabla^2_{\boldsymbol{\chi}\boldsymbol{\chi}}\mathcal{L}$ is not guaranteed to be positive definite (p.d) nor positive semidefinite (p.s.d), which will be denoted $\nabla^2_{\boldsymbol{\chi}\boldsymbol{\chi}}\mathcal{L} \succ 0$ resp. $\nabla^2_{\boldsymbol{\chi}\boldsymbol{\chi}}\mathcal{L} \succeq 0$. Hence, regularization or approximation techniques are applied in order to make the HESSIAN and thus the quadratic objective function (2.51a) at least p.s.d. A widely-used approximation to $\nabla^2_{\boldsymbol{\chi}\boldsymbol{\chi}}\mathcal{L}$ is based on the (damped) BFGS formula [132], which retains positive definiteness of an initial p.d HESSIAN approximation[12] $\mathbf{H}_0 \succ 0$. Since most objective functions arising in context of this thesis are least-square, i.e. they may be reformulated as $l(\boldsymbol{\chi}) = \frac{1}{2}\left\|\boldsymbol{r}(\boldsymbol{\chi})\right\|_2^2$, the so-called GAUSS-NEWTON approximation

$$\nabla^2_{\boldsymbol{\chi}\boldsymbol{\chi}}\mathcal{L}(\boldsymbol{\chi}_i, \boldsymbol{\lambda}_i, \boldsymbol{\mu}_i) \approx \left(\nabla_{\boldsymbol{\chi}}\boldsymbol{r}(\boldsymbol{\chi}_i)\right)^{\mathrm{T}} \left(\nabla_{\boldsymbol{\chi}}\boldsymbol{r}(\boldsymbol{\chi}_i)\right) \tag{2.54}$$

will be used throughout. Although only relying on first-order derivative information, the approximation is guaranteed to be p.s.d and often yields good performance if the initial residuals $\boldsymbol{r}(\boldsymbol{\chi})$ are small [146]. Furthermore, the right-hand side of (2.54) does not depend on the KKT multipliers $(\boldsymbol{\lambda}_i, \boldsymbol{\mu}_i)$, which may be exploited to obtain a simplified SQP implementation. In addition, the following reasoning applies. After using some algebraic identities, the gradient in (2.51a) may be reformulated as

$$\begin{aligned}(\nabla_{\boldsymbol{\chi}}\mathcal{L}(\boldsymbol{\chi}_i, \boldsymbol{\lambda}_i, \boldsymbol{\mu}_i))^{\mathrm{T}}\boldsymbol{d}_{\boldsymbol{\chi}_i} = \;& (\nabla_{\boldsymbol{\chi}} l(\boldsymbol{\chi}_i))^{\mathrm{T}}\boldsymbol{d}_{\boldsymbol{\chi}_i} + \boldsymbol{\lambda}^{\mathrm{T}}\nabla_{\boldsymbol{\chi}}\boldsymbol{c}_{\mathrm{eq}}(\boldsymbol{\chi}_i)\boldsymbol{d}_{\boldsymbol{\chi}_i} + \boldsymbol{\mu}^{\mathrm{T}}\nabla_{\boldsymbol{\chi}}\boldsymbol{c}_{\mathrm{ieq}}(\boldsymbol{\chi}_i)\boldsymbol{d}_{\boldsymbol{\chi}_i} \\ \overset{(2.51\mathrm{b})}{=} & (\nabla_{\boldsymbol{\chi}} l(\boldsymbol{\chi}_i))^{\mathrm{T}}\boldsymbol{d}_{\boldsymbol{\chi}_i} - \boldsymbol{\lambda}^{\mathrm{T}}\boldsymbol{c}_{\mathrm{eq}}(\boldsymbol{\chi}_i) \qquad + \boldsymbol{\mu}^{\mathrm{T}}\nabla_{\boldsymbol{\chi}}\boldsymbol{c}_{\mathrm{ieq}}(\boldsymbol{\chi}_i)\boldsymbol{d}_{\boldsymbol{\chi}_i}\end{aligned}$$

where the constant term $-\boldsymbol{\lambda}^{\mathrm{T}}\boldsymbol{c}_{\mathrm{eq}}(\boldsymbol{\chi}_i)$ can be omitted during optimization. Recalling that inactive constraints do not affect the optimal solution $\boldsymbol{\chi}^*$ and thus may be eliminated from the optimization problem, it is thus reasonable (although not completely correct) to use similar arguments to simplify the last term in view of (2.51c). As a result, the gradient of the Lagrangian function is approximated by

$$\nabla_{\boldsymbol{\chi}}\mathcal{L}(\boldsymbol{\chi}_i, \boldsymbol{\lambda}_i, \boldsymbol{\mu}_i) \approx \nabla_{\boldsymbol{\chi}} l(\boldsymbol{\chi}_i)\ . \tag{2.55}$$

Combining (2.54) and (2.55) then removes the need to evaluate the KKT multipliers in order to derive the sub-QP (2.51). This simplifies implementation of the SQP procedure, which facilitates its real-time application. Another measure to ensure real-time capability is to limit the maximum number of SQP iterations by $i_{\max} \in \mathbb{N}$. If the SQP procedure is used in connection with a receding horizon approach like MPC, i.e. a SQP is solved at every sampling instance, the special case of $i_{\max} = 1$ is known as *real-time iteration* [47].

[12] In literature, a HESSIAN approximation is typically labeled $\mathbf{B}_i$, which is avoided here to preclude confusion with the input coupling matrix of a linear state space, see section 2.3.

Black Box Optimization

In black box optimization no analytic description of the cost nor constraint functions is available, at least partially. Hence, searching for the optimal solution using NEWTON-like approaches is challenging since derivative information can at best be approximated numerically. Model-free optimization routines are therefore dependent on repeatedly querying the optimization problem for candidate solutions and determining (potentially heuristically) search directions based on the collected data. Some examples are *random search*, *pattern search*, *genetic algorithms* or *particle swarm optimization* [136]. In the scope of this thesis, *Bayesian optimization* (BO) is applied to solve black box problems arising in controller tuning, cf. section 4.5.1. In contrast to other alternatives, BO is a sample-efficient approach which can be tailored to different scenarios. Here, *sample-efficiency* refers to the amount of data that is required to derive optimal solutions. For engineering tasks, this correlates to the number of necessary experiments or simulations, each of which may involve considerable effort, time or costs. Hereafter, a brief introduction to BO is included, while the interested reader is pointed to e.g. [69] for more information. A comprehensive overview of BO in the context of automatic control was recently published in [168].

Bayesian optimization is a stochastic approach to optimization, which utilizes both

- probabilistic *surrogate models* to approximate all black box functions, and
- the so-called *acquisition function* $\phi_{\mathrm{acq}} : \mathbb{R}^{n_{\mathrm{opt}}} \to \mathbb{R}$ to assign a utility to each point in the permissible search space.

Optimal solutions are determined iteratively. In each step, the candidate solution with highest utility is identified via maximization of $\phi_{\mathrm{acq}}(\boldsymbol{\chi})$, the optimization problem is evaluated at this point, and the surrogate models are refitted based on the collected observations. Although not imperative, most implementations of BO resort to GAUSSIAN process regression (GPR) to derive non-parametric surrogate models, which requires all unknown functions to be sufficiently smooth. In contrast, there is a wide variety of possible acquisition functions $\phi_{\mathrm{acq}}(\boldsymbol{\chi})$, each yielding a different search behavior during optimization. Among a variety of upsides, BO allows handling non-convex objectives as well as to treat noisy function observations. Since the surrogate models encode all previously function evaluations, the approach is also known to converge rapidly, that is with a minimum amount of data. A drawback is the computational overhead resulting from the repeated optimization of the acquisition function and the (re)training of the surrogate models. BO thus excels at solving optimization problems that are expensive to evaluate and only possess few free variables. Hereafter, some properties of GPR are reviewed before a prototypical BO algorithm is stated.

In GAUSSIAN process regression the functional relation between inputs (*predictors*) and outputs is modeled using GP [145]. The function values are hence considered stochastically

distributed. Compared to the time processes and sequences considered in section 2.6, the index set is not time-related and is thus generally termed *input domain*, which allows for vectorial predictors. In contrast, only a single output will be considered hereafter[13]. The GP then describes a distribution over functions. Following the notation introduced before, the GP approximating a generic mapping $\boldsymbol{x} \mapsto f(\boldsymbol{x})$ is denoted

$$F(\boldsymbol{x}) \sim \mathcal{GP}^f(m(\boldsymbol{x}), k(\boldsymbol{x}, \boldsymbol{x}'))$$

with mean function $m : \mathbb{R}^{n_\mathrm{x}} \to \mathbb{R}$ and covariance function $k : \mathbb{R}^{n_\mathrm{x}} \times \mathbb{R}^{n_\mathrm{x}} \to \mathbb{R}$, i.e.

$$m(\boldsymbol{x}) = E[F(\boldsymbol{x})]\,, \qquad k(\boldsymbol{x}, \boldsymbol{x}') = E[(F(\boldsymbol{x}) - m(\boldsymbol{x}))(F(\boldsymbol{x}') - m(\boldsymbol{x}'))]\,. \tag{2.56}$$

Although both mean and covariance refer to the function values, they are modeled as a direct function of the predictors $\boldsymbol{x} \in \mathbb{R}^{n_\mathrm{x}}$ as part of the regression. The GPR model is then determined by three design choices

- the (prior) *mean* function $m(\boldsymbol{x})$, which defines the GPR's behavior in the absence of information, i.e. at locations where no nearby observations are available,
- the covariance or *kernel* function $k(\boldsymbol{x}, \boldsymbol{x}')$, a prototype function measuring the similarity between data points, thus encoding assumptions about the function f,
- a *likelihood* model that relates observed and expected (latent) function values.

The regression result further depends on the parameterization of the above characteristic functions. In the context of GPR, these parameters are also termed *hyperparameters*. To stress this fact, the dependency is sometimes made explicit by writing e.g. $m(\boldsymbol{x}, \boldsymbol{\theta}_m)$ resp. $k(\boldsymbol{x}, \boldsymbol{x}', \boldsymbol{\theta}_k)$ with hyperparameters $\boldsymbol{\theta}_m$ and $\boldsymbol{\theta}_k$. Besides manual tuning, the stochastic setting of GPR allows fitting the hyperparameters to the available observations by maximizing the associated (log-)likelihood or using cross-validation techniques [145].

In the setting of BO, a popular choice is to assume the prior mean function to be constant, i.e. $m(\boldsymbol{x}, \boldsymbol{\theta}_m) = c$ with $\boldsymbol{\theta}_m = c \in \mathbb{R}$. If a trend in the underlying functional relation is known from expertise e.g. linear functions might be applied to improve the GPR's extrapolation capabilities. In regression, varying kernel functions are utilized depending on the application. Unless specific characteristics such as periodicity matter, two generic functions are the *squared-exponential* (SE) kernel and the Matérn kernel. While the latter allows to derive less smooth models, the SE kernel is considered hereafter for automatic controller tuning, as it is both stationary and (infinitely) differentiable as well as the de facto standard kernel choice. See [169] for a comparison of different GP models

[13] For BO, consideration of a single output is nonrestrictive, assuming that all constraints are mutually independent. In such case, separate models may be trained for each black box function.

in a control-related benchmark problem. The SE kernel in its anisotropic form is given by

$$k(\boldsymbol{x}, \boldsymbol{x}', \boldsymbol{\theta}_k) = \sigma_0^2 \exp\left(-\frac{1}{2}\sum_{i=1}^{n_\mathrm{x}} \frac{(x_i - x_i')^2}{l_i^2}\right) \quad \text{with} \quad \boldsymbol{\theta}_k = (\sigma_0, l_1, \ldots, l_{n_\mathrm{x}})^\mathrm{T} \tag{2.57}$$

where the factor $\sigma_0 \in \mathbb{R}_{\geq 0}$ determines the standard deviation at a given point in the input domain and the individual length scales $l_i \in \mathbb{R}_{\geq 0}$ specify per predictor the range in which a correlation between function values is expected, i.e. $F(\boldsymbol{x})$ and $F(\boldsymbol{x}')$ are uncorrelated if e.g. $(x_1 - x_1')^2 >> l_1^2$ and $x_i = x_i'$ otherwise. In many practical applications, the function values cannot be observed directly, that is without noise. Hence, the observations are assumed probabilistically distributed as well, which is captured by the so-called likelihood model. Most commonly, an additive noise term υ drawn from a mean-free normal distribution is considered, i.e.

$$f_\mathrm{m}(\boldsymbol{x}) = f(\boldsymbol{x}) + \upsilon \qquad \text{with} \qquad \mathcal{V} \sim \mathcal{N}(\boldsymbol{0}, \sigma_\mathcal{V}^2) \tag{2.58}$$

where f_m denotes the observed or measured function value, whereas $f(\boldsymbol{x})$ is the latent equivalent. As the noise standard deviation $\sigma_\mathcal{V}$ tends to zero, the GPR interpolates the observed data. In any other case, the GPR yields a smoothed fit to the training data.

Given a set of training data $\mathcal{D}_\mathrm{train} = \{(\boldsymbol{x}_j, f_{\mathrm{m},j}) \,|\, j = 1, \ldots, p\}$ with $p \in \mathbb{N}_{>0}$ function evaluations $f_{\mathrm{m},j} = f_\mathrm{m}(\boldsymbol{x}_j)$ observed at corresponding locations $\boldsymbol{x}_1, \ldots, \boldsymbol{x}_p$, the GPR allows deriving probabilistic predictions of the latent variable $F(\boldsymbol{x})$ at $q \in \mathbb{N}_{>0}$ testing locations $\boldsymbol{x}_{p+1}, \ldots, \boldsymbol{x}_{p+q}$. Since by assumption of a GP the random vectors $\boldsymbol{F}_\mathrm{m,train} = (F_{\mathrm{m},1} \ \ldots \ F_{\mathrm{m},p})^\mathrm{T}$ and $\boldsymbol{F}_\mathrm{m,pred} = (F_{\mathrm{m},p+1} \ \ldots \ F_{\mathrm{m},p+q})^\mathrm{T}$ are jointly Gaussian distributed, so are $\boldsymbol{F}_\mathrm{m,train}$ and $\boldsymbol{F}_\mathrm{pred} = (F_{p+1} \ \ldots \ F_{p+q})^\mathrm{T}$ under the likelihood model (2.58). Conditioning the predictions on the training data then yields its joint *posterior* distribution, which will be denoted $\boldsymbol{F}_\mathrm{pred}|\mathcal{D}_\mathrm{train} \sim \mathcal{N}(\boldsymbol{\mu}_\mathrm{post}, \boldsymbol{\Sigma}_\mathrm{post})$. The mean vector $\boldsymbol{\mu}_\mathrm{post} \in \mathbb{R}^q$ and covariance matrix $\boldsymbol{\Sigma}_\mathrm{post} \in \mathbb{R}^{q \times q}$ are derived according to

$$\boldsymbol{\mu}_\mathrm{post} = \boldsymbol{\mu}_\mathrm{pred} + \mathbf{K}_\mathrm{train,pred}^\mathrm{T} \left(\mathbf{K}_\mathrm{train,train} + \sigma_n^2 \mathbf{I}_{p\times p}\right)^{-1} (\boldsymbol{f}_\mathrm{m,train} - \boldsymbol{\mu}_\mathrm{train}) \tag{2.59a}$$

$$\boldsymbol{\Sigma}_\mathrm{post} = \mathbf{K}_\mathrm{pred,pred} - \mathbf{K}_\mathrm{train,pred}^\mathrm{T} \left(\mathbf{K}_\mathrm{train,train} + \sigma_n^2 \mathbf{I}_{p\times p}\right)^{-1} \mathbf{K}_\mathrm{train,pred} \tag{2.59b}$$

where the Gramians

$$\mathbf{K} = \left[\begin{array}{c|c} \mathbf{K}_\mathrm{train,train} & \mathbf{K}_\mathrm{train,pred} \\ \hline \mathbf{K}_\mathrm{pred,train} & \mathbf{K}_\mathrm{pred,pred} \end{array}\right]$$

$$= \left[\begin{array}{ccc|ccc} k(\boldsymbol{x}_1, \boldsymbol{x}_1) & \ldots & k(\boldsymbol{x}_1, \boldsymbol{x}_p) & k(\boldsymbol{x}_1, \boldsymbol{x}_{p+1}) & \ldots & k(\boldsymbol{x}_1, \boldsymbol{x}_{p+q}) \\ \vdots & \ddots & \vdots & \vdots & \ddots & \vdots \\ k(\boldsymbol{x}_p, \boldsymbol{x}_1) & \ldots & k(\boldsymbol{x}_p, \boldsymbol{x}_p) & k(\boldsymbol{x}_p, \boldsymbol{x}_{p+1}) & \ldots & k(\boldsymbol{x}_p, \boldsymbol{x}_{p+q}) \\ \hline k(\boldsymbol{x}_{p+1}, \boldsymbol{x}_1) & \ldots & k(\boldsymbol{x}_{p+1}, \boldsymbol{x}_p) & k(\boldsymbol{x}_{p+1}, \boldsymbol{x}_{p+1}) & \ldots & k(\boldsymbol{x}_{p+1}, \boldsymbol{x}_{p+q}) \\ \vdots & \ddots & \vdots & \vdots & \ddots & \vdots \\ k(\boldsymbol{x}_{p+q}, \boldsymbol{x}_1) & \ldots & k(\boldsymbol{x}_{p+q}, \boldsymbol{x}_p) & k(\boldsymbol{x}_{p+q}, \boldsymbol{x}_{p+1}) & \ldots & k(\boldsymbol{x}_{p+q}, \boldsymbol{x}_{p+q}) \end{array}\right]$$

and shorthand notations

$$\boldsymbol{f}_{\mathrm{m,train}} = \begin{pmatrix} f_{\mathrm{m},1} \\ \vdots \\ f_{\mathrm{m},p} \end{pmatrix}, \qquad \boldsymbol{\mu}_{\mathrm{train}} = \begin{pmatrix} m(\boldsymbol{x}_1) \\ \vdots \\ m(\boldsymbol{x}_p) \end{pmatrix}, \qquad \boldsymbol{\mu}_{\mathrm{pred}} = \begin{pmatrix} m(\boldsymbol{x}_{p+1}) \\ \vdots \\ m(\boldsymbol{x}_{p+q}) \end{pmatrix}$$

have been used. Note that $\mathbf{K}_{\mathrm{train,pred}} = \mathbf{K}_{\mathrm{pred,train}}^{\mathrm{T}}$ due to symmetry of the kernel function $k(\boldsymbol{x}, \boldsymbol{x}')$.

In addition to the probabilistic surrogate models based on GPR, the optimization performance of BO is mainly defined by choosing the acquisition function ϕ_{acq}. The acquisition function's main purpose is to maintain a trade-off between *exploration* (sampling away from previous locations to globalize the optimum search) and *exploitation* (sampling in the vicinity of the current optimum to locally improve the solution) during the iterative optimization procedure. Various acquisition functions have been proposed in the literature, most of which stem from either greedy [13], improvement-based [92] or information-theoretic [75], [181] approaches. A comprehensive overview is included in [69]. While the particular choice of acquisition function is deferred to section 4.5.1, a basic BO algorithm is stated below.

Bayesian optimization: Similar to (2.47), consider the deterministic[14] optimization problem

$$\begin{aligned} \boldsymbol{\chi}^* = \ & \arg\min_{\boldsymbol{\chi}} l(\boldsymbol{\chi}) && (2.60) \\ \text{s.t.} \quad & \boldsymbol{c}_{\mathrm{wb}}(\boldsymbol{\chi}) \leq \mathbf{0} && \text{(white box constraints)} \\ & \boldsymbol{c}_{\mathrm{bb}}(\boldsymbol{\chi}) \leq \mathbf{0} && \text{(black box constraints)} \end{aligned}$$

with both white and black box inequality constraints $\boldsymbol{c}_{\mathrm{wb}} : \mathbb{R}^{n_{\mathrm{x}}} \to \mathbb{R}^{n_{\mathrm{wb}}}$ resp. $\boldsymbol{c}_{\mathrm{bb}} : \mathbb{R}^{n_{\mathrm{x}}} \to \mathbb{R}^{n_{\mathrm{bb}}}$. Again, analytical expressions of the white box constraints $\boldsymbol{c}_{\mathrm{wb}}(\cdot)$ are available, whereas satisfaction of the black box constraints $\boldsymbol{c}_{\mathrm{bb}}(\cdot)$ can only be checked by (potentially costly) experiments or simulations. Hence, during BO $n_{\mathrm{bb}}+1$ individual GP models – namely $\mathcal{GP}^{l}$ and $\mathcal{GP}^{c_{\mathrm{bb},1}}, \ldots, \mathcal{GP}^{c_{\mathrm{bb},n_{\mathrm{bb}}}}$ – are fitted to subsequently make data-based predictions about the performance and feasibility of candidate solutions.

The optimization procedure is initialized by querying problem (2.60) for $p_{\mathrm{init}} \in \mathbb{N}_{>0}$ sample candidates $\boldsymbol{\chi}_1, \ldots, \boldsymbol{\chi}_{p_{\mathrm{init}}}$, yielding an initial data set $\mathcal{D}_{p_{\mathrm{init}}} = \{(\boldsymbol{\chi}_k, l_k, \boldsymbol{c}_{\mathrm{bb},k}) \,|\, k = 1, \ldots, p_{\mathrm{init}}\}$. The sample locations may be chosen randomly, equally spaced within the input domain or based on expert knowledge. The observed data is then used to train initial GP models for the objective and black box constraint functions.

Based on the initial surrogate models, optimization is performed iteratively by identifying the input of highest utility, querying the objective and constraint functions at

this location and updating the GP models with the observed response. Accordingly, the following steps are alternated in each iteration $k > p_{\text{init}}$:

1. Retrain the probabilistic surrogate models $\mathcal{GP}^{l}$ and $\mathcal{GP}^{c_{\text{bb},1}}, \ldots, \mathcal{GP}^{c_{\text{bb},n_{\text{bb}}}}$ using all past observations $\mathcal{D}_{k-1}$.
2. Maximize the acquisition function subject to all known white box constraints

$$\begin{aligned} \boldsymbol{\chi}_k = \ & \arg\max_{\boldsymbol{\chi}} \phi_{\text{acq}}(\boldsymbol{\chi}) \\ \text{s.t.} \quad & \boldsymbol{c}_{\text{wb}}(\boldsymbol{\chi}) \leq \mathbf{0} \end{aligned} \tag{2.61}$$

   to determine the location $\boldsymbol{\chi}_k$ of highest utility. Satisfaction of the black box constraints $\boldsymbol{c}_{\text{bb}}(\cdot)$ enters the acquisition function's score. The latter is computed based on probabilistic predictions of the GP surrogate models.
3. Run the black box experiment or simulation with input $\boldsymbol{\chi}_k$ to obtain a new data tuple $(\boldsymbol{\chi}_k, l_k, \boldsymbol{c}_{\text{bb},k})$.
4. Augment the data set, i.e. $\mathcal{D}_k = \mathcal{D}_{k-1} \cup \{(\boldsymbol{\chi}_k, l_k, \boldsymbol{c}_{\text{bb},k})\}$.

The optimization loop is exited if a feasible solution of satisfactory performance is found or a maximum number of iterations is reached.

[14] The optimization scheme naturally extends to the non-deterministic case due to the GPR's ability to account for noisy observations, cf. likelihood model (2.58). In such instances, the optimization problem (2.60) has to be adapted, e.g. by taking the expectation over the objective function and introducing chance constraints.

Chapter 3

Modeling

In scope of this chapter, crane, payload and vessel motions are modeled. After introducing relevant reference frames (section 3.1), a description of the sea state and vessel dynamics is included in section 3.2. Based on a discussion of published crane models (section 3.3.1), the kinematics and dynamics of a KBC are presented, see section 3.3.2 - 3.3.3. Since the theory of predictive control is well-developed for models in state space representation, a corresponding model is derived in section 3.4. A flat system output is proposed in section 3.5, for which the system equations are subsequently inverted. This forms the basis of the control algorithms in chapter 4. The chapter concludes with an overview of the developed simulation environment (section 3.6) and the robot-based test bench (section 3.7).

Key insights:

- Assuming light lifts and a DP system of sufficient performance, a minimal set of exogenous disturbances affecting payload handling is given by the (first-order) wave-induced vessel motions in heave, pitch and roll.
- The union of vessel, crane and payload constitutes a hydraulically driven multi-body system with nonlinear kinematics and dynamics. Modeling approaches reported in literature differ in intend and scope. Weighing model fidelity and computational complexity is key when deriving models intended for control.
- The crane system is differential flat with respect to the output $\boldsymbol{\gamma} = ((\boldsymbol{p}_{\text{load}}^{ned})^{\text{T}} z_{\text{tip}})^{\text{T}}$, where the tip height has been included to render the model square. The flat mappings allow taking a payload-centric control approach while offering a systematic way to account for the wave-induced vessel motions.

3.1 System Overview and Relevant Coordinate Frames

Designing predictive controllers for payload handling at sea requires modeling of the payload, crane, vessel as well as the wave excitation. The considered configuration is depicted in Fig. 3.1. Four coordinate frames are introduced to facilitate modeling of the

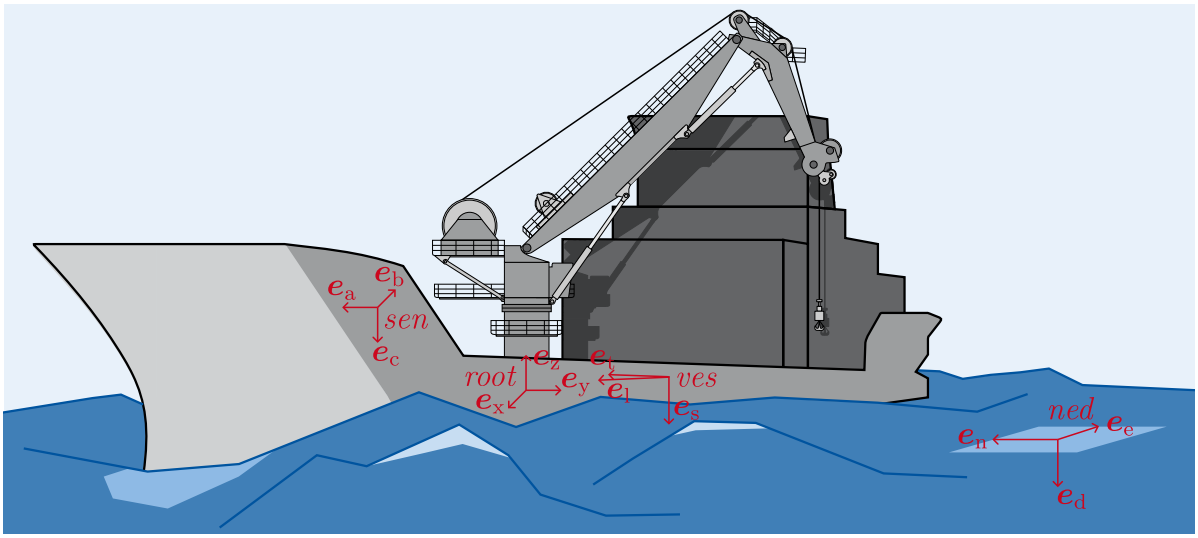

Fig. 3.1: Coordinate frames in crane-based offshore operations – The common reference frame *ned* : $\boldsymbol{O}_0$–$\boldsymbol{e}_\mathrm{n}\boldsymbol{e}_\mathrm{e}\boldsymbol{e}_\mathrm{d}$ is fixed both in time and space. Its orientation is given by the north-east-down (ned) convention. Moving frames *ves* : $\boldsymbol{O}_\mathrm{v}$–$\boldsymbol{e}_\mathrm{l}\boldsymbol{e}_\mathrm{t}\boldsymbol{e}_\mathrm{s}$ and *root* : $\boldsymbol{O}_\mathrm{c}$–$\boldsymbol{e}_\mathrm{x}\boldsymbol{e}_\mathrm{y}\boldsymbol{e}_\mathrm{z}$ are included to describe the pose of vessel and crane, respectively. The *sen* : $\boldsymbol{O}_\mathrm{s}-\boldsymbol{e}_\mathrm{a}\boldsymbol{e}_\mathrm{b}\boldsymbol{e}_\mathrm{c}$ frame maps the internal reference frames of the used sensors.

system and to account for the different reference frames, e.g. of a motion sensor or a human operator. The different frames are specified below.

- The frame *ned* : $\boldsymbol{O}_0-\boldsymbol{e}_\mathrm{n}\boldsymbol{e}_\mathrm{e}\boldsymbol{e}_\mathrm{d}$ is used as global reference system, which is defined tangent to earth's surface (here reflecting the mean sea surface). Its axes are oriented towards true north respectively east, while the third axis is normal to the earth's surface and points towards earth's center. The origin can be placed arbitrarily, although its altitude is usually chosen at neutral sea elevation. Neglecting earth rotation, the frame is considered fixed and inertial.
- The frame *ves* : $\boldsymbol{O}_\mathrm{v}-\boldsymbol{e}_\mathrm{l}\boldsymbol{e}_\mathrm{t}\boldsymbol{e}_\mathrm{s}$ is fixed to the crane vessel[1] and thus is moving as a result of the wave excitation. Its axes are chosen in direction of the vessel's principal axes of inertia. Hence, $\boldsymbol{e}_\mathrm{l}$ will usually point from aft to fore, therefore coinciding with the craft's longitudinal axis. Accordingly, the transversal axis $\boldsymbol{e}_\mathrm{t}$ and sagittal axis $\boldsymbol{e}_\mathrm{s}$ are directed to starboard and bottom, respectively. The origin is typically fixed to some point midship at height of the vessel's water line, see [68] for the relation of different characteristic points. The frame allows expressing the vessel's pose relative to the *ned*-frame.
- The frame *root* : $\boldsymbol{O}_\mathrm{c}-\boldsymbol{e}_\mathrm{x}\boldsymbol{e}_\mathrm{y}\boldsymbol{e}_\mathrm{z}$ is located at the center of the crane base in order to describe the crane configuration locally. While its orientation is mostly arbitrary,

[1] In [68] and related publications the coordinate system is referred to as the body-fixed *b*-frame.

it is intuitive to align $\boldsymbol{e}_{\mathrm{z}}$ with the crane pedestal and select upwards as the positive direction. The frames *ves* and *root* are related by a constant homogeneous transformation $\mathbf{T}_{root}^{ves}$, which has to be calibrated during crane installation.

- The frame $sen : \boldsymbol{O}_{\mathrm{s}} - \boldsymbol{e}_{\mathrm{a}}\boldsymbol{e}_{\mathrm{b}}\boldsymbol{e}_{\mathrm{c}}$ is included to account for the fact, that most sensors yield measurements with respect to some internal reference frame. To simplify the following discussions, all sensors are assumed to be calibrated to the same reference frame. Provided that the sensor package is mounted rigidly, there is a fixed transformation between the *sen*-frame and any vessel-fixed frame.

During payload handling the reference frame relative to which the payload motion is evaluated will change dependent on the task. As crane and vessel experience the same heave, the body-fixed *ves*-frame is essential for avoiding collisions while operating within the deck area, e.g. during loading and discharging. In contrast, a common reference frame like *ned*-coordinates may be adopted while operating outside the vessel. Hereafter, the more general case of stabilizing and positioning the payload relative to a fixed reference frame is examined.

In general, the dynamics of vessel, crane and payload are coupled. In addition, the hydrodynamic interaction with the ocean is complex because not only do incoming waves excite the vessel, but the vessel also displaces the surrounding fluid. In favor of a technically viable model complexity, it is often advisable to approximate the vessel dynamics and to neglect reaction forces of the crane or payload. While the former is usually realized through so-called response amplitude operators (cf. section 3.2), the latter allows to lump the vessel-wave interaction as an exogenous disturbance acting on the crane base. Following [51], separate modeling of crane vessel and payload is acceptable if the lifted object weighs less than 2 % of the vessel's tonnage displacement, i.e. during light lifts. Doing so further allows to assess the performance of the researched payload controllers independently of other control loops at vessel level, e.g. systems for dynamic positioning or active roll stabilization. The different elements in Fig. 3.1 are therefore modeled individually hereafter.

3.2 Vessel Dynamics and Environmental Loads

Hydrodynamics of marine vessels and offshore structures are complex due to the multi-layered interaction (fluid memory effects, buoyancy, ballast forces, ...) between the sea and a floating object. For an early presentation of the theory the interested reader is referred to [62], [114]. The presentation below follows [68]. Given the topic of crane-based offshore operations, the wave-induced motions of vessels at zero speed will be of interest, which is covered by the *seakeeping theory* [68].

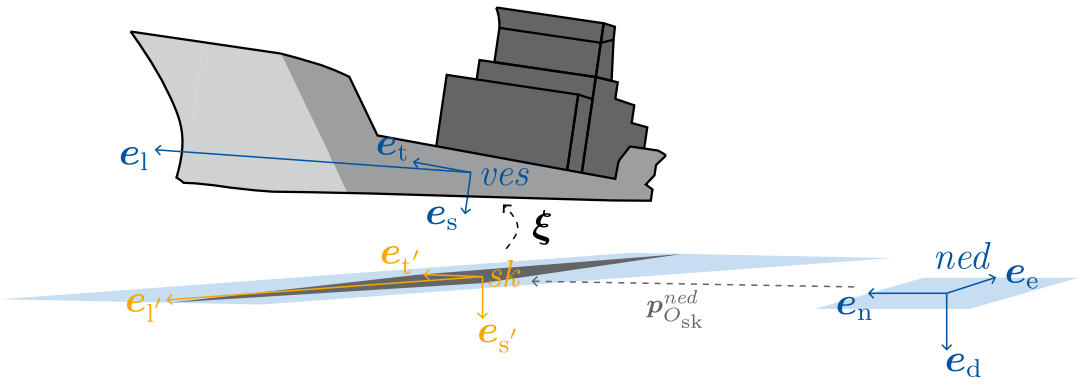

Fig. 3.2: Vessel motions during seakeeping – The vessel exhibits wave-induced motions in six DoF. The displacement $\boldsymbol{\xi}$ is measured in relation to the frame $sk : \boldsymbol{O}_{\mathrm{sk}} - \boldsymbol{e}_{\mathrm{l}'}\boldsymbol{e}_{\mathrm{t}'}\boldsymbol{e}_{\mathrm{s}'}$, which coincides with the vessel-fixed frame *ves* in neutral position, i.e. for zero wave excitation. For stationkeeping (zero propulsion), the frames *sk* and *ned* are related by a static transformation with translational offset $\boldsymbol{p}^{ned}_{\boldsymbol{O}_{\mathrm{sk}}}$ and heading $\bar{\psi}$.

In seakeeping, the vessel's wave-induced motions about a fixed equilibrium state are studied. Since in general the marine craft may move at a (constant) speed U with some heading $\bar{\psi}$, it is convenient to introduce a co-moving frame $sk : \boldsymbol{O}_{\mathrm{sk}} - \boldsymbol{e}_{\mathrm{l}'}\boldsymbol{e}_{\mathrm{t}'}\boldsymbol{e}_{\mathrm{s}'}$ in relation to which the vessel's *surge*, *sway*, *heave*, *roll*, *pitch*, and *yaw* motions can be described, cf. Fig. 3.2. The seakeeping frame is vertically aligned to the global *ned*-frame, while being both rotated an angle $\bar{\psi}$ about the $\boldsymbol{e}_{\mathrm{d}}$-axis and translated according to the vessel's unexcited position. As a result, the frame coincides with the body-fixed *ves*-frame at calm sea and its horizontal $\boldsymbol{e}_{\mathrm{l}'}\boldsymbol{e}_{\mathrm{t}'}$-plane matches the mean sea surface. Similar to the *ned*-frame, the *sk*-frame is inertial. The vessel's wave-induced perturbations are then described by a six-dimensional vector $\boldsymbol{\xi} = ((\boldsymbol{p}^{sk}_{\mathrm{ves}})^{\mathrm{T}}\ (\boldsymbol{o}^{sk}_{\mathrm{ves}})^{\mathrm{T}})^{\mathrm{T}} = (\xi_1\ \xi_2\ \xi_3\ \xi_4\ \xi_5\ \xi_6)^{\mathrm{T}}$, with position offset $\boldsymbol{p}^{sk}_{\mathrm{ves}}$ and attitude offset $\boldsymbol{o}^{sk}_{\mathrm{ves}}$ (Euler angles). Note the kinematic relations

$$\boldsymbol{p}^{ned}_{\mathrm{ves}} = \begin{pmatrix} n_{\mathrm{ves}} \\ e_{\mathrm{ves}} \\ d_{\mathrm{ves}} \end{pmatrix} = \boldsymbol{p}^{ned}_{\boldsymbol{O}_{\mathrm{sk}}}\left(U, \bar{\psi}, t\right) + \mathbf{R}^{ned}_{sk}\left(\bar{\psi}\right) \begin{pmatrix} \xi_1 \\ \xi_2 \\ \xi_3 \end{pmatrix} \tag{3.1a}$$

$$\boldsymbol{o}^{ned}_{\mathrm{ves}} = \begin{pmatrix} \phi_{\mathrm{ves}} \\ \theta_{\mathrm{ves}} \\ \psi_{\mathrm{ves}} \end{pmatrix} = \begin{pmatrix} 0 \\ 0 \\ \bar{\psi} \end{pmatrix} + \begin{pmatrix} \xi_4 \\ \xi_5 \\ \xi_6 \end{pmatrix} . \tag{3.1b}$$

A heading of the crane vessel is irrelevant to the discussion of payload control, as are vessel thrusts unequal to zero. Therefore, the perturbation coordinates $\boldsymbol{\xi}$ revert to the global pose defined with respect to the inertial *ned*-frame, except for a static translation ($\boldsymbol{p}^{ned}_{\boldsymbol{O}_{\mathrm{sk}}} = \text{const.}$). Following the notation in [68], the vessel-fixed linear and angular velocities with respect to *ves* are aggregated in a single vector $\boldsymbol{\nu} \in \mathbb{R}^6$.

In their work, Fossen et al. propose a vessel model similar to that of a normal robot, which for stationkeeping ($U = 0$) simplifies to [68]:

$$\dot{\boldsymbol{\xi}} = \mathbf{J}_{\text{ves}}(\boldsymbol{\xi})\boldsymbol{\nu} \tag{3.2a}$$

$$(\mathbf{M}_{\text{RB}} + \mathbf{M}_{\text{A}})(\dot{\boldsymbol{\nu}} - \dot{\boldsymbol{\nu}}_{\text{c}}) + \mathbf{D}(\boldsymbol{\nu} - \boldsymbol{\nu}_{\text{c}}) + \boldsymbol{\mu} + \mathbf{G}\boldsymbol{\xi} = \boldsymbol{\tau}_{\text{ves}} + \boldsymbol{\tau}_{\text{exog}} \tag{3.2b}$$

with the vessel's inertia matrix $\mathbf{M}_{\text{RB}}$, the (virtual) added mass matrix $\mathbf{M}_{\text{A}}$ accounting for the displacement of the surrounding ocean during vessel motion, the viscous damping matrix $\mathbf{D}$ and the gravitational, buoyancy forces mapped via $\mathbf{G}$. The dynamics (3.2b) are further defined by the fluid memory effects $\boldsymbol{\mu}$, the relative velocity between vessel hull and ocean currents $\Delta\boldsymbol{\nu} = \boldsymbol{\nu} - \boldsymbol{\nu}_{\text{c}}$, as well as the propulsion forces resp. moments $\boldsymbol{\tau}_{\text{ves}}$ and the exogenous disturbances $\boldsymbol{\tau}_{\text{exog}}$ capturing both wave and wind loads. Linear and angular velocities are transformed from body-fixed to inertial frame, i.e. $\boldsymbol{\nu} \mapsto \dot{\boldsymbol{\xi}}$, by virtue of (3.2a). The mapping $\mathbf{J}_{\text{ves}} \in \mathbb{R}^{6\times6}$ is derived in [68] and given by

$$\mathbf{J}_{\text{ves}}(\boldsymbol{\xi}) = \begin{bmatrix} \mathbf{R}_{ves}^{sk}(\boldsymbol{\xi}) & \mathbf{0}_{3\times3} \\ \mathbf{0}_{3\times3} & \mathbf{T}_{ves}(\boldsymbol{\xi}) \end{bmatrix} \quad \text{with} \quad \mathbf{T}_{ves}(\boldsymbol{\xi}) \coloneqq \begin{bmatrix} 1 & \mathrm{s}\xi_4\,\mathrm{t}\xi_5 & \mathrm{c}\xi_4\,\mathrm{t}\xi_5 \\ 0 & \mathrm{c}\xi_4 & -\mathrm{s}\xi_4 \\ 0 & \mathrm{s}\xi_4/\mathrm{c}\xi_5 & \mathrm{c}\xi_4/\mathrm{c}\xi_5 \end{bmatrix} \tag{3.3}$$

where shorthand notations for $\sin(\cdot)$, $\cos(\cdot)$ and $\tan(\cdot)$ have been used, cf. section 2.1. The rotation matrix $\mathbf{R}_{ves}^{sk}$ is given by (2.2) with $\boldsymbol{\theta}_{rpy} = \boldsymbol{o}_{\text{ves}}^{sk}$. Together with the position offset $\boldsymbol{p}_{\text{ves}}^{sk}$ this informs the homogeneous transformation

$$\mathbf{T}_{ves}^{sk}(\boldsymbol{\xi}) = \begin{bmatrix} \mathbf{R}_{ves}^{sk}(\boldsymbol{\xi}) & \boldsymbol{p}_{\text{ves}}^{sk}(\boldsymbol{\xi}) \\ \mathbf{0}_{1\times3} & 1 \end{bmatrix} . \tag{3.4}$$

Noting that $\mathbf{T}_{sk}^{ned}$ is constant by assumption, the kinematic relation between both inertial *ned*-frame and moving *ves*-frame is obtained as $\mathbf{T}_{ves}^{ned}(\boldsymbol{\xi}) = \mathbf{T}_{sk}^{ned}\mathbf{T}_{ves}^{sk}(\boldsymbol{\xi})$, cf. (3.1).

The term $\boldsymbol{\tau}_{\text{exog}}$ in (3.2b) summarizes the effects of wind, waves and ocean currents on the vessel motion. In order to limit the scope of this thesis, primary attention is directed towards wave disturbances, which predominantly contribute to the vessel's heave, rolling and pitching motions. In turn, these account for the majority of payload oscillations. The vessel's remaining DoF (surge, sway and yaw) will be significantly affected by not only waves but also ocean currents and wind gusts[2]. However, such disturbances are less relevant for payload control since they are usually addressed by the vessel's DP system. Looking at the required accuracy for class 3 DP solutions (5 m in position and 3° in heading [54]), such claim may not hold across all sea states. Yet, the closed-loop motions tend to be of low frequency. Furthermore, compensating for drifting motions of the vessel by means of the crane actuators is only feasible within the kinematic constraints of the crane. In order to analyze the derived payload controllers independently of the

[2]In adverse weather, wind may also add to the vessel's rolling motion depending on the hull geometry and the craft's overall inertia.

control loops at vessel level, the following simplification is used throughout, unless stated otherwise:

$$\boldsymbol{\tau}_{\text{exog}} \approx \boldsymbol{\tau}_{\text{wave}} = \begin{pmatrix} 0 & 0 & \tau_{\text{heave}} & \tau_{\text{roll}} & \tau_{\text{pitch}} & 0 \end{pmatrix}^{\text{T}} . \tag{3.5}$$

The wave excitation can be further divided into two parts per DoF, namely first- and second-order forces or moments $\tau_{i,1}$ and $\tau_{i,2}$ with $i \in \{\text{heave}, \text{roll}, \text{pitch}\}$, respectively. The first-order loads show zero-mean oscillatory behavior, whereas the second-order loads are characterized by a slowly varying drift. Both components are usually superimposed additively, i.e. $\tau_i = \tau_{i,1} + \tau_{i,2}$. Note that second-order loads will mainly act on the vessel's surge, sway and yaw DoF. Following the reasoning above, the main focus will be on first-order wave loads hereafter.

Today, specialized programs like ShipX/Veres (MARINTEK, Trondheim, Norway) are used to derive so-called response amplitude operators (RAO), which describe the wave-induced loads on respectively motions of the vessel, cf. Fig. 3.3. A RAO is comparable to a frequency response in that it comprises both magnitude and phase information, which are used to scale the incoming waves. The complex-valued RAOs are computed as a function of the wave frequency ω and incidence angle[3] β. The calculations are based on e.g. the vessel's hull geometry as well as mass distribution and are usually stored in table format. Given the normalized *force* RAO $F(\omega, \beta)$ of a particular vessel, the wave

[3]The incidence or encounter angle is the angle enclosed between (global) wave direction and vessel heading.

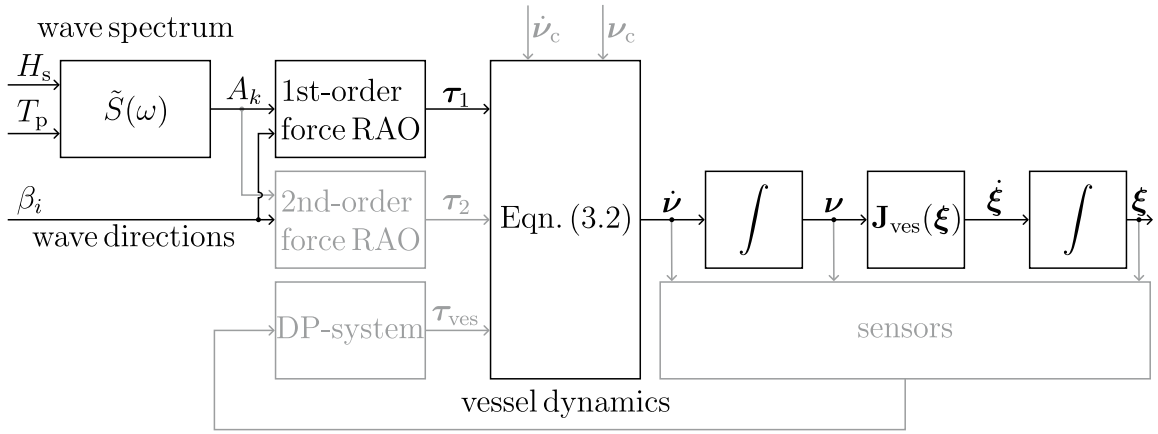

Fig. 3.3: Vessel dynamics informed by force RAOs – The vessel is driven by wave-induced forces resp. moments $\boldsymbol{\tau}_1$ and $\boldsymbol{\tau}_2$, ocean currents $\boldsymbol{\nu}_c$ as well as thruster forces $\boldsymbol{\tau}_{\text{ves}}$ commanded by the DP-system. The sea state is characterized by the significant wave height H_s and modal wave period T_p. Amplitudes A_i and directions β_i of individual wave components are related to the wave loads through RAOs. Motions in the body-fixed frame $\boldsymbol{\nu}$ are transformed to the global seakeeping frame $\dot{\boldsymbol{\xi}}$ by virtue of (3.2a). The primary signal path considered for payload control is highlighted.

loads of first order are determined according to

$$\tau_{i,1} = \sum_{k=1}^{n}\sum_{j=1}^{m} \rho g |F(\omega_k, \beta_j)| A_k \cos\left(\left(\omega_k - \frac{\omega_k}{g} U \cos(\beta_j)\right) t + \angle F(\omega_k, \beta_j) + \epsilon_k\right), \quad (3.6)$$
$$i \in \{\text{heave}, \text{roll}, \text{pitch}\}$$

where $n \in \mathbb{Z}$ wave components ω_k and $m \in \mathbb{Z}$ wave directions β_j have been considered [68]. The remaing quantities are water density ρ, gravitational constant g, forward speed U, time t and amplitude A_k of the k^{th} wave component. In addition, a random phase angle $\epsilon_k \sim \mathcal{U}(0, 2\pi)$ is included per wave component. The wave frequencies ω_k are drawn randomly as well. For this purpose, the (relevant) frequency axis is divided into intervals $\mathcal{I}_k^{\omega}$ of length $\Delta\omega$, whereby $\omega_k \sim \mathcal{U}(\mathcal{I}_k^{\omega})$. The incidence angles β_j may be derived accordingly, i.e. by breaking $[0, \pi]$ in intervals of length $\Delta\beta = \pi/m$ and defining uniform distributions with corresponding supports. In order to simulate (3.6), the wave amplitudes A_k have to be specified, which should reflect the sea state. The relation is established in (3.8) with the help of wave spectra outlined next.

In line with the theory of RAOs, the sea state is described via a wave spectrum $S(\omega, \beta)$, from which the different wave components are inferred. Different spectra have been proposed over the years, see e.g. [68]. Noteworthy, most contributions separate the influences of wave frequency and incidence angle. Directionality is added by means of a spreading function $f_{\text{s}}(\beta)$ such that $S(\omega, \beta) = \tilde{S}(\omega) f_{\text{s}}(\beta)$. In scope of chapter 4, two spectra are utilized for evaluation of the predictive control topologies: The single-peaked JONSWAP (Joint North Sea Wave Project) spectrum $\tilde{S}_{\text{J}}(\omega)$ [74] is probably the most common model used to describe non-fully developed seas. It is parameterized by the significant wave height H_{s} (mean height of the highest one-third waves) and the spectrum's peak frequency[4] ω_{p}. The spectrum is then given by

$$\tilde{S}_{\text{J}}(\omega) = \frac{\alpha_{\text{P}} 2\pi g^2}{\omega^5} \exp\left(-\frac{5}{4}\left(\frac{\omega}{\omega_{\text{p}}}\right)^{-4}\right) \gamma^{\exp\left(-\frac{(\omega-\omega_{\text{p}})^2}{2\sigma^2\omega_{\text{p}}^2}\right)} \quad (3.7a)$$

$$\overset{[53]}{=} \left((1 - 0.287\ln(\gamma))\frac{5}{16}\right) \frac{H_{\text{s}}^2 \omega_{\text{p}}^4}{\omega^5} \exp\left(-\frac{5}{4}\left(\frac{\omega}{\omega_{\text{p}}}\right)^{-4}\right) \gamma^{\exp\left(-\frac{(\omega-\omega_{\text{p}})^2}{2\sigma^2\omega_{\text{p}}^2}\right)} \quad (3.7b)$$

with the additional constants defined as Phillips constant α_{P}, spectral energy ratio γ between JONSWAP and Pierson-Moskowitz [139] spectrum, and peak width scale σ. The following values were already proposed in the original publication [74] and later on adopted by the International Towing Tank Conference (ITTC) [41]

$$\gamma = 3.3\,, \qquad \sigma = \begin{cases} 0.07 & \omega \leq \omega_{\text{p}} \\ 0.09 & \omega > \omega_{\text{p}} \end{cases}.$$

[4] Alternatively, the spectrum can be expressed as a function of the mean wave period T_1 since $\omega_{\text{p}} = 2\pi\, {}^{0.834}/_{T_1}$ [41].

The piecewise definition of the peak width scale σ allows for a skewed spectrum, cf. Fig. 3.4. In contrast to the JONSWAP model, the TORSETHAUGEN spectrum $\tilde{S}_{\mathrm{T}}(\omega)$ features two peaks that map the effects of swell (low-frequency peak) and newly developed waves (high-frequency peak) [172], cf. Fig. 3.4. The resulting wave profiles reflect common observations in the North Sea and are more challenging for automatic control due to the two distinct frequency components. In section 4.2, the TORSETHAUGEN spectrum is therefore used to validate generalizability of the observer-based disturbance prediction algorithm. Since the mathematical definition of $\tilde{S}_{\mathrm{T}}(\omega)$ is significantly more complex than in the case of $\tilde{S}_{\mathrm{J}}(\omega)$, it is omitted here. The interested reader is referred to e.g. [53], [173]. Like the JONSWAP spectrum, the TORSETHAUGEN spectrum is parameterized via the (total) significant wave height H_{s} and the (dominating) peak frequency ω_{p}. The relation between wave amplitude A_k and wave spectrum $\tilde{S}(\omega)$ is then established by

$$\frac{1}{2}A_k^2 = \tilde{S}(\omega_k)\Delta\omega \tag{3.8}$$

see [62]. Hence, equation (3.6) is fully defined. Both spectra can be calculated with the help of the *Marine Systems Simulator* toolbox [67].

When applying the wave spectra in simulation, proper values for wave height and frequency should be specified. In this context, so-called *environmental contours* [53] provide a good point of reference, which are obtained from recorded wave heights and periods for specific sea areas [116], [138]. Probable values are reported in [17] for different sea states, cf. Tab. 3.1. The works of Bayle et al. were later adopted by the North Atlantic Treaty Organization (NATO) for standardizing sea states in the NATO STANAG 4194 (1983). Based on wave data, empirical correlations between $T_{\mathrm{p}} = {}^{2\pi}/_{\omega_{\mathrm{p}}}$ and H_{s} were derived in [91] and [116]. Hereby, the spectra can be parameterized solely on the basis of the significant wave height. The mean relation takes the form

$$T_{\mathrm{p}} = c_1 + c_2 H_{\mathrm{s}}^{c_3} \tag{3.9}$$

where the fitting parameters c_1, c_2, c_3 vary depending on the contribution. For example, the authors in [91] suggest $c_1 = 4.883$, $c_2 = 2.68$ and $c_3 = 0.54$ for an area in the North Sea.

For future reference, the definition of different sea state codes (SSC) according to the World Meteorological Organization (WMO) [134] is reproduced in Tab. 3.1. In favor of better interpretation, the frequency of occurrence per state is indicated as reported in [17] for the North Atlantic. Taking into account the dynamic limitations of current KBC, the investigations in chapter 4 are restricted to wave profiles corresponding to sea state codes 0 to 6, which cover 92.5 % of the observed sea conditions. Exemplary vessel trajectories during moderate and harsh sea are depicted in Fig. 3.5, where both the JONSWAP and TORSETHAUGEN spectra have been used.

Table 3.1: Definition of sea state codes according to [134], alongside typical values of significant wave height H_s and modal wave period T_p [17]. Ranges and probabilities are taken from [17] with respect to the North Atlantic.

Code figure	Description	Wave heights (m)	Probability (%)	mean H_s (m)	range T_p (s)	likely T_p (s)
0	calm (glassy)	0	0	0.05	-	-
1	calm (rippled)	0 - 0.1				
2	smooth (wavelets)	0.1 - 0.5	7.2	0.3	3.3 - 12.8	7.5
3	slight	0.5 - 1.25	22.4	0.88	5.0 - 14.8	7.5
4	moderate	1.25 - 2.5	28.7	1.88	6.1 - 15.2	8.8
5	rough	2.5 - 4	15.5	3.25	8.3 - 15.5	9.7
6	very rough	4 - 6	18.7	5	9.8 - 16.2	12.4
7	high	6 - 9	6.1	7.5	11.8 - 18.5	15.0
8	very high	9 - 14	1.2	11.5	14.2 - 18.6	16.4
9	phenomenal	>14	<0.05	>14	15.7 - 23.7	20.0

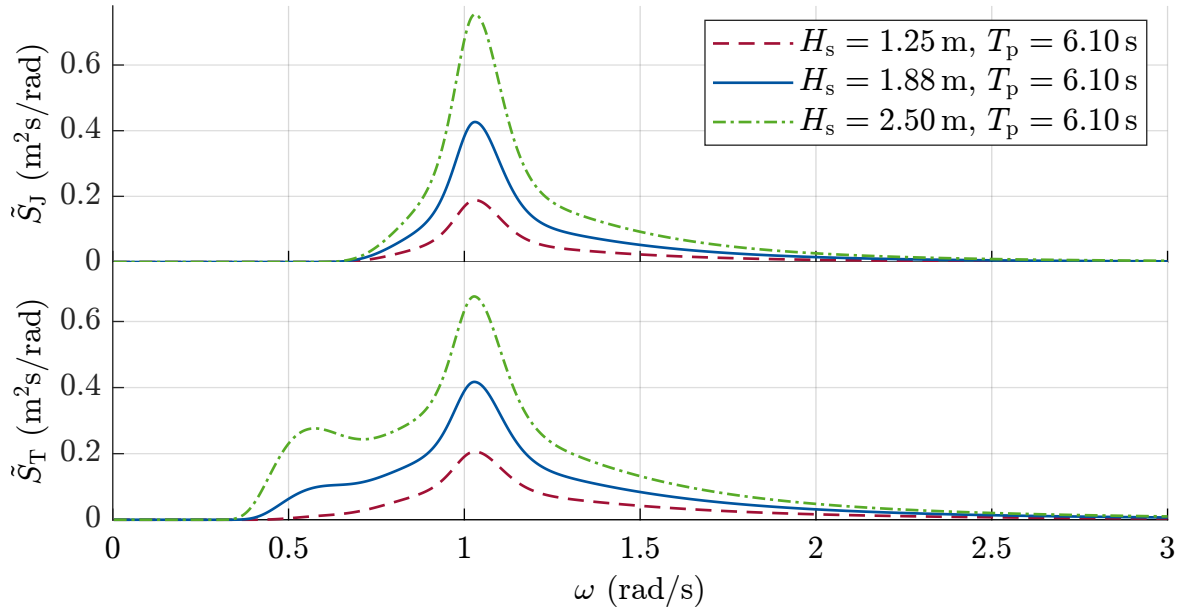

Fig. 3.4: Wave spectra – Both the JONSWAP (top) and TORSETHAUGEN (bottom) spectrum are depicted for varying significant wave heights H_s and a constant modal wave period of $T_p = 6.1\,\mathrm{s}$. Depending on the parameterization, the TORSETHAUGEN spectrum shows two characteristic peaks, reflecting swell and newly developed waves.

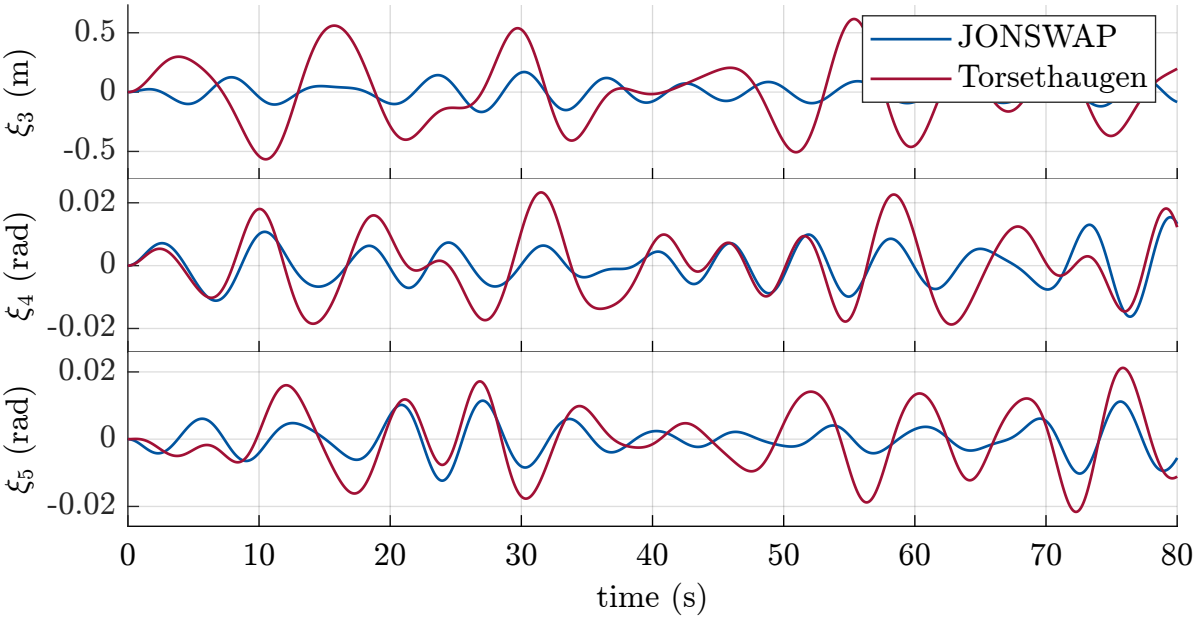

Fig. 3.5: Exemplary vessel trajectories – The first-order wave loads are computed based on the JONSWAP resp. TORSETHAUGEN spectrum ($H_s = 2.5\,\mathrm{m}$, $T_p = 6.1\,\mathrm{s}$). Since all wave components are chosen randomly, the trajectories should only be compared qualitatively. Responses simulated with the help of [67] for a supply vessel.

3.3 Knuckle Boom Crane

Shipboard cranes differ in structure, lift capacity or actuation depending on the area of application. A common type of offshore cranes are knuckle boom cranes (KBC) that possess four hydraulically driven DoF (slewing bearing, main boom, knuckle jib, winch) and therefore offer high flexibility with regard to the realizable working radii. Main boom and knuckle jib are positioned through the luffing resp. folding cylinders, whereas the crane's angular orientation (slewing) and winch are usually actuated by multiple hydraulic axial piston motors. Hoisting and lowering of the suspended payload is mostly accomplished through the main winch, while the remaining crane DoF are utilized to manipulate the horizontal payload position. The cable is paid out via the winch and guided over three sheaves. Modern KBC are equipped with a double-sheave arrangement at the crane tip, which allows for either normal or overhead operation, see Fig. 3.6. As a result, the amount of useable crane configurations is maximized.

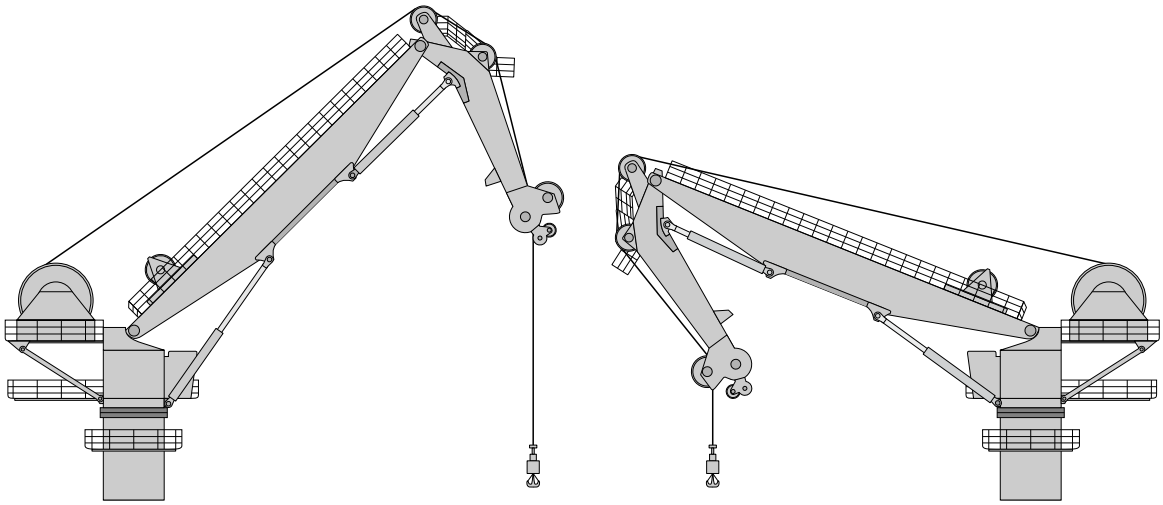

(a) Normal operation **(b)** Overhead operation

Fig. 3.6: Exemplary configurations of a knuckle boom crane – The KBC is equipped with a double-sheave arrangement at its tip, which depending on the crane configuration enables normal (left) as well as overhead (right) operation.

Due to inertia as well as exogenous disturbances, the payload oscillates during operation, yielding pendulum-like payload motions. The researched knuckle boom crane (KBC) is depicted in Fig. 3.7. According with section 3.1, the global *ned*-frame as well as the local *root*-frame are included. Furthermore, two characteristic points, namely the payload and tip position are indicated. Two angles φ_1, φ_2 are introduced to describe spatial payload sway. In order to facilitate modeling of the KBC, two variable spaces are defined:

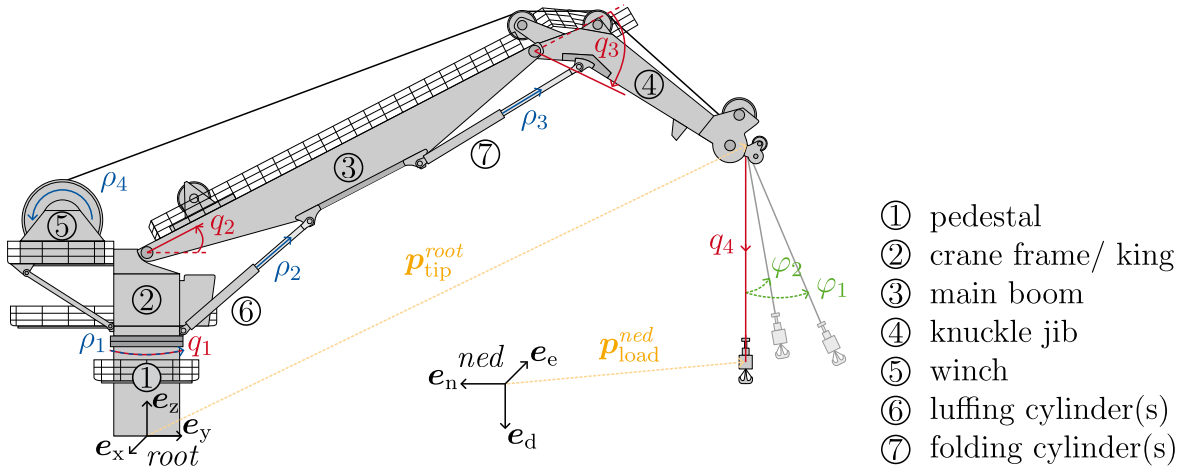

Fig. 3.7: Schematics of a knuckle boom crane – The crane configuration is determined by four DoF, which can be specified by either joint variables $\boldsymbol{q} \in \mathcal{Q}$ (red) or actuator variables $\boldsymbol{\rho} \in \mathcal{P}$ (blue). The payload sway is described via two deflection angles φ_1, φ_2 (green) around the $\boldsymbol{e}_{\text{e}}$- resp. $\boldsymbol{e}_{\text{n}}$-axis of the global *ned*-frame. All counting directions are chosen as per the right-hand convention. The different bodies of the crane system are enumerated and listed on the right. Two characteristic points (yellow) will be referenced during modeling: The payload position $\boldsymbol{p}_{\text{load}}^{ned}$ is defined at the (lumped) center of mass of both payload and hook. The tip position $\boldsymbol{p}_{\text{tip}}^{root}$ marks the payload's suspension point, which lies on the last sheave. Note that the indicated reference frames are illustrative, as both points may be transformed to arbitrary coordinate systems following section 3.2.

- The *joint space* $\mathcal{Q}$ is spanned by the variables $\boldsymbol{q} = (q_1\, q_2\, q_3\, q_4)^{\text{T}}$, with the crane's rotation q_1 about its base, the angles q_2, q_3 of main resp. knuckle boom, and the free cable length q_4 between suspension point and hook, cf. Fig. 3.7. Hence, $[\boldsymbol{q}] = (\text{rad}\,\text{rad}\,\text{rad}\,\text{m})^{\text{T}}$. Besides providing an intuitive representation of the crane configuration, the joint variables are also utilized as generalized coordinates in section 3.3.3. Moreover, the inverse kinematics problem can be readily solved with respect to $\mathcal{Q}$.
- The *actuator space* $\mathcal{P}$ is spanned by the variables $\boldsymbol{\rho} = (\rho_1\, \rho_2\, \rho_3\, \rho_4)^{\text{T}}$, which reflect the deflections of the individual crane actuators. In this context, the cylinder strokes are denoted ρ_2 and ρ_3, while the angular positions of slewing drive and winch motors are represented by ρ_1 resp. ρ_4. The units of the individual vector components are then given by $[\boldsymbol{\rho}] = (\text{rad}\,\text{m}\,\text{m}\,\text{rad})^{\text{T}}$. Naturally, the actuator dynamics and constraints are established with regard to $\mathcal{P}$. As outlined in section 3.3.2, the joint variables $\boldsymbol{q}$ and actuator variables $\boldsymbol{\rho}$ are related by a nonlinear mapping, assuming rigid links.

Hereafter, various modeling approaches for the crane system are reviewed before its

kinematics and dynamics are derived in section 3.3.2 and section 3.3.3, respectively.

3.3.1 Review of Crane Models

Offshore cranes are hydraulically actuated manipulators with a design-dependent number of DoF. Due to the similarity to serial kinematics, methods from robotics can be used for the geometric description of the crane system [113]. Further considering not only the crane system but also the vessel as well as the suspended payload results in a dynamic multi-body system whose individual dynamics are coupled. Various models are proposed in literature, which differ both in terms of fidelity and intended use. In order to analyze the dynamic behavior of offshore cranes, the hydraulic circuit must be modeled in addition to the mechanics of the crane kinematics. To deal with the resulting multi-domain problem, so-called *bond graphs* can be applied, that yield an energy-based and undirected representation of the crane system [31]–[33]. Building on the same modeling approach, the authors in [38] add the flexibility of individual booms to the model by applying *screw theory*. For the sake of simplicity, a planar problem is considered, i.e. effects outside the crane's lateral plane are neglected. Another approach for mapping the limited stiffness of the crane structure is given by [15]. The crane is divided into rigid segments, which are connected via rotary joints, torsion springs and dampers. The derived model is parameterized experimentally using a crane with multiple articulated booms and gripping tool. If the modeling is intended for controller synthesis, idealized models are usually adopted. In [57], [104], motion control of the crane's hydraulic cylinders is studied. The modeling is largely based on rudimentary hydraulic equations describing the cylinders and valves. In contrast, the underlying hydraulics are approximated by simple (signal-based) surrogate models when higher control loops, e.g. for payload stabilization are addressed. In this context, the dynamics of the cylinders [11], [128][5] or the winch [107], [108] are modeled as an ideal first-order lag element. The crane structure is commonly modeled as a dynamic multi-body system whose equations of motion are derived using the Euler-Lagrange approach [84], [113], [119]. The crane model is complemented by the dynamics of the cable, hook and payload. Due to the wide spread of handled payloads, a universal modeling of the payload dynamics is challenging. The literature therefore applies simplified models with lumped parameters, e.g. by assuming a single point mass for the hook-payload assembly. An early review is included in [1]. Approximating the hosting line as a massless connection is reasonable as long as the payload-to-cable mass ratio[6] is sufficiently high [51]. In fact, the assumption is supported by the emergence of modern fiber rope cranes, which feature cables with significantly lower net weight. Besides a rigid connection between

[5]The authors consider a harbor crane with a single boom.

[6]The horizontal eigenperiod of a lifted payload in air is estimated as $T_\mathrm{h} = T_\mathrm{p}(^{M+0.33mL}/_{M+0.45mL})^{0.5}$ with the eigenperiod of a spherical pendulum T_p, the payload mass M, the mass per unit length hoisting line m and the free cable length L [51]. Obviously, $T_\mathrm{h} \approx T_\mathrm{p}$ for $M >> mL$.

payload or crane hook and suspension point (crane tip) [63], [83], [103], [119], [128], [177], a load-dependent elongation of the cable is described in [31], [107]. The latter is mapped via a spring-damper element in the hoist line. A detailed model of the cable guiding is provided by [124]. An analysis of the friction in the hoist system (winch drive, gearbox, sheaves) is included in [125]. For the case of standardized container loads, advanced models are available that also capture payload skew, see [36], [154]. Following [178], double-pendulum dynamics have to be considered for low payload-to-hook mass ratios, as well as rigging lines approaching the free cable length between crane tip and hook.

Discussion and Corollaries

Among the cited modeling approaches, the bond-graph theory is probably best equipped to handle both the mechanics and hydraulics of offshore cranes. However, implementation of the derived models in a model-based controller like MPC is not straightforward, but involves different conversion steps to resolve the implicit model formulation. Furthermore, the complexity associated with multi-domain models is challenging when targeting real-time calculations. Specifically in MPC, the different scale of time constants found across domains is disadvantageous, as the resulting system of differential equations is usually stiff. In such case, balancing time discretization and prediction horizon is a delicate task. For good tracking performance, the prediction horizon should account for the system's slowest dynamics. On the other hand, small intervals between shooting nodes are required to capture faster dynamics. Complying with both requirements yields computational heavy optimization problems, which are detrimental to real-time feasibility. In the context of automated control, reduced models that either simplify or abstract the crane's hydraulics are therefore predominant. Arguably, modeling of the crane's hydraulics is dispensable when considering high-level control objectives as payload stabilization. Yet, the dynamic limitations of the hydraulic system have to be mapped to obtain realistic, i.e. feasible actuations. Since linear surrogate models have shown effective in real-world experiments [11], [147], simplified actuator dynamics will be considered hereafter. Choosing reference velocities for actuators or joints as high-level manipulated variables is reasonable by assumption of layered velocity loops, that reflect common engineering practice. A hierarchic controller design moreover promotes transferability of the payload controller to different crane types, cf. [35], [152].

In line with the aforementioned works, some additional assumptions are made in order to limit the scope of the modeling. Simplifications are adopted for the hoisting system, where the hook-payload assembly is modeled as a point mass exhibiting single-pendulum dynamics and the cable is considered massless as well as constantly taut. Doing so is sensible for crane operations with payloads exceeding both hook and (effective) cable in weight. As mentioned before, this condition is less limiting for modern fibre rope cranes. Still, the payload mass should adhere to the light lift assumption made during

vessel modeling, see section 3.2. In addition, hooks with single fall reeving as well as short rigging lines are implied. Dynamic elongations of the cable are expected to be of particular relevance during subsea lifts, where the cable is directly loaded by waves and ocean currents. For handling operations above sea level, cable elongations are assumed to vary only slowly. The same is postulated for deviations stemming from finite crane stiffness, friction in the sheaves or limited tracking performance of the crane actuators. Hence, they might be addressed by adding integral action to the controller designs or including a disturbance observer, cf. section 4. The assumptions are believed to be not overly restrictive, but should be checked for any particular handling task. Operating conditions outside the specified scope present possible directions for future research.

A limited model fidelity is often acceptable in controller synthesis as long as the characteristic dynamics of the real system are captured and real-time feasibility is ensured. In practice, minor modeling errors are addressed by nature of the closed loop topology or disturbance observers. Yet, poor models may considerably diminish control performance of a MPC, if deviations are significant. The simulative results in chapter 4 should therefore be understood as an upper bound on the obtainable performance. However, they provide valid means of comparing different control strategies. Furthermore, some effort is made to improve informative value e.g. by introducing artificial model mismatch.

3.3.2 Kinematics

The KBC resembles a serial manipulator with an open kinematic chain from crane root to crane tip. Assuming rigid kinematics, its configuration is fully determined by the position of the slewing drive and the hydraulic cylinders. Having said this, the kinematic model is best established in the joint space $\mathcal{Q}$. Both joint and actuator variables are then related by a nonlinear mapping $\boldsymbol{\phi}_{\boldsymbol{\rho}} : \mathcal{Q} \to \mathcal{P}$, which is stated below. The crane is complemented by the hoisting system. The paid out cable can be divided into two parts, one of which is stored in the crane while the other equates to the free cable length between suspension point and hook. The stored cable length is configuration-dependent. The different kinematic relations are illustrated in Fig. 3.8 and modeled separately hereafter. Taking into account the vessel pose and payload deflection, the complete kinematic model allows to derive the global position of both crane tip and payload, i.e. $\boldsymbol{p}_{\mathrm{tip}}^{ned}$ resp. $\boldsymbol{p}_{\mathrm{load}}^{ned}$. In fact, the crane's kinematics present an important nonlinearity during manual payload handling, which must be accounted for by the operator. Similarly, they should be explicitly considered in automated payload control, as the corresponding Jacobian describes the translation of actuator movements into Cartesian tip motions, that are key for payload stabilization, cf. section 4.3. Figure 3.8 illustrates the crane kinematics with respect to the local *root*-frame. As is argued in [124], the cable suspension point lies on the last sheave normal to $\boldsymbol{e}_{\mathrm{d}}$, that is parallel to the mean sea surface and normal to earth's gravity vector. Hence, the suspension point is not fixed but moves as the vessel

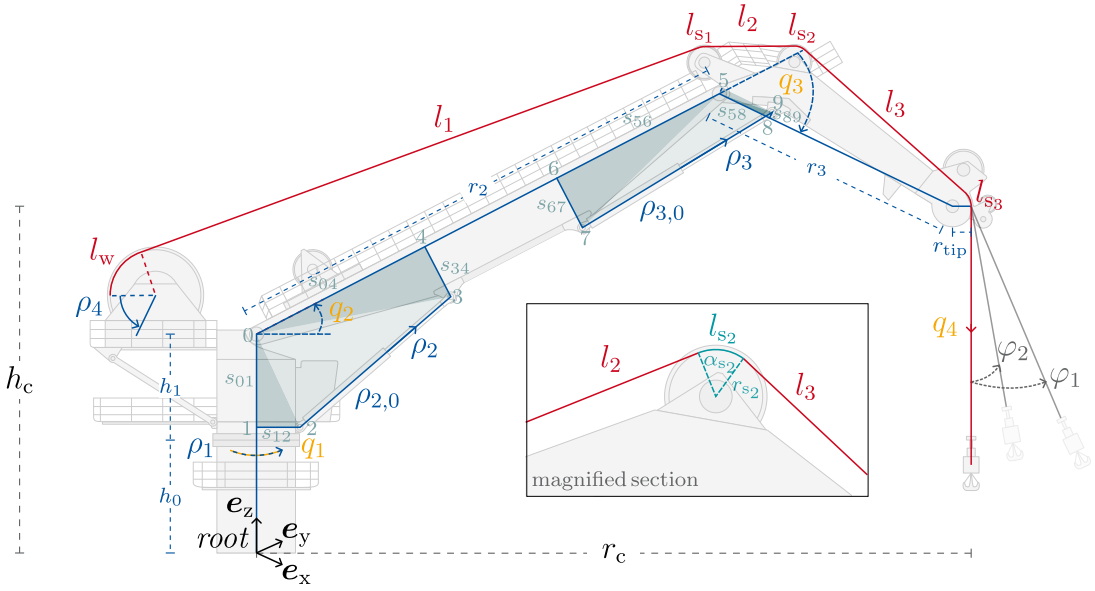

Fig. 3.8: Kinematics of a knuckle boom crane – The crane's kinematic chain includes three revolute joints q_1 to q_3, a free 2-DoF universal joint parameterized by φ_1, φ_2 and a prismatic joint q_4 representing the free cable. Under the assumption of rigid links, actuator variables $\boldsymbol{\rho}$ (blue) are mapped to joint variables $\boldsymbol{q}$ (yellow) solely by geometric cosine relations. For the boom-cylinder assemblies characteristic values s_{ij}, $i, j \in \{0, \ldots, 9\}$ are indicated. The crane's radius r_c is defined as the distance between crane root and crane tip measured in the horizontal plane. The cable is released by the winch and guided over three sheaves. The stored cable length includes segments on resp. between sheaves, i.e. l_{s_k} resp. l_k with $k \in \{1, \ldots, 3\}$, and the winch-related segment l_w. The segment length over a particular sheave is derived based on the sheave radius r_{s_k} and the angle α_{s_k} between the two tangent points.

is displaced by the wave excitation. Recall from section 3.2 the transformation $\mathbf{T}_{ves}^{ned}(\boldsymbol{\xi})$ between inertial and vessel-fixed frame. The latter is related to the crane's *root*-frame by a constant offset $\boldsymbol{p}_{O_{\text{root}}}^{ves} = (l_c\, t_c\, s_c)^{\mathrm{T}}$ and a fixed rotation angle $\boldsymbol{o}_{\text{root}}^{ves} = (0\,0\,\psi_c)^{\mathrm{T}}$, imforming the homogeneous transformations

$$\mathbf{T}_{root}^{ves} = \begin{bmatrix} \mathbf{R}_{root}^{ves}(\boldsymbol{o}_{\text{root}}^{ves}) & \boldsymbol{p}_{O_{\text{root}}}^{ves} \\ \mathbf{0}_{1\times 3} & 1 \end{bmatrix}, \qquad \mathbf{T}_{root}^{ned}(\boldsymbol{\xi}) = \mathbf{T}_{ves}^{ned}(\boldsymbol{\xi})\, \mathbf{T}_{root}^{ves}. \tag{3.10}$$

The kinematic chain from crane root to crane tip can then be modeled using the Denavit-Hartenberg formalism, cf. section 2.1. The crane's DH-parameters with respect to the joint space $\mathcal{Q}$ are summarized in Tab. 3.2. The first transformation $\mathbf{T}_{q_1}^{root}$ describes a simple translation in direction of $\boldsymbol{e}_z$, which is equal to the pedestal height h_0, see Fig. 3.8. The remaining geometric quantities are the king height h_1 as well as the lengths of main boom r_2 and knuckle jib r_3. The last transformation $\mathbf{T}_{tip}^{s_3}$ between third sheave and suspension (tip) point is defined by a rotation angle ϑ_{tip} and a radius

r_{tip}, which are functions of both the vessel's orientation and the crane configuration. For normal operation (Fig. 3.6a), the radius simplifies to that of the third sheave, i.e. $r_{\mathrm{tip}} = r_{\mathrm{s_3}}$. In contrast, the suspension point is located on the fourth sheave during overhead operation. In this case, the variables ϑ_{tip} and r_{tip} subsume an according sequence of transformations from third to fourth sheave resp. from fourth sheave to suspension point. The DH-parameters give rise to the homogeneous transformation

Table 3.2: DH-parameters of the considered KBC, adapted from [S5].

$\mathbf{T}_i^{i-1}$	d_i	ϑ_i	r_i	α_i
$\mathbf{T}_{q_1}^{root}$	h_0	0	0	0
$\mathbf{T}_{q_2}^{q_1}$	h_1	q_1	0	$\pi/2$
$\mathbf{T}_{q_3}^{q_2}$	0	q_2	r_2	0
$\mathbf{T}_{s_3}^{q_3}$	0	q_3	r_3	0
$\mathbf{T}_{tip}^{s_3}$	0	ϑ_{tip}	r_{tip}	0

$$\mathbf{T}_{tip}^{root}\left(\boldsymbol{q}, \vartheta_{\mathrm{tip}}, r_{\mathrm{tip}}\right) = \mathbf{T}_{q_1}^{root}\mathbf{T}_{q_2}^{q_1}\left(q_1\right)\mathbf{T}_{q_3}^{q_2}\left(q_2\right)\mathbf{T}_{s_3}^{q_3}\left(q_3\right)\mathbf{T}_{tip}^{s_3}\left(\vartheta_{\mathrm{tip}}, r_{\mathrm{tip}}\right) , \tag{3.11}$$

which further defines the crane's forward kinematics

$$\boldsymbol{\phi}_{\mathrm{fk}}(\boldsymbol{q}, \vartheta_{\mathrm{tip}}, r_{\mathrm{tip}}) = \begin{bmatrix}\mathbf{I}_{3\times 3} & \mathbf{0}_{3\times 1}\end{bmatrix}\mathbf{T}_{tip}^{root}\left(\boldsymbol{q}, \vartheta_{\mathrm{tip}}, r_{\mathrm{tip}}\right)\begin{pmatrix}\mathbf{0}_{3\times 1}\\ 1\end{pmatrix} = \boldsymbol{p}_{\mathrm{tip}}^{root} . \tag{3.12}$$

An equivalent expression in the global reference frame is obtained by premultiplying (3.11) with (3.10), i.e. $\mathbf{T}_{tip}^{ned}\left(\boldsymbol{\xi}, \boldsymbol{q}\right) = \mathbf{T}_{root}^{ned}\left(\boldsymbol{\xi}\right)\mathbf{T}_{tip}^{root}\left(\boldsymbol{q}, \vartheta_{\mathrm{tip}}, r_{\mathrm{tip}}\right)$. Here, the auxiliary variables $\vartheta_{\mathrm{tip}}, r_{\mathrm{tip}}$ have been omitted from the left-hand argument list, as will be reasoned below. Accordingly, the global tip position is given by

$$\boldsymbol{p}_{\mathrm{tip}}^{ned}\left(\boldsymbol{\xi}, \boldsymbol{q}\right) = \boldsymbol{p}_{\mathrm{root}}^{ned}\left(\boldsymbol{\xi}\right) + \mathbf{R}_{root}^{ned}\left(\boldsymbol{\xi}\right)\boldsymbol{p}_{\mathrm{tip}}^{root}\left(\boldsymbol{q}, \vartheta_{\mathrm{tip}}, r_{\mathrm{tip}}\right) \tag{3.13}$$

where $\boldsymbol{p}_{\mathrm{root}}^{ned}\left(\boldsymbol{\xi}\right) = \left(\mathbf{T}_{root}^{ned}\left(\boldsymbol{\xi}\right)\right)_{1\leq i\leq 3,4}$ and $\mathbf{R}_{root}^{ned}\left(\boldsymbol{\xi}\right) = \left(\mathbf{T}_{root}^{ned}\left(\boldsymbol{\xi}\right)\right)_{1\leq i\leq 3, 1\leq j\leq 3}$, cf. (3.10). As mentioned earlier, the cable suspension point will move depending on the orientation of the last sheave in the earth's gravitational field. In [124], an according modeling approach for a four DoF ship crane is presented, which is adapted for the considered KBC. The following derivation of the fall angle ϑ_{tip} is arguably more compact than the one given in [124]. With regard to Tab. 3.2, equation (3.13) may be reformulated as

$$\boldsymbol{p}_{\mathrm{tip}}^{ned}\left(\boldsymbol{\xi}, \boldsymbol{q}\right) = \boldsymbol{p}_{\mathrm{O_{s_3}}}^{ned}\left(\boldsymbol{\xi}, \boldsymbol{q}\right) + \underbrace{\mathbf{R}_{s_3}^{ned}\left(\boldsymbol{\xi}, \boldsymbol{q}\right)\begin{pmatrix} r_{\mathrm{tip}}\cos(\vartheta_{\mathrm{tip}})\\ r_{\mathrm{tip}}\sin(\vartheta_{\mathrm{tip}})\\ 0\end{pmatrix}}_{=:\Delta\boldsymbol{p}_{\mathrm{tip}}^{ned}} \tag{3.14}$$

where the second term reveals an offset vector $\Delta\boldsymbol{p}_{\mathrm{tip}}^{ned}$ pointing from the third sheave's origin to the tip point in the *ned*-frame. Arguing as before, this vector has to lie within the $\boldsymbol{e}_{\mathrm{n}}\boldsymbol{e}_{\mathrm{e}}$-plane, i.e. its third component Δd_{tip} has to equate to zero, which yields

$$\Delta d_{\mathrm{tip}} = \begin{pmatrix} 0 & 0 & 1 \end{pmatrix} \mathbf{R}_{s_3}^{ned}\left(\boldsymbol{\xi}, \boldsymbol{q}\right) \begin{pmatrix} r_{\mathrm{tip}} \cos(\vartheta_{\mathrm{tip}}) \\ r_{\mathrm{tip}} \sin(\vartheta_{\mathrm{tip}}) \\ 0 \end{pmatrix} \stackrel{!}{=} 0 \tag{3.15}$$

$$\Rightarrow \vartheta_{\mathrm{tip}}(\boldsymbol{\xi}, \boldsymbol{q}) = \operatorname{atan2}\left(\left(\mathbf{R}_{s_3}^{ned}\left(\boldsymbol{\xi}, \boldsymbol{q}\right)\right)_{3,1}, -\left(\mathbf{R}_{s_3}^{ned}\left(\boldsymbol{\xi}, \boldsymbol{q}\right)\right)_{3,2} \right) . \tag{3.16}$$

By establishing the kinematic chain in dependency of the fourth instead of the third sheave, similar expressions can be derived for overhead operations. Albeit being of limited practical relevance, both models (normal and overhead operation) may be combined by interpolating between the resp. tip points, e.g. as a function of the third sheave's cable tangent points. Notably, relation (3.16) depends on both the crane configuration $\boldsymbol{q}$ as well as the vessel displacement $\boldsymbol{\xi}$. Accordingly, the auxiliary variables ϑ_{tip}, r_{tip} can be eliminated from (3.11)-(3.14). For the same reason, finding the inverse mapping to (3.12), i.e. the crane's inverse kinematics $\boldsymbol{\phi}_{\mathrm{ik}} : \mathbb{R}^3 \to \mathcal{Q}$, is challenging. Once the variables ϑ_{tip}, r_{tip} are fixed it is straightforward to calculate the position of the last sheave given a desired tip position $\boldsymbol{p}_{\mathrm{tip}}^{root}$ by rotating (3.14) to the *root*-frame and solving for the sheave's origin position. From this point backwards, the inverse kinematics problem can be solved analytically with the help of symbolic mathematics toolboxes. The crane's inverse kinematics are best conceived in cylindrical coordinates, defined by the crane's slew angle q_1, tip height h_{c} and radius[7] r_{c}, which were already introduced in Fig. 3.8. The fundamental problem then reads

$$x_{\mathrm{tip}} \sin(q_1) - y_{\mathrm{tip}} \cos(q_1) = 0 \tag{3.17a}$$

$$r_3 \cos(q_2 + q_3) + r_2 \cos(q_2) + r_{\mathrm{tip}} \cos(\vartheta_{\mathrm{tip}} + q_2 + q_3) = r_{\mathrm{c}} \tag{3.17b}$$

$$r_3 \sin(q_2 + q_3) + r_2 \sin(q_2) + r_{\mathrm{tip}} \sin(\vartheta_{\mathrm{tip}} + q_2 + q_3) = h_{\mathrm{c}} - h_1 - h_2 \tag{3.17c}$$

with $r_{\mathrm{c}} = \sqrt{x_{\mathrm{tip}}^2 + y_{\mathrm{tip}}^2}$ and $h_{\mathrm{c}} = z_{\mathrm{tip}}$. The solution is somewhat complex and thus omitted here. However, since ϑ_{tip}, r_{tip} are functions of the crane configuration $\boldsymbol{q}$ themselves, the more general problem of finding the roots to

$$\boldsymbol{p}_{\mathrm{tip}}^{root} - \boldsymbol{p}_{\mathrm{O}_{s_3}}^{root}\left(\boldsymbol{q}\right) - \Delta\boldsymbol{p}_{\mathrm{tip}}^{root}\left(\boldsymbol{\xi}, \boldsymbol{q}, \vartheta_{\mathrm{tip}}(\boldsymbol{\xi}, \boldsymbol{q}), r_{\mathrm{tip}}(\boldsymbol{\xi}, \boldsymbol{q})\right) = 0$$

has to be solved, for which no closed form solution is deducible. Complexity may be reduced to the aforementioned case (3.17) by calculating the fall angle ϑ_{tip} based on previous crane configurations, cf. section 3.4 – equation (3.50).

[7] Apart from the crane radius r_{c}, its *outreach* is referenced frequently. The latter is not defined with respect to the crane root but measured between the tip position and the vessel's free edge.

Given the crane tip position $\boldsymbol{p}_{\text{tip}}^{ned}$ according to (3.13) and modeling the cable's suspension point as a universal joint, the payload position $\boldsymbol{p}_{\text{load}}^{ned}$ in the *ned*-frame is determined by

$$\boldsymbol{p}_{\text{load}}^{ned}\left(\boldsymbol{\xi}, \boldsymbol{q}, \boldsymbol{\varphi}\right) = \boldsymbol{p}_{\text{tip}}^{ned}\left(\boldsymbol{\xi}, \boldsymbol{q}\right) + q_4 \begin{pmatrix} \sin(\varphi_2) \\ -\sin(\varphi_1)\cos(\varphi_2) \\ \cos(\varphi_1)\cos(\varphi_2) \end{pmatrix} \tag{3.18}$$

with the free cable length q_4 and the deflection angles $\boldsymbol{\varphi} = (\varphi_1\, \varphi_2)^{\mathrm{T}}$. Note that the payload sway is defined with respect to the *ned*-frame, cf. Fig. 3.7. Thus, φ_1 and φ_2 differ from the angles observed from an operator's point of view, which are usually referred to as *sidelead* resp. *offlead* [48]. Both sets of angles are related by the rotation matrix $\mathbf{R}_{q_2}^{ned}$. For future reference, consider the cone induced by payload and tip position. As per (3.18), the corresponding half-angle $\varphi_{\text{c}} \coloneqq \operatorname{atan}\left({}^{|\Delta r|}/_{|\Delta h|}\right)$ equates to

$$\varphi_{\text{c}} = \operatorname{atan}\left(\frac{\sqrt{\sin(\varphi_2)^2 + \sin(\varphi_1)^2\cos(\varphi_2)^2}}{\cos(\varphi_1)\cos(\varphi_2)}\right) = \operatorname{acos}\left(\cos(\varphi_1)\cos(\varphi_2)\right) \tag{3.19}$$

which may be used to constrain the payload sway by a single figure, cf. section 4.7.4.

The crane kinematics (3.13), (3.18) are complemented by the relation between actuator variables $\boldsymbol{\rho}$ and joint variables $\boldsymbol{q}$. Here, significant nonlinearities arise from the geometry of the boom-cylinder subassemblies, which will be analyzed first. Thereafter, the cable guiding is described in more detail in order to derive the free cable length q_4. All dependencies are aggregated in a single mapping $\boldsymbol{\phi}_{\boldsymbol{\rho}} : \mathcal{Q} \to \mathcal{P}$ in (3.26), whose inverse $\boldsymbol{\phi}_{\boldsymbol{q}} : \mathcal{P} \to \mathcal{Q}$ is given in (3.27), respectively.

For fully retracted luffing cylinders $\rho_2 = \rho_{2,0}$, the main boom is nearly horizontal with regard to the crane's *root*-frame, i.e. $q_2 = 0\,\text{rad}$. By design, the boom is erected when extending the cylinders. Similar, the stroke ρ_3 of the folding cylinders determines the jib angle q_3. Assuming rigid kinematics, three triangles may be defined per boom-cylinder subassembly to derive a mapping from actuator to joint variables, see Fig. 3.8. By applying elementary trigonometry, the following relations are obtained

$$\operatorname{acos}\left(\frac{-(\rho_2+\rho_{2,0})^2 + s_{01}^2 + s_{12}^2 + s_{04}^2 + s_{34}^2}{2\sqrt{s_{01}^2+s_{12}^2}\sqrt{s_{04}^2+s_{34}^2}}\right) + \operatorname{atan}\left(\frac{s_{12}}{s_{01}}\right) + \operatorname{atan}\left(\frac{s_{34}}{s_{04}}\right) = q_2 + \frac{\pi}{2} \tag{3.20a}$$

$$\operatorname{acos}\left(\frac{-(\rho_3+\rho_{3,0})^2 + s_{56}^2 + s_{67}^2 + s_{58}^2 + s_{89}^2}{2\sqrt{s_{56}^2+s_{67}^2}\sqrt{s_{58}^2+s_{89}^2}}\right) + \operatorname{atan}\left(\frac{s_{67}}{s_{56}}\right) - \operatorname{atan}\left(\frac{s_{89}}{s_{58}}\right) = q_3 + \pi \tag{3.20b}$$

which are also described in e.g. [31]. The geometric quantities $s_{ij} > 0$ are indicated in Fig. 3.8. Notably, the mappings (3.20) are characterized by trigonometric functions,

which non-linearly relate the cylinder strokes ρ_2, ρ_3 to the joint angles q_2 and q_3. Further taking into account the crane's forward kinematics (3.12), the change in tip position that follows from cylinder actuations is configuration dependent, a fact that will be revisited in chapter 4 when optimizing the crane's manipulability index.

The hoisting cable is released by the main winch and is guided over a set of three sheaves, which is illustrated in Fig. 3.8. Depending on the operation, the final suspension point lies on the third resp. fourth sheave. In order to measure the paid out cable length, a fixed reference point on the main winch has to be defined. For the sake of simplicity, the reference point is chosen at the boom averted intersection of the winch's outer layer with an imaginary horizontal running through the winch center, see Fig. 3.8. The total cable length is then the sum of the free cable length q_4 and the stored cable length l_c, the latter of which summarizes cable sections l_i, l_{s_i} between resp. on sheaves, i.e.

$$(\rho_{4,0} - \rho_4) r_\mathrm{w} = q_4 + l_\mathrm{c}(\boldsymbol{q}) = q_4 + \underbrace{l_\mathrm{w} + l_1 + l_{\mathrm{s}_1} + l_2 + l_{\mathrm{s}_2} + l_j + l_{\mathrm{s}_j}}_{=: l_\mathrm{c}(\boldsymbol{q})} \ , \ j \in \{3, 4\} \tag{3.21}$$

with the winch radius r_w and a constant offset $\rho_{4,0}$. The offset may be chosen as to restrict the magnitude of ρ_4, e.g. according to $\rho_{4,0} = {}^{l_\mathrm{c}(\boldsymbol{q}(t_0))}/_{r_\mathrm{w}}$. Calculating the stored cable length l_c reverts to the geometric problem of finding common (external[8]) tangents of length l_i to consecutive sheaves. Doing so yields two tangent points per sheave, which further define the cable length l_{s_i} stored on the resp. sheave. Below, the general procedure is exemplified for the segments l_w and l_1 from winch to first sheave. The involved geometry is depicted in Fig. 3.9. Similar concepts can be adopted for the other pairs of sheaves. A thorough presentation is included in e.g. [124].

First, the center points of sheave and winch are referred to the same coordinate frame, yielding the two position vectors $\boldsymbol{p}_\mathrm{w}^{q_2}$ and $\boldsymbol{p}_{\mathrm{s}_1}^{q_2}$. Utilizing the q_2-frame as a reference is arbitrary, but sensible, since the first crane joint q_1 is irrelevant for the relative position of winch and sheave. Both center points span a right-angled triangle (blue) with hypotenuse length d_1, which follows from

$$d_1(\boldsymbol{q}) = \| \boldsymbol{p}_\mathrm{w}^{q_2} - \boldsymbol{p}_{\mathrm{s}_1}^{q_2}(\boldsymbol{q}) \|_2 = \sqrt{(\boldsymbol{p}_\mathrm{w}^{q_2} - \boldsymbol{p}_{\mathrm{s}_1}^{q_2}(\boldsymbol{q}))^\mathrm{T} (\boldsymbol{p}_\mathrm{w}^{q_2} - \boldsymbol{p}_{\mathrm{s}_1}^{q_2}(\boldsymbol{q}))} \tag{3.22}$$

where the argument $\boldsymbol{q}$ has been included to emphasize the dependency on the current crane configuration, which stems from the variable sheave position $\boldsymbol{p}_{\mathrm{s}_1}^{q_2}(\boldsymbol{q})$. Consequently, both cable segments l_1, l_w are functions of the joint variables as well, in particular of q_2 and q_3. By constructing two auxiliary circles – one with radius ${}^{d_1}/_2$ centered at the triangle's hypotenuse midpoint, the other with radius $r_\mathrm{w} - r_{\mathrm{s}_1}$ aligned with the winch

[8] The only exception presents the cable segment l_4 from second to fourth sheave, in which case an internal tangent has to be modeled.

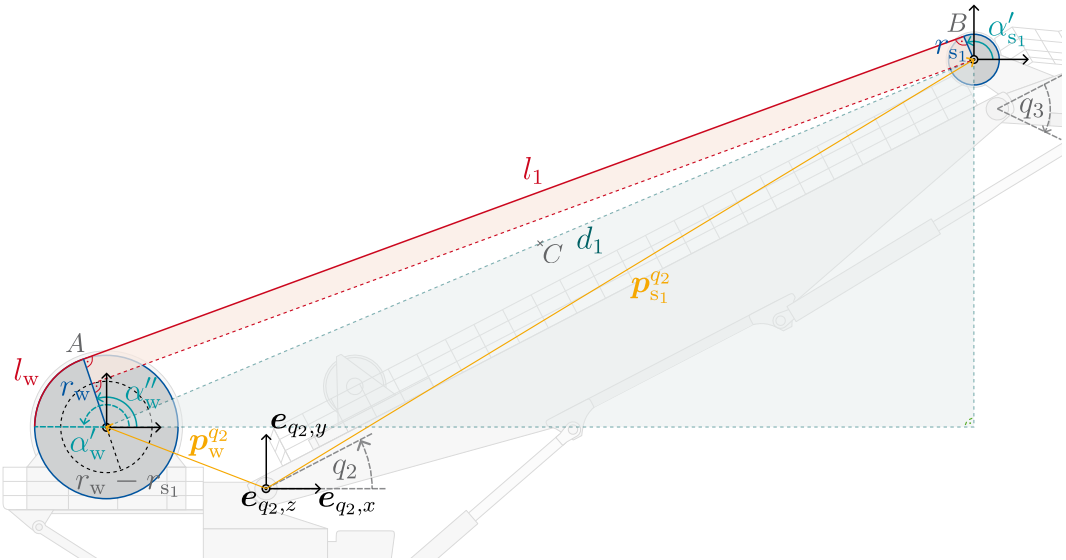

Fig. 3.9: Geometric relations defining the cable segments l_1, l_w – An auxiliary circle (dotted) of radius $r_w - r_{s_1}$ and a right-angled triangle (blue) with hypotenuse length d_1 are introduced to construct the common tangent between winch and first sheave. The length d_1 directly follows from the position vectors $\boldsymbol{p}^{q_2}_w$ and $\boldsymbol{p}^{q_2}_{s_1}$. The tangent points A resp. B correspond to the intersections of the winch's and sheave's outer layers with a cycle of radius $d_1/2$ centered at point C (hypotenuse midpoint). The angles α'_w and α''_w determine the arc length $l_w = (\alpha'_w - \alpha''_w) r_w$.

center point – the following relations can be derived from Fig. 3.9:

$$l_w(\boldsymbol{q}) = \left(\alpha'_w(\boldsymbol{q}) - \alpha''_w(\boldsymbol{q})\right) r_w \tag{3.23}$$

$$l_1(\boldsymbol{q}) = \sqrt{d_1(\boldsymbol{q})^2 - (r_w - r_{s_1})^2} \tag{3.24}$$

where the auxiliary angles α'_w, α''_w are obtained according to

$$\alpha'_w(\boldsymbol{q}) = \pi \tag{3.25a}$$

$$\alpha''_w(\boldsymbol{q}) = \operatorname{atan}\left(\frac{\begin{pmatrix}0 & 1 & 0\end{pmatrix}\left(\boldsymbol{p}^{q_2}_w - \boldsymbol{p}^{q_2}_{s_1}(\boldsymbol{q})\right)}{\begin{pmatrix}1 & 0 & 0\end{pmatrix}\left(\boldsymbol{p}^{q_2}_w - \boldsymbol{p}^{q_2}_{s_1}(\boldsymbol{q})\right)}\right) + \operatorname{asin}\left(\frac{l_1(\boldsymbol{q})}{d_1(\boldsymbol{q})}\right) . \tag{3.25b}$$

Here, the more general case of both auxiliary angles α'_w, α''_w depending on the crane configuration is indicated, which holds true for the crane sheaves. For example, $\alpha'_{s_1}(\boldsymbol{q}) = \alpha''_w(\boldsymbol{q})$, which is specified by (3.25b). The modeling (3.22)-(3.25) is adapted for all pairs of consecutive sheaves, yielding the unknown cable segments l_i, l_{s_i} in (3.21). The geometric

relations (3.20), (3.21) are then combined to establish a single mapping between actuator and joint space according to

$$\boldsymbol{\rho} = \boldsymbol{\phi}_{\boldsymbol{\rho}}(\boldsymbol{q}) = \begin{pmatrix} \rho_{1,0} + \frac{1}{k_\mathrm{s}}(q_1 - q_{1,0}) \\ -\rho_{2,0} + \sqrt{s_{02}^2 + s_{03}^2 - 2s_{02}s_{03}\cos(q_2 - q_{2,0})} \\ -\rho_{3,0} + \sqrt{s_{57}^2 + s_{59}^2 - 2s_{57}s_{59}\cos(q_3 - q_{3,0})} \\ \rho_{4,0} - \frac{1}{r_\mathrm{w}}\left(q_4 - q_{4,0} + l_\mathrm{c}(\boldsymbol{q})\right) \end{pmatrix} \tag{3.26}$$

where a linear model for the slewing unit has been added, that is characterized by the transmission ratio $k_\mathrm{s} \in \mathbb{R}_{>0}$. Offsets in either joint or actuator variables may be included through parameters $\rho_{i,0}$ resp. $q_{i,0}$, $i = 1, \ldots, 4$. Furthermore, the shorthand notations

$$\begin{aligned} &s_{02} = \sqrt{s_{01}^2 + s_{12}^2}\,, \quad s_{03} = \sqrt{s_{04}^2 + s_{34}^2}\,, \quad s_{57} = \sqrt{s_{56}^2 + s_{67}^2}\,, \quad s_{59} = \sqrt{s_{58}^2 + s_{89}^2}\,, \\ &q_{2,0} = \operatorname{atan}\left({}^{s_{12}}\!/_{s_{01}}\right) + \operatorname{atan}\left({}^{s_{34}}\!/_{s_{04}}\right) - {}^{\pi}\!/_{2}\,, \\ &q_{3,0} = \operatorname{atan}\left({}^{s_{67}}\!/_{s_{56}}\right) - \operatorname{atan}\left({}^{s_{89}}\!/_{s_{58}}\right) - \pi \end{aligned}$$

have been introduced to derive a more compact representation. Noteworthy, each of the first three elements in (3.26) depends on a single joint variable q_i. Solving for $q_1, \ldots, q_3$ is therefore straightforward. Since the stored cable length l_c is a function of exactly these DoF, the inverse mapping $\boldsymbol{\phi}_{\boldsymbol{q}} : \mathcal{P} \to \mathcal{Q}$ is well-defined and given by

$$\boldsymbol{q} = \boldsymbol{\phi}_{\boldsymbol{q}}(\boldsymbol{\rho}) = \begin{pmatrix} \phi_{q_1}(\rho_1) \\ \phi_{q_2}(\rho_2) \\ \phi_{q_3}(\rho_3) \\ \phi_{q_4}(\boldsymbol{\rho}) \end{pmatrix} = \begin{pmatrix} q_{1,0} + k_\mathrm{s}(\rho_1 - \rho_{1,0}) \\ q_{2,0} + \operatorname{acos}\left(\left(s_{02}^2 + s_{03}^2 - (\rho_2 + \rho_{2,0})^2\right) / \left(2s_{02}s_{03}\right)\right) \\ q_{3,0} + \operatorname{acos}\left(\left(s_{57}^2 + s_{59}^2 - (\rho_3 + \rho_{3,0})^2\right) / \left(2s_{57}s_{59}\right)\right) \\ q_{4,0} - r_\mathrm{w}(\rho_4 - \rho_{4,0}) - l_\mathrm{c}(\boldsymbol{q})|_{q_j = \phi_{q_j}(\rho_j),\, j=1,\ldots,3} \end{pmatrix} \tag{3.27}$$

with element-wise functions $q_i = \phi_{q_i}(\cdot)$. Finally, the crane's kinematic model is compiled from its forward kinematics (3.12), (3.18), the cable segmentation (3.21) as well as the mapping between actuator and joint space (3.27).

3.3.3 Dynamics

Once the kinematics are established, the rigid body dynamics of the KBC can be derived via the Euler-Lagrange formalism. Similar to [113], four moving bodies are defined as shown in Fig. 3.10, i.e. king assembly, main boom, knuckle jib and payload. Note that there are different approaches to include the hydraulic cylinders, which connect two bodies each. In [37], the barrel mass is added to the former body while the piston is lumped with the following body. In contrast, the authors in [113] attribute each cylinder to a single body. A reference frame $b_i : \boldsymbol{O}_{\mathrm{com}_i} - \boldsymbol{e}_{\mathrm{x}_i}\boldsymbol{e}_{\mathrm{y}_i}\boldsymbol{e}_{\mathrm{z}_i}$, $i = 1, \ldots, 4$ is attached to each body's center of mass (COM), where the resp. axes are aligned with the body's principal axes of inertia. As a result, the inertia tensors $\mathbf{I}_i^{b_i}$ are invariant. Regarding

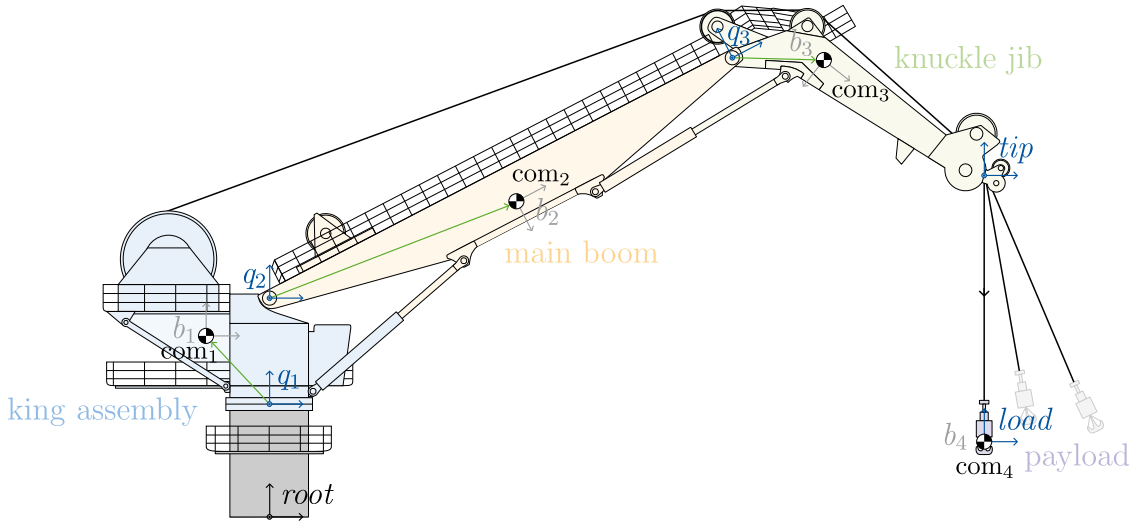

Fig. 3.10: Simplified body assignment for a KBC, adapted from [113] – In order to derive the crane's rigid body dynamics, its structure is divided into four bodys: king assembly (blue), main boom (yellow), knuckle jib (red), payload (purple). Reference frames q_i are attached to the crane joints, cf. Tab. 3.2. Additional frames b_i are fixed to the centers of mass com_i of each body, $i = 1, \ldots, 4$. Frame axes are not labeled as to give a concise depiction. The indicated frames are thus illustrative in nature.

the vessel-crane-payload system, a minimal set of generalized coordinates is given by $\boldsymbol{\zeta} = (\xi_1, \ldots, \xi_6, q_1, \ldots, q_4, \varphi_1, \varphi_2)^{\mathrm{T}} \in \mathbb{R}^{12}$ [S2]. Given homogeneous transformations

$$\mathbf{T}_{b_i}^{ned}\left(\boldsymbol{\xi}, \boldsymbol{q}, \boldsymbol{\varphi}\right) = \begin{bmatrix} \mathbf{R}_{b_i}^{ned}\left(\boldsymbol{\zeta}\right) & \boldsymbol{p}_{\mathrm{b}_i}^{ned}\left(\boldsymbol{\zeta}\right) \\ \mathbf{0}_{1\times 3} & 1 \end{bmatrix} \tag{3.28}$$

between the global *ned*-frame and the body frames b_i, the energy of a particular crane body is calculated according to

$$\mathcal{T}_i = \frac{1}{2} m_i \, \dot{\boldsymbol{\zeta}}^{\mathrm{T}} \left((\mathbf{J}_{\boldsymbol{p}_{\mathrm{b}_i}}^{ned})^{\mathrm{T}} \mathbf{J}_{\boldsymbol{p}_{\mathrm{b}_i}}^{ned} \right) \dot{\boldsymbol{\zeta}} + \frac{1}{2} \dot{\boldsymbol{\zeta}}^{\mathrm{T}} \left((\mathbf{J}_{\boldsymbol{o}_{\mathrm{b}_i}}^{ned})^{\mathrm{T}} \mathbf{R}_{b_i}^{ned} \mathbf{I}_i^{b_i} (\mathbf{R}_{b_i}^{ned})^{\mathrm{T}} \mathbf{J}_{\boldsymbol{o}_{\mathrm{b}_i}}^{ned} \right) \dot{\boldsymbol{\zeta}} \tag{3.29a}$$

$$\mathcal{V}_i = -m_i \, (\boldsymbol{g}^{ned})^{\mathrm{T}} \left(\boldsymbol{p}_{\mathrm{b}_i}^{ned}\left(\boldsymbol{\zeta}\right) - \mathbf{0}^{3\times 1} \right) \tag{3.29b}$$

with the body's kinetic energy $\mathcal{T}_i$, its potential energy $\mathcal{V}_i$, its lumped mass m_i and its inertia tensor $\mathbf{I}_i^{b_i}$. Dependencies of the different quantities on the vector of generalized coordinates $\boldsymbol{\zeta}$ have been omitted from (3.29) to improve readability. In (3.29b), the vector of gravitational acceleration is expressed in the *ned*-frame, i.e. $\boldsymbol{g}^{ned} = (0\,0\,g)^{\mathrm{T}}$. Furthermore, the kinetic energy (3.29a) is derived with respect to the geometric Jacobian

$$\mathbf{J}_{\mathrm{b}_i}^{ned}\left(\boldsymbol{\zeta}\right) = \begin{bmatrix} \mathbf{J}_{\boldsymbol{p}_{\mathrm{b}_i}}^{ned}\left(\boldsymbol{\zeta}\right) \\ \mathbf{J}_{\boldsymbol{o}_{\mathrm{b}_i}}^{ned}\left(\boldsymbol{\zeta}\right) \end{bmatrix} \in \mathbb{R}^{6\times 12} \tag{3.30}$$

which can be partitioned to reveal two matrices $\mathbf{J}^{ned}_{\boldsymbol{p}_{\mathrm{b}_i}}$, $\mathbf{J}^{ned}_{\boldsymbol{o}_{\mathrm{b}_i}}$ relating $\dot{\boldsymbol{\zeta}}$ to the body's linear velocity $\dot{\boldsymbol{p}}^{ned}_{\mathrm{b}_i}$ and angular velocity $\boldsymbol{\omega}^{ned}_{\mathrm{b}_i}$, respectively. See e.g. [159] for an introduction to geometric Jacobians. The system's Lagrangian $L = \sum_{i=1}^{4} \mathcal{T}_i - \mathcal{V}_i$ is simply the sum of the individual energy contributions. Additional terms may be added e.g. to map the limited stiffness of the hoisting cable, in which case the potential energy stored in the extended cable has to be modeled. The crane's equations of motion are then obtained by virtue of the Euler-Lagrange equations of second kind, thus satisfying $\frac{\mathrm{d}}{\mathrm{d}t}\frac{\partial L}{\partial \dot{\zeta}_j} - \frac{\partial L}{\partial \zeta_j} = \tau_{\mathrm{e},j}$ with the aggregated contribution of non-conservative (generalized) forces $\tau_{\mathrm{e},j}$ per DoF and $j = 1, \ldots, 12$. Typical examples of non-conservative forces are actuation forces and torques, as well as friction. For an analysis of friction losses in the hoist system, the reader is referred to [125].

Although, crane models derived via the Euler-Lagrange formalism have been frequently used as plant model in the literature, see e.g. [84], [119], shortcomings in mapping the crane actuators usually limit their practical use in closed-loop control. First, the rigid body dynamics do not capture the dynamic behavior of the crane's hydraulics, which are integral to its performance limitations. The influence of the hydraulic system is discussed in [16]. Furthermore, the model inputs usually revert to either actuator or joint forces and torques, which do not match real manipulated variables. From a low-level perspective, these are given by e.g. the control voltages of the directional control valves (DCV) in the crane's hydraulic circuit. As reasoned in section 3.3.1, layered control loops will be assumed hereafter, which motivates the use of simplified surrogate models. The subsequent modeling follows the presentation in [S2]. The crane's hydraulics are approximated by first-order dynamics

$$\ddot{\rho}_i = \frac{K_i}{T_i}\dot{\rho}_{i,\mathrm{ref}} - \frac{1}{T_i}\dot{\rho}_i \qquad i = 1, \ldots, 4 \tag{3.31}$$

with the time constant T_i, the gain factor K_i and a set value $\dot{\rho}_{i,\mathrm{ref}}$ per actuator. Similar modeling approaches have been used in [11], [107] to describe cylinder and winch dynamics, respectively. Compared to (3.31), however, the authors consider control voltages of the servo valves as inputs. Doing so admits a physical interpretation of the gain factors, which are calculated as a function of the valve's proportional constant of flow rate to input voltage, the volume of the hydraulic motor along its transmission ratio or the cross-sectional area of the cylinders. Using set values as inputs is sensible via an appropriate scaling or the implementation of lower-level tracking controllers. Moreover, set point velocities can be interpreted by a human operator, which contributes to the transparency and transferability of related controller designs. An indication of typical time constants T_i are provided in [48], where minimum requirements for the crane's response time are specified per DoF, see Tab. 3.3. The order of magnitude is in line with values reported in project meetings with different crane manufacturers. The actuator dynamics are complemented by the payload dynamics, which under the assumption in section 3.3.1 resemble those of a spherical pendulum with moving suspension point. With

Table 3.3: Maximum response times for crane-based offshore operations [48]

	hoisting	luffing, folding	slewing
time	2 s	3 s	4 s

reference to (3.29), the time evolution of the payload's deflection angles is inferred from the EULER-LAGRANGE formalism and characterized by

$$\ddot{\boldsymbol{\varphi}} = -\mathbf{M}_{\boldsymbol{\varphi}}^{-1}(\boldsymbol{\varphi}) \left(\mathbf{M}_{\boldsymbol{\xi}}(\boldsymbol{\zeta}) \ddot{\boldsymbol{\xi}} + \mathbf{M}_{\boldsymbol{q}}(\boldsymbol{\zeta}) \ddot{\boldsymbol{q}} + \boldsymbol{f}_{\boldsymbol{\varphi}}(\boldsymbol{\zeta}, \dot{\boldsymbol{\zeta}}) \right) \tag{3.32}$$

where $\boldsymbol{f}_{\boldsymbol{\varphi}}(\cdot)$ denotes Coriolis, centrifugal, gravitational as well as non-conservative effects and the mass matrix $\mathbf{M} \in \mathbb{R}^{2\times 12}$, which satisfies $\mathcal{T}_4 = \frac{1}{2}\dot{\boldsymbol{\zeta}}^{\mathrm{T}}\mathbf{M}\dot{\boldsymbol{\zeta}}$, is partitioned according to the vector of generalized coordinates $\boldsymbol{\zeta}$, i.e.

$$\mathbf{M}\ddot{\boldsymbol{\zeta}} = \begin{bmatrix} \mathbf{M}_{\boldsymbol{\xi}} & \mathbf{M}_{\boldsymbol{q}} & \mathbf{M}_{\boldsymbol{\varphi}} \end{bmatrix} \begin{pmatrix} \ddot{\boldsymbol{\xi}}^{\mathrm{T}} & \ddot{\boldsymbol{q}}^{\mathrm{T}} & \ddot{\boldsymbol{\varphi}}^{\mathrm{T}} \end{pmatrix}^{\mathrm{T}} \tag{3.33}$$

with the individual matrices $\mathbf{M}_{\boldsymbol{\xi}} \in \mathbb{R}^{2\times 6}$, $\mathbf{M}_{\boldsymbol{q}} \in \mathbb{R}^{2\times 4}$, $\mathbf{M}_{\boldsymbol{\varphi}} \in \mathbb{R}^{2\times 2}$. The second-order differential equations (3.32) depend on the vector of joint variables $\boldsymbol{q}$. However, reformulating the payload dynamics as a function of to the actuator variables $\boldsymbol{\rho}$ is straightforward by virtue of (3.27). Differentiating the joint-actuator mapping $\boldsymbol{q} = \boldsymbol{\phi}_{\boldsymbol{q}}(\boldsymbol{\rho})$ twice with respect to time yields

$$\dot{\boldsymbol{q}} = \mathbf{J}_{\boldsymbol{q}}(\boldsymbol{\rho})\dot{\boldsymbol{\rho}} \tag{3.34a}$$

$$\ddot{\boldsymbol{q}} = \mathbf{J}_{\boldsymbol{q}}(\boldsymbol{\rho})\ddot{\boldsymbol{\rho}} + \mathbf{J}_{\dot{\boldsymbol{q}}}(\boldsymbol{\rho}, \dot{\boldsymbol{\rho}})\dot{\boldsymbol{\rho}} \tag{3.34b}$$

with the two Jacobian matrices $\mathbf{J}_{\boldsymbol{q}}(\boldsymbol{\rho}) = \nabla_{\boldsymbol{\rho}}\boldsymbol{\phi}_{\boldsymbol{q}}(\boldsymbol{\rho}) \in \mathbb{R}^{4\times 4}$ and $\mathbf{J}_{\dot{\boldsymbol{q}}}(\boldsymbol{\rho}, \dot{\boldsymbol{\rho}}) = \nabla_{\boldsymbol{\rho}}\dot{\boldsymbol{q}} = {}^{\mathrm{d}}\!/\!_{\mathrm{d}t}\, \mathbf{J}_{\boldsymbol{q}}(\boldsymbol{\rho}) \in \mathbb{R}^{4\times 4}$, which will also be used in chapter 4. For simplicity, the dependency of q_4 on the sea disturbance $\boldsymbol{\xi}$ has been ignored, since the error is neglectable. Substituting (3.27), (3.34a), (3.34b) for $\boldsymbol{q}$, $\dot{\boldsymbol{q}}$, $\ddot{\boldsymbol{q}}$ in (3.32) then gives

$$\ddot{\boldsymbol{\varphi}} = -\mathbf{M}_{\boldsymbol{\varphi}}^{-1}(\boldsymbol{\varphi}) \left(\tilde{\mathbf{M}}_{\boldsymbol{\xi}}(\tilde{\boldsymbol{\zeta}}) \ddot{\boldsymbol{\xi}} + \mathbf{M}_{\boldsymbol{\rho}}(\tilde{\boldsymbol{\zeta}}) \ddot{\boldsymbol{\rho}} + \tilde{\boldsymbol{f}}_{\boldsymbol{\varphi}}(\tilde{\boldsymbol{\zeta}}, {}^{\mathrm{d}}\!/\!_{\mathrm{d}t}\, \tilde{\boldsymbol{\zeta}}) \right) \tag{3.35}$$

with $\tilde{\boldsymbol{\zeta}} = (\xi_1, \ldots, \xi_6, \rho_1, \ldots, \rho_4, \varphi_1, \varphi_2)^{\mathrm{T}} \in \mathbb{R}^{12}$ and

$$\tilde{\mathbf{M}}_{\boldsymbol{\xi}}(\tilde{\boldsymbol{\zeta}}) = \mathbf{M}_{\boldsymbol{\xi}}(\boldsymbol{\zeta})|_{\boldsymbol{q}=\boldsymbol{\phi}_{\boldsymbol{q}}(\boldsymbol{\rho})} \,, \tag{3.36a}$$

$$\mathbf{M}_{\boldsymbol{\rho}}(\tilde{\boldsymbol{\zeta}}) = \mathbf{M}_{\boldsymbol{q}}(\boldsymbol{\zeta})|_{\boldsymbol{q}=\boldsymbol{\phi}_{\boldsymbol{q}}(\boldsymbol{\rho})} \mathbf{J}_{\boldsymbol{q}}(\boldsymbol{\rho}) \,, \tag{3.36b}$$

$$\tilde{\boldsymbol{f}}_{\boldsymbol{\varphi}}(\tilde{\boldsymbol{\zeta}}, {}^{\mathrm{d}}\!/\!_{\mathrm{d}t}\, \tilde{\boldsymbol{\zeta}}) = \boldsymbol{f}_{\boldsymbol{\varphi}}(\boldsymbol{\zeta}, \dot{\boldsymbol{\zeta}})\Big|_{\boldsymbol{q}=\boldsymbol{\phi}_{\boldsymbol{q}}(\boldsymbol{\rho}),\, \dot{\boldsymbol{q}}=\mathbf{J}_{\boldsymbol{q}}(\boldsymbol{\rho})\dot{\boldsymbol{\rho}}} + \mathbf{J}_{\dot{\boldsymbol{q}}}(\boldsymbol{\rho}, \dot{\boldsymbol{\rho}})\dot{\boldsymbol{\rho}} \,. \tag{3.36c}$$

Eventually, the crane's dynamic model is determined by the actuator dynamics (3.31) as well as the payload dynamics (3.35). In practice, the assumption of rigid links and bodies should be verified depending on the payload. In this context, the system may exhibit

additional dynamics due to the limited stiffness of either crane structure, hydraulic cylinders or hoisting cable. Moreover, double pendulum motions of the payload are precluded in section 3.3.1. Acknowledging the limited model fidelity regarding the crane actuators, the considered dynamics should be checked, e.g. if the crane hydraulics are subject to extensive disturbances. Albeit providing a good trade-off between model complexity and real-time feasibility, future research may therefore expand on the modeled relations.

3.3.4 System Constraints

The knuckle boom crane is constrained by both *kinematic* and *dynamic* constraints. The former stems from the limited stroke or deflection of the crane actuators. An overview is given in Tab. 3.4. Noteworthy, bounds on the hydraulic cylinder strokes ρ_2, ρ_3 can be directly related to box constraints on the joint angles q_2, q_3 as the resp. equalities in (3.27) are monotonic. In contrast, constraints on the winch actuator should be conceived in the joint space. Since up to several thousand meters of cable are usually stored on the main winch's drum, the free cable length q_4 may be considered unbounded from above for the assessed scenarios. However, it is lower bounded by $q_4 > q_{4,\min} = 0$, which further ensures that the mathematical system model is well-defined. Modern KBC offer continuous slewing, i.e. q_1 is unconstrained. Yet, slewing might be limited by operational constraints. The crane's workspace (range of tip position) resulting from the constraints

Table 3.4: Kinematic constraints of the considered KBC

i	$q_{i,\min}$	$q_{i,\max}$	$\rho_{i,\min}$	$\rho_{i,\max}$
1	–	–	–	–
2	0 deg	86 deg	0 m	4.67 m
3	−155 deg	−37 deg	0 m	4.87 m
4	0 m	–	–	–

on q_2, q_3 is depicted in Fig. 3.11, where the mode of operation is indicated for $\boldsymbol{\xi} = \mathbf{0}$. It should be noted that the workspace is rotationally symmetric with respect to q_1, such that considering the projection onto the $r_\mathrm{c}h_\mathrm{c}$-plane is sufficient.

Dynamic constraints account for the limited actuator bandwidth as well as the crane's finite hydraulic capacity. As a simplification, both limitations are mapped to box constraints here, see Tab. 3.5. Due to the modeled first-order dynamics, bounds on the

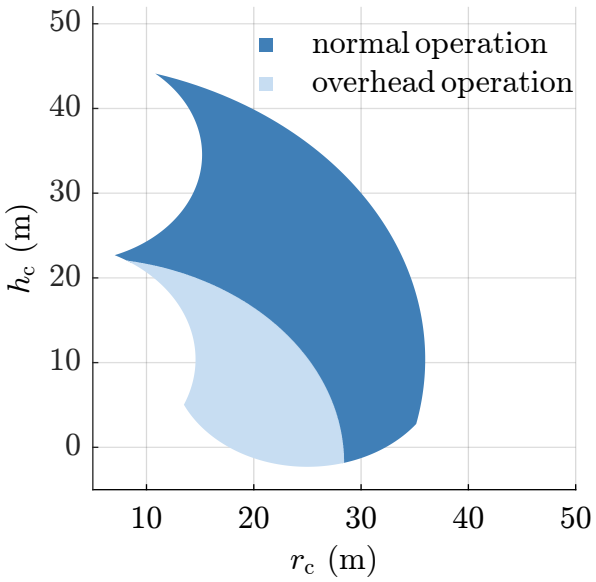

Fig. 3.11: Radial workspace of the KBC – The crane's workspace (tip position $\boldsymbol{p}_{\text{tip}}^{root}$) is rotationally symmetric with respect to its slew axis, thus only its projection onto the $r_c h_c$-plane is shown. Operational mode with respect to the double-sheave assembly at the crane tip is indicated in blue and light blue, respectively.

actuator accelerations can be translated to input constraints, i.e. for $i = 1, \ldots, 4$

$$\delta_{\dot{\rho}}\, \dot{\rho}_{i,\min} \leq \quad \dot{\rho}_i \quad \leq \delta_{\dot{\rho}}\, \dot{\rho}_{i,\max} \tag{3.37a}$$

$$\frac{\dot{\rho}_{i,\min}}{\delta_{\mathrm{T}} T_i} \leq \frac{K_i}{\delta_{\mathrm{T}} T_i} \dot{\rho}_{i,\mathrm{ref}} - \frac{1}{\delta_{\mathrm{T}} T_i} \dot{\rho}_i \leq \frac{\dot{\rho}_{i,\max}}{\delta_{\mathrm{T}} T_i} \tag{3.37b}$$

The additional scaling factor $\delta_{\dot{\rho}} > 0$ will be used in chapter 4 to investigate the impact of velocity limitations on the damping performance of the payload controller(s). Similar, the actuators' time constants T_i will be scaled by $\delta_{\mathrm{T}} > 0$.

Table 3.5: Dynamic constraints of the considered KBC

i	$\dot{\rho}_{i,\min}$	$\dot{\rho}_{i,\max}$	$\ddot{\rho}_{i,\min}$	$\ddot{\rho}_{i,\max}$
1	-0.100 rad/s	0.100 rad/s	-0.025 rad/s^2	0.025 rad/s^2
2	-0.030 m/s	0.030 m/s	-0.010 m/s^2	0.010 m/s^2
3	-0.035 m/s	0.035 m/s	-0.012 m/s^2	0.012 m/s^2
4	-0.690 rad/s	0.690 rad/s	-0.345 rad/s^2	0.345 rad/s^2

In practice, the actuator constraints are interconnected due to the shared HPU. Future research could therefore focus on a constraint mapping that is dependent on the current

operating point. A static approximation may be given by $Q_{\min} \leq \sum_{i=1}^{4} k_{\rho_i}\,\dot{\rho}_i \leq Q_{\max}$ with appropriate flow rate to velocity coefficients k_{ρ_i} and the maximum deliverable flow rate $Q_{\max}$ or $Q_{\min}$, respectively.

3.3.5 Sensors

A decisive step towards increasing the level of automation in crane-based offshore operations is the integration of advanced sensing systems. However, the harsh weather conditions at sea are challenging both in terms of reliable sensor technologies and effective signal processing. While the development of robust sensor packages is outside the scope of this thesis, feedback from e.g. the current payload position or sea state is vital for the discussed control topologies. Hereafter, a minimal sensor setup comprising a vision system and an inertial measurement unit (IMU) is considered. In [S3], tracing the payload's deflection angles $\boldsymbol{\varphi}$ on basis of a marker-based camera system was demonstrated. On the other hand, IMUs or motion reference units (MRU) are the de facto standard for monitoring vessel motions in waves. As pointed out in section 1.3.2, related products are already on the basis of today's AHC systems. See [72] for an introduction to heave filtering.

With regard to Fig. 3.1, a common reference frame $sen : \boldsymbol{O}_{\mathrm{s}} - \boldsymbol{e}_{\mathrm{a}}\boldsymbol{e}_{\mathrm{b}}\boldsymbol{e}_{\mathrm{c}}$ is introduced for both sensors, which reduces the number of required coordinate transformations and thus complexity in the presentation. In practice, the sensor's internal reference frames have to be calibrated to the (arbitrary) *sen*-frame, which may introduce additional model uncertainties in the form of calibration errors. Two sensor models are derived below, that are considered in section 4.2 in order to implement an observer.

The coordinates of *sen*-frame, *ves*-frame and global *ned*-frame are related by

$$\mathbf{T}_{sen}^{ves} = \begin{bmatrix} \mathbf{R}_{sen}^{ves}\left(\boldsymbol{o}_{\mathrm{sen}}^{ves}\right) & \boldsymbol{p}_{O_{\mathrm{sen}}}^{ves} \\ \mathbf{0}_{1\times 3} & 1 \end{bmatrix}, \qquad \mathbf{T}_{sen}^{ned}\left(\boldsymbol{\xi}\right) = \mathbf{T}_{ves}^{ned}\left(\boldsymbol{\xi}\right)\mathbf{T}_{sen}^{ves} \tag{3.38}$$

where a constant offset vector $\boldsymbol{p}_{O_{\mathrm{sen}}}^{ves} = (l_{\mathrm{s}}\; t_{\mathrm{s}}\; s_{\mathrm{s}})^{\mathrm{T}}$ and a fixed rotation angle $\boldsymbol{o}_{\mathrm{sen}}^{ves} = (0\,0\,\psi_{\mathrm{s}})^{\mathrm{T}}$ have been modeled. To process the IMU measurements, linear accelerations as well as angular velocities have to be converted between *ned*- and *sen*-frame. Based on (3.2a) and (3.3), the following relations are established

$$\begin{pmatrix} \boldsymbol{\nu}^{sen} \\ \dot{\boldsymbol{\nu}}^{sen} \end{pmatrix} = \begin{pmatrix} \boldsymbol{v}^{sen} \\ \boldsymbol{\omega}^{sen} \\ \dot{\boldsymbol{v}}^{sen} \\ \dot{\boldsymbol{\omega}}^{sen} \end{pmatrix} = \begin{bmatrix} \mathbf{J}_{\mathrm{sen}}(\mathbf{J}_{\mathrm{ves}}(\boldsymbol{\xi}))^{-1} & \mathbf{0}_{6\times 6} \\ -\mathbf{J}_{\mathrm{sen}}(\mathbf{J}_{\mathrm{ves}}(\boldsymbol{\xi}))^{-1}\dot{\mathbf{J}}_{\mathrm{ves}}(\boldsymbol{\xi},\dot{\boldsymbol{\xi}})(\mathbf{J}_{\mathrm{ves}}(\boldsymbol{\xi}))^{-1} & \mathbf{J}_{\mathrm{sen}}(\mathbf{J}_{\mathrm{ves}}(\boldsymbol{\xi}))^{-1} \end{bmatrix} \begin{pmatrix} \dot{\boldsymbol{\xi}} \\ \ddot{\boldsymbol{\xi}} \end{pmatrix} \tag{3.39}$$

where $\dot{\mathbf{J}}_{\text{ves}}(\boldsymbol{\xi}, \dot{\boldsymbol{\xi}}) = {}^{\mathrm{d}}/_{\mathrm{dt}}\, \mathbf{J}_{\text{ves}}(\boldsymbol{\xi})$ and the fact has been used that the Jacobian

$$\mathbf{J}_{\text{sen}} = \begin{bmatrix} \mathbf{R}_{ves}^{sen}\left(\boldsymbol{o}_{\text{sen}}^{ves}\right) & -\mathbf{R}_{ves}^{sen}\left(\boldsymbol{o}_{\text{sen}}^{ves}\right)\mathbf{S}(\boldsymbol{p}_{O_{\text{sen}}}^{ves}) \\ \mathbf{0}_{3\times 3} & \mathbf{R}_{ves}^{sen}\left(\boldsymbol{o}_{\text{sen}}^{ves}\right) \end{bmatrix} \text{ with } \mathbf{S}(\boldsymbol{p}_{O_{\text{sen}}}^{ves}) = \begin{bmatrix} 0 & -s_{\text{s}} & t_{\text{s}} \\ s_{\text{s}} & 0 & -l_{\text{s}} \\ -t_{\text{s}} & l_{\text{s}} & 0 \end{bmatrix} \tag{3.40}$$

is time-invariant. Moreover, recall that the rotation matrix $\mathbf{R}_{sen}^{ves}$ satisfies $(\mathbf{R}_{sen}^{ves})^{-1} = (\mathbf{R}_{sen}^{ves})^{\mathrm{T}} = \mathbf{R}_{ves}^{sen}$, cf. section 2.1. Apart from the kinematic relations (3.38) and (3.39), each sensor is characterized by its noise behavior.

The vision system yields measurements $\boldsymbol{p}_{\text{load,m}}^{sen}(t_k)$ of the payload position $\boldsymbol{p}_{\text{load}}^{ned}(t)$ at discrete time instances $t_k = t_0 + kT_{\text{s}}$, which are corrupted by additive white noise $\boldsymbol{v}_{\text{cam}}(t_k)$. The noise sequence is assumed uncorrelated and Gaussian, i.e. $\boldsymbol{\mathcal{V}}_{\text{cam},k} \sim \mathcal{GP}(\mathbf{0}, \mathbf{Q}_{\boldsymbol{\mathcal{V}}_{\text{cam}}}\delta_{k-j})$ with zero mean and covariance matrix $\mathbf{Q}_{\boldsymbol{\mathcal{V}}_{\text{cam}}} = \sigma_{\text{cam}}^2\mathbf{I}_{3\times 3}$. Using (2.6c), (3.18) and (3.38), the measurement equation is given by

$$\boldsymbol{p}_{\text{load,m}}^{sen}(t_k) = \left(\mathbf{R}_{sen}^{ned}\left(\boldsymbol{\xi}_k\right)\right)^{\mathrm{T}}\boldsymbol{p}_{\text{load}}^{ned}\left(\boldsymbol{\xi}_k, \boldsymbol{q}_k, \boldsymbol{\varphi}_k\right) - \left(\mathbf{R}_{sen}^{ned}\left(\boldsymbol{\xi}_k\right)\right)^{\mathrm{T}}\boldsymbol{p}_{O_{\text{sen}}}^{ned}\left(\boldsymbol{\xi}_k\right) + \boldsymbol{v}_{\text{cam}}(t_k) \tag{3.41}$$

which can alternatively be reformulated with respect to the actuator space $\mathcal{P}$ by applying (3.27). Equation (3.41) presents a scenario in which the payload position is observed locally from a point on the crane vessel. As a result, the measurement equation is dependent on the vessel deflection $\boldsymbol{\xi}$. Since errors in the vessel position or attitude directly translate to offsets in the computed payload position, positioning in an earth-fixed reference frame becomes challenging. Yet in some instances, e.g. when handling payloads in the deck area, it may be sensible to relate the position of the payload to a local, co-moving frame. In such case, (3.41) is rendered invariant to $\boldsymbol{\xi}$. Motion-compensated cameras present an interesting alternative to eliminate the influence of the vessel's roll and pitching motions. In context of this thesis, a sensor fusion with the measurements of an IMU is assessed. Here the question is to be answered whether the underlying system model can improve the mutual estimation accuracy of load position and vessel pose.

Modern MRU provide accelerometer and angular rate gyro signals of high accuracy. For predefined motion periods and disturbance magnitudes they also yield estimates of the vessel's current heave position and orientation in roll resp. pitch at data rates around 200 Hz [105]. Building on this, measurements from an IMU are utilized for reconstructing and predicting the vessel's motions. The modeling approach is taken from [64]. An IMU's accelerometers and gyros are subject to both deterministic and stochastic disturbances. While deterministic disturbances (turn-on bias, axis alignment errors, ...) may be dealt with by averaging and calibrating the sensor signals, the stochastic disturbances are usually not restricted to white noise processes but are colored. A more detailed model therefore explicitly maps disturbances stemming from angular or velocity random walk (index N), bias instability (index B), rate or acceleration random walk (index K). The

authors in [64] propose the following continuous time noise model

$$\dot{\boldsymbol{x}}_{\mathrm{IMU},i}(t) = \begin{pmatrix} \dot{x}_{\mathrm{B}_i}(t) \\ \dot{x}_{\mathrm{K}_i}(t) \end{pmatrix} = \begin{bmatrix} -\frac{1}{T_{\mathrm{B}_i}} & 0 \\ 0 & 0 \end{bmatrix} \begin{pmatrix} x_{\mathrm{B}_i}(t) \\ x_{\mathrm{K}_i}(t) \end{pmatrix} + \begin{pmatrix} \varepsilon_{\mathrm{B}_i}(t) \\ \varepsilon_{\mathrm{K}_i}(t) \end{pmatrix} \tag{3.42a}$$

$$\upsilon_{\mathrm{IMU},i}(t) = \begin{bmatrix} 1 & 1 \end{bmatrix} \boldsymbol{x}_{\mathrm{IMU},i}(t) \quad + \quad \upsilon_{\mathrm{N}_i}(t) \tag{3.42b}$$

with the correlation time T_{B_i} and the white, Gaussian stochastic processes $\{\mathcal{E}_{\mathrm{B}_i}(t)\}_{t\in[0,\infty)}$, $\{\mathcal{E}_{\mathrm{K}_i}(t)\}_{t\in[0,\infty)}$, $\{\mathcal{V}_{\mathrm{N}_i}(t)\}_{t\in[0,\infty)}$ per sensor channel $i = 1, \ldots, 6$. In order to implement the model (3.42) in an observer, it can be transformed to the discrete time domain using the techniques described in section 2.3. In this context, random sequences are defined

$$\begin{aligned} &\mathcal{E}_{\mathrm{B}_i,k} \sim \mathcal{GP}\left(0, \frac{1}{2} S_{\mathrm{B}_i} T_{\mathrm{B}_i} \left(1 - \exp(-2T_\mathrm{s}/T_{\mathrm{B}_i})\right)\right) \text{ with } S_{\mathrm{B}_i} = {}^{2B_i^2 \ln(2)}/_{\pi(0.4365)^2 T_{\mathrm{B}_i}} \\ &\mathcal{E}_{\mathrm{K}_i,k} \sim \mathcal{GP}(0, K_i^2 T_\mathrm{s}) \\ &\mathcal{V}_{\mathrm{N}_i,k} \sim \mathcal{GP}(0, N_i^2/T_\mathrm{s}) \end{aligned}$$

that in conjunction with the discrete state space model yield the same first- and second-order statistics as (3.42). The parameters N_i, B_i, K_i and T_i are characteristic for any particular IMU and can be derived from the so-called Allan-variance, see [64]. Combining (3.39) and the noise models, then determines the IMU's measurement equations

$$\begin{pmatrix} \boldsymbol{\omega}_\mathrm{m}^{sen}(t_k) \\ \dot{\boldsymbol{v}}_\mathrm{m}^{sen}(t_k) \end{pmatrix} = \begin{pmatrix} \boldsymbol{\omega}^{sen}(\boldsymbol{\xi}_k, \dot{\boldsymbol{\xi}}_k) \\ \dot{\boldsymbol{v}}^{sen}(\boldsymbol{\xi}_k, \dot{\boldsymbol{\xi}}_k, \ddot{\boldsymbol{\xi}}_k) \end{pmatrix} + \begin{pmatrix} \mathbf{0}_{3\times1} \\ [\mathbf{I}_{3\times3}\, \mathbf{0}_{3\times3}] \mathbf{J}_{\mathrm{sen}}(\mathbf{J}_{\mathrm{ves}}(\boldsymbol{\xi}))^{-1} \boldsymbol{g} \end{pmatrix} + \begin{pmatrix} \upsilon_{\mathrm{IMU},1}(t_k) \\ \vdots \\ \upsilon_{\mathrm{IMU},6}(t_k) \end{pmatrix} \tag{3.43}$$

where the vector of gravitational acceleration $\boldsymbol{g}$ is transformed to the *sen*-frame and the deterministic errors have been neglected for simplicity. During observer design it will be further assumed, that the crane joints $q_1, \ldots, q_3$ can be measured according to

$$q_{i,\mathrm{m}}(t_k) = q_{i,k} + \boldsymbol{\upsilon}_{q_i}(t_k) \quad \text{with} \quad \mathcal{V}_{q_i,k} \sim \mathcal{GP}(0, \sigma_{q_i}^2),\ i = 1, \ldots, 3 \tag{3.44}$$

and that the set point velocities $\dot{\boldsymbol{\rho}}_{\mathrm{ref}}$ are directly available.

3.4 Control-Oriented Model

The union of vessel, crane and payload constitutes a dynamic multi-body system with multiple inputs and outputs. Following section 3.2, section 3.3.2 and section 3.3.3 the system is characterized by nonlinear both kinematics and dynamics. In context of model-based control model fidelity and real-time feasibility have to be balanced, which holds especially true in model predictive control since the system model is iterated in order to predict the system trajectories. The model therefore directly correlates with the

resulting complexity of the underlying optimization problem, cf. section 2.5. Up to this point, the different system components were modeled. However, in order to leverage the modeling in a predictive control topology, the derived relations must be compiled into a state space representation (2.32), which is outlined hereafter.

As the state space model is intended for payload control, the primary focus is on the crane-payload subsystem. Accordingly, the wave-induced vessel motions $\boldsymbol{\xi}$ are modeled as an exogenous disturbance. Doing so further renders the controller independent of the particular vessel dynamics (3.2), which is favorable with respect to the controller's complexity and transferability. Yet, varying vessel types may exhibit different dynamics, which should be assessed during controller validation. In terms of a state space representation define the (reduced) disturbance model

$$\dot{\boldsymbol{x}}_{\mathrm{ves}}(t) = \begin{bmatrix} \mathbf{0}_{3\times3} & \mathbf{I}_{3\times3} \\ \mathbf{0}_{3\times3} & \mathbf{0}_{3\times3} \end{bmatrix} \boldsymbol{x}_{\mathrm{ves}}(t) + \begin{pmatrix} \mathbf{0}_{3\times3} \\ \mathbf{I}_{3\times3} \end{pmatrix} \boldsymbol{d}(t) \tag{3.45}$$

with vessel-related states $\boldsymbol{x}_{\mathrm{ves}} = (\xi_3\, \xi_4\, \xi_5\, \dot{\xi}_3\, \dot{\xi}_4\, \dot{\xi}_5)^{\mathrm{T}} \in \mathbb{R}^6$ and inputs $\boldsymbol{d} = (\ddot{\xi}_3\, \ddot{\xi}_4\, \ddot{\xi}_5)^{\mathrm{T}} \in \mathbb{R}^3$. Here, only the vessel's heave, rolling and pitching motions are considered, which are essential to payload control, cf. section 3.2. Following the reasoning in section 3.3.1, the crane's hydraulics are approximated by linear surrogate models. The high-level manipulated variables therefore coincide with the actuator's velocity set points, i.e.

$$\boldsymbol{u} = \begin{pmatrix} \dot{\rho}_{1,\mathrm{ref}} & \dot{\rho}_{2,\mathrm{ref}} & \dot{\rho}_{3,\mathrm{ref}} & \dot{\rho}_{4,\mathrm{ref}} \end{pmatrix}^{\mathrm{T}} \in \mathbb{R}^4 \,. \tag{3.46}$$

Define further the vector of crane-related states

$$\boldsymbol{x}_{\mathrm{kbc}} = \begin{pmatrix} \rho_1 & \cdots & \rho_4 & \varphi_1 & \varphi_2 & \dot{\rho}_1 & \cdots & \dot{\rho}_4 & \dot{\varphi}_1 & \dot{\varphi}_2 \end{pmatrix}^{\mathrm{T}} \in \mathbb{R}^{12} \,. \tag{3.47}$$

The state evolution is then determined by (3.31) and (3.35), respectively. Using matrix notation and transforming into a system of first order differential equations yields

$$\dot{\boldsymbol{x}}_{\mathrm{kbc}}(t) = \begin{pmatrix} \begin{bmatrix} \mathbf{0}_{6\times6} & \mathbf{I}_{6\times6} \end{bmatrix} \boldsymbol{x}_{\mathrm{kbc}}(t) \\ \begin{bmatrix} \mathbf{0}_{4\times6} & \mathbf{A}_{\boldsymbol{\rho}} & \mathbf{0}_{4\times2} \end{bmatrix} \boldsymbol{x}_{\mathrm{kbc}}(t) + \mathbf{B}_{\boldsymbol{\rho}} \boldsymbol{u}(t) \\ -\mathbf{M}_{\boldsymbol{\varphi}}^{-1} \left(\mathbf{M}_{\boldsymbol{\rho}} [\mathbf{0}_{4\times6}\, \mathbf{A}_{\boldsymbol{\rho}}\, \mathbf{0}_{4\times2}] \boldsymbol{x}_{\mathrm{kbc}}(t) + \tilde{\boldsymbol{f}}_{\boldsymbol{\varphi}}(\boldsymbol{x}_{\mathrm{ves}}, \boldsymbol{x}_{\mathrm{kbc}}) + \mathbf{M}_{\boldsymbol{\rho}} \mathbf{B}_{\boldsymbol{\rho}} \boldsymbol{u}(t) + \tilde{\mathbf{M}}_{\boldsymbol{\xi}} \boldsymbol{d}(t) \right) \end{pmatrix} \tag{3.48}$$

where the dependency of the mass matrices on $x_{\mathrm{ves},1}, \ldots, x_{\mathrm{ves},3}$ and $x_{\mathrm{kbc},1}, \ldots, x_{\mathrm{kbc},6}$ have been dropped to increase readability. Furthermore, two matrices

$$\mathbf{A}_{\boldsymbol{\rho}} = \begin{bmatrix} -\frac{1}{T_1} & 0 & 0 & 0 \\ 0 & -\frac{1}{T_2} & 0 & 0 \\ 0 & 0 & -\frac{1}{T_3} & 0 \\ 0 & 0 & 0 & -\frac{1}{T_4} \end{bmatrix}, \qquad \mathbf{B}_{\boldsymbol{\rho}} = \begin{bmatrix} \frac{K_1}{T_1} & 0 & 0 & 0 \\ 0 & \frac{K_2}{T_2} & 0 & 0 \\ 0 & 0 & \frac{K_3}{T_3} & 0 \\ 0 & 0 & 0 & \frac{K_4}{T_4} \end{bmatrix}$$

are introduced yielding a more compact presentation. Since (3.48) is also a function of $\boldsymbol{x}_{\text{ves}}$ as well as $\boldsymbol{d}$, the state evolution is coupled to the vessel motions, which is to be expected. Both state vectors can be concatenated to derive a single state space model

$$\dot{\boldsymbol{x}}(t) = \boldsymbol{f}(\boldsymbol{x}, \boldsymbol{u}, \boldsymbol{d}) = \begin{pmatrix} \boldsymbol{f}_{\text{ves}}(\boldsymbol{x}_{\text{ves}}, \boldsymbol{d}) \\ \boldsymbol{f}_{\text{kbc}}(\boldsymbol{x}_{\text{ves}}, \boldsymbol{x}_{\text{kbc}}, \boldsymbol{u}, \boldsymbol{d}) \end{pmatrix} \text{ with } \boldsymbol{x} = \begin{pmatrix} \boldsymbol{x}_{\text{ves}} \\ \boldsymbol{x}_{\text{kbc}} \end{pmatrix} \tag{3.49}$$

and the mappings $\boldsymbol{f}_{\text{ves}}(\cdot)$, $\boldsymbol{f}_{\text{kbc}}(\cdot)$ defined by (3.45) and (3.48), respectively. The varying list of arguments reveals the assumption of a reactionless crane operation with regard to the vessel. If the state space model is used in a controller, the following simplifications will be applied

$$l_{\text{c}}(\boldsymbol{q}) \approx l_{\text{c}}(\boldsymbol{q}(t - T_{\text{s}})) = \text{const.} \tag{3.50a}$$

$$\vartheta_{\text{tip}}(\boldsymbol{\xi}, \boldsymbol{q}) \approx \vartheta_{\text{tip}}(\boldsymbol{\xi}(t - T_{\text{s}}), \boldsymbol{q}(t - T_{\text{s}})) = \text{const.} \tag{3.50b}$$

which greatly reduce model complexity whilst only introducing minor errors. Here, the fact has been used that both suspension point and stored cable length vary slowly when compared to the controller's execution rate. To conclude modeling, controlled outputs $\boldsymbol{y}$ and measured outputs $\boldsymbol{y}_{\text{m}}$ are defined according to

$$\boldsymbol{y} = \begin{pmatrix} n_{\text{load}} & e_{\text{load}} & d_{\text{load}} & z_{\text{tip}} \end{pmatrix}^{\text{T}} \in \mathbb{R}^4 \,, \tag{3.51a}$$

$$\boldsymbol{y}_{\text{m}} = \begin{pmatrix} (\boldsymbol{p}^{sen}_{\text{load,m}})^{\text{T}} & (\boldsymbol{\omega}^{sen}_{\text{m}})^{\text{T}} & (\dot{\boldsymbol{v}}^{sen}_{\text{m}})^{\text{T}} & q_{1,\text{m}} & \cdots & q_{3,\text{m}} \end{pmatrix}^{\text{T}} \in \mathbb{R}^{12} \,. \tag{3.51b}$$

The output equations are given in (3.18), (3.12) resp. (3.41), (3.43), (3.44). Using the global payload position $\boldsymbol{p}^{ned}_{\text{load}}$ as controlled output yields a load-centric approach to payload handling, see also chapter 4. As will be argued in section 3.5, the crane system is overdetermined (non-square) with respect to its four actuators and the three translational DoF of the payload. In order to exclude ambiguities during control, a fourth output equal to the vertical tip position z_{tip} is added, which will be motivated below.

3.5 Differential Flatness of the Crane System

From a control perspective, finding a flat output $\boldsymbol{\gamma}$ regarding which the system equations can be inverted is advantageous as it facilitates the design of e.g. reference trajectories or open-loop controllers, cf. section 2.4. Flatness is a system characteristic that for gantry-type cranes [103], [185] or onshore boom cranes [11], [128] was already established in literature. The considered offshore KBC differs in its kinematic structure, the number of actuated DoF as well as in the persistent base excitation that is caused by the wave disturbance. A flatness-based analysis of the KBC's dynamics was presented in [S2], which is reproduced hereafter.

As pointed out in section 2.4, the dimension of any flat output $\boldsymbol{\gamma}$ will be equal to the input dimension $\dim(\boldsymbol{\gamma}) = \dim(\boldsymbol{u})$. However, the considered knuckle boom crane is not square with respect to its four actuated DoF (inputs) and the payload's three-dimensional Cartesian position (controlled outputs). Any flat output candidate therefore must comprise a fourth output supplementing the payload position $\boldsymbol{p}_{\text{load}}^{ned}$. Ambiguities in the crane-payload model stem from the fact, that different crane configurations $q_1, \ldots, q_3$ may yield different crane tip heights h_c but identical crane radii r_c, cf. Fig. 3.11. Therefore, the same payload position is obtained when the free cable length q_4 is adjusted accordingly. To resolve the ambiguity, define an output candidate according to

$$\boldsymbol{\gamma} = \begin{pmatrix} \gamma_1 & \cdots & \gamma_4 \end{pmatrix}^\text{T} = \begin{pmatrix} \boldsymbol{p}_{\text{load}}^{ned} \\ z_{\text{tip}} \end{pmatrix} \in \mathbb{R}^4 \tag{3.52}$$

with $z_{\text{tip}} = (0\,0\,1)\,\boldsymbol{p}_{\text{tip}}^{root}$. Clearly, fixing the crane tip height determines the free cable length given a payload position, thus allowing for a one-to-one mapping between $\boldsymbol{q}$ and $\boldsymbol{\gamma}$. To prove that (3.52) is indeed a flat output to system (3.48), all states $\boldsymbol{x}_{\text{kbc}}$ and inputs $\boldsymbol{u}$ should be parameterizable by means of $\boldsymbol{\gamma}$ and its time-derivatives $\boldsymbol{\gamma}^{(i)}$ up to order $\boldsymbol{r}_\gamma$.[9] The latter denotes the system's (vectorial) relative degree, which for the KBC equates to $\boldsymbol{r}_\gamma = (4\,4\,2\,2)^\text{T}$ such that $\sum_{i=1}^{4} r_{\gamma_i} = n = 12$. Following section 2.4, the flat mappings $\boldsymbol{x}_{\text{kbc}} = \boldsymbol{\psi}_{\boldsymbol{x}_{\text{kbc}}}\left(\boldsymbol{\gamma}, \dot{\boldsymbol{\gamma}}, \ldots, \boldsymbol{\gamma}^{(\boldsymbol{\delta})}\right)$ and $\boldsymbol{u} = \boldsymbol{\psi}_{\boldsymbol{u}}\left(\boldsymbol{\gamma}, \dot{\boldsymbol{\gamma}}, \ldots, \boldsymbol{\gamma}^{(\boldsymbol{\delta}+1)}\right)$ have to be established, for which purpose all forces acting on the payload are balanced:

$$m_{\text{load}}\,\ddot{\boldsymbol{p}}_{\text{load}}^{ned} = m_{\text{load}} \begin{pmatrix} 0 \\ 0 \\ g \end{pmatrix} + |\boldsymbol{F}_\text{l}| \begin{pmatrix} -\sin(\varphi_2) \\ \sin(\varphi_1)\cos(\varphi_2) \\ -\cos(\varphi_1)\cos(\varphi_2) \end{pmatrix} \tag{3.53}$$

with the cable force $\boldsymbol{F}_\text{l}$ that is always oriented along the cable in direction of the suspension point (crane tip) [103][10]. In addition, the payload is accelerated by gravitation g. Comparing (3.53) to (3.18) and using matrix notation yields

$$\underbrace{\begin{bmatrix} \ddot{\gamma}_3 - g & 0 & -\ddot{\gamma}_1 \\ 0 & \ddot{\gamma}_3 - g & -\ddot{\gamma}_2 \end{bmatrix}}_{=:\,\boldsymbol{\Sigma}(\ddot{\boldsymbol{\gamma}})} \boldsymbol{p}_{\text{tip}}^{ned} = \underbrace{\begin{pmatrix} \gamma_1\,(\ddot{\gamma}_3 - g) - \ddot{\gamma}_1\gamma_3 \\ \gamma_2\,(\ddot{\gamma}_3 - g) - \ddot{\gamma}_2\gamma_3 \end{pmatrix}}_{=:\,\boldsymbol{\varsigma}(\boldsymbol{\gamma},\ddot{\boldsymbol{\gamma}})} \tag{3.54}$$

where the unknowns $|\boldsymbol{F}_l|$, m_{load}, q_4 are eliminated. Since (3.54) is overdetermined it can not be directly solved for the tip position $\boldsymbol{p}_{\text{tip}}^{ned}$. Yet, the number of free variables can be reduced by recalling that the crane's tip height is part of the flat output, i.e. $\gamma_4 = z_{\text{tip}}$. The tip position is then retrieved by transforming (3.54) to the crane's *root*-frame via (3.10) and appending z_4:

$$\boldsymbol{p}_{\text{tip}}^{root} = \tilde{\boldsymbol{\Sigma}}\left(\ddot{\boldsymbol{\gamma}}, \boldsymbol{\xi}\right)^{-1} \tilde{\boldsymbol{\varsigma}}\left(\boldsymbol{\gamma}, \ddot{\boldsymbol{\gamma}}, \boldsymbol{\xi}\right) \tag{3.55}$$

[9] The analysis is restricted to the crane-payload subsystem $(\boldsymbol{x}_{\text{kbc}}, \boldsymbol{u})$ as trying to invert the exogenous disturbance model $(\boldsymbol{x}_{\text{ves}}, \boldsymbol{d})$ is implausible in the first place. Neither is $\boldsymbol{d}$ manipulable nor can the vessel pose be controlled by the crane actuators.

[10] In [103], the authors analyze a disturbance-free overhead crane with three DoF.

with

$$\tilde{\boldsymbol{\Sigma}}\left(\ddot{\boldsymbol{\gamma}},\boldsymbol{\xi}\right)=\begin{bmatrix}\boldsymbol{\Sigma}\left(\ddot{\boldsymbol{\gamma}}\right)\mathbf{R}_{root}^{ned}\left(\boldsymbol{\xi}\right)\\ \begin{pmatrix}0&0&1\end{pmatrix}\end{bmatrix},\qquad \tilde{\boldsymbol{\varsigma}}\left(\boldsymbol{\gamma},\ddot{\boldsymbol{\gamma}},\boldsymbol{\xi}\right)=\begin{pmatrix}\boldsymbol{\varsigma}\left(\boldsymbol{\gamma},\ddot{\boldsymbol{\gamma}}\right)-\boldsymbol{\Sigma}\left(\ddot{\boldsymbol{\gamma}}\right)\boldsymbol{p}_{O_{\text{root}}}^{ned}\left(\boldsymbol{\xi}\right)\\ \gamma_4\end{pmatrix}.$$

Equation (3.55) is solved for ρ_1, ρ_2, ρ_3 by applying the crane's inverse kinematics $\boldsymbol{\phi}_{\text{ik}}(\cdot)$ and mapping the result to the actuator space in terms of (3.26). The actuator variables are thus established as a function of the flat output, its time-derivatives and the vessel pose

$$\begin{pmatrix}\rho_1&\rho_2&\rho_3\end{pmatrix}^{\mathrm{T}}=\boldsymbol{\psi}_1\left(\boldsymbol{\gamma},\ddot{\boldsymbol{\gamma}},\boldsymbol{\xi}\right)=\left(\boldsymbol{\phi}_{\boldsymbol{\rho}}\circ\boldsymbol{\phi}_{\text{ik}}\right)\left(\tilde{\boldsymbol{\Sigma}}\left(\ddot{\boldsymbol{\gamma}},\boldsymbol{\xi}\right)^{-1}\tilde{\boldsymbol{\varsigma}}\left(\boldsymbol{\gamma},\ddot{\boldsymbol{\gamma}},\boldsymbol{\xi}\right)\right)\tag{3.56}$$

A similar approach is chosen for η_4. By generalizing Pythagoras's theorem to three dimensions, the free cable length q_4 is obtained as

$$q_4^2=\left(n_{\text{load}}-n_{\text{tip}}\right)^2+\left(e_{\text{load}}-e_{\text{tip}}\right)^2+\left(d_{\text{load}}-d_{\text{tip}}\right)^2.$$

Reformulating and using (3.54) yields

$$q_4=\left(\gamma_3-d_{\text{tip}}\right)\sqrt{1+\left(\ddot{\gamma}_1^2+\ddot{\gamma}_2^2\right)/\left(\ddot{\gamma}_3-g\right)^2}\tag{3.57}$$

where d_{tip} can be substituted by an expression depending only on the flat output (and the vessel pose), see (3.56), (3.12), and (3.10). Equating (3.57) and (3.26) allows solving for ρ_4, which further determines the map $\rho_4=\psi_2\left(\boldsymbol{\gamma},\ddot{\boldsymbol{\gamma}},\boldsymbol{\xi}\right)$. Aggregating (3.56) and $\psi_2(\cdot)$ gives

$$\boldsymbol{\rho}=\boldsymbol{\psi}_{\boldsymbol{\rho}}\left(\boldsymbol{\gamma},\ddot{\boldsymbol{\gamma}},\boldsymbol{\xi}\right)=\begin{pmatrix}\boldsymbol{\psi}_1\left(\boldsymbol{\gamma},\ddot{\boldsymbol{\gamma}},\boldsymbol{\xi}\right)\\ \psi_2\left(\boldsymbol{\gamma},\ddot{\boldsymbol{\gamma}},\boldsymbol{\xi}\right)\end{pmatrix}.\tag{3.58}$$

The payload's deflection angles are obtained from comparing (3.18) and (3.53), yielding

$$\boldsymbol{\varphi}=\boldsymbol{\psi}_3\left(\boldsymbol{\gamma},\ddot{\boldsymbol{\gamma}}\right)=\begin{pmatrix}\operatorname{atan}\left(\ddot{\gamma}_2/-\left(\ddot{\gamma}_3-g\right)\right)\\ -\operatorname{atan}\left(\ddot{\gamma}_1\Big/\sqrt{\left(\ddot{\gamma}_3-g\right)^2+\ddot{\gamma}_2^2}\right)\end{pmatrix}.\tag{3.59}$$

Differentiating (3.58) and (3.59) with respect to time yields expressions for $\dot{\boldsymbol{\rho}}$ and $\dot{\boldsymbol{\varphi}}$, respectively. The relations may then be concatenated to derive a flat mapping of the entire state $\boldsymbol{x}_{\text{kbc}}$, i.e.

$$\boldsymbol{x}_{\text{kbc}}=\boldsymbol{\psi}_{\boldsymbol{x}_{\text{kbc}}}\left(\boldsymbol{\gamma},\dot{\boldsymbol{\gamma}},\ddot{\boldsymbol{\gamma}},\boldsymbol{\gamma}^{(3)},\boldsymbol{\xi},\dot{\boldsymbol{\xi}}\right).\tag{3.60}$$

Differentiating once more allows eliminating both $\dot{\boldsymbol{\rho}}$ and $\ddot{\boldsymbol{\rho}}$ in (3.31), which when solved for $\dot{\boldsymbol{\rho}}_{\text{ref}}$ determines the flat input parameterization

$$\boldsymbol{u}=\boldsymbol{\psi}_{\boldsymbol{u}}\left(\boldsymbol{\gamma},\dot{\boldsymbol{\gamma}},\ddot{\boldsymbol{\gamma}},\boldsymbol{\gamma}^{(3)},\boldsymbol{\gamma}^{(4)},\boldsymbol{\xi},\dot{\boldsymbol{\xi}},\ddot{\boldsymbol{\xi}}\right).\tag{3.61}$$

Equations (3.60) and (3.61) provide the required flat mappings, which suggests that $\boldsymbol{\gamma}$ is indeed a flat output to system (3.48). The relations further admit an interpretation

of the wave-induced vessel motions, which present an additional source term. Strictly speaking, flatness only applies to scenarios with $\dot{\boldsymbol{\xi}} = \ddot{\boldsymbol{\xi}} = \mathbf{0}$. Still, even in the disturbed case, effective control laws can be designed on the basis of (3.61), cf. chapter 4 and [S1], [S2]. Here, the derived mappings offer a systematic way to incorporate predictions of the vessel motions by means of a feed-forward compensation.

3.6 Simulation Environment

All algorithms of chapter 4 are developed and implemented in *Matlab* (The MathWorks Inc., Natick, Massachusetts, USA). Over the course of the thesis project, an accompanying simulation environment has been set up in the subpackage *Simulink*, which integrates the presented models of vessel (section 3.2), KBC and payload (section 3.3.2 - section 3.3.5). Wave excitations are computed with the help of the *Marine Systems Simulator* toolbox published by [67], that allows to draw random sea state realizations from different distributions $\tilde{S}(\omega)$ and calculate the vessel response, cf. [68]. The kinematic relations of section 3.3.2 are implemented in Matlab's *Symbolic Toolbox* and compiled to m-functions, which may be called from the simulation. In this context, the associated Jacobians are also calculated analytically and code generated thereafter. Since the crane kinematics include various trigonometric functions, its dynamics become extensive in code size when established symbolically. Within the scope of this thesis, a tool for algorithmic differentiation *CasADi* [8] is therefore applied, which yields more efficient codes for Jacobians and Hessian matrices. The tool is also used to derive the (S)QP-components required for e.g. model predictive control, see also section 2.7. The interface between *CasADi* framework and *Simulink* are s-functions, for which the *CasADi* expressions are first (automatically) compiled to C code. Noteworthy, the latter does also provide the basis for generating machine-oriented real time code, cf. section 3.7. Within the simulation all signals are organized in bus objectives, such that the simulated trajectories of different variables are readily available. Last, the *Simulink* package offers so-called *model references*, that enable code-reuse and facilitate comparing different implementations e.g. of a MPC. If not stated otherwise, a RUNGE-KUTTA solver of fourth order is used to simulate the system at a fixed rate of $f_\mathrm{s} = 1\,\mathrm{kHz}$.

The simulation environment allows analyzing the effects of different

- wave excitations (spectrum $\tilde{S}(\omega)$, significant wave height H_s, peak frequency ω_p),
- initial crane configurations $\boldsymbol{q}(t_0)$ and target positions $\boldsymbol{r}_\mathrm{load}^{ned}$,
- as well as control topologies (target selector, MPC).

The wave's incidence direction, ocean currents and gust are omitted from the investigations. If not stated otherwise, payload stabilization will be studied at heights of 6 m above

sea level and varying crane radii, cf. recommendations in [48]. Below, a frequency sweep with regard to the wave peak frequency $\omega_\mathrm{p} \in [0.41, 1.03]\,\mathrm{rad/s}$ at $H_\mathrm{s} = 2\,\mathrm{m}$ is presented in Fig. 3.12. The maximum payload sway angle $\varphi_{\mathrm{c,max}} = \max(\varphi_\mathrm{c}(t))$ during unforced operation ($\boldsymbol{u} = \boldsymbol{0}$) allows for a BODE-like interpretation of the wave-induced payload oscillations. Note that the vessel itself has a frequency response, which is described by its RAOs, see section 3.2. Furthermore, the payload oscillations are reduced to a single characteristic value. Hence, the analogy to a magnitude response is only qualitative.

Maximum payload oscillations are obtained around $\omega_\mathrm{p} = 0.75\,\mathrm{rad/s}$, which does not coincide with the natural frequency $\omega_0 = (g/q_4)^{0.5} = 0.79\,\mathrm{rad/s}$ of the payload pendulum. Of course, the wave disturbance is not a single harmonic oscillation but features a superposition of frequencies in three DoF. Also, the vessel acts as a filter, which is one reason why the frequency of maximum payload resonance is shifted. Yet, the difference is minor such that increasing payload oscillations should be expected, when the wave's peak frequency approaches the natural frequency of the suspended payload, i.e. $\omega_\mathrm{p} \to \omega_0$.

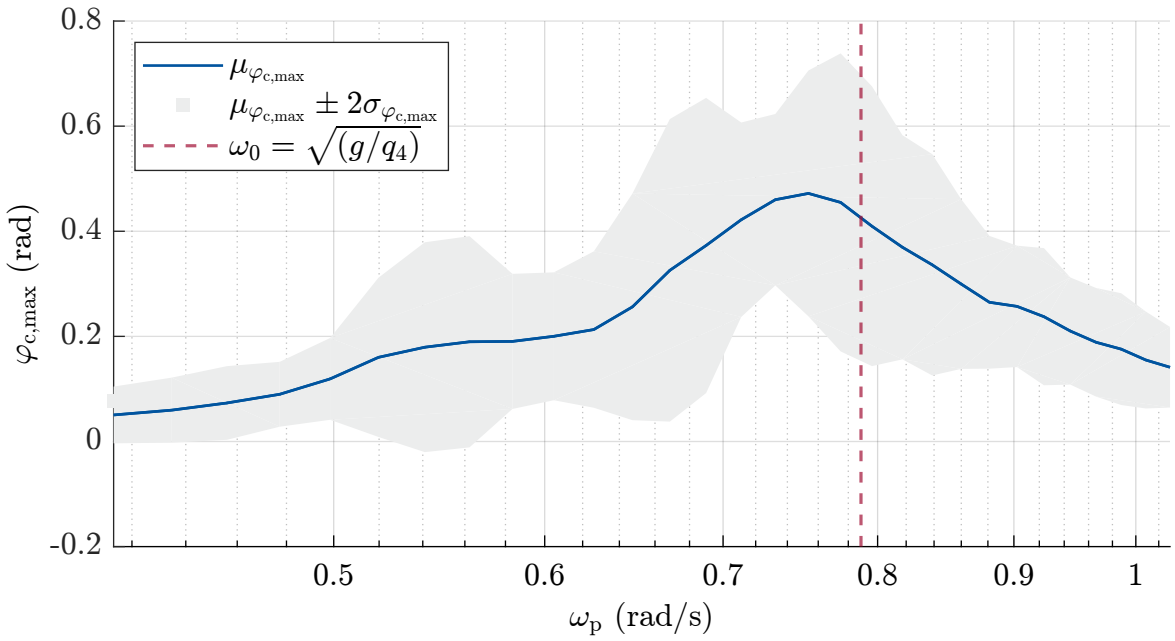

Fig. 3.12: Maximum payload sway angle during frequency sweep of the wave disturbance – The wave disturbance is drawn from a JONSWAP spectrum with $H_\mathrm{s} = 2.5\,\mathrm{m}$ and varying peak frequencies $\omega_\mathrm{p} \in [0.41, 1.03]\,\mathrm{rad/s}$. The frequency range is chosen according to SSC 4 in Tab. 3.1. The natural frequency ω_0 (red) of a mathematical pendulum of length $l = q_4$ is indicated. Each sea state is simulated five times for random seeds. The results are averaged (mean $\mu_{\varphi_{\mathrm{c,max}}}$, standard deviation $\sigma_{\varphi_{\mathrm{c,max}}}$).

3.7 Robot-based Test Bench

During the project, a robot-based test bench was developed in order to examine the researched operating and control concepts at laboratory scale. The first demonstrator was presented in [S3]. The test setup is built around an industrial 6 DoF *KR16* robot (KUKA AG, Augsburg, Germany), which emulates the knuckle boom crane. Due to the differing number of joints, the crane movements are recreated by means of its tip position $\boldsymbol{p}_{\text{tip}}^{ned}$, which (after scaling) is tracked by the robot. A payload is suspended from the robot's TCP yielding realistic load behavior. Furthermore, the objective of damping out payload oscillations via moving the crane tip is reproduced. In order to manipulate the cable length, a winch was constructed that is driven by a stepper motor (Nanotec Electronic GmbH & Co. KG, Feldkirchen, Germany). The KR16 is controlled using the Robot Sensor Interface (RSI) provided by the robot's control unit, while the payload position is monitored by an optical tracking system (*DTrack2* system, ART, Weilheim i.OB, Germany). A performance real-time target machine (Speedgoat GmbH, Liebefeld, Switzerland) executes the control topology and handles communication. Data exchange is realized in a local network, with separate UDP connections established for both the robot and the camera system. The winch motor is interfaced via CANOpen. The robot

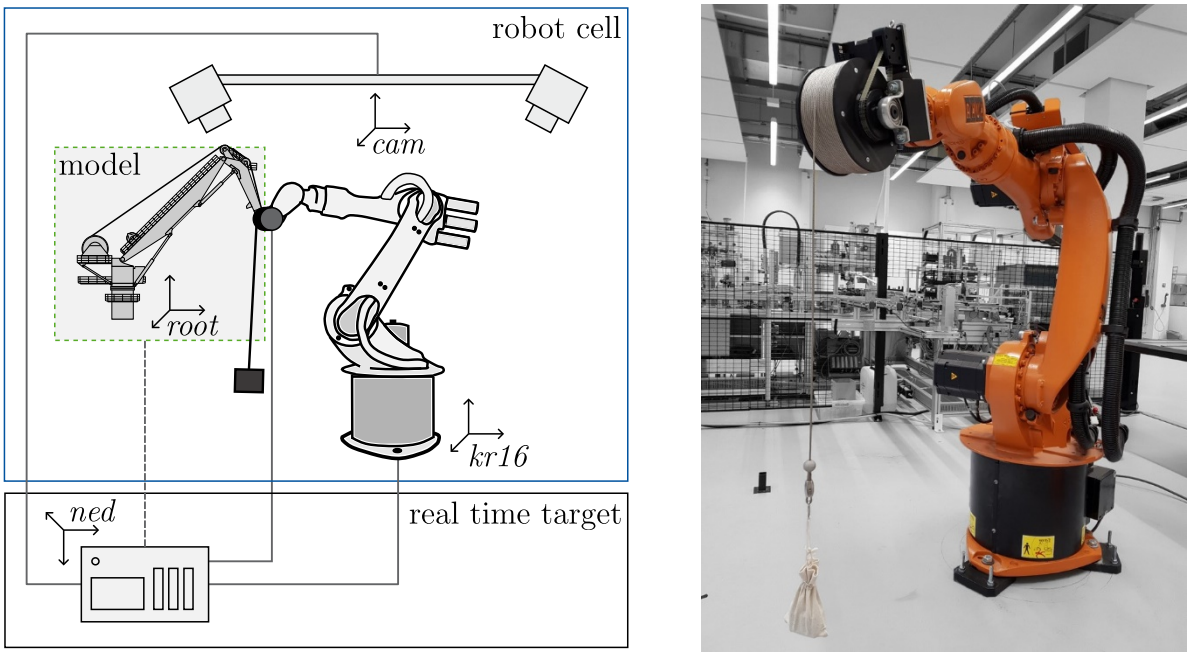

(a) Schematics of test bench adopted from [S5]

(b) Photo of test bench

Fig. 3.13: Robot-based test bench – The laboratory setup includes an industrial robot (KR16), a winch actuator, a camera tracking system as well as a real time target machine. A schematic representation (left) and photo (right) of the test bench are depicted.

is operated with a cycle time of 12 ms, whereas the program running on the real-time machine is executed every 6 ms to ensure communication integrity. A schematic depiction of the robot-based test bench is given in Fig. 3.13.

Some practical limitations should be noted: Since the different dimensions of crane and robot correspond to a 1:40 scaling, the payload dynamics observed in the test bench are much faster (factor $\sqrt{40}$). Hence, the control task is more challenging as the required cycle times decrease. This is especially cumbersome for MPC, where already some engineering is required to derive real-time feasible codes. Both the modeled actuator dynamics and the vessel motions have to be adjusted to reflect the faster payload dynamics and to maintain a realistic ratio between the resp. time constants. Another discrepancy stems from the RSI, which accepts cyclic position commands. In contrast, the crane model adopts velocity control loops. The actuator signals are thus integrated before being forwarded to the robot. The velocity set points are thus tracked in average. Given that the robot's cycle times are sufficiently fast compared to the crane actuators, this error is believed to be small. However, the robot controller also applies a moving average filter to the commanded positions to limit the resulting jerk. The filter is fixed at system level and introduces a delay of multiple cycle times. As a result, the system's phase margin decreases so that the tested controllers have to be tuned less aggressive. Last, the simulated vessel motions are added to the translational TCP movement. Changes in orientation are not mapped.

Chapter 4

Control

After modeling approaches for both crane and vessel have been presented in chapter 3, predictive control strategies aiming at stabilizing the payload during persistent wave disturbances are described hereafter. The presentation draws on the results of the previously published contributions [S1], [S2], [S5]. The chapter expands on the required state estimation as well as controller analysis. A thorough assessment of overall applicability of MPC for payload control is provided. The researched control topology is depicted in Fig. 4.1. The control task is first outlined in section 4.1, where different objectives are discussed and translated into practical performance measures. In the context of predictive payload controllers, two challenges have to be addressed: To resolve the crane's inherent ambiguity during control, secondary control objectives are introduced and integrated by means of an optimization-based target selector (section 4.3). Furthermore, the (exogenous) vessel

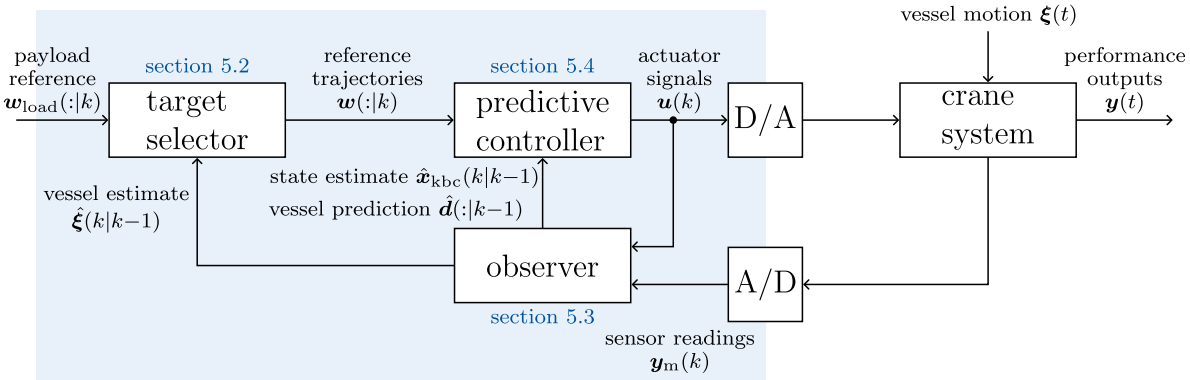

Fig. 4.1: Predictive control topology – The central MPC calculates actuation signals $\boldsymbol{u}(k)$ at each sampling instance k. The discrete signal is then converted to the continuous time domain by virtue of a digital-to-analog (D/A) converter, which is assumed to function as a zero-order hold (ZOH). Different controller designs are discussed in section 4.4. The required feedback is provided by an observer, which estimates the vessel and crane state $\boldsymbol{x}_{\text{ves}}$ resp. $\boldsymbol{x}_{\text{kbc}}$ on basis of the sampled sensor readings $\boldsymbol{y}_{\text{m}}$. In section 4.2, a MHE design allowing for short-time predictions $\hat{\boldsymbol{d}}(:|k-1)$ of the vessel motion $\boldsymbol{\xi}(t)$ over the MPC's prediction horizon is presented. The topology is complemented by a target selector providing reference trajectories $\boldsymbol{w}(:|k)$ for the controller. Details are included in section 4.3.

motions have to be predicted as to provide disturbance trajectories for the MPC. For this purpose, an MHE design is summarized in section 4.2. An integral part of this thesis is the investigation of different discretization techniques that compile the MPC's OCP to performant and real-time feasible codes. In particular, three approximations referred to as linearized MPC (LMPC), nonlinear MPC (NMPC) and flatness-based MPC (FMPC) are derived in section 4.4.2 - 4.4.4. All designs are evaluated in simulation both for control performance and computational complexity, cf. section 4.5. Contrastable results are obtained by automated controller tuning (see section 4.5.1). A load chart-like performance map is established in section 4.5.3, where also the influence of different actuator dynamics is addressed. Results from the robot-based test bench are presented in section 4.6. The chapter concludes with an outlook on *safe* offshore operations in section 4.7, discussing MPC in connection with operator-in-the-loop topologies.

Key insights:

- Moving horizon estimation allows estimating crane and ship states as well as providing short-term predictions of the vessel motions using a sum of modes approximation. Challenges arise when adjusting the filtering horizon to the MPC's prediction horizon.
- A target selector can be used to integrate secondary control objectives. Optimizing the crane configuration with respect to its manipulability ellipsoid yields improved ASC capabilities.
- Linear and flatness-based MPC formulations yield real-time capable codes, while nonlinear MPC is not. The flatness-based approach shows promise but requires complex initialization, which reduces robustness. A linear MPC was successfully tested in a laboratory test bench.
- Control performance is mainly limited by actuator constraints, with proposed performance indices dropping with higher sea state codes.
- Predictive safety filters present a direct extension of MPC-based payload controllers for promoting operational safety at lower LoA including operator-in-the-loop scenarios. Yet, designing not overly restrictive safe sets that both are forward invariant and ensure recursive feasibility is challenging.

4.1 Definition of the Control Task

Payload handling at sea involves different control tasks: The objective of payload *stabilization* reverts to the classic problem of disturbance rejection, where the control task equates to the damping of wave-induced payload oscillations. The objective may

be formulated in terms of a constant payload position in any suitable reference frame. Stabilization is crucial, for example, before loading or unloading the payload in order to prevent collisions in the loading zone. Respective controller designs may be used as assistance system (LoA 2) to support the operator during handling. Following section 1.3 - section 1.4, the problem of payload stabilization is usually further divided into active heave compensation (AHC) and anti-sway control (ASC). While for AHC the control task directly translates to tracking a vertical payload position, there is no direct equivalent in ASC. Most commonly, some deflection angles like sidelead or offlead [48] are defined, which describe the payload sway relative to the crane tip and therefore allow assessing ASC performance. The objective of *tracking* refers to the task of transferring the payload from its current to a target position. Here, the controller has to not only account for the swell disturbance but also to realize the required payload motion. In line with section 1.2, such controllers would be associated with higher levels of automation (LoA 3 - 4). In the scope of this thesis, predictive controller designs are studied both for payload stabilization and reference tracking. In section 4.1.1, a unified objective for MPC is derived.

Today, no standardized way of comparing different controller designs exists. In literature, the time evolution of the vertical payload position respectively its deflection angles are analyzed under active control, usually with the aim of demonstrating convergence and vanishing control errors. Product specifications of e.g. AHC solutions further aggregate the characteristics into a single indicator that specifies the compensable heave amplitudes in steady state operation, that is at single (constant) heave periods. Dynamic effects are thus neglected. From the perspective of operational safety, the transient controller performance is paramount as well. Therefore, a set of performance measures is proposed in section 4.1.2, which allows rating not only the steady state but also the transient controller behavior. The introduced measures are applied throughout this chapter in order to compare different controller designs.

4.1.1 Control Objective

With reference to the OCP (2.30), an essential part of any MPC is the design of the cost functionals $L : \mathcal{X} \times \mathcal{U} \times \mathcal{Y} \times \mathbb{R} \to \mathbb{R}_{\geq 0}$, $L_{T_\mathrm{p}} : \mathcal{X}_{T_\mathrm{p}} \to \mathbb{R}_{\geq 0}$ rating the system trajectories and the final state. The latter plays an increasingly important role the shorter the prediction horizon T_p has to be chosen due to limitations in the computational resources. Otherwise, the control behavior is mostly governed by the stage costs $L(\cdot)$ and the constraints. Below different approaches to design $L(\cdot)$ in context of crane-based payload handling are discussed.

- Referring to the state of the art in section 1.3.2, one popular concept for ASC is based on the dissipation of energy from the payload oscillation. Accordingly, one

might try to reduce the payload energy by choosing

$$L_1(\boldsymbol{x}_{\mathrm{kbc}}, \boldsymbol{x}_{\mathrm{ves}}) = \mathcal{T}_{\mathrm{load}}(\boldsymbol{x}_{\mathrm{kbc}}, \boldsymbol{x}_{\mathrm{ves}}) + \mathcal{V}_{\mathrm{load}}(\boldsymbol{x}_{\mathrm{kbc}}, \boldsymbol{x}_{\mathrm{ves}}) \tag{4.1}$$

where the payload's kinetic and potential energy are calculated from (3.29). Doing so minimizes the average payload energy over the prediction horizon. Depending on the wave excitation, this does not necessarily lead to satisfactory disturbance rejection. To obtain a continuous reduction in payload energy, the stage costs may be adapted as to maximize the energy loss at all times, i.e. $L_2(\boldsymbol{x}_{\mathrm{kbc}}, \boldsymbol{x}_{\mathrm{ves}}) = {}^{\mathrm{d}}\!/\!_{\mathrm{d}t} L_1$. Particular care must be taken to ensure that impractical crane configurations are precluded. For example, zero free cable lengths $q_4 = 0$ might be favorable from an energy point of view. A common drawback of energy-based approaches is the problem that integrating a target payload position is not straightforward. Hence, the presented objectives are not suited for tracking. Even for payload stabilization, additional measures are advisable to ensure proper payload damping and operational safety.

- In AHC the vertical payload position should be rendered invariable regarding some reference frame *cs*. Similar, ASC can be formulated in terms of two sway angles φ_1, φ_2 that should approach zero under perfect control. Both objectives can be combined into a single function

$$L_3(\boldsymbol{x}_{\mathrm{kbc}}, \boldsymbol{x}_{\mathrm{ves}}, t) = \frac{1}{2}\, q_{\mathrm{h}} \left(p^{cs}_{\mathrm{load},3}(\boldsymbol{x}_{\mathrm{kbc}}, \boldsymbol{x}_{\mathrm{ves}}) - w^{cs}_{\mathrm{load},3}(t) \right)^2 + \frac{1}{2}\, q_{\varphi} \left(\varphi_1^2(t) + \varphi_2^2(t) \right) \tag{4.2}$$

where q_{d}, $q_{\varphi} \in \mathbb{R}_{\geq 0}$ are positive weighting coefficients and $w^{cs}_{\mathrm{load},3}$ denotes a target for the vertical payload position $p^{cs}_{\mathrm{load},3}$. The reference frame *cs* can be chosen depending on the application. While the *ves*-frame might be used during liftoff to guarantee a relative offset between payload and vessel deck, the global *ned*-frame provides a fixed reference outside the vessel. Various contributions utilize objective functions similar to $L_3(\cdot)$ either for AHC or ASC. Yet, extending the approach from payload stabilization to tracking is not intuitive as it would require defining reference trajectories for the deflection angles. As an exception, payload transfer may be realized by virtue of (4.2) under quasi-static operation. For this purpose, low-speed motions are superimposed onto the crane tip that are tracked by the payload thanks to the faster disturbance rejection.

- A payload-centric approach was presented in [S2]. Utilizing the Cartesian payload position $\boldsymbol{p}^{cs}_{\mathrm{load}}$ as controlled variable directly translates to both trajectory tracking and payload stabilization. While the reference $\boldsymbol{w}^{cs}_{\mathrm{load}}(t) = \text{const.}$ is fixed during stabilization, a time-resolved profile might be used during automated trajectory tracking. As before, the choice of an appropriate reference frame *cs* remains as a

design criterion. The stage costs are then given by

$$L_4(\boldsymbol{x}_{\mathrm{kbc}}, \boldsymbol{x}_{\mathrm{ves}}, t) = \frac{1}{2} \left\| \boldsymbol{p}_{\mathrm{load}}^{cs} \left(\boldsymbol{x}_{\mathrm{kbc}}, \boldsymbol{x}_{\mathrm{ves}} \right) - \boldsymbol{w}_{\mathrm{load}}^{cs}(t) \right\|_{\mathbf{Q}_{\mathrm{p}}}^2 \tag{4.3}$$

with the weighting matrix $\mathbf{Q}_{\mathrm{p}} \in \mathbb{R}^{3\times3}$, which enables emphasizing e.g. vertical position offsets in order to add means of prioritization to the design. Objective (4.3) presents a typical least-squares formulation, often encountered in MPC. In its basic form, the control error is evaluated the same irrespective of the time instance within the prediction horizon. However, noting that the payload is mainly controlled indirectly via manipulating the crane tip, an immediate improvement in the control error is far-fetched. A steady reduction in payload oscillations may therefore better reflect the system characteristics. In this context, the integral time-weighted error (ITSE) is known to yield less aggressive controllers when used for controller tuning. Accordingly, a time-weighted version of (4.3)

$$L_5(\boldsymbol{x}_{\mathrm{kbc}}, \boldsymbol{x}_{\mathrm{ves}}, t) = \frac{1}{2}\, t \left\| \boldsymbol{p}_{\mathrm{load}}^{cs} \left(\boldsymbol{x}_{\mathrm{kbc}}, \boldsymbol{x}_{\mathrm{ves}} \right) - \boldsymbol{w}_{\mathrm{load}}^{cs}(t) \right\|_{\mathbf{Q}_{\mathrm{p}}}^2 \tag{4.4}$$

may be adopted for predictive payload handling offshore.

Besides considering performance outputs, it is standard to also include costs for the actuator utilization $L_{\mathrm{u}}(\boldsymbol{u})$ to avoid high dynamic actuations, which may reduce the actuators' service lives or cause mechanical damage. A common choice is to penalize the change in actuation, i.e. by adding

$$L_{\mathrm{u}}(\boldsymbol{u}) = \frac{1}{2} \left\| {}^{\mathrm{d}}\!/_{\mathrm{d}t}\, \boldsymbol{u}(t) \right\|_{\mathbf{Q}_{\mathrm{u}}}^2 \tag{4.5}$$

to any of the previous stage costs $L_1(\cdot)$ - $L_5(\cdot)$. As before, the matrix $\mathbf{Q}_{\mathrm{u}} \in \mathbb{R}^{m\times m}$ can be used to further balance individual actuators or to adjust the impact of the different stage costs.

In economic MPC the state evolution is not specified. Rather, the terminal state is constrained such as to fulfill the control task. The stage costs are then determined from a generic performance cost function that does not have to be least-squares. Still, the actuator usage L_{u} is part of many examples. For payload stabilization an economic MPC formulation presents an interesting option, since it circumvents the problem of prescribing the payload trajectory, when the ultimate goal is just attaining and maintaining a given payload position. However, the persistent wave excitation in combination with the usually decreasing prediction accuracy over the finite prediction horizon renders establishing forward invariance challenging. As a result, no satisfactory control performance was achieved with an economic formulation in the course of this thesis project. Therefore, least-squares objectives are examined exclusively from this point forward.

4.1.2 Performance Indicators

When comparing different controller designs, it is necessary to establish common performance indicators. Various measures are used in the literature, most of which equate to a steady state offset analysis. Tailored to the use case, e.g. AHC or ASC, the vertical payload position or its deflection angles may be examined. Since the researched control schemes aim at spatial payload stabilization resp. tracking of spatial payload trajectories, the Euclidean distance from the reference

$$e_{\mathrm{r}}(t) = \sqrt{\left(\boldsymbol{p}_{\mathrm{load}}^{ned}\left(t\right) - \boldsymbol{w}_{\mathrm{load}}^{ned}(t)\right)^{\mathrm{T}}\left(\boldsymbol{p}_{\mathrm{load}}^{ned}\left(t\right) - \boldsymbol{w}_{\mathrm{load}}^{ned}(t)\right)} \tag{4.6a}$$

presents an obvious figure for controller accuracy. The fact that the Euclidean distance has a direct practical meaning is also advantageous, as it can be used for planning safe operations once a bound has been determined for a specific controller, cf. section 4.7.4. Two additional error variables are considered to provide further information on the control accuracy in various dimensions. Besides the vertical payload offset

$$e_{\mathrm{h}}(t) = d_{\mathrm{load}}(t) - w_{\mathrm{load},3}(t) \tag{4.6b}$$

the horizontal error is mapped via (3.19), i.e.

$$e_{\mathrm{s}}(t) = \varphi_{\mathrm{c}}(t) = \operatorname{acos}\left(\cos(\varphi_1(t))\cos(\varphi_2(t))\right) \tag{4.6c}$$

which accounts for both sway angles φ_1, φ_2. Considering all three error variables enables not only to evaluate the control accuracy, but also to gain insight in a controller's AHC and ASC capabilities.

In addition to a controller's accuracy in steady state, its transient response is just as important for operational safety. From a practical viewpoint, it is sensible to reduce the error trajectories defined in (4.6) to a few performance indicators. Arguing that for payload stabilization any controller should

- initially induce damping in the oscillating payload and
- ultimately confine the payload motions to a small vicinity of the reference,

an analogy to the properties of a second-order system may be drawn. The latter is characterized by its damping coefficient, natural frequency as well as a gain factor. From a performance perspective, only the envelope of the system response is of interest, which informs the following function prototype

$$h_i(t) = \begin{cases} e_{0,i} & \text{for} \quad t < \tau_i \\ \left(e_{0,i} - e_{\infty,i}\right)\exp\left(-d_i\omega_0(t-\tau_i)\right) + e_{\infty,i} & \text{for} \quad t \geq \tau_i \end{cases} \tag{4.7}$$

with the (maximum) initial error $e_{0,i} \in \mathbb{R}_{\geq 0}$, the steady state error $e_{\infty,i} \in \mathbb{R}_{\geq 0}$, the damping coefficient $d_i \in \mathbb{R}_{\geq 0}$ and $i \in \{\mathrm{r}, \mathrm{s}, \mathrm{h}\}$. An additional delay $\tau_i \in \mathbb{R}_{\geq 0}$ (response time) is included to account for the fact, that an instantaneous reduction in the control error might not be possible depending on the sea state and due to the indirect actuation of the payload. The damping coefficient is normalized by the natural frequency $\omega_0 = \sqrt{g/q_4(t_0)}$ of a pendulum with cable length equal to the undisturbed crane system. Note, that the cable length will change during operation due to actuation of the winch. Yet, the average free cable length will be close to its initial value given that the heave motion is mean-free, i.e. $\lim_{T\to\infty} {}^1\!/_T \int_0^T q_4(t)\mathrm{d}t \approx q_4(t_0)$. A visualization of (4.7) is given in Fig. 4.2. Fitting envelopes of type (4.7) to the error trajectories (4.6) yields a set

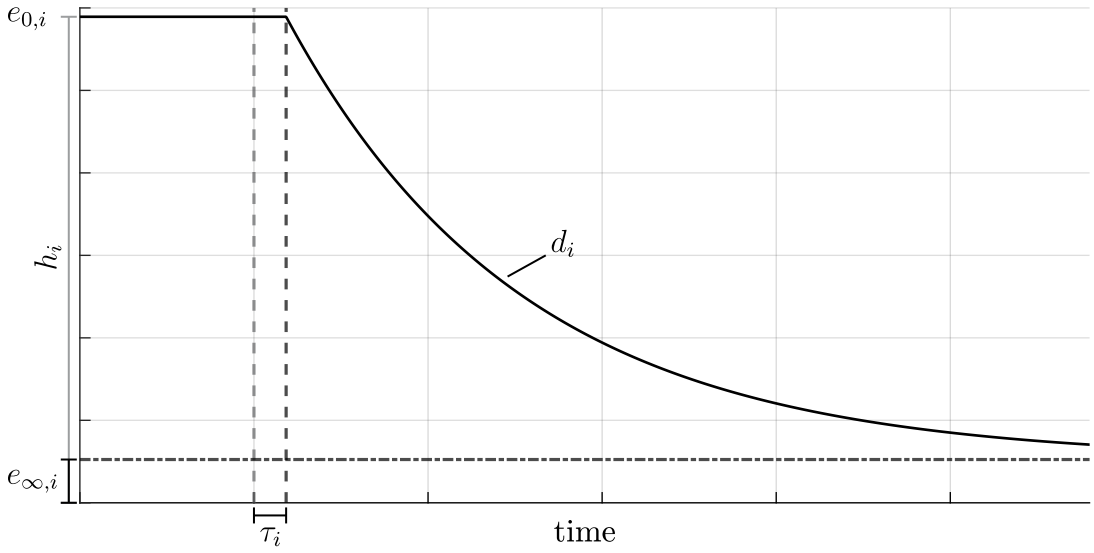

Fig. 4.2: Schematic of an error envelope – The error envelope $h_i(t)$ is characterized by four parameters, namely the initial error $e_{0,i} \in \mathbb{R}_{\geq 0}$, the steady state error $e_{\infty,i} \in \mathbb{R}_{\geq 0}$ and the damping coefficient $d_i \in \mathbb{R}_{\geq 0}$.

$\mathcal{PI} = \{e_{0,i}, e_{\infty,i}, d_i, \tau_i \,|\, i = \mathrm{r}, \mathrm{s}, \mathrm{h}\}$ of twelve performance indicators. From an application viewpoint, the damping coefficient d_i and the error $e_{\infty,i}$ are of particular interest, as they can be associated with the controller's transient resp. steady state behavior. The remaining indicators do in large part depend on the wave disturbance and the system state at controller initialization. Hence, they hold little information about the particular controller design. For reference, the presented methodology is applied to exemplary closed loop trajectories in Fig. 4.3. The recorded error trajectories are depicted in Fig. 4.3a, where five random wave realizations have been simulated with $H_\mathrm{s} = 0.8\,\mathrm{m}$ and $\omega_\mathrm{p} = 0.87\,\mathrm{rad/s}$. The controller is activated at $t = 60\,\mathrm{s}$. For illustration purposes, the last simulation run is highlighted in blue. In Fig. 4.3b envelopes have been fitted to the respective error signals, indicating that the used controller yields fast damping while

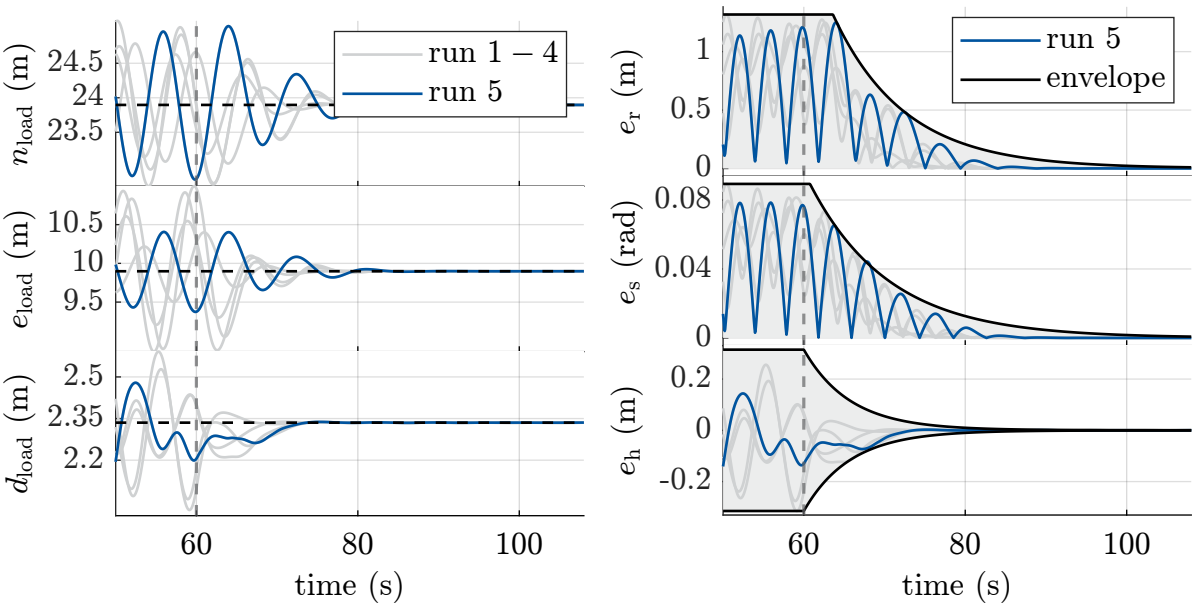

(a) Payload trajectories

(b) Error trajectories and envelopes

Fig. 4.3: Performance measures of exemplary closed loop trajectories – The crane system is simulated for five random wave realizations drawn from a JONSWAP spectrum with $H_{\text{s}} = 0.8\,\text{m}$ and $\omega_{\text{p}} = 0.87\,\text{rad/s}$. The payload trajectories (left) converge to their respective reference (dotted line) after controller initialization at $t = 60\,\text{s}$. From the payload trajectories three error signals $e_i(t)$ with $i \in \{\text{r}, \text{s}, \text{h}\}$ are calculated, shown on the right. Respective error envelopes $h_i(t)$ are fitted to each set of error trajectories.

achieving minimal steady state errors. Yet, the transient control behavior for sway and heave reduction varies. Since the vertical payload position can be manipulated directly via the winch, the heave envelope $h_{\text{h}}(t)$ shows a smaller delay time when compared to the sway envelope $h_{\text{s}}(t)$.

In order to fit envelopes $h_i(t)$ to a set of $j \in \mathbb{N}$ error trajectories $e_{i,j}(t)$, the largest signal value at each time instance is calculated before solving a nonlinear optimization problem, which reads

$$\begin{aligned}\left(e_{0,i}^*, e_{\infty,i}^*, d_i^*, \tau_i^*\right) = \ & \arg \min_{e_{0,i}, e_{\infty,i}, d_i, \tau_i} \frac{1}{2} \sum_{k=0}^{T/T_{\text{s}}} \left(\bar{e}_i(t_0 + kT_{\text{s}}) - h_i(t_0 + kT_{\text{s}})\right)^2 \\ & \text{s.t.} \quad \bar{e}_i(t_0 + kT_{\text{s}}) - h_i(t_0 + kT_{\text{s}}) \leq 0 \qquad \forall\, k \in [0, T/T_{\text{s}}]\end{aligned} \tag{4.8}$$

where $\bar{e}_i(t)$ denotes the signal inferred from the maximum of the error trajectories $e_{i,j}(t)$ at each time instance k, i.e. $\bar{e}_i(t_0 + kT_{\text{s}}) \geq e_{i,j}(t_0 + kT_{\text{s}})$, $\forall k, j$. The number of free variables can be reduced by determining $e_{0,i}^*$ as the maximum error over the entire trajectory. The optimization problem (4.8) is solved with the help of the genetic algorithm package provided in MATLAB. Optimal solutions are calculated within a few seconds.

4.2 Estimation of Vessel and Crane State

Most formulations of model predictive control are based on state feedback [146]. In particular, the current vessel and crane state are required to initialize the open loop prediction of the system trajectories at each time step. Since not all system states in (3.49) can be measured directly, an observer design is necessary to recover the state trajectories from the sensor data, cf. section 3.3.5. The persistent wave excitation of the vessel further necessitates to predict the vessel motions in order to obtain meaningful open loop predictions within the MPC. This requires means of extrapolating the past vessel motions, which is addressed in section 4.2.1. Subsequently, two observer concepts based on a MHE design are presented in section 4.2.2.

4.2.1 Parameterization of the Vessel Motions

Nowadays, the use of motion reference unit (MRU) resp. inertial measurement unit (IMU) is common practice in the offshore sector, with AHC solutions presenting one popular example. An IMU will provide angular rates and accelerations with respect to its body-fixed reference frame. When mounted on a ship deck, the measurements reflect the vessel's (wave-induced) motions. As a common simplification, the vessel is assumed to exhibit mean-free oscillations around its hydrodynamic equilibrium point. This motivates high-pass filtering the IMU measurements [72], which after rotation may be integrated to obtain the vessel's heave position and orientation, respectively. Yet, the question of how to extrapolate the future vessel motions persists.

Here, the approach in [107], [109] is adopted and extended from the prediction of the vessel's heave motion to the three-dimensional case, which further covers the vessel's rolling and pitching motions. The basic idea is to approximate the vessel's motions via the sum of $n_\mathrm{d} \in \mathbb{N}$ modes whose parameters are estimated at runtime, i.e.

$$\xi_i(t) = x_{\mathrm{ves},i-2}(t) \approx \sum_{j=1}^{n_\mathrm{d}} \Xi_{i,j} \sin(\omega_{i,j} t + \varphi_{i,j}) = \sum_{j=1}^{n_\mathrm{d}} A_{i,j} \sin(\omega_{i,j} t) + B_{i,j} \cos(\omega_{i,j} t) \tag{4.9a}$$

$$\dot{\xi}_i(t) = x_{\mathrm{ves},i+1}(t) \approx \sum_{j=1}^{n_\mathrm{d}} A_{i,j}\omega_{i,j} \cos(\omega_{i,j} t) - B_{i,j}\omega_{i,j} \sin(\omega_{i,j} t) \tag{4.9b}$$

$$\ddot{\xi}_i(t) = d_{i-2}(t) \quad \approx \sum_{j=1}^{n_\mathrm{d}} -A_{i,j}\omega_{i,j}^2 \sin(\omega_{i,j} t) - B_{i,j}\omega_{i,j}^2 \cos(\omega_{i,j} t) \tag{4.9c}$$

with $i \in \{3, 4, 5\}$. Note that the mode's amplitude $\Xi_{i,j} \in \mathbb{R}_{\geq 0}$ and phase $\varphi_{i,j} \in (-\pi, \pi]$

are related to the quantities $A_{i,j} \in \mathbb{R}$, $B_{i,j} \in \mathbb{R}$ by

$$\Xi_{i,j} = \sqrt{A_{i,j}^2 + B_{i,j}^2}, \qquad \varphi_{i,j} = \operatorname{atan2}(B_{i,j}, a_{i,j}), \tag{4.10a}$$

$$A_{i,j} = \Xi_{i,j} \cos(\varphi_{i,j}), \qquad B_{i,j} = \Xi_{i,j} \sin(\varphi_{i,j}) \ . \tag{4.10b}$$

While both representations in (4.9a) are equivalent, the latter is chosen out of numerical considerations. The former has been used in [107], [109]. Modeling the vessel motions as sum of sine and cosine signals has multiple advantages. First, the estimated disturbance signals are guaranteed to be mean-free, which renders high-pass filtering obsolete. Second, the vessel motions can be easily extended beyond the current time step as the periodic modes ensure boundness of the extrapolated trajectories. Last, the signal-based approach does not require explicit knowledge about the vessel or its dynamics.

Finding an initial parameterization

When used in context of a state observer, it is necessary to determine an initial parameterization of all modes. If the parameters are far off the observer performance will degrade substantially. In order to find a "good" initial guess, an initial episode of recorded sensor data is analyzed for its frequency information similar to the procedure in [107]. Noteworthy, a data storage for past sensor readings is already part of the MHE topology, implemented hereafter. Following [68], the IMU's accelerometers admit the following (crude) approximation of the vessel orientation

$$\xi_4(t) \approx \quad \operatorname{atan}\left(\frac{\dot{v}_{\mathrm{f},2}^{sen}}{\dot{v}_{\mathrm{f},3}^{sen}}\right) \tag{4.11}$$

$$\xi_5(t) \approx -\operatorname{atan}\left(\frac{\dot{v}_{\mathrm{f},1}^{sen}}{\sqrt{(\dot{v}_{\mathrm{f},2}^{sen})^2 + (\dot{v}_{\mathrm{f},3}^{sen})^2}}\right) \tag{4.12}$$

where $\dot{v}_{\mathrm{f},i}^{sen}$ are filtered versions of the accelerometers' measurements $\dot{v}_{\mathrm{m},k}^{sen}$, $k \in \{1,2,3\}$. Using the obtained vessel orientation, an estimate of the heave period and amplitude can be derived. The approximation is sensible for slow wave-induced vessel motions with zero mean.

Based on the approximated vessel trajectories, a fast Fourier transform (fft) is applied to retrieve frequency, amplitude and phase estimates $(\hat{\omega}_{i,j}^0, \hat{\Xi}_{i,j}^0, \hat{\varphi}_{i,j}^0)$ of every mode. The individual modes are identified as the local maxima of the derived spectra. Finally, the estimated parameters are converted utilizing (4.10b). The approach is visualized in Fig. 4.4.

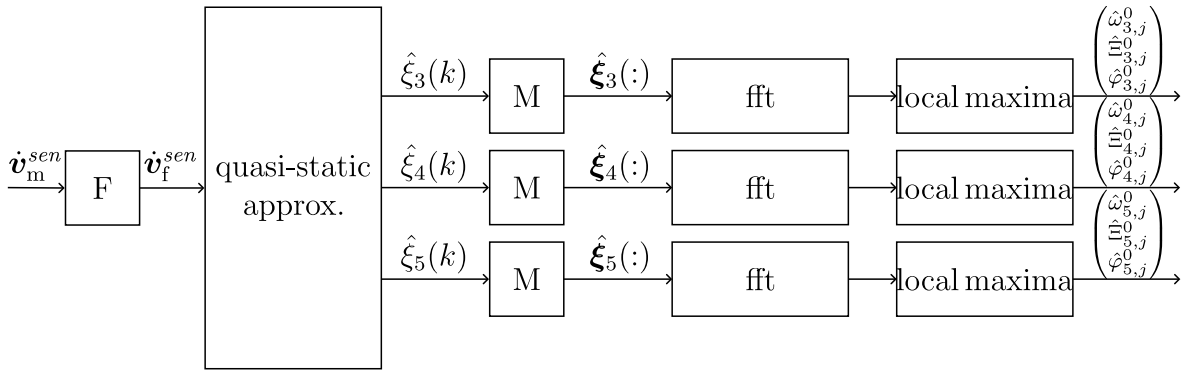

Fig. 4.4: Initial guess of vessel motion – The accelerometers' measurements $\dot{v}_{\mathrm{m},i}^{sen}$ are filtered via F. The filtered samples $\dot{v}_{\mathrm{m},i}^{sen}(k)$ are used to approximate the vessel state, yielding estimates $\hat{\xi}_3(k)$, $\hat{\xi}_4(k)$, $\hat{\xi}_5(k)$. Entire episodes $\hat{\boldsymbol{\xi}}_i(:)$ are analyzed via a fast FOURIER transformation and subsequent maxima search to obtain initial parameter guesses $(\hat{\omega}_{i,j}^0, \hat{\Xi}_{i,j}^0, \hat{\varphi}_{i,j}^0)$.

4.2.2 Observer Design

Based on the sensor readings $\boldsymbol{y}_{\mathrm{m}} \in \mathbb{R}^{12}$ of camera, IMU and encoders the observer has to reconstruct the crane and vessel states $\boldsymbol{x}_{\mathrm{kbc}} \in \mathbb{R}^{12}$ resp. $\boldsymbol{x}_{\mathrm{kbc}} \in \mathbb{R}^6$, cf. section 3.4. With the parameterization of the vessel motions according to (4.9), the task simplifies to the estimation of the crane states alongside the set of disturbance parameter tuples $\{(\omega_{i,j}, \Xi_{i,j}, \varphi_{i,j}) | i \in \{3,4,5\} \wedge j = 1, \ldots, n_{\mathrm{d}}\}$, where $n_{\mathrm{d}} \in \mathbb{N}$ denotes the number of modes used for approximation. However, referring to section 3.3.5 the IMU measurements are corrupted by colored noise processes. Thus, estimating the IMU's stochastic bias becomes necessary. Yet, its dynamic model (3.42) is not observable. Following common practice, a single random walk process is modeled for each gyroscope respectively accelerometer. Accordingly, a total of six bias states $\boldsymbol{z} = (z_1 \ \ldots \ z_6)^{\mathrm{T}}$ is modeled whose dynamics are given by

$$\dot{z}_i = 0 + \boldsymbol{\varepsilon}_{z_i}, \qquad \mathcal{E}_{z_i,k} \sim \mathcal{GP}(0, \sigma_{z_i}^2) \tag{4.13}$$

for $i = 1, \ldots, 6$. Concatenating yields the observer state $\boldsymbol{x}_{\mathrm{o}} = (\boldsymbol{x}_{\mathrm{kbc}}^{\mathrm{T}} \, \boldsymbol{z}^{\mathrm{T}})^{\mathrm{T}} \in \mathbb{R}^{18}$, which is complemented by the vector of mode parameters

$$\boldsymbol{p}_{\boldsymbol{\xi}} = (\omega_{3,1} \, \Xi_{3,1} \, \varphi_{3,1} \ \ldots \ \omega_{3,n_{\mathrm{d}}} \, \Xi_{3,n_{\mathrm{d}}} \, \varphi_{3,n_{\mathrm{d}}} \ \ldots \ \omega_{5,1} \, \Xi_{5,1} \, \varphi_{5,1} \ \ldots \ \omega_{5,n_{\mathrm{d}}} \, \Xi_{5,n_{\mathrm{d}}} \, \varphi_{5,n_{\mathrm{d}}})^{\mathrm{T}} \tag{4.14}$$

which consists of $\dim(\boldsymbol{p}_{\boldsymbol{\xi}}) = 9n_{\mathrm{d}}$ elements. Referring back to section 2.6, in MHE an estimate of the state trajectory $\hat{\boldsymbol{x}}_{\mathrm{o}}(: | k-1) = (\hat{\boldsymbol{x}}_{\mathrm{o}}(k - {}^{T_{\mathrm{f}}}/_{T_{\mathrm{e}}} | k-1)^{\mathrm{T}} \ \ldots \ \hat{\boldsymbol{x}}_{\mathrm{o}}(k|k-1)^{\mathrm{T}})^{\mathrm{T}}$ is derived over the filter horizon T_{f} given measurements $\boldsymbol{y}_{\mathrm{m}}(:) = (\boldsymbol{y}_{\mathrm{m}}(k - {}^{T_{\mathrm{f}}}/_{T_{\mathrm{e}}})^{\mathrm{T}} \ \ldots \ \boldsymbol{y}_{\mathrm{m}}(k-1)^{\mathrm{T}})^{\mathrm{T}}$ up to time instance $t = t_0 + (k-1)T_{\mathrm{e}}$, where T_{e} is the observer's cycle time[1].

[1]We will implicitly assume that T_{e} is equal to the sample time of the slowest sensor or a multiple hereof.

In contrast to the states $\boldsymbol{x}_\mathrm{o}$, only a single set of variables $\boldsymbol{p}_{\boldsymbol{\xi}}$ is fitted over the moving horizon. The vessel trajectory resp. $(\hat{\boldsymbol{x}}_\mathrm{ves}(:|k-1), \hat{\boldsymbol{d}}(:|k-1))$ is computed by evaluating (4.9) for $t = -T_\mathrm{f}, -T_\mathrm{f}+T_\mathrm{e}, \ldots, 0$. Note, that the same query points are applied at each sampling instance. Thus, the mode parameters have to be propagated through time. By applying basic trigonometric identities to

$$\sum_{j=1}^{n_\mathrm{d}} A_{i,j}^{k+1} \sin(\omega_{i,j}^{k+1} t) + B_{i,j}^{k+1} \cos(\omega_{i,j}^{k+1} t) = \sum_{j=1}^{n_\mathrm{d}} A_{i,j}^{k} \sin(\omega_{i,j}^{k}(t+T_\mathrm{e})) + B_{i,j}^{k} \cos(\omega_{i,j}^{k}(t+T_\mathrm{e}))$$

and solving for $(A_{i,j}^{k+1}, B_{i,j}^{k+1}, \omega_{i,j}^{k+1})$, the following iteration laws are obtained

$$\omega_{i,j}^{k+1} = \omega_{i,j}^{k} \tag{4.15a}$$

$$A_{i,j}^{k+1} = \sqrt{(A_{i,j}^{k})^2 + (B_{i,j}^{k})^2} \cos\left(\mathrm{atan2}(B_{i,j}^{k}, A_{i,j}^{k}) + \omega_{i,j}^{k} T_\mathrm{e}\right) \tag{4.15b}$$

$$B_{i,j}^{k+1} = \sqrt{(A_{i,j}^{k})^2 + (B_{i,j}^{k})^2} \sin\left(\mathrm{atan2}(B_{i,j}^{k}, A_{i,j}^{k}) + \omega_{i,j}^{k} T_\mathrm{e}\right) \tag{4.15c}$$

where (other than before) an additional superscript has been used to indicate the time instance. With (3.48), (4.13), (4.15) the time evolution of all quantities is known. For implementing either an EKF or a MHE, the dynamics (3.48), (4.13) have to be discretized, cf. section 2.3. In the scope of this thesis, two observer designs were investigated that are depicted in Fig. 4.5. The first observer topology in Fig. 4.5a follows a typical moving horizon design, where a MHE is implemented to handle the entire estimation task. An advantage resides in the fact, that a single sensor fusion could benefit from all measurements, which may improve the estimates. On the downside, the computational complexity associated with estimating all states, biases and mode parameters restricts the feasible size of the moving horizon T_f. Yet, longer horizons in particular promote both convergence and stability of the observer. For the benefit of to real-time feasibility, the second topology shown in Fig. 4.5b splits the task of state reconstruction and mode resp. bias estimation. While the MHE-portion only processes the IMU measurements, the remaining data is handled by a computationally more efficient EKF. Contrary to the superior execution times, the potential gain in estimation accuracy when fusing both IMU and camera measurements is lost. For implementation details on the EKF, the reader is referred to page 50. The optimization problems arising in both MHEs are listed below, see (4.16) and (4.20) respectively.

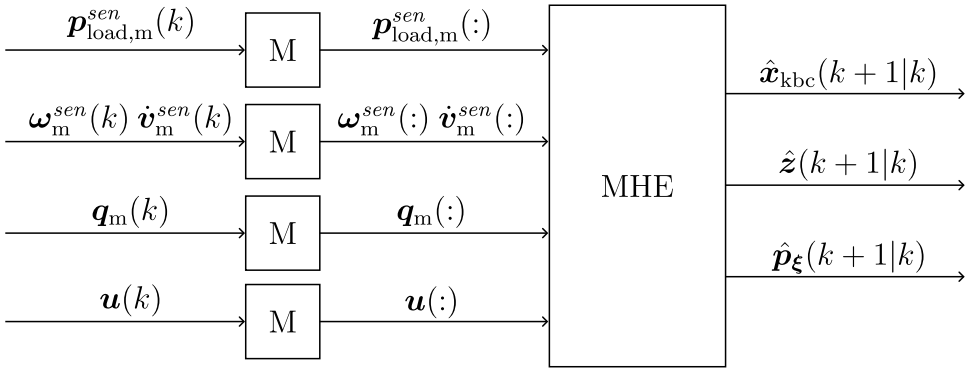

(a) Holistic observer design containing a single MHE

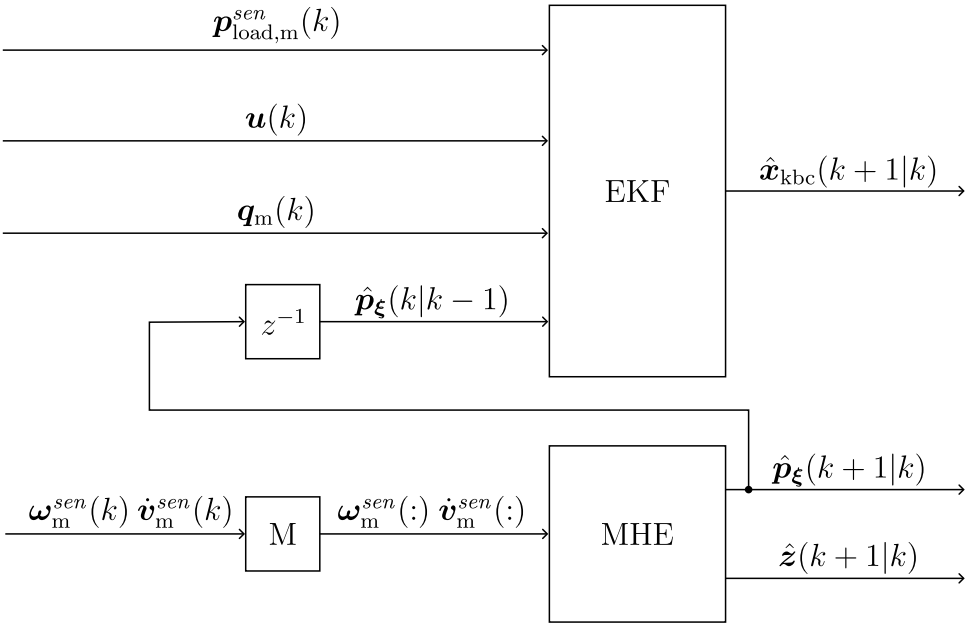

(b) Structured observer design incorporating both an EKF and a MHE

Fig. 4.5: Holistic and structured observer designs – Both topologies utilize the measured output $\boldsymbol{y}_{\mathrm{m}} = ((\boldsymbol{p}^{sen}_{\mathrm{load,m}})^{\mathrm{T}}\,(\boldsymbol{\omega}^{sen}_{\mathrm{m}})^{\mathrm{T}}\,(\dot{\boldsymbol{v}}^{sen}_{\mathrm{m}})^{\mathrm{T}}\,\boldsymbol{q}^{\mathrm{T}}_{\mathrm{m}})^{\mathrm{T}}$ alongside the manipulated variables $\boldsymbol{u}$ to derive a priori estimates of the states $\hat{\boldsymbol{x}}_{\mathrm{kbc}}(k+1|k)$, biases $\hat{\boldsymbol{z}}(k+1|k)$ and mode parameters $\hat{\boldsymbol{p}}_{\boldsymbol{\xi}}(k+1|k)$. The first design (top) implements a MHE to handle the entire sensor fusion. In contrast, the second design (bottom) applies a moving horizon only to estimate the mode parameters and IMU biases, while the state estimation is performed by an EKF.

Full state observer:

$$\min_{\boldsymbol{x}_\mathrm{o}(:),\boldsymbol{p}_{\boldsymbol{\xi}}} \; L_0(\boldsymbol{x}_\mathrm{o}(k-N_\mathrm{f}),\boldsymbol{p}_{\boldsymbol{\xi}}) + \sum_{i=k-N_\mathrm{f}}^{k} L\left(\boldsymbol{\varepsilon}(i),\boldsymbol{v}(i)\right) \tag{4.16}$$

$$\begin{aligned}
\text{s.t.} \quad \boldsymbol{\varepsilon}(i) &= \boldsymbol{x}_\mathrm{o}(i+1) - \left(\mathrm{IRK2} \circ \boldsymbol{f}_\mathrm{o}\right)\left(\boldsymbol{x}_\mathrm{o}(i),\boldsymbol{u}(i),\boldsymbol{p}_{\boldsymbol{\xi}}\right) && i = k-N_\mathrm{f},\ldots,k \\
\boldsymbol{v}(i) &= \boldsymbol{y}_\mathrm{m}(i) - \boldsymbol{h}_\mathrm{o}\left(\boldsymbol{x}_\mathrm{o}(i),\boldsymbol{u}(i),\boldsymbol{p}_{\boldsymbol{\xi}}\right) && i = k-N_\mathrm{f},\ldots,k \\
\mathbf{0} &\geq \mathbf{A}_\mathrm{o}\boldsymbol{x}_\mathrm{o}(i) + \boldsymbol{b}_\mathrm{o} && i = k-N_\mathrm{f},\ldots,k+1 \\
\mathbf{0} &\geq \mathbf{A}_\mathrm{p}\boldsymbol{p}_{\boldsymbol{\xi}} \quad + \boldsymbol{b}_\mathrm{p}
\end{aligned}$$

where the state equation $\boldsymbol{f}_\mathrm{o}(\cdot)$ and output equation $\boldsymbol{h}_\mathrm{o}(\cdot)$ are informed by (3.48), (4.13) resp. (3.41), (3.43), (3.44). The arrival cost $L_0(\cdot)$ and stage cost $L(\cdot)$ are chosen according to

$$L_0(\boldsymbol{x}_\mathrm{o}(k-N_\mathrm{f}),\boldsymbol{p}_{\boldsymbol{\xi}}) = \frac{1}{2}\left\| \begin{pmatrix} \boldsymbol{x}_\mathrm{o}(k-N_\mathrm{f}) \\ \boldsymbol{p}_{\boldsymbol{\xi}} \end{pmatrix} - \begin{pmatrix} \hat{\boldsymbol{x}}_\mathrm{o}(k-N_\mathrm{f}|k-N_\mathrm{f}-1) \\ \hat{\boldsymbol{p}}_{\boldsymbol{\xi}}(k-N_\mathrm{f}|k-N_\mathrm{f}-1) \end{pmatrix} \right\|^2_{\mathbf{Q}_0^{-1}} \tag{4.17}$$

$$L\left(\boldsymbol{\varepsilon}(i),\boldsymbol{v}(i)\right) = \frac{1}{2}\left\|\boldsymbol{\varepsilon}(i)\right\|^2_{\mathbf{Q}_{\boldsymbol{\varepsilon}}^{-1}} + \frac{1}{2}\left\|\boldsymbol{v}(i)\right\|^2_{\mathbf{Q}_{\boldsymbol{v}}^{-1}} \ . \tag{4.18}$$

Last, the polytopic inequality constraints characterized by $\mathbf{A}_\mathrm{o}$, $\mathbf{A}_\mathrm{p}$, $\boldsymbol{b}_\mathrm{o}$, $\boldsymbol{b}_\mathrm{p}$ encode requirements on the free variables, namely

$$\rho_{j,\min} \leq x_{\mathrm{o},j}(i) \leq \rho_{j,\max} \qquad j = 1,\ldots,4 \tag{4.19a}$$

$$0 \leq \omega_{l,j} \leq \omega_{\max} \qquad l = 3,\ldots,5 \qquad j = 1,\ldots,n_\mathrm{d} \tag{4.19b}$$

$$\omega_{l,j-1} - \omega_{l,j} \leq -\Delta\omega_{\min} \qquad l = 3,\ldots,5 \qquad j = 2,\ldots,n_\mathrm{d} \tag{4.19c}$$

with upper bounds $\rho_{j,\max}$ and lower bounds $\rho_{j,\min}$ on the actuator deflections, as well as bounds on the estimated mode frequencies $\omega_{\max}$ resp. its minimal difference $\Delta\omega_{\min}$.

Note, that there is no stage cost on $\boldsymbol{p}_{\boldsymbol{\xi}}$. Optimizing only one set of parameters conforms to the case of a state with noise-free state equation, whose dynamics equate to zero. Hence, the corresponding weighting matrix would tend to infinity, such that an additional stage cost can be omitted. In contrast, the arrival cost does depend on $\boldsymbol{p}_{\boldsymbol{\xi}}$ as well as its a priori estimate $\hat{\boldsymbol{p}}_{\boldsymbol{\xi}}(k-N_\mathrm{f}|k-N_\mathrm{f}-1)$. The weighting matrix $\mathbf{Q}_0$ is calculated recursively via a Riccati iteration, see section 2.6. Here, it is reasonable to define an artificial noise covariance for $\boldsymbol{p}_{\boldsymbol{\xi}}$, which lower bounds its error covariance. Thus, the algorithm may always innovate its mode parameter estimation if needed. Since the NLP originating from (4.16) is of the least-squares type, it can conveniently be solved by an SQP approach utilizing a Gauss-Newton approximation (2.54) of the Hessian matrix, cf. section 2.7. The MHE definition provided here differs from section 2.6 in the definition of the moving horizon. In fact, an additional state is added to the horizon, assuming

that $\boldsymbol{y}_\mathrm{m}(k)$ has already been processed. Normally, this would change the observation task to the derivation of a posterior estimates. However, the shift or rather addition in considered time instances is more rooted in the computational complexity of the MHE algorithm. Solving the underlying NLP will usually take up to one sampling interval. It is thus reasonable to make a priori estimates about $\hat{\boldsymbol{x}}_\mathrm{o}(k+1|k)$, which is calculated during $t \in [kT_\mathrm{e}, (k+1)T_\mathrm{e}]$. This way, an a priori estimate of the current state is available at each sampling instance, which also forms the basis of the MPC schemes in section 4.4.

Structured state observer:

$$\begin{aligned}
\min_{\boldsymbol{z}(:),\boldsymbol{p}_{\boldsymbol{\xi}}} \; & L_0(\boldsymbol{z}(k-N_\mathrm{f}),\boldsymbol{p}_{\boldsymbol{\xi}}) + \sum_{i=k-N_\mathrm{f}}^{k} L\left(\boldsymbol{\varepsilon}(i),\boldsymbol{v}(i)\right) && && (4.20)\\
\text{s.t.} \quad & \boldsymbol{\varepsilon}(i) = \boldsymbol{z}(i+1) - \boldsymbol{z}(i) && i = k-N_\mathrm{f},\dots,k\\
& \boldsymbol{v}(i) = \begin{pmatrix} \boldsymbol{\omega}_\mathrm{m}^{sen}(i) \\ \dot{\boldsymbol{v}}_\mathrm{m}^{sen}(i) \end{pmatrix} - \tilde{\boldsymbol{h}}\left(\boldsymbol{z}(i),\boldsymbol{p}_{\boldsymbol{\xi}}\right) && i = k-N_\mathrm{f},\dots,k\\
& \boldsymbol{0} \quad \geq \mathbf{A}_\mathrm{p}\boldsymbol{p}_{\boldsymbol{\xi}} \quad + \boldsymbol{b}_\mathrm{p}
\end{aligned}$$

where the fact has been used, that $\boldsymbol{z}$ describes random walk processes and that the reduced output equation $\bar{\boldsymbol{h}}(\cdot)$ is informed by (3.43) alone. The arrival cost $L_0(\cdot)$ and stage cost $L(\cdot)$ are chosen equivalent to the full state observer (4.16), i.e.

$$L_0(\boldsymbol{z}(k-N_\mathrm{f}),\boldsymbol{p}_{\boldsymbol{\xi}}) = \frac{1}{2}\left\| \begin{pmatrix} \boldsymbol{z}(k-N_\mathrm{f}) \\ \boldsymbol{p}_{\boldsymbol{\xi}} \end{pmatrix} - \begin{pmatrix} \hat{\boldsymbol{z}}(k-N_\mathrm{f}|k-N_\mathrm{f}-1) \\ \hat{\boldsymbol{p}}_{\boldsymbol{\xi}}(k-N_\mathrm{f}|k-N_\mathrm{f}-1) \end{pmatrix} \right\|^2_{\mathbf{Q}_0^{-1}} \tag{4.21}$$

$$L\left(\boldsymbol{\varepsilon}(i),\boldsymbol{v}(i)\right) = \frac{1}{2}\left\|\boldsymbol{\varepsilon}(i)\right\|^2_{\mathbf{Q}_{\boldsymbol{\varepsilon}}^{-1}} + \frac{1}{2}\left\|\boldsymbol{v}(i)\right\|^2_{\mathbf{Q}_{\boldsymbol{v}}^{-1}} \; . \tag{4.22}$$

Last, inequality constraints for the mode parameters $\boldsymbol{p}_{\boldsymbol{\xi}}$ are included as before

$$0 \leq \quad \omega_{l,j} \qquad \leq \omega_\mathrm{max} \qquad l = 3,\dots,5 \qquad j = 1,\dots,n_\mathrm{d} \tag{4.23a}$$

$$-\omega_{l,j} + \omega_{l,j-1} \leq -\Delta\omega_\mathrm{min} \qquad l = 3,\dots,5 \qquad j = 2,\dots,n_\mathrm{d} \tag{4.23b}$$

with bounds on the estimated mode frequencies ω_max and its minimal difference $\Delta\omega_\mathrm{min}$. As shown in Fig. 4.2.2, the crane states are estimated in parallel using an EKF.

Compared to (4.16), the NLP derived from (4.20) is of much smaller complexity. A comparison of both observers in terms of estimation accuracy and real-time-feasibility is presented next.

4.2.3 State Reconstruction

Both observer designs are tested in simulation for two wave disturbances. First, a JONSWAP spectrum (3.7) with $H_s = 0.8\,\mathrm{m}$ and $\omega_p = 0.87\,\mathrm{rad/s}$ is investigated. Then, the observer performance for a TORSETHAUGEN spectrum of same characteristic values is studied. The sensor models are parameterized with realistic values. The IMU characteristics are taken from [131], where the authors identified the model of a tactical-grade STIM300 MEMS IMU.

In Fig. 4.6, the spectrograms (i.e. the time-resolved frequency contents) of the vessel motions are plotted for both disturbance cases. Here, a moving time window of 12 s have been used for the time-frequency analysis. The window length thus fits a full period of the peak frequency ω_p. In contrast to other spectrograms, the color scale maps the magnitude information instead of the power content of each frequency. The dominant mode is highlighted in red. The two spectra suggest that the vessel motions are governed by a fundamental frequency which only varies slowly. As expected, the TORSETHAUGEN spectrum yields motions containing multiple modes, although of smaller magnitude. The

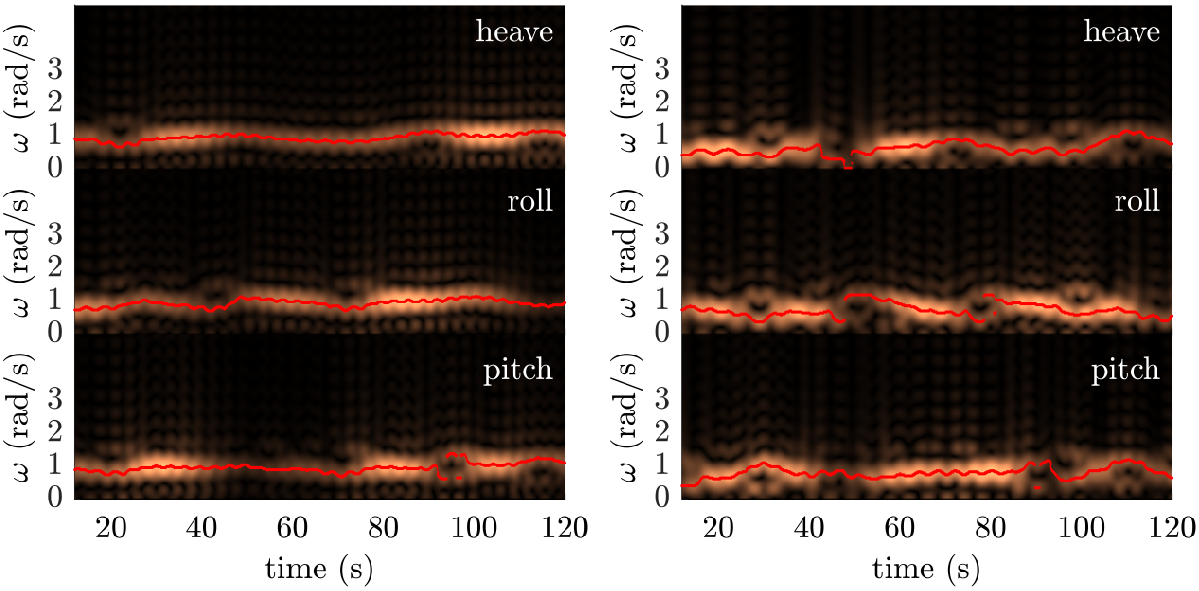

(a) JONSWAP excitation **(b)** TORSETHAUGEN excitation

Fig. 4.6: Spectrograms of exemplary vessel motions – The frequency content of the vessel motions are depicted for wave profiles drawn from a JONSWAP spectrum (left) and TORSETHAUGEN spectrum (right), both of which are parameterized according to $H_s = 0.8\,\mathrm{m}$ and $\omega_p = 0.87\,\mathrm{rad/s}$. A window length of 12s is applied. The dominant mode is highlighted in red.

estimation results of both state observers during JONSWAP excitation are shown in

Fig. 4.7. The ship response is approximated using three modes. To limit the scope, the analysis is restricted to the reconstructed vessel motions $\xi_i(t)$ with $i \in \{3, 4, 5\}$ and the payload deflection angles φ_1, φ_2. The simulated ground truth is shown in blue, while the estimated trajectories are depicted in red resp. green. After convergence of the filters, the estimates closely follow the true system trajectories. On closer inspection, it is noticeable that system and observed trajectories match better in frequency and phase than in amplitude. For the vessel motions, only small differences between full and structured state observer could be observed, that are apparent mostly during the initial transients. Yet, the structured observer shows considerable more uncertainty around the payload deflection angles. The results should be interpreted taking into account the only manual tuning. The observer designs were also tested for a TORSETHAUGEN excitation, for

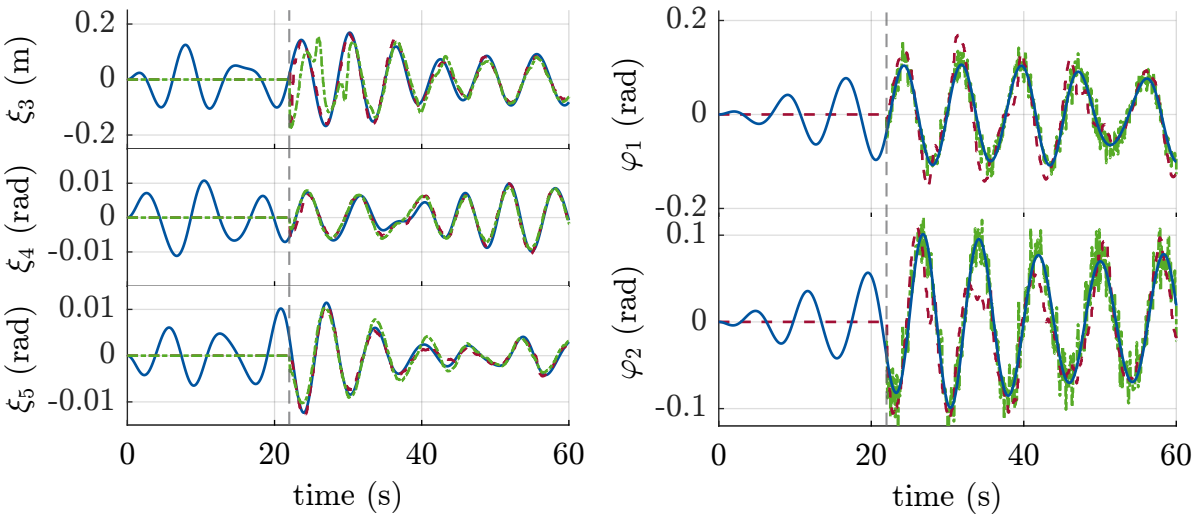

(a) Vessel trajectories **(b)** Payload trajectories

Fig. 4.7: Observer performance during JONSWAP excitation – The estimates of the full state observer (red) and structured state observer (green) are compared to the simulated (blue) vessel motions (left) and payload deflections (right) for wave disturbances sampled from a JONSWAP spectrum with $H_\mathrm{s} = 0.8\,\mathrm{m}$ and $\omega_\mathrm{p} = 0.87\,\mathrm{rad/s}$. The observers are initialized at $t = 22\,\mathrm{s}$ (dotted gray line).

which attaining a reasonable observer performance proved challenging. In particular, the filter parameterization used during the JONSWAP excitation did not generate adequate estimates. Increasing the number of estimated modes by one and retuning the covariance matrices yielded more accurate estimates. Notably, the initial transients until the filters converge to reasonable estimates are more pronounced compared to the case of the JONSWAP excitation. The computational complexity of both observers differs due to the varying size of the underlying optimization problems (4.16) and (4.20). In Tab. 4.1, the recorded computation times for the simulation case in Fig. 4.7 are summarized. The same parameterization (horizon length, sample time, number of SQP iterations, ...) is

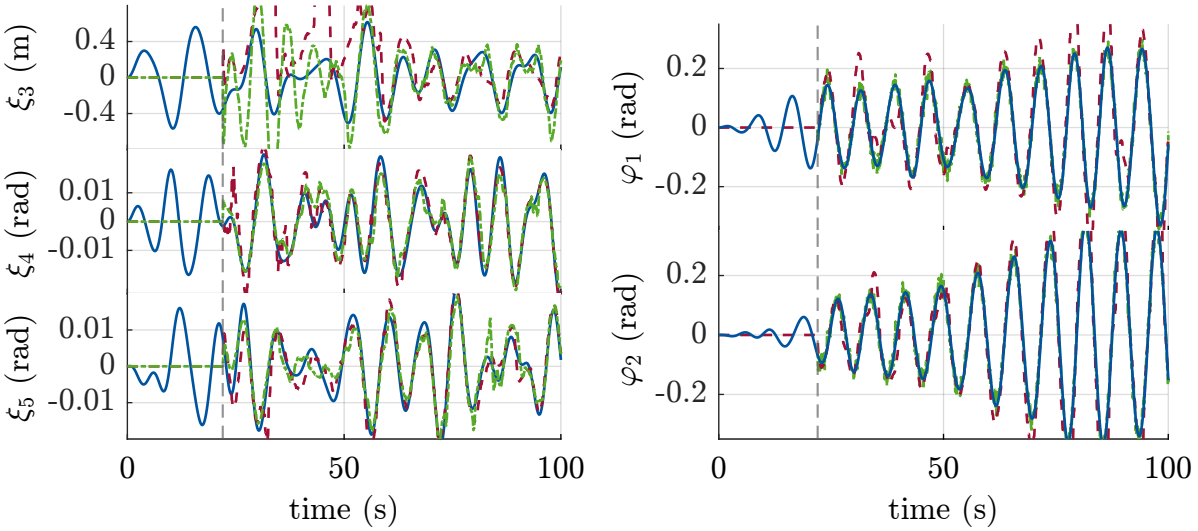

(a) Vessel trajectories

(b) Payload trajectories

Fig. 4.8: Observer performance during TORSETHAUGEN excitation – The estimates of the full state observer (red) and structured state observer (green) are compared to the simulated (blue) vessel motions (left) and payload deflections (right) for wave disturbances sampled from a TORSETHAUGEN spectrum with $H_\mathrm{s} = 0.8\,\mathrm{m}$ and $\omega_\mathrm{p} = 0.87\,\mathrm{rad/s}$. The observers are initialized at $t = 22\,\mathrm{s}$ (dotted gray line).

used for both MHE. The computation times are analyzed for their mean value μ_{t_c} and standard deviation σ_{t_c}. The comparison is qualitative, since the absolute computation times are e.g. hardware- and solver-specific. As expected, the structured state observer performs much faster compared to the holistic MHE design. This is mainly due to the difference in optimization variables, which amounts to a third. Looking at the set cycle time of $T_\mathrm{e} = 0.1\mathrm{s}$, only the structured observer design is real-time feasible.

Table 4.1: Computational times of the different observer designs

design	μ_{t_c} (s)	σ_{t_c} (s)
full	0.1812	0.0557
structured	0.0280	0.0142

4.2.4 Short-time Prediction of the Vessel Motions

In context of an MPC an estimate of the future vessel motions is required to derive open loop predictions of the system trajectories. Hence, the accuracy of the short-time extrapolation becomes crucial. Up to this point, the a priori estimates of the one-step

ahead vessel and crane state vectors $\hat{\boldsymbol{x}}_{\mathrm{ves}}(k+1|k)$ resp. $\hat{\boldsymbol{x}}_{\mathrm{kbc}}(k+1|k)$ were analyzed, see section 4.2.3. In contrast, the focus here is on the prediction error of $\hat{\boldsymbol{x}}_{\mathrm{ves}}(:|k)$ over the MPC's prediction horizon T_{p}. The fundamental challenge is depicted in Fig. 4.9. The presented MHE-based observer designs gather IMU measurements over a horizon of length T_{f} and subsequently fit a sum of modes to the (transformed) data. Doing so results in an estimated set of parameters characterizing the vessel motions over the filter horizon. Extrapolation to the prediction horizon is then straightforward by evaluating (4.9) for $t = T_{\mathrm{s}}, 2T_{\mathrm{s}}, \ldots, T_{\mathrm{p}}$, yielding $\hat{\boldsymbol{\xi}}(:|k)$. To assess the prediction accuracy the following error measure is introduced

$$e_{\mathrm{p}}(T,k) = \sqrt{\sum_{i=1}^{T/T_{\mathrm{s}}} \frac{T_{\mathrm{s}}}{T} \|\boldsymbol{\xi}(kT_{\mathrm{e}} + iT_{\mathrm{s}}) - \hat{\boldsymbol{\xi}}(i|k)\|_{\boldsymbol{\Lambda}}^2} \tag{4.24}$$

with a weighting matrix $\boldsymbol{\Lambda} \in \mathbb{R}^{d\times d}$, the data sample time T_{s} and a free multiple $T = mT_{\mathrm{s}} \in \mathbb{R}_{\leq T_{\mathrm{p}}}$ of the same, $m \in \mathbb{N}$. In the simulative setting, the choice of T_{s} is only lower bounded by the step time of the simulation. However, setting $T_{\mathrm{s}} = T_{\mathrm{c}}$ is reasonable considering the use case. The error measure (4.24) constitutes a *root-mean-square* error of variable length. Hereafter, different values of T are used to assess the prediction accuracy over varying time horizons. The error (4.24) may be calculated for each iteration k of the observer. The resulting error trajectories reflect the convergence behavior of the observer, before eventually varying within a certain error band. For analysis, summarizing the error trajectories by their respective mean value

$$\mu_{e_{\mathrm{p}}}(T) = \frac{1}{n}\sum_{i=1}^{n} e_{\mathrm{p}}(T,k) \tag{4.25}$$

with the number of recorded samples n is sensible, as it allows quantifying the average error that is to be expected over a prediction horizon of $T_{\mathrm{p}} = T$. In Fig. 4.10, the prediction performance of the structured observer design is assessed for different combinations of prediction length T and moving filtering horizon T_{f}. In favor of a simplified presentation, multiple intersections of the three-dimensional performance map are depicted in Fig. 4.10a and Fig. 4.10b, respectively. As would be expected from the time variant modes in Fig. 4.6, the average prediction error increases with the prediction time T as the estimated disturbance parameters $\boldsymbol{p}_{\boldsymbol{\xi}}$ loose validity. Moreover, the data points shown in Fig. 4.10a suggest that the prediction error is worse for short filtering horizons. The trend is confirmed in Fig. 4.10b, where uneven filtering horizons furthermore yield local maxima in prediction error. This may be linked to the interaction of the filtering horizon and the dominant period but could also stem from the observer parameterization, that was not optimized for different filtering horizons. Overall, the question of a viable prediction horizon as a function of the filtering horizon is a complex one that should be answered by means of closed loop comparisons, cf. section 4.5. Yet, the prediction performance should benefit from longer horizons, although computational complexity will increase simultaneously.

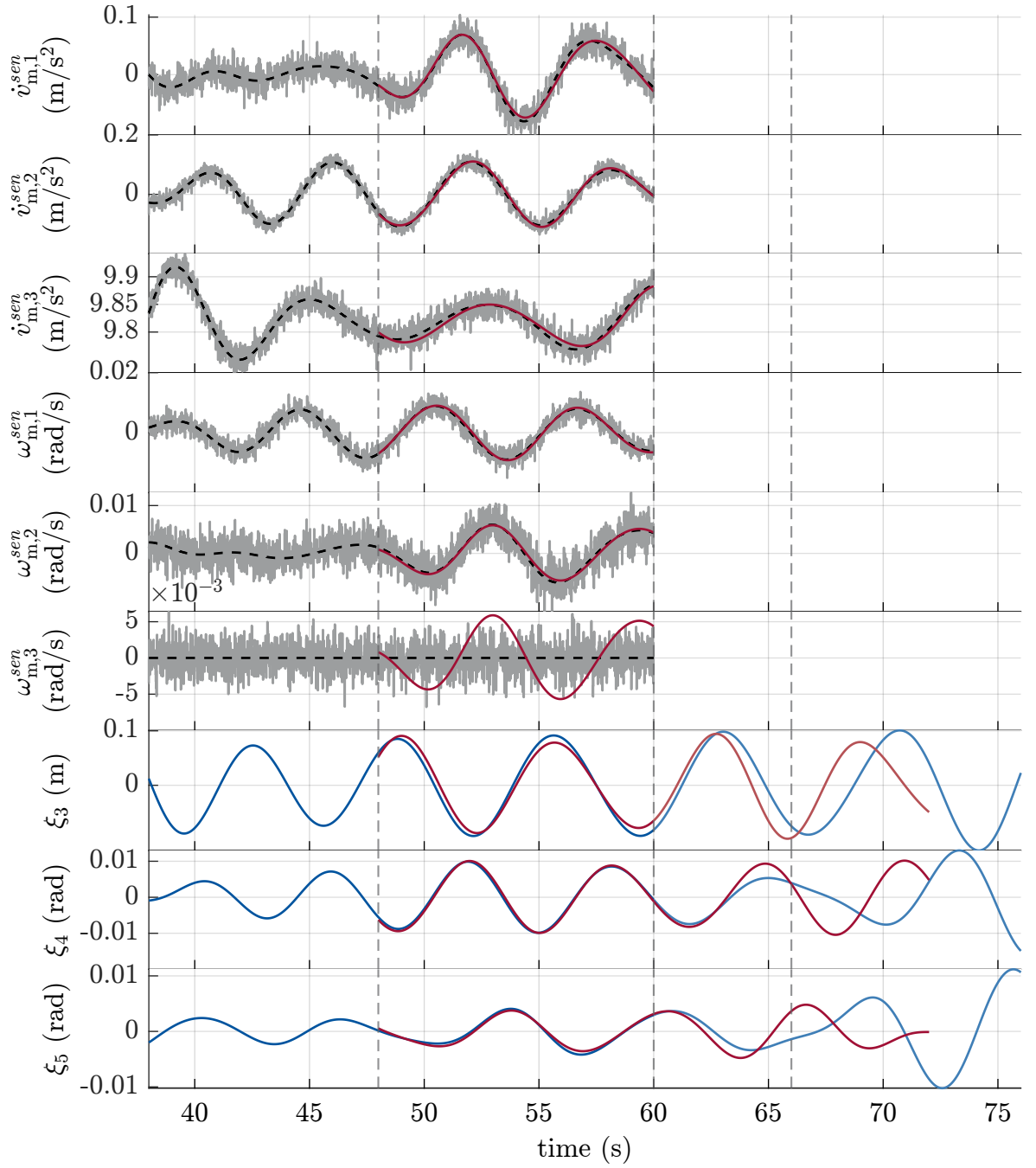

Fig. 4.9: Observer-based prediction of the vessel motions – The IMU measurements (top six plots) are collected over the filter horizon $T_\mathrm{f} = 12\,\mathrm{s}$ and used to fit a harmonic motion profile at $t = 60\mathrm{s}$, cf. section 4.2.1. The vessel motions are then extrapolated over the MPC's prediction horizon $T_\mathrm{p} = 6\,\mathrm{s}$. Shown trajectories are measurements (black), simulated ground truth (blue) and estimates (red).

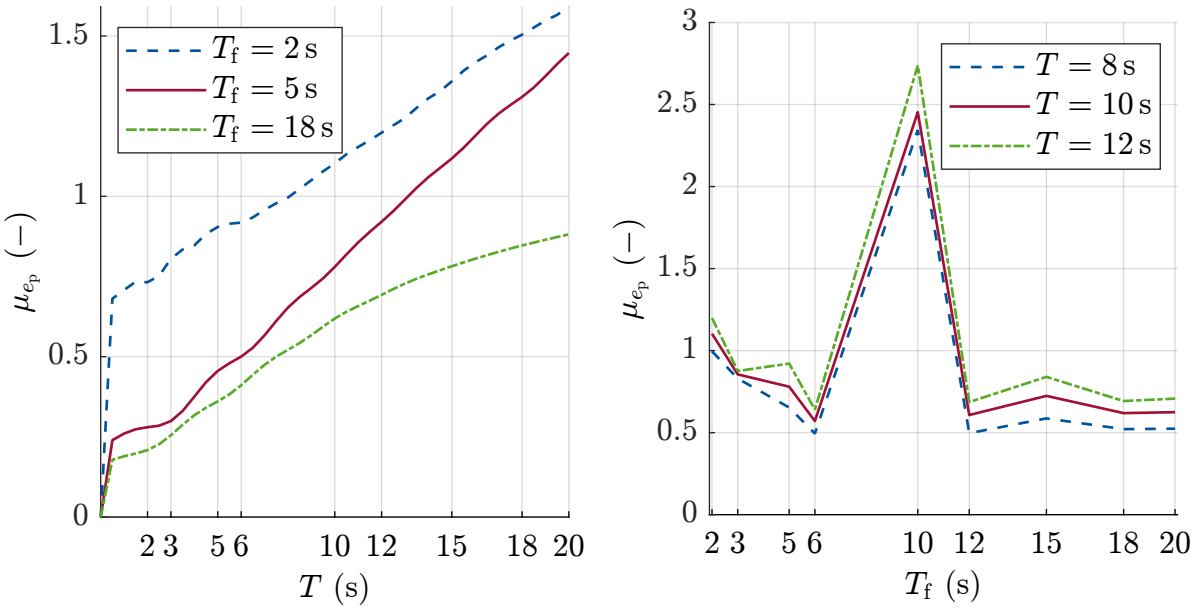

(a) Prediction error as function of the prediction length T

(b) Prediction error as function of the filtering horizon T_f

Fig. 4.10: Prediction performance of the MHE – The average prediction error μ_{e_p} over a simulation run is depicted for different combinations of moving horizon T_f and prediction length T. The weighting matrix $\mathbf{\Lambda}$ is chosen diagonal, where the entries reflect the respective maximum signal amplitude. Various intersections of the three-dimensional performance map are presented.

4.2.5 Discussion of the observer designs

Two observer designs were proposed for reconstructing the vessel and crane state as well as to provide means of predicting the vessel motions. Both concepts build on a MHE that processes the IMU measurements. From a system's perspective, the approximation of the vessel motions via sums of modes and subsequent estimation of the mode parameters is elegant, as no model of the specific vessel is required. However, the approach suffers from the considered setup not including additional position sensors that could be used to correct the estimated states and biases. A conclusive benefit of fusing the sensor data of the comoved camera was not observed. Instead, the holistic MHE proved challenging with respect to real-time feasibility. Up to this point, only the structured observer design yields real-time feasible computation times. Last, the extrapolation (prediction) capabilities of the algorithms were studied. While the relation of different parameters such as the prediction and filtering horizon requires further understanding, the simulation data suggests that the sensor-observer setup is able to provide short-time predictions of the vessel motions for MPC. Additional research may be directed towards the robustness of the disturbance estimation in conjunction with different wave and vessel models. Also,

model uncertainties like misalignments in e.g. the IMU's reference frame should be investigated before implementing the approach in a real world scenario.

4.3 Target Selection

The considered KBC possesses four hydraulically driven DoF to manipulate the payload position. In comparison to traditional boom cranes, the knuckle jib adds to the crane's flexibility, e.g. during close proximity operation. As argued in section 3.5, the four actuators render the crane redundant with respect to the payload's three-dimensional Cartesian position, which is illustrated in Fig. 4.11. Since the crane kinematics allow for different tip heights h_c at a constant crane radius r_c (red line in Fig. 4.11), the same payload position is obtained by multiple crane configurations assuming that the free cable length q_4 is adjusted accordingly. As a result, the payload can be lowered either by winch actuation or by moving the crane tip. As the realizable vertical travel is limited, nodding boom maneuvers are of less importance in most crane operations. Yet, for automatic control the problem of ambiguity arises. Given a reference position $\boldsymbol{w}_\mathrm{load}^{ned}$ for the payload, the crane's tip height remains as a free variable. In [S2], incorporation of secondary control objectives via optimization of the tip height was studied. The presented target selector is summarized below, starting with the general problem formulation in section 4.3.1. Thereafter, a particular objective on the basis of the crane's manipulability is derived in section 4.3.2, which is then tested simulative in section 4.3.3.

4.3.1 Optimization Problem

The target selector aims at finding an optimal tip height z_tip^* with reference to the crane's *root*-frame that is consistent with a given payload reference $\boldsymbol{w}_\mathrm{load}^{ned}$. To this end, the flat mapping (3.58) can be used to translate the output reference to the crane's actuator space $\mathcal{P}$, which informs the following general optimization problem

$$
\begin{aligned}
z_\mathrm{tip}^* = \ \arg\min_{z_\mathrm{tip}} \quad & J\left(\boldsymbol{\rho}\right) \\
\text{s.t.} \quad & \boldsymbol{\rho} \in \mathcal{P} \ , \\
& \boldsymbol{\rho} = \boldsymbol{\psi}_\rho \left(\boldsymbol{z} = \begin{pmatrix} \boldsymbol{w}_\mathrm{load}^{ned} \\ z_\mathrm{tip} \end{pmatrix}, \ddot{\boldsymbol{\gamma}} = \boldsymbol{0}, \boldsymbol{\xi} \right)
\end{aligned}
\tag{4.26}
$$

with some objective function $J\left(\boldsymbol{\rho}\right)$ rating the crane configuration and the extended (flat) output $\boldsymbol{\gamma}$. Note, that for applications other than payload stabilization $\ddot{\boldsymbol{w}}_\mathrm{load}^{ned}$ will be unequal to zero, e.g. during trajectory tracking. By virtue of the constraints, the optimal tip height z_tip^* is dependent on not only the given payload reference $\boldsymbol{w}_\mathrm{load}^{ned}$ but also the current vessel pose $\boldsymbol{\xi}$. During operation, the vessel pose is estimated by an observer,

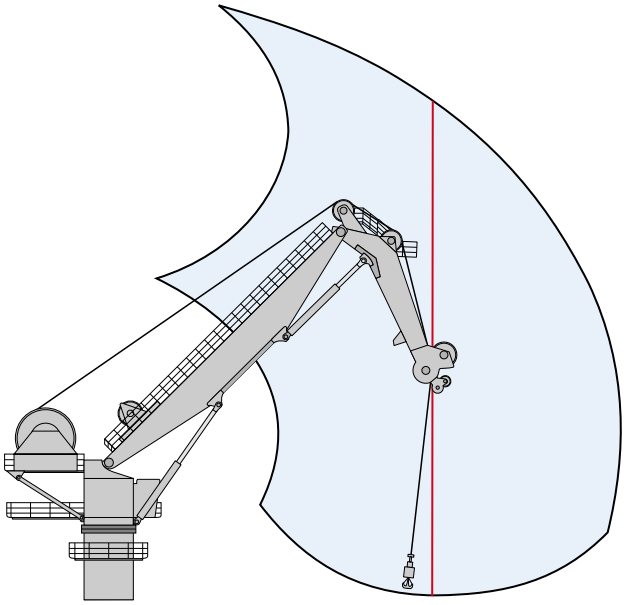

Fig. 4.11: Ambiguity of the payload actuation – The crane is redundant with respect to manipulation of the payload's vertical position. The crane tip can be configured to different heights at the same radii, cf. red line. The ambiguity arises if the free cable length is actuated accordingly.

i.e. $\boldsymbol{\xi} \approx \hat{\boldsymbol{\xi}}$. In general, arbitrary objective functions may be designed depending on the application. Next, a particular choice maximizing the crane's manipulability, i.e. its ability to translate actuator movements into tip velocities, is discussed in the context of payload stabilization.

4.3.2 Crane Manipulability

A fundamental strategy to dissipate energy from an oscillating payload is based on the repeated horizontal alignment of crane tip and payload. During payload stabilization, the ASC performance of the crane is thus closely connected to its capability to move in the *north-east*-plane. To understand how the transmission of actuator to Cartesian end effector (i.e. tip) velocities varies with the crane configuration, the so-called *manipulability ellipsoid* [159] of a serial manipulator may be assessed. In this context, consider the set of unit norm actuator velocities $\dot{\boldsymbol{\rho}}^{\mathrm{T}}\dot{\boldsymbol{\rho}} = 1$. These yield tip velocities in the Cartesian space, which satisfy

$$(\dot{\boldsymbol{p}}_{\mathrm{tip}}^{root})^{\mathrm{T}} \left(\mathbf{J}_{\phi_{\mathrm{fk}}}(\boldsymbol{\rho})^{-1}\right)^{\mathrm{T}} \mathbf{J}_{\phi_{\mathrm{fk}}}(\boldsymbol{\rho})^{-1} \dot{\boldsymbol{p}}_{\mathrm{tip}}^{root} = 1 \tag{4.27}$$

with the Jacobin $\mathbf{J}_{\phi_{\mathrm{fk}}}(\rho) = \nabla_{\rho_{1,\dots,3}} \boldsymbol{\phi}_{\mathrm{fk}}(\boldsymbol{\rho}) \in \mathbb{R}^{3\times 3}$, cf. (3.12). The inverse of $\mathbf{J}_{\phi_{\mathrm{fk}}}$ is well-defined on $\mathcal{P}$, since the crane structure has no singular configurations. In order to

assess the tip velocity in the $\boldsymbol{e}_\mathrm{n}\boldsymbol{e}_\mathrm{e}$-plane, (4.27) is rotated to the global *ned*-frame by

$$(\dot{\boldsymbol{p}}_\mathrm{tip}^{ned})^\mathrm{T}\mathbf{R}_{root}^{ned}(\boldsymbol{\xi})\left(\mathbf{J}_{\phi_\mathrm{fk}}^{-1}(\boldsymbol{\rho})\right)^\mathrm{T}\mathbf{J}_{\phi_\mathrm{fk}}^{-1}(\boldsymbol{\rho})\left(\mathbf{R}_{root}^{ned}(\boldsymbol{\xi})\right)^\mathrm{T}\dot{\boldsymbol{p}}_\mathrm{tip}^{ned} = 1 \tag{4.28}$$

before being queried at a planar velocity $\dot{\boldsymbol{p}}_\mathrm{tip}^{ned} = (\dot{n}\,\dot{e}\,0)^\mathrm{T}$ yielding

$$\begin{pmatrix}\dot{n} & \dot{e}\end{pmatrix}\mathbf{M}(\boldsymbol{\rho},\boldsymbol{\xi})\begin{pmatrix}\dot{n} & \dot{e}\end{pmatrix}^\mathrm{T} = 1 \tag{4.29}$$

where $\mathbf{M}$ denotes the upper 2×2 block matrix of the quadratic form's core in (4.28). Equation (4.29) characterizes an ellipse whose principal axes describe the crane's manipulability. For ASC, isotropic manipulability regarding all directions in the $\boldsymbol{e}_\mathrm{n}\boldsymbol{e}_\mathrm{e}$-plane is desirable, which correlates to the ellipse's area $A = \frac{\pi}{\sqrt{\det\mathbf{M}}}$. Following [S2], the target selector's objective function is then inferred as

$$J_\mathrm{me}(\boldsymbol{\rho},\boldsymbol{\xi}) = \frac{1}{2}\left(\det\mathbf{M}(\boldsymbol{\rho},\boldsymbol{\xi})\right)^2 \tag{4.30}$$

which under minimization maximizes the ellipse's area. For vanishing wave disturbances a lookup table can be generated that holds the manipulability index (4.30) depending on the crane configuration. Since the costs are invariant to rotations around the crane tower, the table may be also queried by specifying a pair of crane radius and tip height, i.e. $(r_\mathrm{c}, h_\mathrm{c})$. A visualization of the lookup table is included in Fig. 4.12, where the negative cost function $-J_\mathrm{me}(\boldsymbol{\rho},\mathbf{0})$ is plotted for convenience. Crane configurations of high manipulability are marked in green, while small manipulability is indicated by blue shades. The mapping is non-convex, which complicates online optimization of (4.29). However, the disturbance-free lookup table could be used to efficiently generate initial guesses of the optimal solution. In practice, one might not be interested in finding the global manipulability optimum but rather opt for a near local minimum that does not require large tip travel.

4.3.3 Simulative Validation

Optimizing the crane's manipulability aims at an improved utilization of actuator capacity during payload stabilization. In [S2], the payload response to persistent wave disturbances is studied under active control with target selection. A nonlinear controller based on feedback linearization is used to close the control loop. For details on the controller design, please refer to the aforementioned contribution. Noteworthy, the controller requires the optimized tip height reference trajectory to be continuously differentiable up to the fourth order due to the crane's relative degree, cf. section 2.4 resp. section 3.5. This can easily be realized by filtering the output of the target selector, i.e. the optimized crane tip height z_tip^*, by a fourth order system.

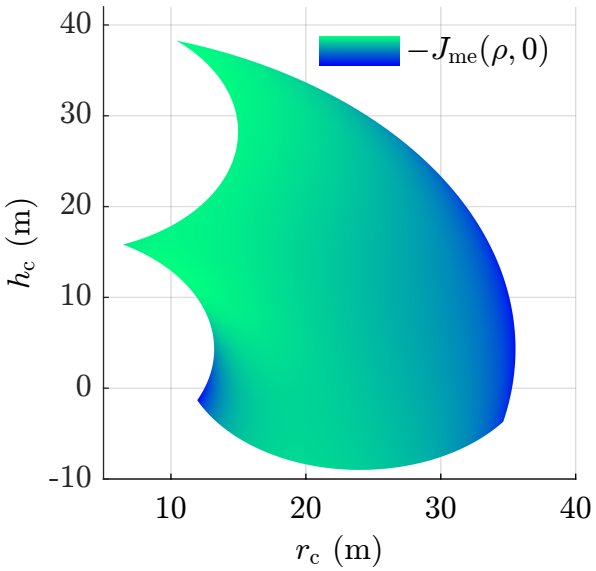

Fig. 4.12: Depiction of the manipulability index – The objective (4.30) is visualized for zero vessel deflection, i.e. $\boldsymbol{\xi} = \mathbf{0}$. For improved interpretability, the negative costs are plotted such that regions of high manipulability are marked in green, while configurations of small manipulability are shaded blue.

The following results are reproduced from [S2]. The closed loop payload response with and without target selector is depicted in Fig. 4.13 for a JONSWAP excitation of $H_s = 2\,\mathrm{m}$ and $\omega_p = 0.72\,\mathrm{rad/s}$. The control performance without target selection is poor as the Euclidean error decays only slowly. Looking at the manipulated variables reveals that the controller operates near or on the actuator constraints most of the time. On the other hand, smaller steady state offsets are observed when optimizing the tip height. The performance measures are summarized below in Tab. 4.2. The data suggests, that the target selector mainly affects the anti-sway performance. Since objective (4.30) is designed just for that, the simulation results seem plausible.

Table 4.2: Performance measures of control with and without target selection

(a) Target selector off

i	d_i	$e_{\infty,i}$
r	0.06	0.92 m
s	0.05	0.05 rad
h	–	0.22 m

(b) Target selector on

i	d_i	$e_{\infty,i}$
r	0.07	0.57 m
s	0.03	3e−3 rad
h	–	0.39 m

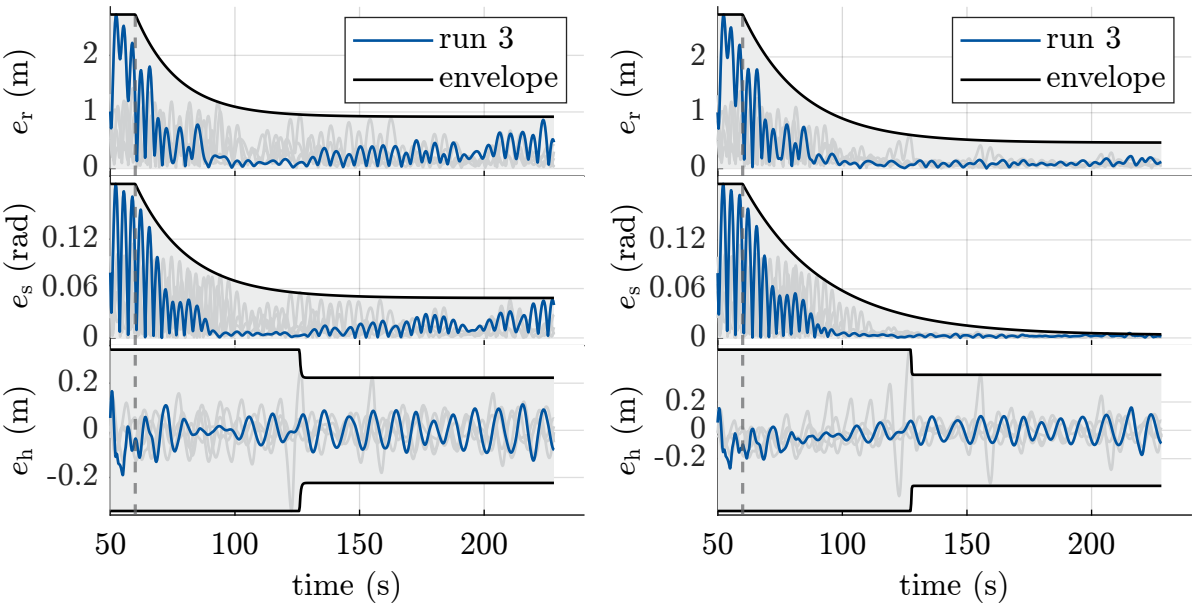

(a) Target selector off

(b) Target selector on

Fig. 4.13: Error trajectories for control with and without target selection – The crane system is simulated for random wave realizations drawn from a JONSWAP spectrum with $H_s = 2\,\mathrm{m}$ and $\omega_p = 0.72\,\mathrm{rad/s}$. The controller is activated at $t = 60\,\mathrm{s}$. The payload trajectories are assessed by means of their error signals $e_i(t)$ with $i \in \{\mathrm{r}, \mathrm{s}, \mathrm{h}\}$. On the left, a constant tip height reference is used. In contrast, the simulations on the right apply a target selector to optimize the crane tip height with regard to the crane's manipulability.

4.4 Predictive Payload Controller

In section 1.4, multiple deficits with regard to current approaches to payload control at sea were indicated. In particular, active heave compensation (AHC) and anti-sway control (ASC) are usually treated separately, whereby the coupling between both vertical and horizontal payload oscillations is disregarded. In addition, the limited dynamics of the crane actuators are often ignored during controller synthesis. Feasibility of the actuation signals may in principle be obtained trough appropriate tuning of most control schemes. However, the required level of actuation will depend on the sea state. The latter furthermore informs varying magnitudes in the feedback signals, which renders controller tuning challenging. Model predictive control presents an elegant way to explicitly consider both deficits by design. While coupled payload motions are inherently mapped by the underlying system model from section 3.4, the actuator limitations can be included as constraints to the resulting OCP, cf. section 2.5 and section 4.4 respectively. Yet, similar to the MHE presented above, model predictive controllers are computational involved

such that derivation of real-time feasible codes present a main challenge when applying MPC. Hereafter, three different techniques to discretize the OCP are discussed both in terms of obtainable controller performance and computational times.

4.4.1 Preliminaries to Predictive Payload Control

In MPC theory two distinct horizons are usually considered. The prediction horizon T_p defines the time span over which the system trajectories are evaluated. To restrict computational complexity of the controller design it is further common practice to define a control horizon $T_\mathrm{u} < T_\mathrm{p}$ after which the control inputs are kept constant, i.e. $\boldsymbol{u}(k+t_i|k) = \boldsymbol{u}(k+T_\mathrm{u}|k)\ \forall\, t_i \geq T_\mathrm{u}$. In this way, the number of free variables in the MPC's optimization problem and hence its computational complexity is reduced. Unfortunately, the approach has an adverse effect on predictive payload stabilization, as the persistent wave excitation precludes the possibility of a constant actuation signal yielding high control performance. Therefore, other means of reducing the computational complexity have to be investigated. In scope of this work, B-Splines are applied to restrict the admissible solution space of input trajectories $\boldsymbol{u}(:|k)$ to

$$u_i(k+t|k) = S_{B,i}(t) = \sum_{j=1}^{m+l-2} \alpha_{i,j} B_{j,l}(t) = \left(B_{1,l}\left(t\right)\ \ldots\ B_{d,l}\left(t\right)\right)\boldsymbol{\alpha}_i \qquad i = 1,\ldots,4$$
$$t \in [0, T_\mathrm{p}]$$

with the spline basis functions $B_{j,l}$, the spline order l, number of knots m and number of basis functions $d = m + l - 2$, see section 2.2. Note that the substitution does also cover the standard MPC formulation with one free variable per sampling instance and actuator. For this, a zero-order spline with equidistant knots placed at intervals of T_c has to be specified. Depending on the spline order and number of inner knots, notable saves in optimization variables can be obtained. An exemplary input trajectory is shown in Fig. 4.14, where all sampled inputs $u(:|k)$ are spanned by a quadratic spline curve with knots at every tenth sampling interval. The difference in optimization parameters for all actuators would be 90%.

Irrespective of the specific MPC formulation, a general challenge lies in the computational complexity of predictive algorithms. The receding horizon approach in conjunction with numerical optimization yields codes that usually require computation times of hundreds of milliseconds up to multiple seconds. It is thus impractical to process the current sensor readings, calculating the MPC problem and triggering a change in actuation all at an instance. For most applications it is thus reasonable to shift the considered control problem by one time step T_c. As a result, the first free manipulated variable considered for MPC is not $\boldsymbol{u}(k|k)$ but $\boldsymbol{u}(k+1|k)$. The current input to the system is read from memory, which from a system theory viewpoint is realized by a unit delay or

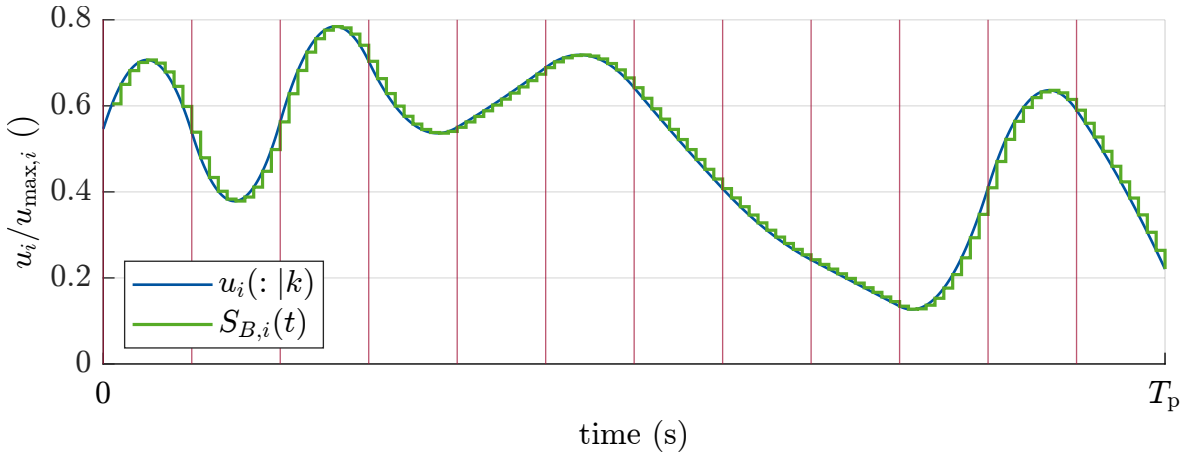

Fig. 4.14: Spline approximation of input trajectory – The input trajectory (green) is constrained by a spline (blue). The latter is defined by its (quadratic) order and the knot sequence along the prediction horizon T_p, indicated in red.

memory block. Recalling that an optimization-based observer was introduced in section 4.2, alignment of the different modules become important. The considered sequencing is depicted in Fig. 4.15. Computational wise the emergence of multicore CPUs in modern control hardware allow for the concurrent solving of both MHE and MPC. Thus, the timing restriction is one cycle time T_s for each module. For simplicity, it will be assumed that $T_\mathrm{c} = T_\mathrm{e} = T_\mathrm{s}$. In practice, the sample rates of different actuators and sensors has to be considered during system engineering.

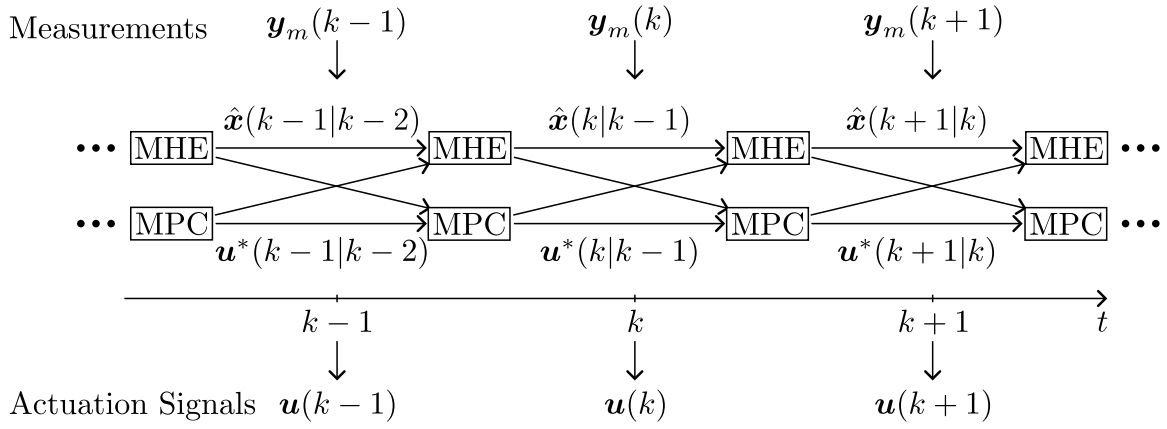

Fig. 4.15: Scheduling in receding horizon estimation and control – At each time instance i, the MHE and MPC are computed concurrently starting at the a priori estimate $\hat{\boldsymbol{x}}(i|i-1)$ and optimized input $\boldsymbol{u}^*(i|i-1)$ calculated during the previous time step.

All following MPC formulations are based on the definition of the control task in section

4.1.1, which covers both payload stabilization and trajectory tracking. Distinctions stem from the way the OCP Eq. (2.30) is compiled to a finite program. The presented approaches draw from the own publications [S5] and [S1].

4.4.2 Linear Model Predictive Control

The computational complexity of a predictive payload controller stems from the nonlinear system dynamics (3.49). A straightforward way to mitigate the effects of nonlinearities during prediction is to linearize the system beforehand. The linearization is updated at each sampling instance, realizing a *successive* linearization scheme. After time discretization a linear MPC can be established, which gives rise to the following algorithm:

Linear MPC: The system dynamics (3.49) and performance output equations (3.51a) are linearized around the current a priori state estimates $\hat{\boldsymbol{x}}(k|k-1) = (\hat{\boldsymbol{x}}_{\mathrm{kbc}}(k|k-1)^{\mathrm{T}}\, \hat{\boldsymbol{x}}_{\mathrm{kbc}}(k|k-1)^{\mathrm{T}})^{\mathrm{T}}$ and the inputs $\boldsymbol{u}^*(k|k-1)$, $\hat{\boldsymbol{d}}(k|k-1)$. The latter is provided by the observer alongside the state estimates, cf. section 4.2. Doing so yields a linear system description

$$\dot{\boldsymbol{x}} \approx \mathbf{A}\boldsymbol{x} + \mathbf{B}_{\mathrm{u}}\boldsymbol{u} + \mathbf{B}_{\xi}\boldsymbol{d} + \mathbf{I}_{n\times n}\bar{\boldsymbol{x}} \tag{4.31a}$$

$$\boldsymbol{y} \approx \mathbf{C}\boldsymbol{x} + \mathbf{D}_{\mathrm{u}}\boldsymbol{u} + \mathbf{D}_{\xi}\boldsymbol{d} + \mathbf{I}_{p\times p}\bar{\boldsymbol{y}} \tag{4.31b}$$

where the shorthand notations

$$\bar{\boldsymbol{x}} = \dot{\boldsymbol{x}}(k) - \mathbf{A}\hat{\boldsymbol{x}}(k|k-1) - \mathbf{B}_{\mathrm{u}}\boldsymbol{u}^*(k|k-1) - \mathbf{B}_{\xi}\hat{\boldsymbol{d}}(k|k-1)$$

$$\bar{\boldsymbol{y}} = \boldsymbol{y}(k) - \mathbf{C}\hat{\boldsymbol{x}}(k|k-1) - \mathbf{D}_{\mathrm{u}}\boldsymbol{u}^*(k|k-1) - \mathbf{D}_{\xi}\hat{\boldsymbol{d}}(k|k-1)\ .$$

have been introduced to improve readability. A time-discrete version is obtained by applying the matrix exponential (2.27) to (4.31a) giving

$$\boldsymbol{x}_{k+1} \approx \mathbf{A}_{\mathrm{d}}\boldsymbol{x}_k + \mathbf{B}_{\mathrm{u,d}}\boldsymbol{u}_k + \mathbf{B}_{\xi,\mathrm{d}}\boldsymbol{d}_k + \mathbf{E}\bar{\boldsymbol{x}} \tag{4.32a}$$

$$\boldsymbol{y}_k \approx \mathbf{C}\ \boldsymbol{x}_k + \mathbf{D}_{\mathrm{u}}\ \ \boldsymbol{u}_k + \mathbf{D}_{\xi}\ \ \boldsymbol{d}_k + \mathbf{I}_{p\times p}\bar{\boldsymbol{y}} \tag{4.32b}$$

with the discrete system matrices $\mathbf{A}_{\mathrm{d}}$, $\mathbf{B}_{\mathrm{u,d}}$, $\mathbf{B}_{\xi,\mathrm{d}}$, $\mathbf{E}$, cf. (2.27). The optimization problem is established by iterating (4.32), which complies with a *single-shooting* approach. After reformulating (4.32) in terms of the relative change in actuation $\boldsymbol{u}(k+1) = \boldsymbol{u}(k) + \Delta\boldsymbol{u}(k)$ the output prediction satisfies

$$\mathbf{y}\,(:|k) = \boldsymbol{\Omega}\hat{\boldsymbol{x}}\,(k|k-1) + \boldsymbol{\Theta}\boldsymbol{u}^*\,(k|k-1) + \boldsymbol{\Phi}\Delta\mathbf{u}\,(:|k)$$

which can then be used to derive a quadratic program (QP) from the cost function

$$\begin{aligned} J &= \sum_{i=k}^{k+N_\mathrm{p}} \frac{1}{2} \left\| \boldsymbol{y}(i|k) - \boldsymbol{w}(i) \right\|_{\mathbf{Q}_\mathrm{y}}^2 + \frac{1}{2} \left\| \Delta \boldsymbol{u}(i) \right\|_{\mathbf{Q}_\mathrm{u}}^2 \\ &= \sum_{i=k}^{k+N_\mathrm{p}} \frac{1}{2} \left\| \begin{pmatrix} \boldsymbol{p}_\mathrm{load}^{ned}(i|k) - \boldsymbol{w}_\mathrm{load}^{ned}(i) \\ z_\mathrm{tip}(i|k) - w_\mathrm{tip}(i) \end{pmatrix} \right\|_{\mathbf{Q}_\mathrm{y}}^2 + \frac{1}{2} \left\| \Delta \boldsymbol{u}(i) \right\|_{\mathbf{Q}_\mathrm{u}}^2 \end{aligned} \tag{4.33}$$

alongside the linear box constraints

$$\boldsymbol{x}_\mathrm{kbc,min} \leq [\mathbf{0}_{12\times 6}\, \mathbf{I}_{12\times 12}]\, \boldsymbol{x}(i) \leq \boldsymbol{x}_\mathrm{kbc,max} \qquad i = k, \ldots, k+N_\mathrm{p} \tag{4.34a}$$

$$\boldsymbol{u}_\mathrm{min} \leq \boldsymbol{u}(i) \leq \boldsymbol{u}_\mathrm{max} \qquad i = k, \ldots, k+N_\mathrm{p}-1 \tag{4.34b}$$

with lower and upper bounds $\boldsymbol{x}_\mathrm{kbc,min}$, $\boldsymbol{x}_\mathrm{kbc,max}$, $\boldsymbol{u}_\mathrm{min}$, $\boldsymbol{u}_\mathrm{max}$ and $N_\mathrm{p} = T_\mathrm{p}/T_\mathrm{c} \in \mathbb{N}$.

Most times, additional slack variables are included in (4.33) and (4.34) to guarantee feasibility of the optimization problem. For implementation details, please refer to [S5].

4.4.3 Nonlinear Model Predictive Control

In contrast to an LMPC, most nonlinear MPC formulations resort to a combination of numerical integration scheme (2.28) and a multiple-shooting approach, see e.g [146]. As a consequence, the predicted states $\boldsymbol{x}(:|k)$ become additional optimization variables that are linked by equality constraints. The resulting nonlinear program (NLP) resembles that of an MHE, cf. (4.16).

Nonlinear MPC:

$$\min_{\boldsymbol{x}(:|k),\boldsymbol{u}(:|k)} \sum_{i=k}^{k+N_\mathrm{p}} L\left(\boldsymbol{x}(i), \boldsymbol{u}(i)\right) \tag{4.35}$$

$$\begin{aligned} \text{s.t.} \quad \mathbf{0} &= \boldsymbol{x}(i+1) - (\mathrm{ERK4} \circ \boldsymbol{f})\left(\boldsymbol{x}(i), \boldsymbol{u}(i), \boldsymbol{d}(i)\right) && i = k, \ldots, k+N_\mathrm{p}-1 \\ \mathbf{0} &= \boldsymbol{y}(i) - \boldsymbol{h}\left(\boldsymbol{x}(i), \boldsymbol{u}(i), \boldsymbol{d}(i)\right) && i = k, \ldots, k+N_\mathrm{p} \\ \boldsymbol{x}_\mathrm{kbc,min} &\leq [\mathbf{0}_{12\times 6}\, \mathbf{I}_{12\times 12}]\, \boldsymbol{x}(i) \leq \boldsymbol{x}_\mathrm{kbc,max} && i = k, \ldots, k+N_\mathrm{p} \\ \boldsymbol{u}_\mathrm{min} &\leq \boldsymbol{u}(i) \leq \boldsymbol{u}_\mathrm{max} && i = k, \ldots, k+N_\mathrm{p}-1 \end{aligned}$$

The state equation $\boldsymbol{f}(\cdot)$ and output equation $\boldsymbol{h}(\cdot)$ are given in (3.49) resp. (3.18), and (3.12). As before, the number of samples taken over the prediction horizon is denoted

$N_\mathrm{p} = T_\mathrm{p}/T_\mathrm{c} \in \mathbb{N}$. The costs $L(\cdot)$ are chosen as in the case of the LMPC:

$$L\left(\boldsymbol{x}(i), \boldsymbol{u}(i)\right) = \frac{1}{2} \left\| \boldsymbol{h}\left(\boldsymbol{x}(i), \boldsymbol{u}(i), \boldsymbol{d}(i)\right) - \boldsymbol{w}(i) \right\|^2_{\mathbf{Q}_\mathrm{y}} + \frac{1}{2} \left\| \Delta \boldsymbol{u}(i) \right\|^2_{\mathbf{Q}_\mathrm{u}} \ . \tag{4.36}$$

Since the optimization problem is nonlinear, an SQP approach is applied in order to solve (4.35) online. Hence, a sequence of quadratic subproblems is derived, see section 2.7. As (4.36) is furthermore of least-squares type, the Hessian can be approximated using the Gauss-Newton algorithm in (2.54).

Due to the *multiple-shooting* scheme the resulting Hessian usually features a band structure. However, few numeric QP-solvers are equipped to take advantage of structured Hessians. Even worse is the fact, that the increased number of optimization variables may considerably slow down optimization or affect the solution accuracy taking into account the limited time budget during online calculation. To circumvent this problem, one can apply *condensing* methods pre optimization that make use of the linearized equality constraints

$$\begin{aligned} \boldsymbol{c}_\mathrm{eq}(\boldsymbol{x}(:|k), \boldsymbol{u}(:|k)) \approx\ & \boldsymbol{c}_\mathrm{eq}(\boldsymbol{x}_j(:|k), \boldsymbol{u}_j(:|k)) \\ & + \left(\nabla_{\boldsymbol{x}(:|k)} \boldsymbol{c}_\mathrm{eq}(\boldsymbol{x}_j(:|k), \boldsymbol{u}_j(:|k))\right) \boldsymbol{d}_{\boldsymbol{x}_j(:|k)} \\ & + \left(\nabla_{\boldsymbol{u}(:|k)} \boldsymbol{c}_\mathrm{eq}(\boldsymbol{x}_j(:|k), \boldsymbol{u}_j(:|k))\right) \boldsymbol{d}_{\boldsymbol{u}_j(:|k)} = 0 \end{aligned}$$

to eliminate free variables equal to the number of free states $\dim(\boldsymbol{x}(:|k))$. The index j denotes the current decision variables which are used for linearization during the jth SQP iteration. There are various condensing schemes, differing in complexity and numerical robustness. In scope of this thesis, an algorithm based on QR-factorization is used, see [20] for details. An evaluation of prominent condensing approaches is included in [156].

The stated optimization problem (4.35) applies an explicit Runge-Kutta method to discretize the continuous system dynamics. In practice, an implicit formulation using an IRK2 scheme has proven more suitable for the predictive payload controller. While the control performance remains similar between both integration schemes, the lower order implicit version reduces computational complexity and thus allows for finer sample rates or longer prediction horizons. In this instance, each equality constraint also depends non-linearly on $\boldsymbol{x}(i+1)$.

4.4.4 Flatness-Based Model Predictive Control

The basic idea behind the flatness-based MPC presented in [S1] is to leverage the differential flatness of the crane system to avoid the computational and performance

downsides associated with numerically integrating the system dynamics. This is possible due to the flat mappings that provide an algebraic relation between the flat output $\boldsymbol{\gamma}$ and the states $\boldsymbol{x}_{\mathrm{kbc}}$ or inputs $\boldsymbol{u}$. The control task then reverts to the planning of optimal trajectories. The controller synthesis can thus be carried out completely in the continuous time domain. Also, the crane's differential flatness provides an intuitive way to spatial payload control. Thanks to the inversion of the system equations, a flat OCP is by design payload-centric as it directly considers the Cartesian payload trajectories, while the crane states only appear as constraints.

Flatness-based MPC: The flat OCP is given by

$$\begin{aligned}
\min_{\boldsymbol{\gamma}(\cdot)} \; & \int_{t_0}^{t_0+T_\mathrm{p}} L_f\left(\boldsymbol{\gamma}, \ldots, \boldsymbol{\gamma}^{(\mathbf{4})}, \boldsymbol{w}\right) \mathrm{d}t && (4.37)\\
\text{s.t. } \boldsymbol{x}_{\mathrm{kbc}}(t_0) &= \boldsymbol{\psi}_{\boldsymbol{x}_{\mathrm{kbc}}}\left(\boldsymbol{\gamma}, \dot{\boldsymbol{\gamma}}, \ddot{\boldsymbol{\gamma}}, \boldsymbol{\gamma}^{(3)}, \boldsymbol{\xi}, \dot{\boldsymbol{\xi}}\right)\Big|_{t=t_0} \\
\boldsymbol{u}(t_0) &= \boldsymbol{\psi}_{\boldsymbol{u}}\left(\boldsymbol{\gamma}, \dot{\boldsymbol{\gamma}}, \ddot{\boldsymbol{\gamma}}, \boldsymbol{\gamma}^{(3)}, \boldsymbol{\gamma}^{(4)}, \boldsymbol{\xi}, \dot{\boldsymbol{\xi}}, \ddot{\boldsymbol{\xi}}\right)\Big|_{t=t_0} \\
\boldsymbol{x}_{\mathrm{kbc,min}} &\leq \boldsymbol{\psi}_{\boldsymbol{x}_{\mathrm{kbc}}}\left(\boldsymbol{\gamma}, \dot{\boldsymbol{\gamma}}, \ddot{\boldsymbol{\gamma}}, \boldsymbol{\gamma}^{(3)}, \boldsymbol{\xi}, \dot{\boldsymbol{\xi}}\right) \leq \boldsymbol{x}_{\mathrm{kbc,max}} \qquad \forall\, t \in [t_0, t_0 + T_\mathrm{p}] \\
\boldsymbol{u}_{\min} &\leq \boldsymbol{\psi}_{\boldsymbol{u}}\left(\boldsymbol{\gamma}, \dot{\boldsymbol{\gamma}}, \ddot{\boldsymbol{\gamma}}, \boldsymbol{\gamma}^{(3)}, \boldsymbol{\gamma}^{(4)}, \boldsymbol{\xi}, \dot{\boldsymbol{\xi}}, \ddot{\boldsymbol{\xi}}\right) \leq \boldsymbol{u}_{\max} \qquad \forall\, t \in [t_0, t_0 + T_\mathrm{p}]
\end{aligned}$$

with a reference trajectory $\boldsymbol{w} \in \mathbb{R}^{\dim(\boldsymbol{\gamma})}$ of appropriate dimension that has to be continuously differentiable up to the crane's relative degree $\boldsymbol{r}$. The flat mappings $\boldsymbol{\psi}_{\boldsymbol{x}_{\mathrm{kbc}}}(\cdot)$, $\boldsymbol{\psi}_{\boldsymbol{u}}(\cdot)$ from (3.60) resp. (3.61) are used to map the state and actuator constraints, whereas the equality constraints ensure continuity between the measured and predicted output trajectories. In contrast to the LMPC and NMPC a tailored cost function is used, which is modeled as

$$L_f\left(\boldsymbol{\gamma}, \ldots, \boldsymbol{\gamma}^{(\mathbf{4})}, \boldsymbol{w}\right) = \frac{1}{2}\|\boldsymbol{\gamma}(t) - \boldsymbol{w}(t)\|^2_{\mathbf{Q}_\gamma} + \frac{1}{2}\|\boldsymbol{\gamma}^{(3)}(t) - \boldsymbol{w}^{(3)}(t)\|^2_{\mathbf{Q}_r}\,. \tag{4.38}$$

Hence, both the tracking error and its third derivative (jerk) are penalized according to the weighting matrices $\mathbf{Q}_\gamma$, $\mathbf{Q}_r \succeq 0$. The reason for altering the objective lies in the possibility to precompute the Hessian matrix, which can be exploited to speed up numerical optimization online.

While (4.37) only contains algebraic relations, the solution space for $\boldsymbol{\gamma}(t)$ is still infinite. The amount of admissible solutions is therefore restricted by constraining the flat output trajectory to a spline function. In particular, B-Splines are used for their good numerical condition, cf. section 2.2. The flat OCP is reformulated by

substituting

$$\gamma_i(t) = S_{B,i}(t) = \sum_{j=1}^{m+l-2} \alpha_{i,j} B_{j,l}(t) = \left(B_{1,l}(t) \ \dots \ B_{d,l}(t)\right) \boldsymbol{\alpha}_i \qquad i = 1, \dots, 4 \quad (4.39)$$

with the vector of spline coefficients $\boldsymbol{\alpha}_i = (\alpha_{i,1} \ \dots \ \alpha_{i,d})^{\mathrm{T}}$. The number of basis functions $d = m + l - 2$ results directly from the spline order l as well as the number of (inner) knots m. In order to ensure high enough differentiability of $\boldsymbol{\gamma}(t)$, the spline order is lower-bounded by the crane's relative degree. Yet, the number of free variables in (4.37) and thus its computational complexity can be adjusted by choosing the knot sequence $t_0 \leq \tau_1, \tau_2, \dots, \tau_m \leq t_0 + T_\mathrm{p}$.

At every time step, an optimal output trajectory $\boldsymbol{\gamma}^*(t)$ is derived by optimizing the spline parameters $\boldsymbol{\alpha}_i$, with $i = 1, \dots, 4$. Utilizing the Spline properties below, the output trajectories and its derivatives are calculated for $t = t_0 + T_\mathrm{c}$ in order to compute

$$\boldsymbol{u}^*(k+1|k) = \boldsymbol{\psi}_{\boldsymbol{u}} \left(\boldsymbol{\gamma}^*, \dot{\boldsymbol{\gamma}}^*, \ddot{\boldsymbol{\gamma}}^*, (\boldsymbol{\gamma}^*)^{(3)}, (\boldsymbol{\gamma}^*)^{(4)}, \boldsymbol{\xi}, \dot{\boldsymbol{\xi}}, \ddot{\boldsymbol{\xi}} \right) \Big|_{t=t_0+T_\mathrm{c}} . \quad (4.40)$$

For controller synthesis two properties of the used B-Splines are advantageous. First, when evaluating $S_{B,i}(t)$ for a given sequence of query points $\boldsymbol{t}_Q = t_1, \dots, t_p$, the result can be brought to matrix form

$$\left(\gamma_i(t_1) \ \dots \ \gamma_i(t_\mathrm{p})\right)^{\mathrm{T}} = \underbrace{\begin{bmatrix} B_{1,l}(t_1) & \dots & B_{d,l}(t_1) \\ \dots & & \dots \\ B_{1,l}(t_\mathrm{p}) & \dots & B_{d,l}(t_\mathrm{p}) \end{bmatrix}}_{=: \mathbf{B}_l(\boldsymbol{t}_Q)} \boldsymbol{\alpha}_i \quad (4.41)$$

given an equidistant knot sequence. This will prove helpful, when evaluating the output trajectory $\boldsymbol{\gamma}(t)$ over the prediction horizon in order to compute the integral in Eq. (4.37). In fact, the integral can be solved exactly noting that the spline trajectories are piecewise polynomials of degree $l - 1$. Therefore, a GAUSS-LEGENDRE quadrature [88] can be applied, which is detailed in [S1]. Since the prediction horizon recedes, it is always evaluated at the same points meaning that $\mathbf{B}_l(\boldsymbol{t}_Q)$ has to be derived only once. Second, the derivative of a B-Spline is again a B-Spline of smaller order, which can be described by the same spline parameters $\boldsymbol{\alpha}_i$, i.e.

$$\left(\gamma_i^{(k)}(t_1) \ \dots \ \gamma_i^{(k)}(t_p)\right)^{\mathrm{T}} = \mathbf{B}^{l-k}(\boldsymbol{t}_Q) \mathbf{P}_k \boldsymbol{\alpha}_i \quad (4.42)$$

with an order-dependent mapping matrix $\mathbf{P}_k \in \mathbb{R}^{(d-k)\times d}$. This simplifies evaluating the flat mappings in (4.37) immensely.

Noticeably, the optimal actuation signal (4.40) is a function of not only the output trajectories but also the vessel motions. This makes initializing the flat OCP (4.37)

challenging. In normal MPC, vanishing actuations $\boldsymbol{u}(:|k) = \mathbf{0}$ are often a viable initial guess. However, this does not hold for the spline parameters, as vanishing parameters would equate to zero outputs. Neither initializing the splines with respect to the reference is reasonable, since in case of initial offsets high actuation signals may occur. As argued in [S1], driving the system away from its free response may render the optimization problem infeasible. As an initialization strategy, the system states are iterated by means of a RUNGE-KUTTA approach for zero control input $\boldsymbol{u} = 0$, yielding the unforced system trajectories $\hat{\boldsymbol{x}}(\cdot|k)$. An initial set of spline parameters is then derived from solving an unconstrained least-squares problem

$$\min_{\boldsymbol{\alpha}_i} \sum_{i=1}^{N} (\hat{\boldsymbol{x}}(k+i|k) - \boldsymbol{\psi}_{\boldsymbol{x}_{\mathrm{kbc}}}(\cdot)|_{t=t_0})^2 + (\mathbf{0} - \boldsymbol{\psi}_{\boldsymbol{u}}(\cdot)|_{t=t_0})^2 \,. \tag{4.43}$$

For a perfect fit and system prediction, the spline trajectories will coincide with the system's free response to the wave excitation for which $\boldsymbol{u} = \mathbf{0}$.

In [S1], the initial guess is determined by fitting directly to the predicted output trajectories. Yet, this is less stable from a numerical viewpoint since the output dimension is smaller than the state dimension. Similar, the OCP was constrained to the measured output (derivations), the latter of which was calculated using higher order sliding modes. Yet, higher order derivatives exhibit considerable noise, which is why including the model (3.60) resp. (3.61) directly in the equality constraints is numerically beneficial.

4.5 Simulative Controller Evaluation

Simulating the crane system is subject to a variety of influencing parameters, such as the chosen wave characteristics (H_{s}, ω_{p}), the reference position $\boldsymbol{w}_{\mathrm{load}}$ or the radius r_{c} at which the crane has to operate. Over the course of this thesis project, a fair share of simulations has been conducted, some of which are presented below. Despite considerable effort to capture the system's dominant characteristics, mismatch between a real crane system and both simulation and test bench is to be expected. The included results should therefore be taken as an indicator, how predictive control could add to offshore payload handling.

After briefly recapitulating the parameterization of LMPC, NMPC and FMPC in section 4.5.1, different simulation scenarios are assessed, ranging from payload stabilization (section 4.5.2) to an example of trajectory tracking (section 4.5.4). Furthermore, the effect of different sea states and actuator limitations is investigated in section 4.5.3.

4.5.1 Controller Parameterization

All three MPC formulations posses multiple parameters that need to be tuned for both control performance and real-time feasibility. For the subsequent simulations, a consistent prediction horizon of $T_\mathrm{p} = 12\,\mathrm{s}$ has been chosen for all controllers. On the one hand, the peak periods of most sea states are thus covered. On the other hand, the results from section 4.2.1 suggest that for longer horizons the prediction error will increase notably. In case of the NMPC, the input trajectories are parameterized by splines of order two, which turned out essential in deriving reasonable code sizes. Using polynomials of first order would further reduce computational complexity. Yet, the increased differentiability seems reasonable considering that the manipulated variables equate to reference velocities in actor space. Second order splines ensure the ability to compute continuous acceleration profiles for the actuators, which gains importance when dealing with layered control loops at actuator level.

Across all controller designs a sample time of $T_\mathrm{c} = 0.1\,\mathrm{s}$ is targeted. While higher execution rates could be realized with the FMPC, no satisfactory results were obtained when hard restricting the NMPC to 100 ms. Last, the weighting matrices of the respective controllers, i.e. $\mathbf{Q}_\mathrm{u}$, $\mathbf{Q}_\mathrm{y}$ (LMPC, NMPC) and $\mathbf{Q}_\gamma$, $\mathbf{Q}_\mathrm{r}$ (FMPC), are chosen diagonal. The elements were tuned using Bayesian optimization (BO) to account for the black box nature of the tuning problem, cf. section 2.7. Compared to other optimization routines, BO is known to be sample-efficient, which for the tuning of different MPCs becomes crucial as time becomes a budget. Different acquisition functions $\phi_\mathrm{acq} : \mathbb{R}^{n_\mathrm{opt}} \to \mathbb{R}$ were implemented over the course of this thesis project. Eventually, most tuning problems were solved by using the expected improvement (EI) acquisition function

$$\phi_\mathrm{EI} = (\mu - f(x^*))\Phi(\frac{\mu - f(x^*)}{\sigma}) + \sigma\varphi(\frac{\mu - f(x^*)}{\sigma}) \tag{4.44}$$

that starting at a random set of samples quickly finds good but maybe not globally optimal solutions. The index is calculated based on the GP's predicted mean μ, predicted standard deviation σ and the currently best observed value $f(x^*)$. The functions $\Phi(\cdot)$ and $\varphi(\cdot)$ represent the cumulative distribution and probability density function of the normal distribution.

4.5.2 Stabilization Performance of LMPC, NMPC and FMPC

The three presented predictive control schemes (LMPC, NMPC, FMPC) are evaluated for an exemplary sea state of $H_\mathrm{s} = 2\mathrm{m}$, $\omega_\mathrm{p} = 0.72\,\mathrm{rad/s}$. The error trajectories alongside the actuation signals are depicted in Fig. 4.16 - Fig. 4.18. The computational times are reported in Tab. 4.3.

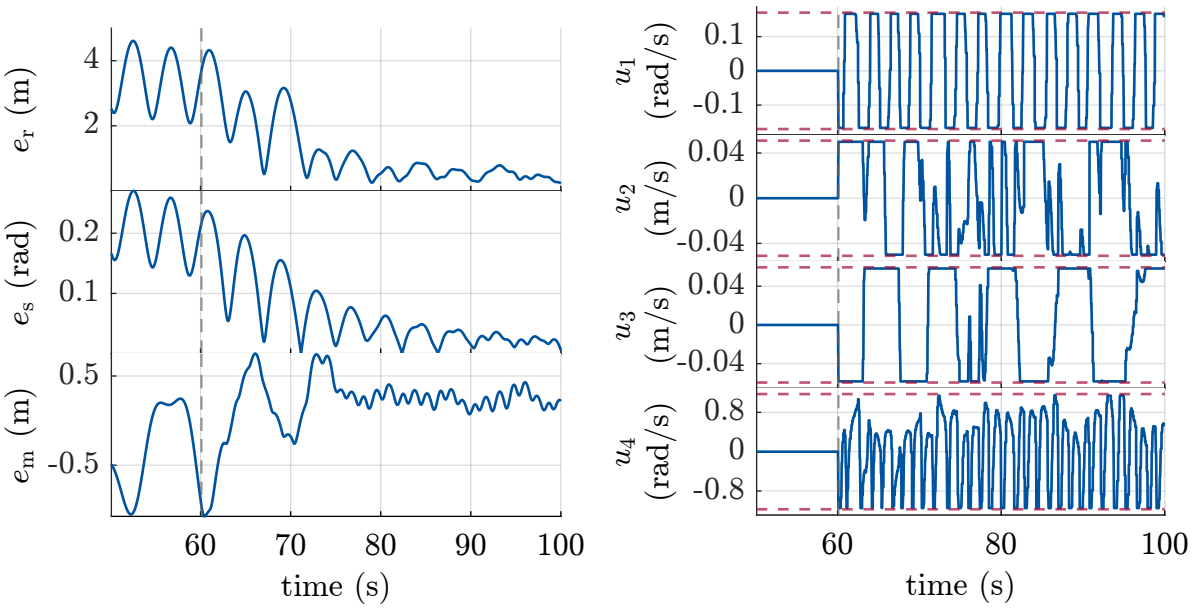

(a) Error trajectories **(b)** Input trajectories

Fig. 4.16: Payload stabilization with a LMPC at moderate seas

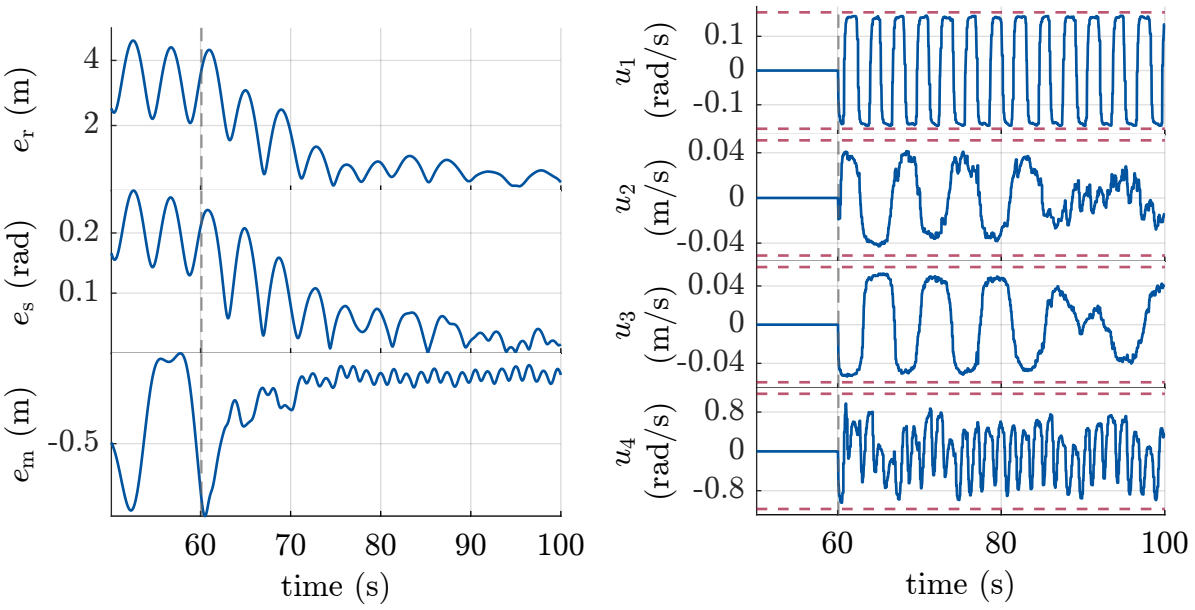

(a) Error trajectories **(b)** Input trajectories

Fig. 4.17: Payload stabilization with a NMPC at moderate seas

All MPC versions attain comparable performances with respect to the Euclidean error e_r, where the NMPC shows the best convergence behavior. Also, the NMPC is the

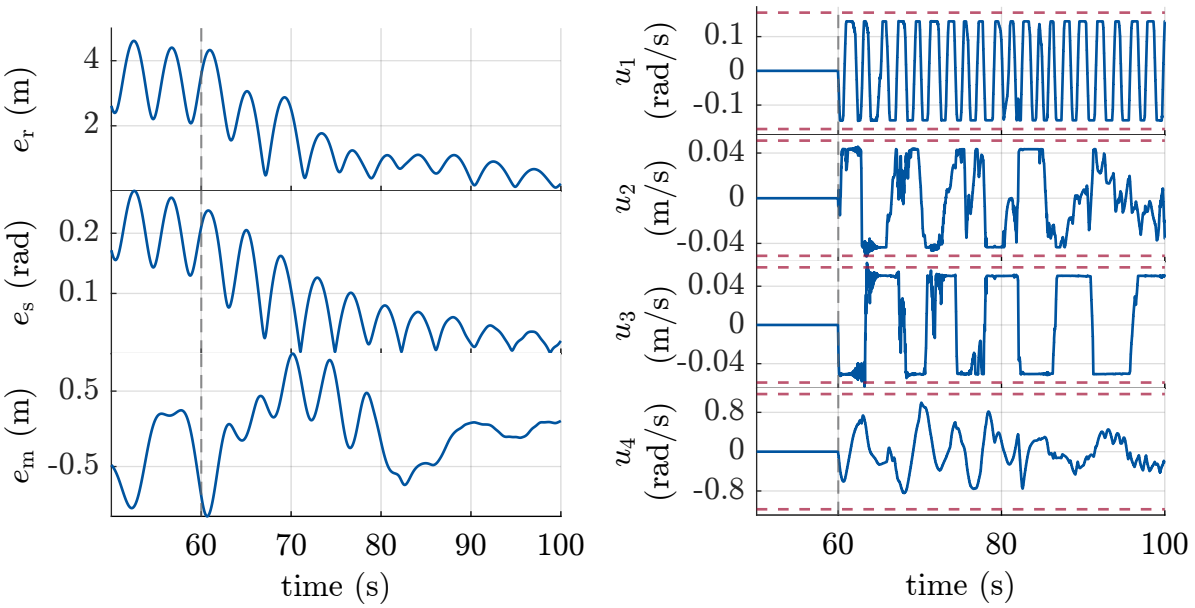

(a) Error trajectories

(b) Input trajectories

Fig. 4.18: Payload stabilization with a FMPC at moderate seas

only MPC formulation that realizes mean free oscillations with respect to the heave dimension. However, the observed deviations may stem from non-optimal tuning instead of a systematic difference in controller behavior. Looking at the actuator signals, all MPC take full advantage of all actuators. The NMPC yields the smoothest input trajectories. With respect to computational times, only the LMPC and FMPC meet the targeted maximum computation time of 100 ms and are thus real-time feasible, cf. Tab. 4.3.

Table 4.3: Computational times of the different MPC designs

design	μ_{t_c} (s)	σ_{t_c} (s)
LMPC	0.0272	0.0014
NMPC	0.2504	0.0105
FMPC	0.0186	0.0048

4.5.3 Stabilization Performance as Function of the Sea State and Actuator Capacity

The attainable control performance in large parts depends on the crane's maximum actuator dynamics as well as the present sea state. Hereafter, the implemented (N)MPC

is assessed for a series of different wave conditions and actuator limitations in order to answer the question, up to which sea state predictive payload stabilization is feasible. As a reference the sea state codes (SSC) in Tab. 3.1 are used. For each SSC a representative set of wave parameters (H_s, ω_p) is evaluated, which are summarized below. The simulations are restricted to SSC 1 - SSC 6, which account for over 90% of the observed sea conditions.

Table 4.4: Sea state parameterization

SSC	1	2	3	4	5	6
H_s (m)	0.05	0.30	0.88	1.88	3.25	5.00
ω_p (s)	0.72	0.84	0.84	0.72	0.65	0.51

With reference to chapter 3, the dynamic limitations of the crane's hydraulic actuators are mapped to constraints on the system states and inputs. The parameterization in Tab. 3.5 reflects ordinary actuator technology. Using this as a starting point, a scaling factor $\delta_{\dot\rho} \geq 1$ is applied to study the effect of different actuator capacities on the controller performance, i.e.

$$\delta_{\dot\rho}\, \dot\rho_{i,\min} \leq \dot\rho_i \leq \delta_{\dot\rho}\, \dot\rho_{i,\max} \qquad i = 1, \ldots, 4 \tag{4.45}$$

The simulations are repeated twice for $\delta_{\dot\rho} \in \{1, 3\}$, the results of which are shown in Fig. 4.19. As expected, the control performance decreases with the sea state code, up to

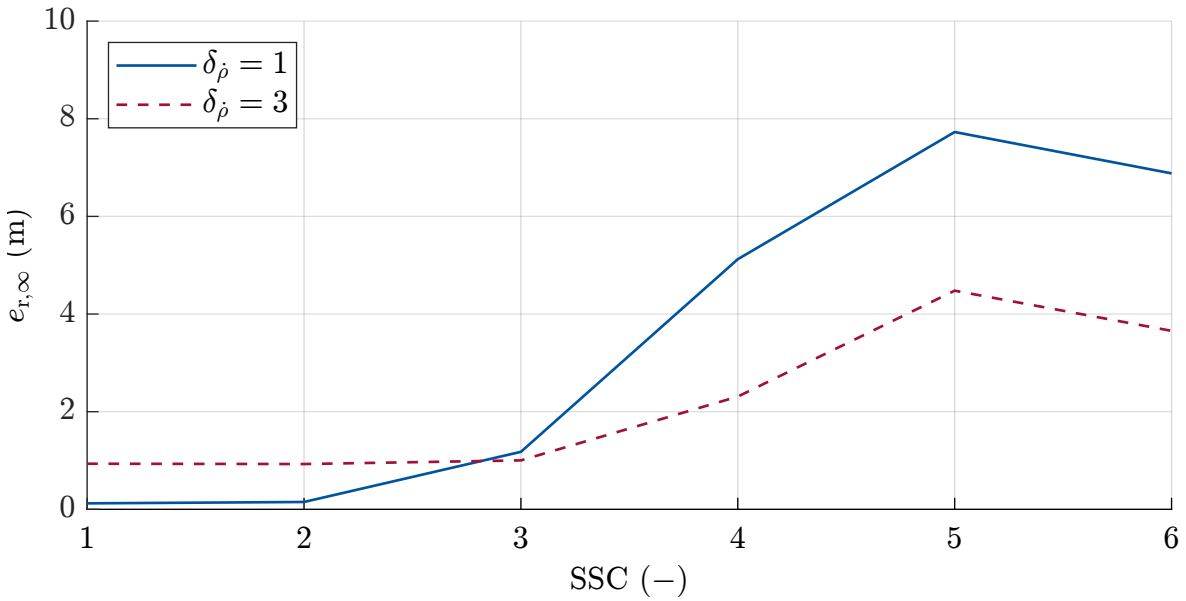

Fig. 4.19: Performance map of NMPC for different sea state codes and actuator classes

the point where no meaningful payload stabilization is achieved. Yet, the data suggests

that actuators of higher maximum velocity may enlarge the admissible weather window. The contrary behavior for $\delta_{\dot{\rho}} = 1$ resp. $\delta_{\dot{\rho}} = 3$ at SSC 1 and 2 is likely neglectable considering the small overall amplitudes. In the future, the performance map should be extended to different scaling factors per actuator to study related questions. As an interesting side effect, the presented approach provides means to specify requirements for future system engineering.

4.5.4 Trajectory Tracking with FMPC

The control objective in section 4.1.1 admits both payload stabilization and trajectory tracking. First presented in [S1], the assessment of the FMPC's qualitative tracking performance is reproduced in Fig. 4.20, where a primitive reference trajectory $\boldsymbol{w}_{\text{load}}$ for the payload is specified. Persistent wave disturbances are generated according to the scenario in section 4.5.2. In the beginning, the FMPC is operated in stabilization mode, i.e. the payload reference is constant. The payload oscillations are quickly damped such that at $t = 120$s payload transfer is initialized. As can be seen in Fig. 4.20a, the FMPC is mostly able to maintain a small control error also during trajectory tracking. The actuation signals shown in Fig. 4.20a saturate frequently, which is one explanation why some residual payload oscillations occur momentarily. The averaged and maximum Euclidean error e_{r} over each phase are given in Tab. 4.5. For more details, the reader is referred to [S1]. The recorded computation times required to solve the flat OCP are given in Fig. 4.21. The absolute values should be considered with caution, as the used hardware will have a big impact on computation times. Still, computation times around 6 ms far outperform other nonlinear MPC formulations. The controller is executed at 100 Hz. At a few sampling instances, the FMPC just violates the timing restriction, which is believed to be neglectable considering that there should be further room for code improvement.

Table 4.5: Euclidean error during trajectory tracking taken from [S1]

phase	*I*	*II*	*III*	*IV*
mean e_{r} (m)	1.50	0.10	0.07	0.09
max e_{r} (m)	3.05	0.36	0.42	0.47

The results demonstrate the MPC's ability to handle stabilization and tracking problems likewise. From an application point of view, the fact that no reparameterization nor a change in control structure is necessary to uphold precise payload handling, presents an important advantage of predictive control strategies over conventional controller designs. Yet, further research should delve deeper into the interdependency of reference trajectory and simultaneous disturbance rejection. Both tasks are realized using the

same hydraulic actuators, such that actuator saturation and a subsequent decrease in disturbance rejection is increasingly likely for faster reference trajectories.

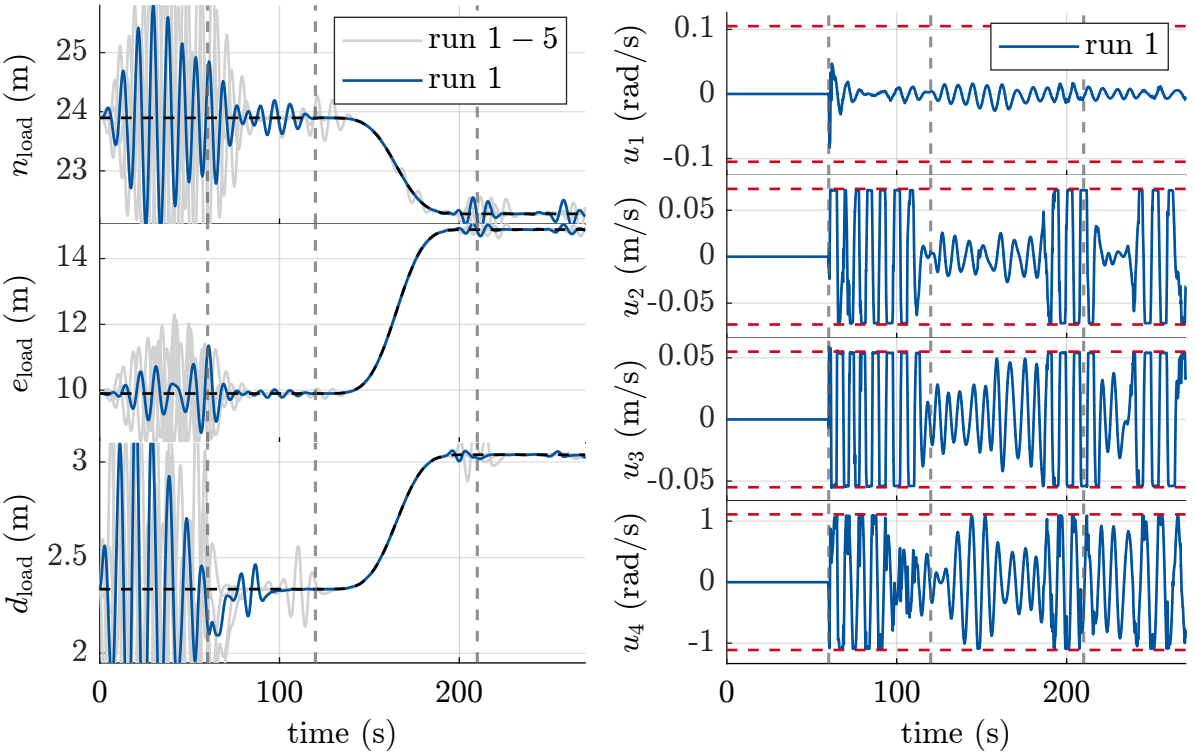

(a) Payload trajectories **(b)** Input trajectories

Fig. 4.20: Tracking performance of FMPC at moderate seas, adopted from [S1]

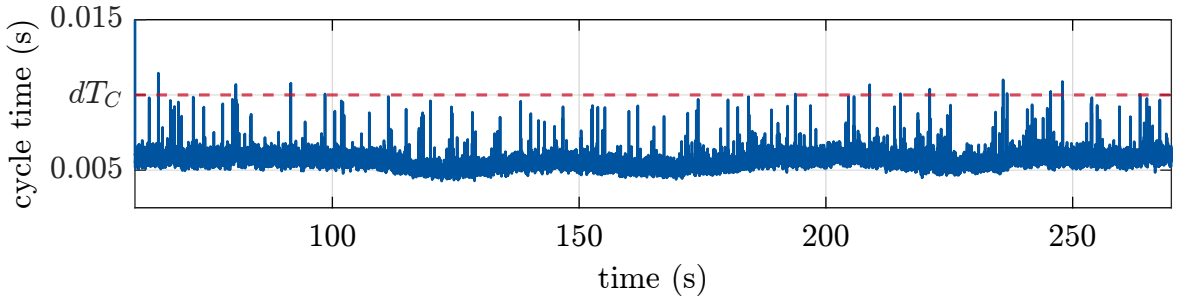

Fig. 4.21: Computation times of FMPC during trajectory tracking

4.6 Experimental Controller Validation

Subsequent to the simulative results, the predictive control topology is validated experimentally in a laboratory test setup. The robot-based test bench was already introduced in section 3.7 alongside its technical limitations. In particular, the small scale nature of the demonstrator poses challenges to the implementation of a predictive control strategy as the payload dynamics are much faster. Yet, it is believed that the test bench provides added value during controller synthesis by means of a more realistic environment to test the controller against common pitfalls like time delays in communication, sensor noise or restricted computational hardware. In context of the experiments detailed below, the main objective was to realize a model predictive payload controller in lab that provides additional damping to a swinging payload. The robot-based nature of the test bench allows for reproducible test conditions, such that runs with and without control can be compared properly. Due to the limited stroke in vertical direction, the main focus is on the controller's ASC performance, which following section 1.3 presents the more involved control task. The included results were first presented in [S3], while an extended version was published later in [S5].

4.6.1 Test Scenario

In the experiments, the payload is initially deflected to a predefined angle of about 1.05 rad. The uncontrolled payload motions are then compared to the closed loop response of the system. Following chapter 3, the payload sway is conveniently described by the two deflection angles φ_1 and φ_2, respectively. A (linear) MPC using an objective similar to (4.2) was implemented using MATLAB/Simulink and compiled to C-Code running on a real-time machine, cf. section 3.7. The control topology is complemented by an EKF that provides the required state feedback, Fig. 4.22. Since the deflection angles can not be measured directly, the EKF fuses data from a 3D camera with the joint signals of the robot. The latter emulates the knuckle boom crane and also realizes the initial payload deflection. The entire algorithm is executed at a cycle time of 12 ms, which matches the KR16 robot's command interval. To account for potential inaccuracies in parameter calibration and coordinate systems, the state vector is augmented with an error state $\boldsymbol{x}_\Delta$, compensating for geometrical deviations that could otherwise lead to incorrect deflection angle estimates and degrade system performance and stability. In contrast to the simulative results above, the crane joint accelerations are used as (virtual) manipulated variables, which considering the crane's differential flatness, could be translated to the model in section 3.4 but yields a more compact dynamic model in context of the test bench. This is key, noting that the MPC has to be calculated at strict real-time within 12 ms. The complete formulation of the EKF and MPC are included in [S5].

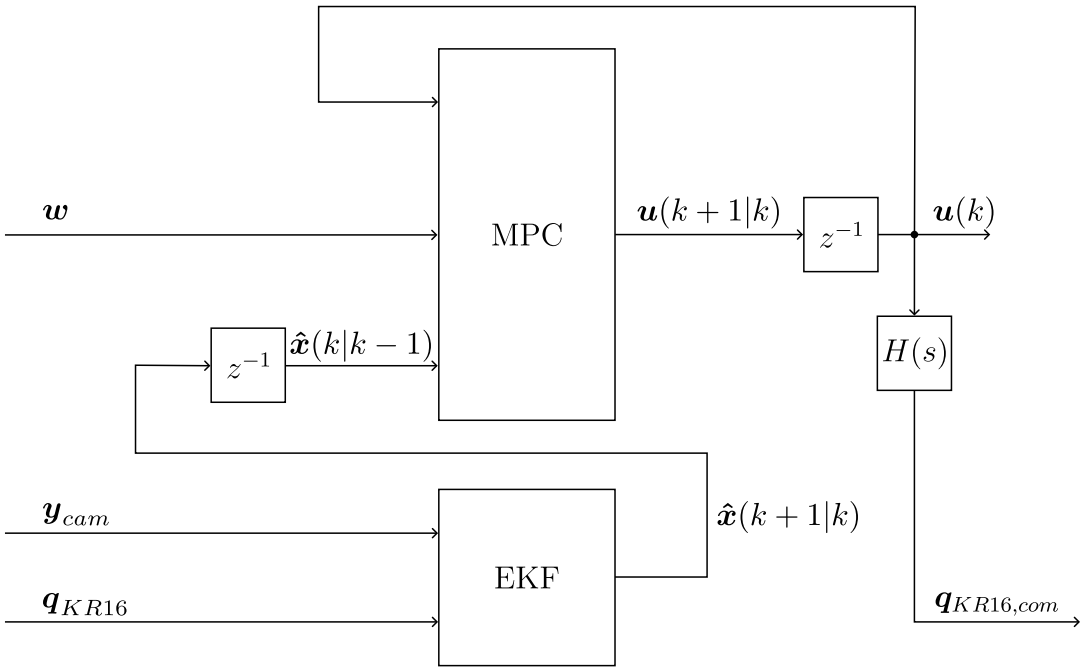

Fig. 4.22: Predictive control topology used in laboratory tests – The payload deflection angles are controlled by an LMPC with successive linearization. State feedback is provided by an EKF fusing camera and robot data ($\boldsymbol{y}_{cam}, \boldsymbol{q}_{KR16}$). The calculated actuator velocities have to be integrated and then transformed ($H(s)$) to a set of joint angles $\boldsymbol{q}_{KR16,com}$ for the robot, that are then commanded via the robot sensor interface (RSI).

4.6.2 Results and Discussion

To assess the sway reduction induced by the MPC, trajectories of the payload deflection angles with and without active control are compared in Fig. 4.23. For the controlled case, initial payload deflections were rapidly confined to a plane and deceased much faster as in the uncontrolled experiments. However, complete elimination of the payload oscillation took a considerable amount of time. It should be noted that the controller was tuned conservative due to the considerable delay introduced by the robot's control unit. The system constraints remained within acceptable ranges, with brief tolerance margin violations considered manageable. The presentation is scaled as were the dynamic constraints placed on the controller due to the increased dynamics at the laboratory scale. The resulting joint velocities $\dot{\boldsymbol{q}}$ reflect the payload's natural frequency, which is to be expected for effective ASC. In conclusion, the predictive control strategy was able to induce reasonable damping in the payload oscillation while keeping system states within predefined limits, supporting the previous simulative findings and suggesting viability of

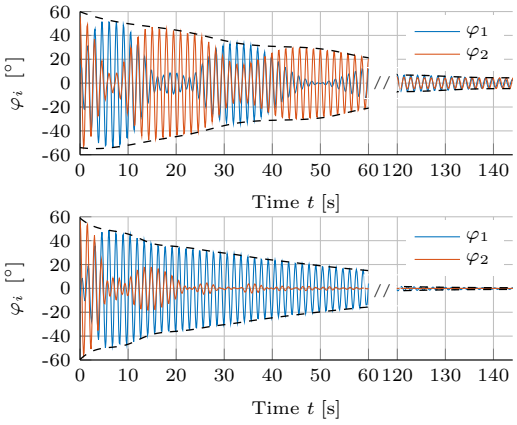

(a) Payload deflection trajectories

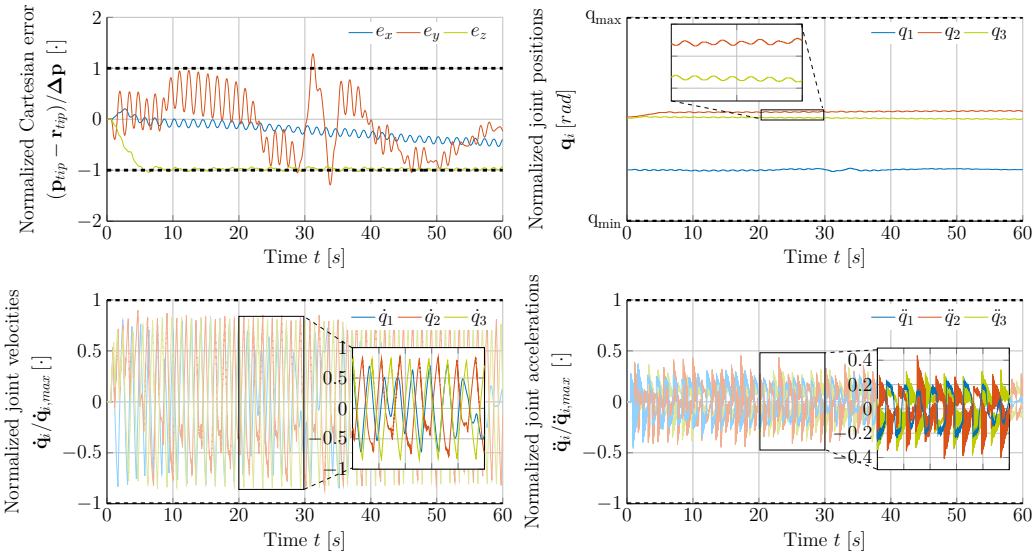

(b) Crane trajectories

Fig. 4.23: Experimental Validation of a MPC – Initial payload deflections are damped by a LMPC based on successive linearization. The payload trajectories without control (top) with active control (bottom) are shown in Fig. 4.23a. The corresponding crane trajectories are given in Fig. 4.23b.

the MPC approach for payload handling in crane-based offshore operations. Furthermore, the observer-based compensation of calibration or modeling errors was demonstrated. The experiments lay a foundation for future research to also assess different control schemes, e.g. the FMPC that during initial testing was challenged by the test bench's peculiarities.

4.7 Perspectives on Safe Offshore Operations

The predictive payload controllers discussed in section 4.4 implicitly assume a LoA > 2 as exclusive access to the actuators is presumed, i.e. no additional input from a human operator is taken into consideration. Likewise, the presented schemes are focused predominately on payload stabilization or trajectory tracking. Control performance is assessed in a vacuum by means of the metrics introduced in section 4.1.2. While comparing the closed-loop trajectories to a second order systems offers a meaningful way to assess both transient and steady-state payload behavior, the actual values attained by the different controllers remain ambiguous without further context. Besides control performance the notion of *safety* gained increased interest in control literature over the last decade, so much so that it was named as one of the emerging methodologies in "Control for Societal-scale Challenges: Road Map 2030" [5], a roadmap by leading scientists from the field of automation technology. Here, safety broadly refers to a system being *free from unacceptable risk*. This is in contrast to classical control theory, where controllers are synthesized that optimize for a distinct set of performance metrics, e.g. by minimizing the effects of exogenous inputs on weighted or normalized controlled outputs in a generalized plant setting [161]. While both stabilization and tracking tasks may be integral parts adding to a system's safety, the safety concept takes a more holistic approach when evaluating system resp. automation solutions.

The following sections provide an outlook on safe payload handling with ship cranes from a control perspective. The focus is on the transferability of the model-based control concepts presented before to the context of safe offshore operations. As safety is best assessed system-wide across different tasks, an exhaustive presentation of the topic would require an in-depth analysis of all hardware components, software modules as well as a higher fidelity environment simulation. While such analysis is beyond the scope of this work, related investigations offer a promising direction for future research, cf. section 6.3. In the following, different notions of safety are presented in section 4.7.1, before assessing payload oscillations as safety-critical for offshore operations in section 4.7.2. Thereafter, two model-based assistive safety systems, namely an *autonomous emergency braking* module and a so-called *safety filter* for monitoring or correcting operator inputs, are discussed in section 4.7.3 and section 4.7.4, respectively.

4.7.1 Notions of Safety

The concept of *safety* is a multifaceted one as it usually hinges on all system components (hardware, software), the application scenario as well as potential interactions with humans, the environment or other systems. With increasing relevance in the context of (partially) autonomous systems, various efforts for standardization have been recorded,

see e.g. ISO/IEC Guide 51: *Safety aspects – Guidelines for their inclusion in standards* [87], IEC 62061: *Safety of machinery - Functional safety of safety-related control* [80] or DIN EN 14439: *Cranes - safety - tower cranes* [49]. Depending on the standardizing body, the area of application or the entity where risk is addressed various sub-concepts of safety are defined, e.g. *cybersecurity*, *process safety*, *passive safety*, *structural safety*, *operational safety* or *functional safety*. A brief summary of common terms and categorization approaches relevant in the context of automatization solutions is included below:

Safety: Following ISO/IEC Guide 51, *safety* refers to the "freedom from risk which is not tolerable" [87], where *risk* is the "combination of the probability of occurrence of harm and the severity of that harm" [87]. Finally, the term *harm* covers "injury or damage to the health of people, or damage to property or the environment" [87]. The guideline further stresses the fact that safety does not equate to the absence of any hazards (potential sources of harm) as some residual risk is inevitable in all systems. Safety therefore asks for the implementation of protective measures that reduce the overall risk to tolerable levels. Risk mitigation strategies in offshore cranes range from a correct dimensioning and defined safety distances [55] to safety functions such as motion limiters, slack rope detectors or overload protection systems [48].

Safety Function: In IEC 62061, a *safety function* is "intended to maintain the safe condition of the machine or to prevent an immediate increase in the risk(s) in respect of a specific hazardous event" [80]. The norm furthermore suggests that safety functions are usually triggered by input events and yield an output reaction i.e. an actuation. For offshore cranes, an exemplary safety function is given by an automatic overload protection system (AOPS): An AOPS monitors the current load to detect overloading (hazard), which might lead to e.g. structural failure or dropped loads. To transfer the system to a safe state, i.e. to provide a rapid and load controlled pay out of wire rope until the overload is reduced, DIN EN 13852 [48] stipulates deactivating hoisting and slewing breaks, applying hoist tension and slew torque control (actuation), overriding the low hoist motion limiters and issuing an AOPS alarm at the control station.

Functional Safety: As per IEC 62061, *functional safety* is a subset of overall safety concerned with "the correct functioning of the SCS and other risk reduction measures" [80], where the safety-related control system (SCS) implements a safety function realizing risk reduction for a defined hazard up to a given target *safety integrity level* (SIL). The notion therefore applies whenever a system's control topology or automation contributes to risk reduction. For the previous example of an AOPS (safety function), functional safety is ensured when proper operation of the AOPS is verified in accordance with the defined SIL, e.g. functionality should be available for all reeving configurations within a specified excursion envelope and should not be prevented by a single failure in the system [48].

Operational Safety: Despite being frequently used across standards and guidelines, to the best of the author's knowledge, no normative definition of *operational safety*

exists. We will adopt safe operation as being indicated by tolerable risk levels under normal operating conditions, considering the system's intended use, constraints such as workspace limitations, and expectable disturbances. In the context of manual offshore lifting, adherence to operational requirements falls under the responsibility of the crane operator also in face of adverse weather conditions or sea states. In literature, task specific specifications of operational constraints might be set out, e.g. for the conveyance of personnel a maximum allowable lowering and hoisting speed of $0.5\,\mathrm{m/s}$ as well as an upper bound on the weather window (average wind speeds $\leq 10\,\mathrm{m/s}$ and significant wave heights $H_\mathrm{s} \leq 2\,\mathrm{m}$) have to be respected [55]. For off-board lifts additional risks from relative motions of the payload have to be considered. Operational safety may also be extended to a human operator's ability to safely control the system. Here, predictability of the system reaction to control inputs as well as reliability of offered functionalities become key. Accordingly, the crane's main motion controls are required to "provide predictable smooth response proportional to the position of the control levers" [48] while also minimizing hysteresis behavior and offering a defined neutral position.

Besides normative definitions, there are field-specific interpretations and specifications of safety. In automated control, safety is often linked to the notion of *forward invariance* of some safe subset of the system's state space [24]. In other words, once the safe region is reached the dynamic system stays there provided adequate input trajectories. A more formal definition is given below:

Forward Invariance: From a control perspective, safety may be related to the *forward invariance* of a *safe set* $\mathcal{S} = \{\boldsymbol{x} \in \mathbb{R}^n : \boldsymbol{l}(x) \geq 0\}$, i.e. for any initial state $\boldsymbol{x}(t_0) = \boldsymbol{x}_0 \in \mathcal{S}$ the system trajectories stay within the safe set $\boldsymbol{x}(t) \in \mathcal{S} \quad \forall\, t$. All safety constraints are therefore coded by the function $\boldsymbol{l}(x)$ dividing the state space in safe and unsafe regions, respectively. However, guaranteeing forward invariance of $\mathcal{S}$ is usually difficult when dealing with actuator constraints. The set of all initial conditions yielding state trajectories confined to $\mathcal{S}$ while admitting feasible control actions is known as *viability kernel* $\mathcal{V} = \{\boldsymbol{x}_0 \in \mathcal{S} : \boldsymbol{x}(t_0) = \boldsymbol{x}_0 \Rightarrow \exists\, \boldsymbol{u}(t)$ such that $\boldsymbol{x}(t) \in \mathcal{S} \quad \forall\, t\}$, cf. [12].

The aforementioned control roadmap [5] acknowledges four different safety paradigms, two of which directly relate to the concept of forward invariance: In *deterministic safety* the safety defining function $\boldsymbol{l}(x)$ is required to be positive, while in *probabilistic safety* a chance constraint $P(\boldsymbol{x} \in \mathcal{S}) > \rho$ with confidence level $\rho < 1$ can be introduced to assess average or worst case scenarios in a stochastic setting. The remaining paradigms give a societal interpretation respectively temporal and event-based formulation of safety. Beyond safety notions the roadmap further highlights challenges associated with *safety-critical control*, *safety-critical autonomy* and *safety-critical learning*. Given the complex setup of an offshore handling operation, the referenced safe autonomy stack is of particular interest as it stresses that safe autonomy will be dependent on low level actuator control, middle level trajectory planning, and high level decision-making, as well as the interaction

between those layers. Please refer to [5] and the references therein for an overview of safety concepts related to each layer.

A control scheme suitable for operator-in-the-loop scenarios that aims at rendering a safe (sub-)set forward invariant while minimizing the change from a desired actuation is known as *active set invariance filter* [73] or since then *safety filter*. In order to implement safety filters two main concepts are proposed in literature: The first leverages a Control Lyapunov-like function[2] $b(\boldsymbol{x})$ called *control barrier function* (CBF) to define a safe level-set, which is used in a safety-guaranteeing constraint $L_{\boldsymbol{f}}b(\boldsymbol{x}) + L_{\boldsymbol{h}}b(\boldsymbol{x})\boldsymbol{u} \geq -\alpha(b(\boldsymbol{x}))$ with the state function $\boldsymbol{f}(\cdot)$, output function $\boldsymbol{h}(\cdot)$ (2.17) and an extended class $\mathcal{K}$ function $\alpha(\cdot)$ [7]. Another approach translates the idea of (robust) MPC yielding *predictive safety filters* [180]. Here, the safety set is mapped implicitly as the feasible set of the underlying optimization problem. The often latter incorporates a safe (controlled invariant) terminal set $\mathcal{S}_{\mathrm{f}}$, which might be conservative. Applying predictive safety filter in offshore handling tasks is discussed in section 4.7.4.

4.7.2 Safety Functions in Crane-Based Offshore Operations

As outlined in section 1.1 to section 1.3, offshore payload handling is a demanding task that is performed manually by human crane operators. One of the main hazards faced in offshore operations stems from swinging motions of the suspended payload that are induced by the sea swell exciting the vessel and crane base, respectively. If not considered properly, oscillations of the payload can result in collisions with the environment, which can harm the vessel, ship deck personnel or off-board objects when e.g. servicing a wind turbine. Uncontrolled payload motions are thus safety-critical. As a result, related risk is usually dependent on operator experience, which especially holds true in adverse weather conditions.

The newest draft of DIN EN 13852 [48] lists crane assistant functions as promising means to improve operational safety. While AHC systems are well-established and do support the operator in vertical payload handling, assistive functions for sway reduction or spatial payload stabilization are still missing, cf. section 1.4. New developments further target different layers of the autonomy stack and include approaches for deck motion detection, hook position detection, lift-off and landing assistant, anti-swing assistant (cf. ASC), people detection, handsfree slinging, or collision prevention. Yet, at the time of writing, commercial implementations are scarce. Also, a current trend towards lower LoAs is evident, which may partly be due to the technical and legal challenges associated with full automated solutions. In line with these observations, two model-based approaches for safety functions of LoA 1-2 assisting the crane operator in an operator-in-the-loop

[2] In literature, the CBF is often denoted by $h(\cdot)$, which is avoided here to preclude confusions with the output mapping $\boldsymbol{h}(\cdot)$ (2.17b).

configuration are discussed below. To limit the scope of the discussions, a deterministic safety notion will be applied. In contrast, probabilistic formulations might prove more suitable in the future noting the high levels of uncertainty and stochastic disturbances encountered offshore.

4.7.3 Model-Based Emergency Braking

Inspired by the field of autonomous driving, an assistive safety function realizing emergency braking can be considered to help the operator avoiding collisions. In vehicles, sensor information is used to detect possible collisions (hazard) ahead of time, in which case breaking is triggered (actuation). In contrast to vehicles, not all DoF of the payload are manipulated directly. When further taking into account the persistent wave excitation this suggests that a safe state is not attained by simply ceasing actuation, i.e. breaking. Still, the presented modeling (section 3.3.1) and controller concepts (section 4.4) offer means to automatically assess payload motions, predicting future payload trajectories and reducing payload oscillations when needed. A simple concept of an assistive safety function based on motion prediction, cone approximation of future payload sway and collision detection is depicted in Fig. 4.24.

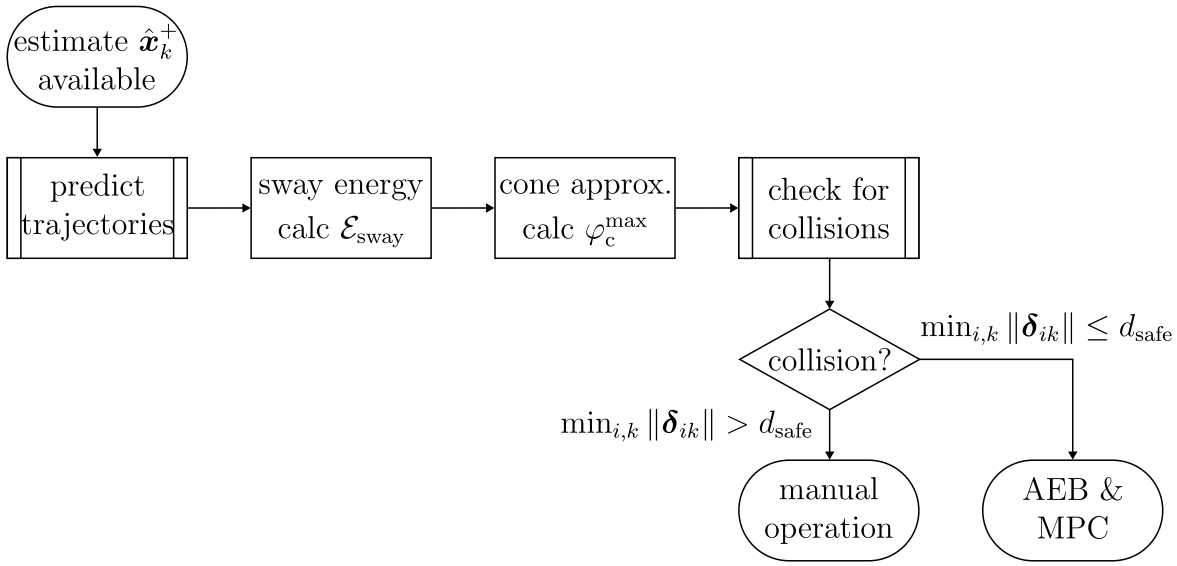

Fig. 4.24: Flow chart of a simple model-based AEB function – At time $t = t_k$, the payload motions are predicted starting at state $\hat{\boldsymbol{x}}_k^+ = \hat{\boldsymbol{x}}(t_k|t_k)$ estimated by an observer. From the predicted sway energy $\mathcal{E}_{\text{sway}}$, a conservative cone is derived by calculating an upper bound on its half-angle $\varphi_{\text{c}}^{\max}$. The cone is then checked for collision given i point clouds representing obstacles. If the minimum distance falls short of a safe distance d_{safe}, manual operation is ceased for payload stabilization via MPC.

At each sampling instance $t = t_k$, the payload motions are predicted over a time horizon T_p by numerically integrating the dynamic system model (3.49) using a Runge-Kutta scheme as before

$$\hat{\boldsymbol{x}}(t_k + (i+1)T_\mathrm{s}|t_k) = (\mathrm{ERK4} \circ \boldsymbol{f}) \left(\hat{\boldsymbol{x}}(t_k + i\,T_\mathrm{s}|t_k), \boldsymbol{u}(t_k + i\,T_\mathrm{s}|t_k) = \boldsymbol{0}, \hat{\boldsymbol{d}}(t_k + i\,T_\mathrm{s}|t_k) \right) \tag{4.46}$$

with $i = 0, \ldots, {}^{T_\mathrm{p}}/_{T_\mathrm{s}} - 1$, cf. section 2.3. To propagate the system states a current state estimate $\hat{\boldsymbol{x}}_k^+ = \hat{\boldsymbol{x}}(t_k|t_k)$ is required, which is computed based on the available sensor data via e.g. one of the observers presented in section 4.2.2. As we are interested in the state evolution under breaking behavior, all manipulated variables are set to zero. Note, that the commanded velocities $\boldsymbol{u} = (\dot{\rho}_{1,\mathrm{ref}}\ \dot{\rho}_{2,\mathrm{ref}}\ \dot{\rho}_{3,\mathrm{ref}}\ \dot{\rho}_{4,\mathrm{ref}})^\mathrm{T}$ are filtered by the modeled system dynamics, such that the crane does not come to a hold immediately. If not violating other safety requirements, smooth breaking actions are preferred over common emergency stops that could stress the crane actuators and structure.

The predicted system state $\hat{\boldsymbol{x}}(t_k + T_\mathrm{p}|t_k)$ then informs a cone approximating the maximum future payload deflection as per the sway energy stored in the pendulum-like configuration of crane tip and suspended payload. The cone is defined by its half-angle $\varphi_\mathrm{c}^\mathrm{max}$ and its height $h_\mathrm{c} = \hat{q}_4(t_k + T_\mathrm{p}|t_k)$, the latter being equal to the free cable length q_4 after breaking. In order to determine the half-angle φ_c, recall the kinetic and potential energy of a particular crane body (including payload b_4) defined in (3.29), which after normalizing the potential energy such that a motionless payload hanging straight down yields zero sway energy $\mathcal{E}_\mathrm{sway} = 0$ gives

$$\begin{aligned} \mathcal{E}_\mathrm{sway}(\boldsymbol{\zeta}, \dot{\boldsymbol{\zeta}}) &= \mathcal{T}_\mathrm{load} + \mathcal{V}_\mathrm{load} - \mathcal{V}_\mathrm{load}|_{\boldsymbol{\varphi}=\boldsymbol{0}} \\ &= \frac{1}{2} m_\mathrm{load} \| \mathbf{J}_{\boldsymbol{p}_\mathrm{tip}}^{ned}(\boldsymbol{\xi}, \boldsymbol{q}) \begin{pmatrix} \dot{\boldsymbol{\xi}} \\ \dot{\boldsymbol{q}} \end{pmatrix} + \dot{q}_4 \boldsymbol{r}_\varphi(\boldsymbol{\varphi}) + q_4 \mathbf{J}_{\boldsymbol{r}_\varphi} \dot{\boldsymbol{\varphi}} \|^2 \\ &\quad + m_\mathrm{load} g q_4 \left(1 - \cos(\varphi_1)\cos(\varphi_2)\right) \end{aligned} \tag{4.47}$$

with $\boldsymbol{\zeta} = (\xi_1, \ldots, \xi_6, q_1, \ldots, q_4, \varphi_1, \varphi_2)^\mathrm{T} \in \mathbb{R}^{12}$, the payload mass m_load, the Jacobian $\mathbf{J}_{\boldsymbol{p}_\mathrm{tip}}^{ned} = {}^{\partial \boldsymbol{p}_\mathrm{tip}^{ned}(\boldsymbol{\xi}, \boldsymbol{q})}/_{\partial (\boldsymbol{\xi}\, \boldsymbol{q})^\mathrm{T}}$ and the shorthand notations

$$\boldsymbol{r}_\varphi := \begin{pmatrix} \sin(\varphi_2) \\ -\sin(\varphi_1)\cos(\varphi_2) \\ \cos(\varphi_1)\cos(\varphi_2) \end{pmatrix}, \quad \mathbf{J}_{\boldsymbol{r}_\varphi} = \frac{\partial \boldsymbol{r}_\varphi(\boldsymbol{\varphi})}{\partial \boldsymbol{\varphi}} = \begin{bmatrix} 0 & \cos(\varphi_2) \\ -\cos(\varphi_1)\cos(\varphi_2) & \cos(\varphi_1)\sin(\varphi_2) \\ -\sin(\varphi_1)\cos(\varphi_2) & -\cos(\varphi_1)\sin(\varphi_2) \end{bmatrix}.$$

Equation (4.47) is formulated in joint space for convenience but can be readily transformed to the actuator space by applying (3.27). The relation can also be expressed in dependence of a cone's half-angle φ_c

$$\mathcal{E}_\mathrm{sway}(\boldsymbol{\zeta}, \dot{\boldsymbol{\zeta}}) = \frac{1}{2} m_\mathrm{load} \| \mathbf{J}_{\boldsymbol{p}_\mathrm{tip}}^{ned}(\boldsymbol{\xi}, \boldsymbol{q}) \begin{pmatrix} \dot{\boldsymbol{\xi}} \\ \dot{\boldsymbol{q}} \end{pmatrix} + \dot{q}_4 \boldsymbol{r}_\varphi(\boldsymbol{\varphi}) + q_4 \mathbf{J}_{\boldsymbol{r}_\varphi} \dot{\boldsymbol{\varphi}} \|^2 + m_\mathrm{load} g q_4 \left(1 - \cos(\varphi_\mathrm{c})\right) \tag{4.48}$$

noting that $\cos(\varphi_c) = \cos(\varphi_1)\cos(\varphi_2)$ as per (3.19). At the point of maximum payload deflection, the cone's half-angle φ_c is maximized as the kinetic part of the energy vanishes. The searched half-angle can then be approximated by

$$\varphi_c^{\max} \approx \arccos\left(1 - \frac{\mathcal{E}_{\text{sway}}(\boldsymbol{\zeta}, \dot{\boldsymbol{\zeta}})}{m_{\text{load}} g q_4}\right)\Bigg|_{\boldsymbol{\zeta}=\hat{\boldsymbol{\zeta}}(t_k+T_p|t_k),\dot{\boldsymbol{\zeta}}=\hat{\dot{\boldsymbol{\zeta}}}(t_k+T_p|t_k),q_4=\hat{q}_4(t_k+T_p|t_k)} \tag{4.49}$$

where the predicted quantities derived from (4.46) are used for evaluation.

Note, that both crane actuation and wave disturbances determine the sway energy of the suspended payload. While crane actuation is ceased under simulated breaking, the same is not true for the persistent wave excitation. As a result, the sway energy resp. payload deflection may take its maximum in $[t_k, t_k + T_p]$ or beyond. Assuming small changes in sway energy seems reasonable for low SSC, where typical wave periods are larger than the crane actuators' time constants and thus the required prediction horizons. In all other cases, the safety function should permit fast enough execution rates, such that the sliding window scheme resulting from repeated execution offers sufficient robustness. Another challenge stems from the underlying state propagation that requires a predicted disturbance trajectory, a problem that was already discussed in section 4.2.1. To compensate for an underestimated sway energy based on inaccurate wave predictions, conservatism can be added to the safety function by

- using the maximum stored energy over $[t_k, t_k + T_p]$ as worst case estimate when calculating (4.49), or
- inflating the cone approximation by a predefined safety offset, i.e. $\tilde{\varphi}_c^{\max} = \varphi_c^{\max} + \varphi_{\text{off}}$ with $\varphi_{\text{off}} \in \mathbb{R}_{>0}$ and $\varphi_c^{\max} + \varphi_{\text{off}} < \pi/2$.

As a first assistive measure, the predicted cone can be visualized to the operator to simplify assessment of future payload sway. Referring back to section 4.7.2, there is active industry research aiming at improved vision systems to detect obstacles in the crane's workspace. Such information can be easily integrated to calculate a risk measure from the approximated cone by determining shortest distances between cone and obstacles, a problem widely considered in e.g. computer vision or the video game industry. A straightforward and fast to calculate approach is included below. Given a (preprocessed) point cloud $\mathcal{P}_{\text{obj},i} = \{\boldsymbol{p}^{ned}_{\text{obj},ij} \in \mathbb{R}^3 \,|\, j = 1, \ldots, n\}$ of n measured points $\boldsymbol{p}^{ned}_{\text{obs},ij}$ belonging to an obstacle $i = 1, \ldots, l$, a collision with the calculated cone can be checked by sampling m points $\mathcal{P}_{\text{cone}} = \{\boldsymbol{p}^{ned}_{\text{cone},k} = \boldsymbol{p}^{ned}_{\text{cone}}(u_k, v_k) \in \mathbb{R}^3 \,|\, u_k \sim \mathcal{U}(0,1),\, v_k \sim \mathcal{U}(-\pi, \pi),\, k = 1, \ldots, m\}$ from the cone equation

$$\boldsymbol{p}^{ned}_{\text{cone}}(u, v) = \boldsymbol{p}^{ned}_{\text{tip}} + u \begin{pmatrix} \cos(v)\sin(\varphi_c^{\max}) q_4 \\ \sin(v)\sin(\varphi_c^{\max}) q_4 \\ q_4 \end{pmatrix} \tag{4.50}$$

and subsequently solving $n_{\text{total}} = m \times l$ linear optimization problems[3]

$$\begin{aligned} \min_{\boldsymbol{\alpha}_{ik}} \ & \boldsymbol{c}^{\mathrm{T}} \boldsymbol{\alpha}_{ik} \\ \text{s.t.} \ & \begin{bmatrix} \boldsymbol{p}^{ned}_{\text{obj},i1} & \cdots & \boldsymbol{p}^{ned}_{\text{obj},in} \end{bmatrix} \boldsymbol{\alpha}_{ik} = \boldsymbol{p}^{ned}_{\text{cone},k} \\ & \|\boldsymbol{\alpha}_{ik}\|_1 = 1 \\ & -\mathbf{I}_{n\times n} \boldsymbol{\alpha}_{ik} \leq 0 \end{aligned} \tag{4.51}$$

with the free variables $\boldsymbol{\alpha}_{ik} \in \mathbb{R}^{n\times 1}$ and an arbitrary (positive) weighting $\boldsymbol{c} \in \mathbb{R}^{n\times 1}$. If any of the problems (4.51) has a solution, the cone and an obstacle are in collision. Mathematically, the point $\boldsymbol{p}^{ned}_{\text{cone},k}$ is known to lie within the convex hull induced by the point cloud $\mathcal{P}_{\text{obj},i}$ if (4.51) has a solution. Note that the number of optimization problems can be huge. Yet, the resulting linear programs can be solved rapidly. Further logics can be implemented to reduce the number of points in the point cloud leading to smaller optimization problems or excluding far away obstacles reducing n_{total}. The optimization problem can be easily extended to determine shortest distances by introducing slack variables $\boldsymbol{\delta} \in \mathbb{R}^6$ with linear weighting $\lambda \in \mathbb{R}$ and $\lambda \gg 0$, such that a solution to (4.51) always exists.

$$\begin{aligned} \min_{\boldsymbol{\alpha}_{ik}, \boldsymbol{\delta}_{ik}} \ & \boldsymbol{c}^{\mathrm{T}} \boldsymbol{\alpha}_{ik} + \lambda \boldsymbol{\delta}_{ik} \\ \text{s.t.} \ & \begin{bmatrix} \boldsymbol{p}^{ned}_{\text{obj},i1} & \cdots & \boldsymbol{p}^{ned}_{\text{obj},in} \end{bmatrix} \boldsymbol{\alpha}_{ik} = \boldsymbol{p}^{ned}_{\text{cone},k} + \begin{bmatrix} \mathbf{I}_{3\times 3} & -\mathbf{I}_{3\times 3} \end{bmatrix} \boldsymbol{\delta}_{ik} \\ & \|\boldsymbol{\alpha}_{ik}\|_1 = 1 \\ & -\mathbf{I}_{n\times n} \boldsymbol{\alpha}_{ik} \leq 0 \\ & -\mathbf{I}_{6\times 6} \boldsymbol{\delta}_{ik} \leq 0 \end{aligned} \tag{4.52}$$

Safety actions can then be taken based on thresholding $\min \|\boldsymbol{\delta}_{ik}\|$ using a predefined minimum safe distance d_{safe}. While implementing an alarm-based safety function is straightforward, another possibility is taking control from the operator and activating one of the MPC presented in section 4.4 with the current payload position $\hat{\boldsymbol{p}}^{ned}_{\text{load}}(t_k|t_k)$ as reference, see Fig. 4.24. This automatically induces braking behavior and payload stabilization. Noting that both the crane actuator dynamics and controller performance are limited, the safety margin d_{safe} should be chosen higher than the MPC's steady state error $e_{\infty,\text{r}}$ respectively $e_{\infty,\text{s}}$, see section 4.5.3. Two plots illustrating the described safety function in a simple scenario including a KBC and a stationary wall-like obstacle are given in Fig. 4.25. In the depicted example, the crane is at rest before performing a simple slewing motion, thus adding sway energy to the payload. Figure 4.25 shows three snapshots. For the initial configuration the crane's tip position and the cone's position coincide as the crane is just starting moving. Accordingly, the calculated cone radius

[3]Alternatively, one could check $n_{\text{total}} = n \times l$ obstacle points for collision with the cone, i.e. reverse the role of point cloud and point under investigation.

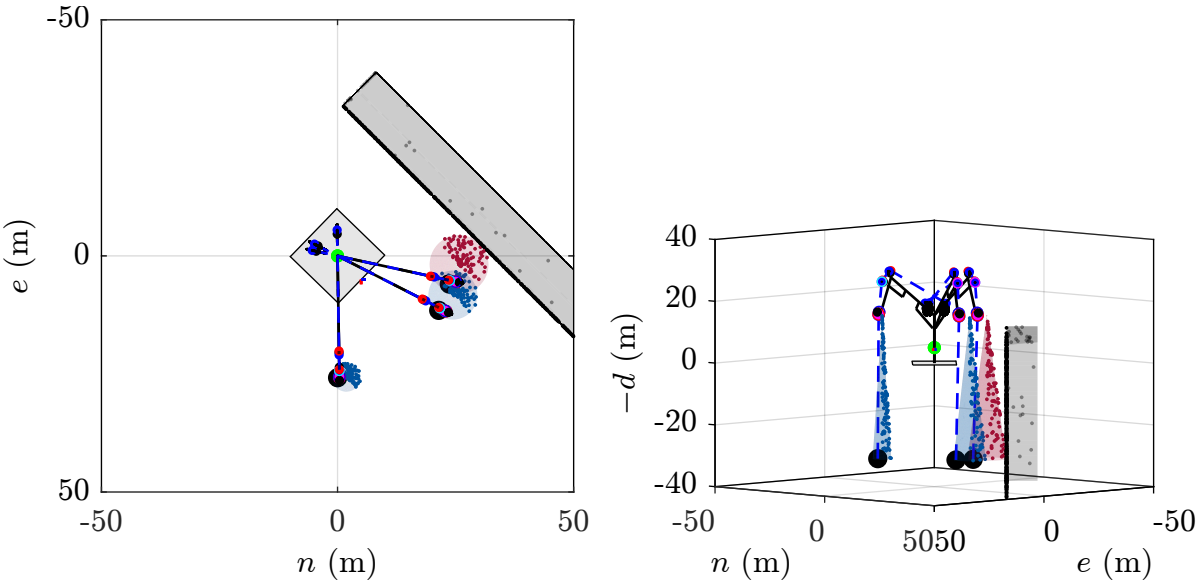

(a) Top view **(b)** Side view

Fig. 4.25: Exemplary behavior of model-based emergency braking – The simulated scenario models a KBC, a wall-like obstacle as well as a simple slewing motion. The minimum distances between the cone and the obstacle are color-coded, i.e., a blue cone symbolizes normal operation, whereas a red cone indicates that the acceptable safety distance is breached.

resp. half-angle is the smallest among the three snapshots. The payload's cone radius then increases over time as more sway energy is added to the payload. The predictive nature of the trajectory calculation can be observed in the second snapshot. Accounting for the delay in braking, the predicted payload cone runs ahead of the crane. Eventually, the cone violates the defined safety margin of 0.5 m, indicated by a red colored cone. Without model uncertainties or exogenous disturbances, braking would effectively prevent a collision with the wall. In practice, including bigger safety distances and reducing the built-up sway energy e.g. through automatic control is advisable to ensure safe operation.

The presented model-based emergency braking is a direct corollary of the control-oriented model derived in section 3.4 as well as the underlying payload prediction applied in section 4.4. While it might provide straightforward but effective means to reduce the risk of collisions, it requires advances in real-time environment detection not yet available. Scalability to a real-world environment would have to be investigated. Moreover, robustness against model uncertainties and disturbances should be checked extensively. The safety function primarily anticipates a hazardous event, i.e. a collision, and then initiates braking or takes control from the human operator to apply automatic payload stabilization. While this is appropriate for an emergency function, it is not suitable for

an assistance system that supports the operator in safe payload handling.

4.7.4 Predictive Safety Filter

In recent years, so-called *safety filters* gained increasing attention to realize safety-critical control [5], [73]. Safety filters are applied in between a nominal, potentially unsafe controller and the plant, cf. Fig. 4.26. The key idea is to adapt the nominal input $\boldsymbol{u}_\mathrm{d}$ only if a safety risk is detected. In all other cases $\boldsymbol{u} = \boldsymbol{u}_\mathrm{d}$. While related concepts have been used to increase safety for controllers featuring active learning, the results can also easily be transferred to manual control, i.e., to operator-in-the-loop topologies, where the nominal input is provided by a human operator. Safety filters thus present a promising approach for implementing a safety assistive function for offshore cranes that could already be integrated at lower LoA.

Different approaches for realizing safety filters are reported in literature. A widely adopted concept leverages so-called *control barrier functions*, which link to LYAPUNOV theory. An example of a safety filter based on control barrier functions is given in [73]. Yet, the task of designing suitable barrier functions is a nontrivial one and usually requires expert knowledge as well as problem- or operation-specific insight. Poorly constructed safe sets and barrier functions may result in overly restrictive filtering or infeasibility of the underlying optimization problem. Given the context of this thesis, a more appealing approach formulates *predictive safety filters* that generalize the idea of MPC in order to ensure that the system trajectories stay within a safe set $\mathcal{S}$ [179]. Following [170], a predictive safety filter can be defined through a receding-horizon optimal control problem

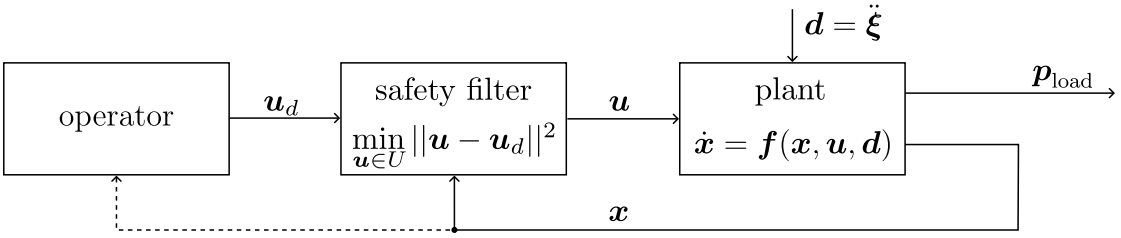

Fig. 4.26: Schematics of a Safety Filter – The operator input $\boldsymbol{u}_\mathrm{d}$ is filtered by an intermediate safety filter in case the desired input would lead to hazardous situations. Yet, as long as the nominal input is considered safe $\boldsymbol{u} = \boldsymbol{u}_\mathrm{d}$. Block diagram adapted from [73].

reading

$$\begin{aligned} \min_{\boldsymbol{x}(:|k),\boldsymbol{u}(:|k)} \quad & \|\boldsymbol{u}_\mathrm{d} - \boldsymbol{u}(k|k)\|_2^2 \\ \text{s.t.} \quad & \boldsymbol{x}(i|k) \quad = (\mathrm{ERK4} \circ \boldsymbol{f})\left(\boldsymbol{x}(i), \boldsymbol{u}(i), \boldsymbol{d}(i)\right) \quad i = k, \ldots, k + N_\mathrm{p} - 1 \\ & \boldsymbol{x}(i|k) \quad \in \mathcal{X} \quad i = k, \ldots, k + N_\mathrm{p} \\ & \boldsymbol{u}(i|k) \quad \in \mathcal{U} \quad i = k, \ldots, k + N_\mathrm{p} - 1 \\ & \boldsymbol{x}(k + N_\mathrm{p}|k) \in \mathcal{S}_\mathrm{f} \subset \mathcal{X} \end{aligned} \tag{4.53}$$

with the sets of admissible inputs $\mathcal{U}$ and states $\mathcal{X}$. Furthermore, the terminal state $\boldsymbol{x}(k + N_\mathrm{p}|k)$ is constrained to lie in a safe (controlled invariant) terminal set $\mathcal{S}_\mathrm{f}$, which might be conservative but ensures recursive feasibility of (4.53). In other words, if at some point the system trajectories enter the safe terminal set $\mathcal{S}_\mathrm{f}$, the existence of a feasible input belonging to $\mathcal{U}$ that keeps the system state in $\mathcal{S}_\mathrm{f}$ is guaranteed. Safety requirements are mapped via state constraints, i.e. the set $\mathcal{X}$. As a result, the safety set $\mathcal{S}$ referenced before is not included explicitly but mapped implicitly as the feasible set of the optimization problem. Comparing (4.53) to the predictive payload controllers presented in section 4.4, the objective function no longer promotes tracking of an output reference trajectory but tracking of a desired input. Hence, the filtered output $\boldsymbol{u}^*(k|k)$ is equal to the operator's input $\boldsymbol{u}_\mathrm{d}$ as long as there exists a residual input trajectory $\boldsymbol{u}(i|k)$, $i = k+1, \ldots, k+N_\mathrm{p}-1$ such that the input sequence $\boldsymbol{u}(:|k) = (\boldsymbol{u}(k|k) = \boldsymbol{u}_\mathrm{d}, \boldsymbol{u}(k+1|k), \ldots, \boldsymbol{u}(k+N_\mathrm{p}-1|k))$ leads to state trajectories not violating any constraints. Otherwise, the operator's input is varied (filtered) in a minimal sense to ensure constraint compliance over the entire prediction horizon. Form a functional point of view, the safety filter thus plans backup trajectories towards a safe terminal set starting close to the provided operator input.

When applying the concept of a predictive safety filter to payload handling at sea, most of the results from section 4.4 can be directly transferred. The question then becomes how to integrate safety constraints when defining $\mathcal{X}$ and which terminal set $\mathcal{S}_\mathrm{f}$ to use.

Arguably, mapping every obstacle directly in $\mathcal{X}$ is impractical because of the dynamic that is changing environment typically found offshore. Introducing time-variant constraints is possible in theory but comes at the risk of jeopardizing recursive feasibility of (4.53). Thus, additional precautions would have to be established to guarantee that the optimization problem remains solvable over time. Circling back to the notion of *predictability* picked up e.g. in DIN 13852 [48], it might therefore be more expedient to include more generic, time-invariant safety constraints at controller level, some examples being listed next.

- Constraining the maximum allowable payload sidelead or offlead: As before, the maximum payload sway can be readily assessed by virtue of the cone induced by payload and tip position. A prototype constrain therefore may follow

$$\varphi_\mathrm{c}(i|k) = \operatorname{acos}\left(\cos(\varphi_1(i|k))\cos(\varphi_2(i|k))\right) \leq \varphi_\mathrm{c}^\mathrm{safe} \tag{4.54}$$

with a predefined safety bound $\varphi_{\mathrm{c}}^{\mathrm{safe}}$ on the cone's half-angle φ_{c}. Note that the cone's half angle is a direct though nonlinear function of two system states φ_1 and φ_2, which are already predicted as part of the safety filter.

• Constraining the maximum admissible relative payload travel from the crane tip in the *ne*-plane: The constraint is a direct extension of (4.54) when Cartesian measures hold more operational relevant information than pure deflection angles, e.g. during collision avoidance. A prototype constrain incorporating a safety margin $d_{\mathrm{load}}^{\mathrm{safe}} \in \mathbb{R}_{>0}$ reads

$$d_{\mathrm{load}}^{ne}(i|k) = q_4(i|k)\sqrt{\left(1 - \left(\cos\left(\varphi_1(i|k)\right)\cos\left(\varphi_2(i|k)\right)\right)^2\right)} \leq d_{\mathrm{load}}^{\mathrm{safe}} \tag{4.55}$$

or equivalently

$$q_4(i|k)^2 - q_4(i|k)^2\left(\cos\left(\varphi_1(i|k)\right)\cos\left(\varphi_2(i|k)\right)\right)^2 \leq \left(d_{\mathrm{load}}^{\mathrm{safe}}\right)^2 .$$

Here the fact that the payload motions in reality do not fallow a cone, but a spherical sector with constant vertical offset equal to the free cable length q_4 has been used to derive a simplified constraint.

• Constraining the crane motions with respect to operational requirements: Different standards suggest various safety specifications, which can be included as state constraints if applicable. One previously mentioned requirement limits the lowering and hoisting speeds when conveying personnel, which could be mapped via

$$-v_{\mathrm{cable}}^{\max} \leq \dot{q}_4(i|k) \leq v_{\mathrm{cable}}^{\max} \tag{4.56}$$

with the velocity constraint $v_{\mathrm{cable}}^{\max} = 0.5\,\mathrm{m/s}$ according to [55]. In other operations in proximity of obstacles, the crane's workspace might be restricted. Related safety constraints can be formulated in the crane's actuator space $\mathcal{P}$, joint space $\mathcal{Q}$ or Cartesian workspace, respectively.

$$\boldsymbol{\rho}_{\min}^{\mathrm{safe}} \leq \boldsymbol{\rho}(i|k) \leq \boldsymbol{\rho}_{\max}^{\mathrm{safe}} \tag{4.57a}$$

$$\boldsymbol{q}_{\min}^{\mathrm{safe}} \leq \boldsymbol{q}(i|k) \leq \boldsymbol{q}_{\max}^{\mathrm{safe}} \tag{4.57b}$$

$$\boldsymbol{p}_{\mathrm{tip,min}}^{\mathrm{safe}} \leq \boldsymbol{p}_{\mathrm{tip}}^{\{ned,root\}}(i|k) \leq \boldsymbol{p}_{\mathrm{tip,max}}^{\mathrm{safe}} \tag{4.57c}$$

For the sake of simplicity, the inequalities in (4.57) present box constraints with more complex formulations or combinations being straightforward. Various shapes can already be realized by choosing a variable proper space. It should also be noted that the variables for the joint and Cartesian workspaces are already nonlinear functions of the predicted state variables (actuator variables) and potentially wave disturbance.

Defining a suitable terminal set $\mathcal{S}_{\mathrm{f}}$ is more complex as it has to be forward invariant under active control. As a subset of the admissible state space $\mathcal{S}_{\mathrm{f}} \subset \mathcal{X}$, all states $\boldsymbol{x} \in \mathcal{S}_{\mathrm{f}}$ must adhere to the previously established state constraints. From a technical point of

view, the safe terminal set is lower bounded by the achievable control performance in the face of actuator limitations. A first terminal set can thus be obtained from the results in section 4.5 also taking into account the error metrics set out in section 4.1.2. However, as already demonstrated in section 4.3, the control performance does also depend on the crane configuration. Hence, safety constraints on the tip height as of (4.57) may restrict achievable control performance further. Finally, the safe terminal set should be chosen conservative, i.e. the safety constraints in $\mathcal{X}$ should be less strict. This is important to not render overly restrictive safety filters assuming control authority continuously. The payload controllers evaluated in section 4.5 considered sole actuator access for the purpose of payload stabilization. As a human operator would also have to implement payload transfer, reduced actuator capacity available for payload stabilization should be accounted for when designing $\mathcal{X}$. Otherwise, the safety filter may enforce the optimal control policy of a predictive payload controller.

If neither $\mathcal{X}$ nor $\mathcal{S}_\mathrm{f}$ change over time, this enables the human operator to create an internal model of the safety function, become accustomed to it, build trust, and predict the system's reactions. The latter is especially relevant, given that the presented safety filter does contradict with DIN 13852, which stipulates that the "controls of the main motions (hoisting, slewing, luffing, travelling, folding and telescoping) shall provide predictable smooth response proportional to the position of the control levers ..." [48]. Since the safety filter may override the operator's input, the crane motions can theoretically differ from the lever signals. This might be acceptable, as long as the safety filter acts in a small vicinity of the operator input. The safety filter's input constraints can also be extended to only allow for corrections in direction of the desired input, i.e. by adding $\boldsymbol{u}(k|k)\boldsymbol{u}_\mathrm{d}(k) \geq 0$ to $\mathcal{U}$. Such safety filter could slow down or speed up the operator input if deemed advantageous but would outsource the task of payload stabilization to the operator. Pitfalls with the safety filter's feasibility are likely. Another promising mechanism for maintaining synchronization between the operator and the crane system outside the safety filter is the addition of haptic feedback systems to the control elements, see [S4] for a preliminary investigation.

The safety filter (4.53) takes a standard state space formulation. However, flatness-based designs are conceivable as well. While all state constraints can be readily transferred by the algebraic flat mappings (3.60), the planning of backup trajectories would simplify to calculating a single output trajectory. As with the predictive payload controllers presented in section 4.4, this has the potential to reduce computation times. For practical implementation of a safety filter targeting offshore payload handling related questions of a suitable formulation, an extended analysis of influencing factors, e.g. the role of different sea states, and the mapping within the designed safety set should be researched. Still, predictive safety filters are believed to be a promising approach to transfer the researched predictive payload controllers to operator-in-the-loop scenarios. In order to account for the multitude of uncertainties that arise in offshore operations, e.g. with regard to wave disturbances, sensing or model mismatch, extensions to the predictive

safety filter using robust techniques from MPC theory can be considered. Exemplary implementations are already reported in the literature, see e.g. [180]. Finally, including a safety filter not only realizes safety-critical control but also promotes safety across the autonomy stack. For example, if the crane system is proven to adhere to a maximum relative payload travel of $d_{\text{load}}^{\text{safe}}$, this safety margin can be used in higher level path or trajectory planning. Here, collision free operations can be planned by using e.g. artificial potential fields [182]. The latter is furthermore simplified by applying the crane's flatness property derived in section 3.5. Because of this, payload trajectories can be planned directly. Higher level trajectory planning furthermore facilitates consideration of dynamic obstacles as planning is usually performed at slower execution rates. Implementing such safe planner and extend it to online (re)planning presents promising directions for future research.

Chapter 5

Revisiting the Research Questions

In section 1.4, four deficits of the current state of the art regarding payload handling with offshore cranes were identified, namely the limited transferability of closed-loop topologies proposed for onshore tower or overhead cranes to shipboard cranes, the lack of holistic control approaches for spatial payload stabilization, the rudimentary evaluation of payload controllers against sea disturbances found in literature, as well as the absence of safety-related objectives in controller design. The main body of this thesis (chapter 3-chapter 4) explored model-based modules for (partially) automated payload handling, hypothesizing that predictive control strategies allow answering the aforementioned deficits. In the preceding sections, simulative and test bench results for different modules were presented. The findings were then put into the context of operational safety in section 4.7. Based on the gained insights, the research questions $\mathtt{Q}_1$ - $\mathtt{Q}_4$ originally defined on page 15 are restated and discussed below.

($\mathtt{Q}_1$) How should the control task be formulated within a predictive controller to obtain a real-time capable algorithm while ensuring precise payload handling?

In section 4.1 different objectives for payload handling were discussed. As outlined, a direct consideration of the Cartesian payload position as controlled output allows for both payload stabilization and trajectory tracking, hence providing the most generic formulation. Arguably, other candidate outputs merely present proxies for the payload position, which ultimately has to be controlled in any handling task. What is more, the payload position was proven to be part of a flat system output (3.52) that allows to invert the system dynamics, thus opening up new avenues for controller synthesis. In contrast to most literature, this thesis therefore adopted a payload-centric approach.

After definition of an according receding horizon optimal control problem, three methods for compiling the resulting OCP to a finite program were tested. For the LMPC and NMPC single- as well as multiple-shooting formulations were investigated. To account for the numerical solver used during online calculation, condensing schemes were implemented in order to compute dense quadratic programs that sped up optimization. Similar techniques were utilized in case of the FMPC. Yet, in a flatness-based MPC no time-discretization is needed as the solution space is rendered finite by using prototype functions (splines) to parameterize the free system trajectories. To make the results comparable, automatic controller tuning via black-box surrogate optimization (Bayesian

optimization) was carried out. Still, biases due to suboptimal tuning can not be ruled out. In view of the findings in section 4.5.2, only the LMPC using single shooting and the FMPC can be calculated under real-time budgets. All MPC schemes attained comparable performance indices in the conducted simulative study. While showing promising control performance, the FMPC is challenged by its dependency on a proper initialization. On the other hand, LMPC often calculated more aggressive input trajectories, which might stem from the higher prediction errors as result of the inherent system linearization. Yet, related issues are believed to be resolvable through adapted controller tuning. FMPC and LMPC thus both present viable MPC formulations for predictive payload control.

When discussing real-time capability of predictive payload controllers, the required state estimation and target selection should not be neglected. While target selection is usually fast to compute, estimation of the vessel, crane and payload states is computational heavy. This is especially true for the presented MHE, which based on another nonlinear program provides state estimates alongside short term predictions of the vessel motions. The latter can add to the prediction accuracy in LMPC and NMPC but is imperative for FMPC. Yet, real-time feasible computation times were only obtained when using a structured observer that sacrifices inter-sensor information for computational performance. Proper balancing of MPC and MHE design parameters regarding total computational time budgets remains an open task for future research.

Finally, it should be noted that the attainable control performance may in fact be less dependent on the MPC formulation but on the limitations of the crane actuators, or more specifically, the crane's HPU. A performance map illustrating the dependency is included in section 4.5.3, showing a notable decline in performance indicators once the SSC exceeds the actuator capacity of the crane.

($\mathtt{Q}_2$) Is it possible to leverage the redundancy of the KBC's kinematics in context of a control system?

From a control perspective, resolving the crane's redundancy is not only reasonable but also necessary in order to obtain well-defined controller behavior. This is particularly true for the flatness-based controller designs that have a square plant as prerequisite. As shown in section section 4.3, the redundant nature of the crane can be removed by specifying a target tip height in the crane's root frame. Secondary control objectives besides payload handling can then be incorporated into the automation solution using an optimization-based target selector. Adopting an optimization-based approach not only comes with design flexibility regarding the implemented objective but also allows to map safety requirements that may e.g. restrict the admissible crane tip height. Also, online optimization makes it possible to include the actual wave disturbance when computing favorable tip heights. In context of this thesis, the crane configuration was optimized depending on the crane's manipulability in the *ne*-plane, which proved beneficial for ASC performance, cf. section 4.3.3. However, dynamic adjustments of the target crane

configuration, e.g., to the sea state, increase the actuator utilization, which is may lead to elevated mechanical wear. In future research, other objectives could be assessed to leverage the redundancy of the KBC. An interesting proposition is to artificially increase the variance of the average free cable length, which could mitigate the cable's stress associated with steady AHC operations, see [155].

($\mathtt{Q}_3$) Up to which sea state is it feasible to decouple the payload from the wave excitation?

Today's AHC systems are marketed with a heave amplitude that can be compensated at a given significant wave height, which is a simplified representation of the admissible sea state. Arguably, the dominant wave period is as important when evaluating control performance with limited actuator dynamics. As demonstrated in section 4.3.3, the ASC performance can be improved by optimizing the crane configuration so that actuator motions are translated as far as possible into horizontal tip motions. The converse holds true as well. If the crane operation is limited to configuration spaces of low manipulability, control performance is expected to decline. Another influencing factor observed during controller evaluation was controller tuning, which can be tweaked in order to favor either AHC or ASC performance. With these caveats in mind, highly precise trajectory tracking via an FMPC was demonstrated in simulation, cf. section 4.5.4. With a Euclidean error below $0.5\,{}^{\mathrm{m}}/_{\mathrm{s}}$ during the entire trajectory tracking, a decoupling of the payload motion from moderate sea disturbances seems feasible. The results would have to be checked in practice and be repeated for different scenarios. In general, the achievable control accuracy proved dependent on the modeled actuator constraints. With the available data, the simulation results in section 4.5.3 suggest that depending on the actuator class SSC 3-4 are an upper bound for today's crane technology. Yet, a definitive answer to $\mathtt{Q}_3$ is complicated by the multitude of affecting factors as well as dependent on the practical definition of a decoupled payload motion. The presented methodology and implemented simulation environment should however facilitate studies of performance maps based on different sea states, crane configurations or actuator capacities.

($\mathtt{Q}_4$) How can safety be defined and subsequently addressed during planning and control?

Safety is widely understood as the absence of unacceptable risk. While derived notions as *functional safety* are standardized, *operational safety* is less clearly defined. Following section 4.7.1, safe offshore operations fulfill operational requirements such as maximum hoisting speeds, boom travels or pendulum swing, that reduce the residual risk to tolerable levels during normal operation. Here, normal operation covers different tasks as well as expectable disturbance scenarios, i.e. sea states. It is commonly accepted that automatic control can provide means to ensure adherence to operational constraints with the researched predictive payload controllers being exemplary realizations of high LoA safety functions. Payload stabilization implicitly adds to collision-free handling operations.

Addressing collision avoidance in dynamic environments explicitly at controller level seems challenging when targeting universally applicable as well as real-time feasible controllers. Hence, more generic safety constraint candidates were discussed in section 4.7.4, with the half-angle of the cone induced by the oscillating payload and crane tip, the horizontal payload travel relative to the crane tip as well as a direct mapping of workspace or motion restrictions being exemplary prototype constraints that can be integrated in an optimal control problem. If reliably tracked, these constraints could also be used in higher level planning algorithms. Yet, payload controllers assuming sole control authority may hold little value in today's manual operated handling operations. Instead, solutions for assistive safety functions suitable for operator-in-the-loop topologies seem to be more relevant mid-term.

Besides the question of how to formulate safety in an offshore operation, practical ways of designing and incorporating assistive safety functions are key. In this context, two assistive functions translating concepts from the previously presented model-based predictive payload controllers were outlined in section 4.7.3 and section 4.7.4, respectively. The predictive emergency braking is designed to monitor handling operations and take control authority in case of a predicted collision. It leverages model-based state and sway energy prediction, as well as a cone approximation, to assess worst-case payload oscillations and implement collision avoidance. Yet, manual control is unrestricted. Predictive safety filters present a promising extension of MPC to obtain safety certificates in manual controlled handling tasks. The operator input is compared to calculated safe backup trajectories and adjusted if no future input trajectory keeps the system safe. Safety filter offer the possibility of ensuring adherence to safety constraints at all times, at which point the aforementioned metrics can be mapped to safety margins during planning, thus promoting safety across the autonomy stack. Challenges of implementing safety filters arise from the need of recursive feasibility as well as the possible perceived loss of authority on part of the operator. The predictive payload controllers in section 4.4 inform a lower bound on the controlled forward invariant (terminal) safety set. The integration of haptic feedback into the control elements could alleviate the problem of decoupling operator and system when correcting actions are issued. Undoubtedly, the discussed topics can only serve as a first perspective on safe payload handling at sea.

Chapter 6

Potentials of Predictive Control in Offshore Payload Handling

This chapter serves as a comprehensive overview of the conducted research, highlighting key findings and indicating further potentials of predictive control strategies for safe payload handling in crane-based offshore operations. In section 6.1 the research context is restated, before the presented work and results are recapitulated in section 6.2. The thesis concludes with comments on possible further improvements to predictive payload control, as well as suggestions for future research directions summarized in section 6.3.

6.1 Research Context and Relevance

The presented research activities were carried out under the *SFI Offshore Mechatronics* initiative funded by the Norwegian Research Council. In this context, this thesis investigates the topic of predictive control strategies facilitating safe payload handling during crane-based offshore operations.

As reiterated by current reports of the OECD and IEA, as well as international political agendas, the maritime sector is projected to remain economically significant through 2050. At the same time, the ocean-based industries face considerable challenges, e.g. high costs associated with not only installation but also operation and maintenance of offshore installations as well as an increasing shortage of skilled worker. With oil platforms and wind parks moving to deeper seas, the need for automation will intensify. Offshore lifting and handling applications with ship cranes form an integral part of today's maritime sector, with the maintenance of offshore energy plants, installation of drilling sites and ship-to-ship cargo transfer only presenting exemplary applications.

In contrast to onshore tower cranes, ship cranes are often implemented as hydraulic knuckle boom cranes (KBC) that feature an additional knuckle boom offering an increased level of flexibility as well as enabling small working radii. Another key difference is the increased level of exogenous disturbances found offshore. Waves persistently excite the vessel and crane base, causing the suspended payload to oscillate. Payload deflections further occur during high gusts or crane maneuvers. Oscillating payloads are detrimental

to operational efficiency as well as safety, such that handling operations have to be ceased in adverse weather conditions, which further increases costs. As to this day, payload handling is performed manually, efficiency as well as safety of crane operations depend on the experience of the crane operator. Increasing the level of automation (LoA) through layered control loops respectively assistant functions is regarded as promising means to simplify lifting operations, improve operational safety, and reduce costs.

A comprehensive review of the current state of the art in crane automatization is included in section 1.3, which found four main deficits with regard to offshore handling tasks: First, while the body of literature on swing reduction in crane applications is vast, the transferability of (onshore) approaches to offshore KBC is limited. For example, popular input shaping techniques fall short in face of persistent wave disturbances due to their open-loop nature. Furthermore, considerable fewer control strategies have been proposed for knuckle boom cranes, none of which explicitly took advantage of the additional degree of freedom. Second, stabilization of vertical or horizontal payload oscillations, also referred to as active heave compensation (AHC) and anti-sway control (ASC), are addressed separately. While AHC solutions are well-established in industry, there is a continued need for more capable controllers accounting for the payload's coupled motions and providing ASC capabilities as well as spatial stabilization. Third, most contributions in the field use oversimplifying representations of the vessel-crane dynamics or the wave disturbance when evaluating controllers, such that no standardized way to indicate controller performance exists. Finally, scientific literature focuses predominantly on induced payload damping, while the broader concept of operational safety is omitted from discussions.

The primary research hypothesis addresses whether predictive control strategies can resolve these deficits and promote safe offshore handling operations. The investigations are restricted to hydraulic knuckle boom cranes, during handling of light payloads above sea level, in a static scenario. The objectives include synthesises of a unified, model-based controller concept for spatial payload stabilization, exploitation of the KBC's redundancy, as well as assessment of operational safety from a control perspective. For this, a control-oriented model of the vessel, crane and payload system was derived, a flexible simulation environment including different wave spectra as well as the dynamic system models was set up, and different automation modules (controller, observer, target selector) were developed. Contributions to the fields of control engineering and offshore mechatronics lie in the thorough but control-oriented model, the integration of differential flatness with MPC that allowed for a load-centered control topology with both AHC and ASC capabilities, the developed moving horizon estimator (MHE) based short-term prediction of the vessel motions, and the optimization-based target selector framework that resolves the crane redundancy. The implemented simulation environment and performed analyses are believed to form a sound basis for coming developments. Finally, the discussed safety concepts open up exciting avenues for future research. A summary of the presented work and results is included hereafter.

6.2 Research Summary and Conclusion

This thesis developed and systematically evaluated model-predictive control strategies for spatial payload control. To enable model-based predictions, a dynamical model describing the multibody system of vessel, crane and payload was derived. Auxiliary modules in an optimization-based state observer and target selector complemented the proposed controller topology.

As a first contribution, this thesis presents a detailed modeling (chapter 3) of all system elements, including coordinate transformations, kinematics, and dynamics. The vessel motions were modeled according to literature, and light lifts as well as the existence of a performant dynamic positioning (DP) system were assumed to motivate a reduced set of considered vessel motions in heave, pitch and roll. The vessel motions could then be calculated from stochastic wave spectra, first order force response amplitude operators (RAO) as well as Fossen's roboter-like vessel model. A toolbox implementation was used to render vessel dynamics and environmental loads in the developed simulation environment implemented in MATLAB/ Simulink. Two wave spectra (JONSWAP, Torsethaugen) were chosen for the later evaluation studies. While the JONSWAP spectrum presents the de facto standard in many scientific contributions, the Torsethaugen spectrum features two distinct peak frequencies. After reviewing existing crane models of different scope and purpose, rigid body dynamics were derived for the KBC and payload assembly based on the Euler-Lagrange approach. Neglecting the crane's hydraulic subsystem is justified given layered control loops and the objective of payload control. The actuator dynamics were approximated by linear surrogate models. In contrast, the nonlinear kinematic relations between actuator space and joint space were included. The model extends the current state of the art by explicitly modeling the cable guide, sheave support points, and the effective suspension point by geometric considerations. Modeling was complemented by a minimal sensor setup (vision system, encoders, inertial measurement unit (IMU)), following typical industry instrumentation. A control-oriented state space model is derived that can be calculated in real-time. Eventually, differential flatness of the proposed system model was proven, which is a first for offshore KBCs. The proposed flat output was constructed from the global payload position and local crane tip height. The derived flat mappings give an algebraic relation between system states or inputs and the flat output as well as its time derivatives. Besides providing a systematic way to assess the wave-induced vessel motions from the payload's point of view, the flat mappings enable a payload-centric control approach. This is in contrast to conventional payload controllers controlling the crane tip while keeping payload deflections small. In conclusion to modeling, a flexible simulation environment allowing to test payload controllers against different wave disturbances and a control-oriented model tailored to real-time controller synthesis are provided, while the conducted flatness analysis delivers new structural insights into the payload handling problem.

Any of the predictive payload controllers require the current state of vessel, crane and payload as well as short-term predictions of the vessel motions to obtain meaningful open loop predictions. Beyond baseline state estimators reported in literature, this thesis presents observer designs (section 4.2), which also extrapolate past vessel motions. To do so, the vessel motions were approximated by a sum of harmonic modes, which in context of AHC systems was already used successful in literature to model the vessel's heave motion. This signal-based approach offers three main advantages: mean-free disturbance approximation without high-pass filtering, easy extension of vessel motions due to boundness of the periodic modes, and no need for an explicit vessel model. The state estimation was extended to also yield estimates of the modes' parameters as well as the IMU's stochastic biases. Due to the rapidly increasing number of unknown variables and parameters, two modes per vessel DoF seemed to max out computational budgets. Two MHE-based observer schemes – holistic and structured – were developed and compared. The holistic observer uses a single optimization problem to incorporate all sensor data, while the structured observer separates state reconstruction (EKF part) and mode/bias estimation from IMU readings (MHE part), enhancing computational speed. Simulative findings for two wave spectrums revealed good state estimation and adequate disturbance predictions over limited horizons. The prediction error increases monotonic with longer prediction horizons, which was to be expected given the limited number of modeled modes. A local peak in the error metric is observed when varying the filtering horizon, which might hint at an unfavorable ratio of filtering horizon and dominant wave period. Real-time feasibility (100 ms) was established for the structured observer, while the holistic approach took up to six time longer to derive estimates. Noteworthy, a conclusive benefit of fusing the IMU data with the comoved camera was not observed under the tested conditions.

Target selection (section 4.3) plays an important role in rendering the control task unique. The ambiguity arises from the fact that the payload position does not change when the crane tip is moved vertically at a constant working radius while the crane winch is operated in opposite direction, i.e., there are motions in null space. Fixing the crane tip height with respect to the crane's root frame removes the ambiguity. An optimization-based framework for target selection was put forward. An objective function was derived from the notion of manipulability ellipsoids known from robotics. The idea is to maximize the motion transmission from actuator space to Cartesian workspace, in particular with respect to the north-east plane as to support ASC. Evidence from moderate sea-state simulations suggest that smaller error metrics in steady state can indeed be attained when the target selector is active. The presented framework can be readily extended by new objective functions.

As part of the first research question, three different MPC formulations – linear model predictive controller (LMPC), nonlinear model predictive controller (NMPC), flatness-based model predictive controller (FMPC) – for payload stabilization resp. handling were tested. Starting with a generic optimal control problem (OCP), different control

objectives (energy-based, ASC-related, payload-centric) were discussed, where only the payload-centric approach penalizing the Euclidean distance between reference and payload position directly applies to both stabilizing and tracking tasks. This direct approach to payload control first combines AHC and ASC in a single controller, thus extending known literature. The three implemented MPC schemes differ in the approach taken to discretize the OCP (LMPC: successive linearization before time discretization, NMPC: numerical integration before quadratic expansion, FMPC: trajectory parameterization and no time discretization). While the LMPC is formulated as single-shooting problem, the NMPC was more conveniently build as a multiple-shooting problem. However, adding a condensing step to the sequential quadratic programming (SQP) resulting from the NMPC formulation was identified as critical for obtaining optimizers in reasonable times when using dense QP solver. The flatness-based MPC presents a non-standard formulation, unique to this thesis. In fact, the flat system calculus reduces the OCP to a planning problem that calculates optimal trajectories of the (flat) output. As a result, substantial speed-ups in computational times were demonstrated on a simulated tracking task at moderate seas, which can be attributed to a proper tuning of the low level spline approximation. The different MPC formulations were assessed in different case studies. To make results comparable, a unified set of error metrics informed by a second order system response of proposed error variables was applied. In addition, Bayesian optimization (BO) was performed to tune each individual controller to the same tuning objective, here chosen as the root-mean-square of the Euclidean tracking error. Based on insights from simulations, solely LMPC and FMPC were feasible under real-time conditions. In particular, NMPC required computational times ten times higher than those of LMPC. FMPC outperformed LMPC in obtained cycle times, while stabilization performance was comparable across all MPC variants. A performance map describing the steady state Euclidean error as a function of the Sea State Code (SSC) revealed a strong dependency of the achievable control performance on both the sea state and the available actuator capacity. Further investigations will be necessary to also factor in workspace related deratings. Finally, LMPC was validated on a laboratory test bench, supporting the feasibility of predictive payload control in practice.

The main body of this thesis concluded with a discussion on how predictive payload control strategies could promote or be extended to operational safety (section 4.7). Safe offshore operations minimize residual risks during normal operation to acceptable levels by ensuring safety requirements like maximum hoisting speeds or payload deflections. Collisions with the ship deck, personnel or machinery present a central hazard that stems from oscillating payloads. Automatic payload control can restrict payload motions thus adding to a reduction of risks. However, high LoA conflict with the current technological as well as legal state of industry found offshore. Assistive safety functions suited for operator-in-the-loop scenarios might therefore hold bigger upside mid-term. Two assistive functions were outlined, translating concepts from the previously presented model-based predictive payload controllers. While a predictive emergency braking function offers

means to monitor crane operations and take control authority in case of a predicted collision, the described predictive safety filter plans safe backup trajectories and varies the operator input if the latter can not be continued such that the system is kept safe under active control. In the context of safe (forward invariant) set design, generic safety constraints were motivated. Examples include bounds on the horizontal payload travel relative to the crane tip, or restricting the payload's sidelead and offlead angles via a single cone half-angle. The performance of the predictive payload controllers was identified as lower bound for the safe (terminal) set. As a derivation of MPC theory, the concept of predictive safety filters is of particular interest, as it offers new potential for the studied payload controllers.

Predictive control strategies fulfill on the promise of providing a flexible framework that allows to realize unified payload stabilization, to track more complex handling trajectories and to easily incorporate actuator or state constraints. The conducted evaluation studies suggest that the chosen MPC formulation is more important to the achievable cycle times than to the resulting control performance. The sea state code up to which the payload can be decoupled from the disturbance-induced vessel motions is bounded by the available actuator capacity, which will likely always be a limiting factor on MPC control performance. Predictive safety filters are identified as a promising path to transfer and deploy the concepts of this work near-term, adding assistive safety functions to operator-in-the-loop systems.

6.3 Outlook

The presented work provides insights into the topic of predictive control strategies for offshore payload handling. Extensions and opportunities for future research arise in a variety of contexts. A selection of possible topics and activities is summarized below.

The scope of this thesis was restricted to hydraulic knuckle boom cranes, the handling of light payloads above sea level, and a static scenario beyond wave-induced motions. Each single restriction might be removed in the future in order to assess predictive payload controllers for different crane structures (e.g. simple boom cranes), develop extensions that also estimate and subsequently compensate for wind loads or study subsea lifting operations, where the crane experiences direct ocean loads and the payload is subject to a multitude of disturbances when entering the splash zone. In-depth investigations of collision avoidance systems would also need to include dynamic obstacles, which have not yet been considered.

The derived model of vessel, crane and payload is believed to achieve a good tradeoff between model fidelity and real-time capability. Yet, some simplifications had been made, that should be checked in the future. First, the assumption of reactionless crane

operations with regard to the vessel motions does not hold for heavy lifts, in which case interconnected dynamics should be assessed. Furthermore, the modeled box constraints on the actuator variables may be overly simplifying noting the common feed by the central HPU. Therefore, load distribution may have to be incorporated in the payload controller or target selector. Last, the effects of residual vessel motions in the three neglected DoF on the closed-loop crane operations could be investigated.

The presented target selector can be readily extended by additional objective function designs. When applying AHC, the harmonic nature of the wave excitation leads to an approximately periodic actuation of the crane winch. As a result, the same cable segments are bend over the crane sheaves repeatedly, which increases the cable stress. In an attempt to reduce the cable stress, a target selection policy could be conceived that aims to increase the variance of the free cable length. Doing so, would likely lead to a wider distribution of cable segments bend over the crane sheaves, thus reducing mechanical wear of the cable.

The designed state observer will have to be validated under real-world conditions. Additional routines e.g., to stabilize the IMU readings might be necessary. Robustness to sensor misalignment or short term loss of data were not considered. From an application point of view, the question of a robust sensor unit combining different modalities and rendering robust sensor fusion in adverse weather remains open. Theoretical investigations should explore optimal parameterizations of MHE and MPC given a total computational time budget.

A comprehensive treatment of possible MPC formulations for predictive payload control is included in the main body of this thesis. Further work could expand on control performance during concurrent trajectory tracking and disturbance rejection. Extensions by robust MPC techniques could be advantageous if the nominal controllers show diminished control performance during practical validation. Yet, another intriguing opportunity for research is presented by the topic of operational safety and shared safety-critical control. While predictive safety filters are a promising starting point, the entire autonomy stack from planning to decision-making is vastly unexplored for crane-based offshore operations. Finally, transferring the FMPC scheme to other applications and comparing it to baseline MPC implementations is interesting from a control theoretical perspective.

Appendix A

Supplementary Information

Parameterization of polynomials for path planning

In section 2.2, two types of polynomials (interpolating and approximating) are discussed in order to restrict the design space during planning of a multipoint path. The included example is reproduced here for convenience, cf. Fig. 2.5. Besides the initial and final waypoints $(\sigma_\mathrm{l}, \mathtt{p}_\mathrm{l})$ respective $(\sigma_\mathrm{u}, \mathtt{p}_\mathrm{u})$, a sequence of five via-points $\{(\sigma_1, \mathtt{p}_1), \ldots, (\sigma_5, \mathtt{p}_5)\}$ is given. Two polynomials of $6th$ degree $P_k(\sigma) = \sum_{j=0}^{6} a_j^k \sigma^j \in \Pi_6$, $k \in \{\mathrm{int}, \mathrm{app}\}$ are fitted to the data points, for which the different parameterizations are derived hereafter:

In case of the interpolating polynomial $P_\mathrm{int}(\sigma)$ seven equalities of the form $\mathtt{p}_i = P_\mathrm{int}(\sigma_i)$, $i \in \{l, u, 1, \ldots, 5\}$ are concatenated using matrix notation, yielding

$$\begin{pmatrix} \mathtt{p}_\mathrm{l} \\ \mathtt{p}_\mathrm{u} \\ \mathtt{p}_1 \\ \vdots \\ \mathtt{p}_5 \end{pmatrix} = \begin{bmatrix} 1 & \sigma_\mathrm{l} & \ldots & \sigma_\mathrm{l}^6 \\ 1 & \sigma_\mathrm{u} & \ldots & \sigma_\mathrm{u}^6 \\ 1 & \sigma_1 & \ldots & \sigma_1^6 \\ \vdots & \vdots & \vdots & \vdots \\ 1 & \sigma_5 & \ldots & \sigma_5^6 \end{bmatrix} \begin{pmatrix} a_0^\mathrm{int} \\ \\ \vdots \\ \\ a_6^\mathrm{int} \end{pmatrix}$$

which can be easily solved for the coefficients a_j^int by a single matrix inversion.

In case of the approximating polynomial $P_\mathrm{app}(\sigma)$ the coefficients a_j^app are determined by solving the following optimization problem

$$\begin{aligned} \min_{a_0^\mathrm{app}, \ldots, a_6^\mathrm{app}} \quad & \sum_{i \in \{l,u,1,\ldots,5\}} \frac{1}{2} \left(\mathtt{p}_i - P_\mathrm{app}(\sigma_i)\right)^2 + \frac{\alpha}{2} \left(\left. \frac{\mathrm{d}^2 P_\mathrm{app}(\sigma)}{\mathrm{d}\sigma^2} \right|_{\sigma=\sigma_i} \right)^2 \\ s.t. \quad & P_\mathrm{app}(\sigma_\mathrm{l}) = \mathtt{p}_\mathrm{l} \\ & P_\mathrm{app}(\sigma_\mathrm{u}) = \mathtt{p}_\mathrm{u} \end{aligned}$$

which accounts for not only the distance between polynomial and via-points but also the path's curvature. Here, a scalar factor $\alpha \in \mathbb{R}_{>0}$ is introduced to weigh the two objectives. In order to attain both the initial and final waypoints exactly, the corresponding equalities are included as hard constraints.

Bibliography

[1] Abdel-Rahman, E. M. ; Nayfeh, A. H. ; Masoud, Z. N., Dynamics and Control of Cranes: A Review, *Journal of Vibration and Control*, vol. 9, no. 7, pp. 863–908, Jul. 2003. DOI: 10.1177/1077546303009007007.

[2] Abel, D. ; Bollig, A.: *Rapid Control Prototyping, Methoden und Anwendungen*, 1st ed. Springer Berlin, Heidelberg, 2006. DOI: https://doi.org/10.1007/3-540-29525-9.

[3] Adamson, J. E.: Efficient Heave Motion Compensation for Cable-Suspended Systems, in *Conference on Underwater Intervention*, New Orleans, Louisiana, USA, Feb. 2003, p. 7.

[4] Adamy, J.: *Nichtlineare Systeme und Regelungen*. Berlin, Heidelberg: Springer Berlin Heidelberg, 2018. DOI: 10.1007/978-3-662-55685-6.

[5] Alleyne, A. ; Allgöwer, F. ; Ames, A. D., *et al.*: *Control for Societal-Scale Challenges: Roadmap 2030*, Annaswamy, A. ; Johansson, K. ; Pappas, G., Eds. IEEE Control Systems Society Publication, May 2023, © 2023 Institute of Electrical and Electronics Engineers (IEEE). [Online]. Available: https://ieeecss.org/control-societal-scale-challenges-roadmap-2030.

[6] Almutairi, N. B. ; Zribi, M., Sliding Mode Control of a Three-dimensional Overhead Crane, *Journal of Vibration and Control*, vol. 15, no. 11, pp. 1679–1730, Nov. 2009. DOI: 10.1177/1077546309105095.

[7] Ames, A. D. ; Xu, X. ; Grizzle, J. W. ; Tabuada, P., Control barrier function based quadratic programs for safety critical systems, *IEEE Transactions on Automatic Control*, vol. 62, no. 8, pp. 3861–3876, 2017. DOI: 10.1109/TAC.2016.2638961.

[8] Andersson, J. A. E. ; Gillis, J. ; Horn, G. ; Rawlings, J. B. ; Diehl, M., CasADi – A software framework for nonlinear optimization and optimal control, *Mathematical Programming Computation*, vol. 11, no. 1, pp. 1–36, 2019. DOI: 10.1007/s12532-018-0139-4.

[9] Andrei, N.: *Modern Numerical Nonlinear Optimization* (Springer Optimization and Its Applications). Cham: Springer International Publishing, 2022, vol. 195. DOI: 10.1007/978-3-031-08720-2.

[10] Arnold, E. ; Sawodny, O. ; Neupert, J. ; Schneider, K.: Anti-sway system for boom cranes based on a model predictive control approach, in *IEEE International Conference Mechatronics and Automation, 2005*, vol. 3, Niagara Falls, Ont., Canada: IEEE, 2005, pp. 1533–1538. DOI: 10.1109/ICMA.2005.1626783.

[11] Arnold, E. ; Neupert, J. ; Sawodny, O. ; Schneider, K.: Trajectory Tracking for Boom Cranes Based on Nonlinear Control and Optimal Trajectory Generation, in *2007 IEEE International Conference on Control Applications*, Singapore: IEEE, Oct. 2007, pp. 1444–1449. DOI: 10.1109/CCA.2007.4389439.

[12] Aubin, J.-P. ; Bayen, A. M. ; Saint-Pierre, P.: *Viability theory: new directions*. Springer Science & Business Media, 2011. DOI: https://doi.org/10.1007/978-3-642-16684-6.

[13] Auer, P., Using Confidence Bounds for Exploitation-Exploration Trade-offs, *Journal oif Machine Learning Research*, vol. 3, pp. 297–422, Nov. 2002.

[14] Bak, M. ; Hansen, M. ; Karimi, H., Robust Tool Point Control for Offshore Knuckle Boom Crane, *IFAC Proceedings Volumes*, vol. 44, no. 1, pp. 4594–4599, Jan. 2011. DOI: 10.3182/20110828-6-IT-1002.03004.

[15] Bak, M. K. ; Hansen, M. R., Analysis of Offshore Knuckle Boom Crane - Part One: Modeling and Parameter Identification, *Modeling, Identification and Control: A Norwegian Research Bulletin*, vol. 34, no. 4, pp. 157–174, 2013. DOI: 10.4173/mic.2013.4.1.

[16] Bak, M. K. ; Hansen, M. R., Analysis of Offshore Knuckle Boom Crane - Part Two: Motion Control, *Modeling, Identification and Control: A Norwegian Research Bulletin*, vol. 34, no. 4, pp. 175–181, 2013. DOI: 10.4173/mic.2013.4.2.

[17] Bales, S. L., Designing Ships to the Natural Environment, *Naval Engineers Journal*, vol. 95, no. 2, pp. 31–40, Mar. 1983. DOI: 10.1111/j.1559-3584.1983.tb00574.x.

[18] Barge Master: *3D Motion Compensated Crane*, https://www.barge-master.com/fileadmin/user_upload/Documenten/PDF/BM-T40_Motion_Compensated_Knuckle_boom_crane/BM-MA-FL-4003-Rev8_Barge_Master_-_BM-T40_Spec_sheet.pdf. (visited on 06/02/2024).

[19] Bartolini, G. ; Pisano, A. ; Usai, E., Second-order sliding-mode control of container cranes, *Automatica*, vol. 38, no. 10, pp. 1783–1790, Oct. 2002. DOI: 10.1016/S0005-1098(02)00081-X.

[20] Bemporad, A. ; Cimini, G.: *Reduction of the number of variables in parametric constrained least-squares problems*, 2020. arXiv: 2012.10423 [math.OC]. [Online]. Available: https://arxiv.org/abs/2012.10423.

[21] Betts, J. T.: *Practical Methods for Optimal Control and Estimation Using Nonlinear Programming* (Advances in Design and Control), 2nd ed. Philadelphia: Society for Industrial and Applied Mathematics, 2010.

[22] Biagiotti, L. ; Melchiorri, C.: *Trajectory Planning for Automatic Machines and Robots*. Berlin, Heidelberg: Springer Berlin Heidelberg Springer e-books, 2008.

[23] Blackburn, D. ; Singhose, W. ; Kitchen, J. ; Patrangenaru, V. ; Lawrence, J. ; Kamoi, T. ; Taura, A., Command Shaping for Nonlinear Crane Dynamics, *Journal of Vibration and Control*, vol. 16, no. 4, pp. 477–501, Apr. 2010. DOI: 10.1177/1077546309106142.

[24] Blanchini, F., Set invariance in control, *Automatica*, vol. 35, no. 11, pp. 1747–1767, 1999. DOI: https://doi.org/10.1016/S0005-1098(99)00113-2.

[25] Bo, H. ; Yongchun, F. ; Ning, S.: Anti-sway control of an overhead crane with persistent disturbances by Lyapunov method, in *2015 34th Chinese Control Conference (CCC)*, Hangzhou, China: IEEE, Jul. 2015, pp. 889–894. DOI: 10.1109/ChiCC.2015.7259752.

[26] Brown, R. G. ; Hwang, P. Y. C.: *Introduction to Random Signals and Applied Kalman Filtering: With MATLAB Exercises*, 4. ed. Hoboken, NJ: Wiley, 2012.

[27] Bucy, R. S. ; Joseph, P. D.: *Filtering for stochastic processes with applications to guidance*. Interscience Publishers, N.Y., 1968.

[28] Bundesministerium für Wirtschaft und Energie (BMWi): *Maritime agenda 2025 - für die zukunft des maritimen wirtschaftsstandorts deutschland*, 2017. [Online]. Available: https://www.bmwk.de/Redaktion/DE/Publikationen/Wirtschaft/maritime-agenda-2025.pdf?__blob=publicationFile&v=1 (visited on 07/30/2024).

[29] Chen, H. ; Zhang, R. ; Liu, W. ; Chen, H., A time optimal trajectory planning method for offshore cranes with ship roll motions, *Journal of the Franklin Institute*, vol. 359, no. 12, pp. 6099–6122, Aug. 2022. DOI: 10.1016/j.jfranklin.2022.06.007.

[30] Chen, W.-H. ; Yang, J. ; Guo, L. ; Li, S., Disturbance-Observer-Based Control and Related Methods—An Overview, *IEEE Transactions on Industrial Electronics*, vol. 63, no. 2, pp. 1083–1095, Feb. 2016. DOI: 10.1109/TIE.2015.2478397.

[31] Chu, Y. ; Æsøy, V.: A Multi-Body Dynamic Model Based on Bond Graph for Maritime Hydraulic Crane Operations, in *Volume 1: Offshore Technology; Offshore Geotechnics*, St. John's, Newfoundland, Canada: American Society of Mechanical Engineers, May 2015, V001T01A010. DOI: 10.1115/OMAE2015-41616.

[32] Chu, Y. ; AEsoy, V. ; Zhang, H. ; Bunes, O.: Modelling And Simulation Of An Offshore Hydraulic Crane, in *ECMS 2014 Proceedings Edited by: Flaminio Squazzoni, Fabio Baronio, Claudia Archetti, Marco Castellani*, ECMS, May 2014, pp. 87–93. DOI: 10.7148/2014-0087.

[33] Chu, Y. ; Hatledal, L. I. ; Æsøy, V. ; Ehlers, S. ; Zhang, H., An Object-Oriented Modeling Approach to Virtual Prototyping of Marine Operation Systems Based on Functional Mock-Up Interface Co-Simulation, *Journal of Offshore Mechanics and Arctic Engineering*, vol. 140, no. 2, p. 021 601, Apr. 2018. DOI: 10.1115/1.4038346.

[34] Chu, Y. ; Li, G. ; Hatledal, L. I. ; Holmeset, F. T. ; Zhang, H., Coupling of dynamic reaction forces of a heavy load crane and ship motion responses in waves, *Ships and Offshore Structures*, vol. 16, no. sup1, pp. 58–67, Aug. 2021. DOI: 10.1080/17445302.2021.1907066. (visited on 06/02/2024).

[35] Chu, Y. ; Sanfilippo, F. ; Asoy, V. ; Zhang, H.: An effective heave compensation and anti-sway control approach for offshore hydraulic crane operations, in *2014 IEEE International Conference on Mechatronics and Automation*, Tianjin: IEEE, Aug. 2014, pp. 1282–1287. DOI: 10.1109/ICMA.2014.6885884.

[36] Cibicik, A. ; Myhre, T. A. ; Egeland, O.: Modeling and Control of a Bifilar Crane Payload, in *2018 Annual American Control Conference (ACC)*, Milwaukee, WI: IEEE, Jun. 2018, pp. 1305–1312. DOI: 10.23919/ACC.2018.8431375.

[37] Cibicik, A. ; Pedersen, E. ; Egeland, O., Dynamics of luffing motion of a flexible knuckle boom crane actuated by hydraulic cylinders, *Mechanism and Machine Theory*, vol. 143, p. 103 616, 2020. DOI: https://doi.org/10.1016/j.mechmachtheory.2019.103616.

[38] Cibicik, A. ; Tysse, G. O. ; Egeland, O., Determination of Reaction Forces of a Deck Crane in Wave Motion Using Screw Theory, *Journal of Offshore Mechanics and Arctic Engineering*, vol. 141, no. 6, p. 061 604, Dec. 2019. DOI: 10.1115/1.4043701.

[39] Ciccarella, G. ; Dalla Mora, M. ; Germani, A., A Luenberger-like observer for nonlinear systems, *International Journal of Control*, vol. 57, no. 3, pp. 537–556, Mar. 1993. DOI: 10.1080/00207179308934406. (visited on 06/02/2024).

[40] Clarke, D. ; Mohtadi, C. ; Tuffs, P., Generalized predictive control—part i. the basic algorithm, *Automatica*, vol. 23, no. 2, pp. 137–148, 1987. DOI: https://doi.org/10.1016/0005-1098(87)90087-2.

[41] Committee, I. S.: Report of the seakeeping committee, in *The 17th International Towing Tank Conference*, Goteborg, Sweden, 1984, pp. 457–534.

[42] Dahmen, W. ; Reusken, A. ; Reusken, A.: *Numerik für Ingenieure und Naturwissenschaftler*, 2nd ed. Springer Berlin, Heidelberg, 2008. DOI: https://doi.org/10.1007/978-3-540-76493-9.

[43] De Boor, C.: *A Practical Guide to Splines: With 32 Figures* (Applied Mathematical Sciences 27), Rev. ed. New York: Springer, 2001.

[44] Del Vecchio, D. ; Murray, R.: Observability and local observer construction for unknown parameters in linearly and nonlinearly parameterized systems, in *Proceedings of the 2003 American Control Conference, 2003.*, vol. 6, Denver, CO, USA: IEEE, 2003, pp. 4748–4753. DOI: 10.1109/ACC.2003.1242473.

[45] Denavit, J. ; Hartenberg, R. S., A Kinematic Notation for Lower-Pair Mechanisms Based on Matrices, *Journal of Applied Mechanics*, vol. 22, no. 2, pp. 215–221, Jun. 1955. DOI: 10.1115/1.4011045.

[46] Development, O.: *The Ocean Economy in 2030* (OECD Report Series). IWA Publishing, 2017. DOI: https://doi.org/10.1787/9789264251724-en.

[47] Diehl, M. ; Bock, H. ; Schlöder, J. P. ; Findeisen, R. ; Nagy, Z. ; Allgöwer, F., Real-time optimization and nonlinear model predictive control of processes governed by differential-algebraic equations, *Journal of Process Control*, vol. 12, no. 4, pp. 577–585, Jun. 2002. DOI: 10.1016/S0959-1524(01)00023-3.

[48] *DIN EN 13852-1:2021-06-Draft, Cranes – offshore cranes – part 1: General-purpose offshore cranes*, Deutsches Institut für Normung e.V. (DIN), 2021. DOI: https://dx.doi.org/10.31030/3216807.

[49] *DIN EN 14439:2010-03, Cranes – safety – tower cranes*, Deutsches Institut für Normung e.V. (DIN), 2010. DOI: https://dx.doi.org/10.31030/1529041.

[50] *DNV-ST-N001, Marine operations and marine warranty*, DNV AS, 2023.

[51] *DNV-RP-N103, Modelling and analysis of marine operations*, DNV AS, 2017.

[52] *DNV-RP-N201, Lifting appliances used in subsea operations*, DNV AS, 2019.

[53] *DNV-RP-C205, Environmental conditions and environmental loads*, DNV AS, 2019.

[54] *DNV-ST-0111, Assessment of station keeping capability of dynamic positioning vessels*, DNV AS, 2021.

[55] *DNV-ST-0377, Shipboard lifting appliances*, DNV AS, 2022.

[56] Donkov, V. ; Andersen, T. O. ; Ebbesen, M. K. ; Pedersen, H. C.: Applying Digital Hydraulic Technology on a Knuckle Boom Crane, in *The Ninth Workshop on Digital Fluid Power*, Aalborg, Denmark, Sep. 2017, p. 15.

[57] Donkov, V. H. ; Andersen, T. O. ; Pedersen, H. C. ; Ebbesen, M. K.: Application of Model Predictive Control in Discrete Displacement Cylinders to Drive a Knuckle Boom Crane, in *2018 Global Fluid Power Society PhD Symposium (GFPS)*, Samara: IEEE, Jul. 2018, pp. 408–413. DOI: 10.1109/GFPS.2018.8472363.

[58] Driscoll, F. R. ; Nahon, M. ; Lueck, R. G., A Comparison of Ship-Mounted and Cage-Mounted Passive Heave Compensation Systems, *Journal of Offshore Mechanics and Arctic Engineering*, vol. 122, no. 3, pp. 214–221, Aug. 2000. DOI: 10.1115/1.1287167.

[59] Dubins, L. E., On Curves of Minimal Length with a Constraint on Average Curvature, and with Prescribed Initial and Terminal Positions and Tangents, *American Journal of Mathematics*, vol. 79, no. 3, p. 497, Jul. 1957. DOI: 10.2307/2372560. JSTOR: 2372560. (visited on 06/02/2024).

[60] Dybedal, J.: *3D Sensor Placement and Embedded Processing for People Detection in an Industrial Environment*, Ph.D. dissertation, University of Agder, 2023.

[61] Fahrmeir, L. ; Kneib, T. ; Lang, S.: *Regression, Modelle, Methoden und Anwendungen*, 2nd ed. Springer Berlin, Heidelberg, 2009. DOI: https://doi.org/10.1007/978-3-642-01837-4.

[62] Faltinsen, O. M.: *Sea Loads on Ships and Offshore Structures* (Cambridge Ocean Technology Series), 1st ed. Cambridge: Cambridge University Press, 1999.

[63] Fang, Y. ; Wang, P. ; Sun, N. ; Zhang, Y., Dynamics Analysis and Nonlinear Control of an Offshore Boom Crane, *IEEE Transactions on Industrial Electronics*, vol. 61, no. 1, pp. 414–427, Jan. 2014. DOI: 10.1109/TIE.2013.2251731.

[64] Farrell, J. A. ; Silva, F. O. ; Rahman, F. ; Wendel, J., Inertial Measurement Unit Error Modeling Tutorial: Inertial Navigation System State Estimation with Real-Time Sensor Calibration, *IEEE Control Systems*, vol. 42, no. 6, pp. 40–66, Dec. 2022. DOI: 10.1109/MCS.2022.3209059.

[65] Fliess, M. ; Lévine, J. ; Martin, P. ; Rouchon, P., Sur les systèmes non linéaires différentiellement plats, 1992.

[66] Fliess, M. ; Lévine, J. ; Martin, P. ; Rouchon, P., Flatness and defect of non-linear systems: Introductory theory and examples, *International Journal of Control*, vol. 61, no. 6, pp. 1327–1361, 1995. DOI: 10.1080/00207179508921959.

[67] Fossen, T. I. ; Perez, T.: *Marine systems simulator (mss)*, https://github.com/cybergalactic/MSS, 2004. (visited on 06/02/2024).

[68] Fossen, T. I.: *Handbook of Marine Craft Hydrodynamics and Motion Control*. Chichester, West Sussex: Wiley, 2011.

[69] Garnett, R.: *Bayesian Optimization*, 1st ed. Cambridge University Press, Jan. 2023. DOI: 10.1017/9781108348973.

[70] Gelb, A.: *Applied Optimal Estimation*. MIT Press, 1974.

[71] Global Wind Energy Council: *Global wind report 2023*, 2023. [Online]. Available: https://gwec.net/globalwindreport2023/ (visited on 07/30/2024).

[72] Godhaven, J.-M.: Adaptive tuning of heave filter in motion sensor, in *IEEE Oceanic Engineering Society. OCEANS'98. Conference Proceedings*, vol. 1, Nice, France: IEEE, 1998, pp. 174–178. DOI: 10.1109/OCEANS.1998.725731.

[73] Gurriet, T. ; Singletary, A. ; Reher, J. ; Ciarletta, L. ; Feron, E. ; Ames, A.: Towards a framework for realizable safety critical control through active set invariance, in *2018 ACM/IEEE 9th International Conference on Cyber-Physical Systems (ICCPS)*, 2018, pp. 98–106. DOI: https://doi.org/10.1109/ICCPS.2018.00018.

[74] Hasselmann, K. ; Barnett, T. P. ; Bouws, E. ; Carlson, H. ; Cartwright, D. E. ; Enke, K. ; Gienapp, H. ; Hasselmann, D. E. ; Kruseman, P. ; Meerburg, A. ; Müller, P. ; Olbers, D. J. ; Richter, K. ; Sell, W. ; Walden, H.: *Measurements of Wind-Wave Growth and Swell Decay during the Joint North Sea Wave Project*. Hamburg: Deutsches Hydropraphisches Institut, 1973, vol. 12.

[75] Hennig, P. ; Schuler, C. J., Entropy Search for Information-Efficient Global Optimization, *Journal of Machine Learning Research*, no. 13, pp. 1809–1837, 2012.

[76] Hermann, R. ; Krener, A., Nonlinear controllability and observability, *IEEE Transactions on Automatic Control*, vol. 22, no. 5, pp. 728–740, Oct. 1977. DOI: 10.1109/TAC.1977.1101601.

[77] Huster, A. ; Bergstrom, H. ; Gosior, J. ; White, D.: Design and operational performance of a standalone passive heave compensation system for a work class ROV, in *OCEANS 2009*, Biloxi, MS: IEEE, Oct. 2009, pp. 1–8. DOI: 10.23919/OCEANS.2009.5422276.

[78] International Energy Agency (IEA): *World energy outlook 2019*, https://iea.blob.core.windows.net/assets/98909c1b-aabc-4797-9926-35307b418cdb/WEO2019-free.pdf, 2019. (visited on 07/30/2024).

[79] *IEC 60050-351:2013, International electrotechnical vocabulary - part 351: Control technology*, International Electrotechnical Commission (IEC), 2013.

[80] *IEC 62061:2021, Safety of machinery – functional safety of safety-related control systems*, International Electrotechnical Commission (IEC), 2021.

[81] International Energy Agency (IEA): *World energy outlook 2023*, https://www.iea.org/reports/world-energy-outlook-2023/overview-and-key-findings, 2023. (visited on 07/30/2024).

[82] Isidori, A.: *Nonlinear control systems*. London: Springer, 1999.

[83] Ismail, R. M. T. R. ; Ha, Q. P.: Trajectory tracking and anti-sway control of three-dimensional offshore boom cranes using second-order sliding modes, in *2013 IEEE International Conference on Automation Science and Engineering (CASE)*, Madison, WI, USA: IEEE, Aug. 2013, pp. 996–1001. DOI: 10.1109/CoASE.2013.6654071.

[84] Ismail, R. M. T. R. ; That, N. D. ; Ha, Q. P.: Offshore Container Crane Systems with Robust OptimalSliding Mode Control, in *31st International Symposium on Automation and Robotics in Construction*, Sydney, Australia, Jul. 2014. DOI: 10.22260/ISARC2014/0020. (visited on 06/02/2024).

[85] *ISO 12480-1:1997-03, Cranes – safe use – part 1: General*, International Organization for Standardization (ISO), 1997.

[86] *ISO 15513:2000-05, Cranes – competency requirements for crane drivers (operators), slingers, signallers and assessors*, International Organization for Standardization (ISO), 2000.

[87] *ISO/IEC GUIDE 51:2014(E), Safety aspects – guidelines for their inclusion in standards*, International Organization for Standardization (ISO)/ International Electrotechnical Commission (IEC), 2014.

[88] Jacobi, C., Ueber gauß neue methode, die werthe der integrale näherungsweise zu finden., *Journal für die reine und angewandte Mathematik*, vol. 1826, no. 1, pp. 301–308, 1826. DOI: https://doi.org/10.1515/crll.1826.1.301.

[89] Jakubowski, A. ; Milecki, A.: The Investigations of Hydraulic Heave Compensation System, in *Automation 2018*, Szewczyk, R. ; Zieliński, C. ; Kaliczyńska, M., Eds., vol. 743, Cham: Springer International Publishing, 2018, pp. 380–391. DOI: 10.1007/978-3-319-77179-3_36.

[90] Jensen, K. J. ; Kjeld Ebbesen, M. ; Rygaard Hansen, M., Development of Point-to-Point Path Control in Actuator Space for Hydraulic Knuckle Boom Crane, *Actuators*, vol. 9, no. 2, p. 27, Apr. 2020. DOI: 10.3390/act9020027.

[91] Johannessen, K. ; Meling, T. ; Haver, S., Joint distribution for wind and waves in the northern north sea, *International Journal of Offshore and Polar Engineering*, vol. 12, no. 1, pp. 1–8, Mar. 2002.

[92] Jones, D. R. ; Schonlau, M. ; Welch, W. J., Efficient Global Optimization of Expensive Black-Box Functions, *Journal of Global Optimization*, vol. 13, no. 4, pp. 455–492, 1998. DOI: 10.1023/A:1008306431147. (visited on 06/02/2024).

[93] Julier, S. ; Uhlmann, J., Unscented Filtering and Nonlinear Estimation, *Proceedings of the IEEE*, vol. 92, no. 3, pp. 401–422, Mar. 2004. DOI: 10.1109/JPROC.2003.823141.

[94] Julier, S. J. ; Uhlmann, J. K.: New extension of the Kalman filter to nonlinear systems, in *AeroSense '97*, Kadar, I., Ed., Orlando, FL, USA, Jul. 1997, p. 182. DOI: 10.1117/12.280797. (visited on 06/02/2024).

[95] Kalman, R. E., A New Approach to Linear Filtering and Prediction Problems, *Journal of Basic Engineering*, vol. 82, no. 1, pp. 35–45, Mar. 1960. DOI: 10.1115/1.3662552.

[96] Kalman, R. E. *et al.*, Contributions to the theory of optimal control, *Bol. soc. mat. mexicana*, vol. 5, no. 2, pp. 102–119, 1960.

[97] Kant, K. ; Zucker, S. W., Toward Efficient Trajectory Planning: The Path-Velocity Decomposition, *The International Journal of Robotics Research*, vol. 5, no. 3, pp. 72–89, Sep. 1986. DOI: 10.1177/027836498600500304.

[98] Karush, W.: "Minima of functions of several variables with inequalities as side conditions," in *Traces and Emergence of Nonlinear Programming*, Giorgi, G. ; Kjeldsen, T. H., Eds. Springer Basel, 2014, pp. 217–245. DOI: https://doi.org/10.1007/978-3-0348-0439-4_10.

[99] Ketelsen, S. ; Schmidt, L. ; Donkov, V. H. ; Andersen, T. O., Energy Saving Potential in Knuckle Boom Cranes using a Novel Pump Controlled Cylinder Drive, *Modeling, Identification and Control*, vol. 39, no. 2, pp. 73–89, 2018. DOI: 10.4173/mic.2018.2.3.

[100] Khintchine, A., Korrelationstheorie der stationären stochastischen prozesse, *Mathematische Annalen*, vol. 109, no. 1, pp. 604–615, 1934. DOI: https://doi.org/10.1007/BF01449156.

[101] Kimiaghalam, B. ; Homaifar, A. ; Sayarrodsari, B.: An application of model predictive control for a shipboard crane, in *Proceedings of the 2001 American Control Conference. (Cat. No.01CH37148)*, Arlington, VA, USA: IEEE, 2001, 929–934 vol.2. DOI: 10.1109/ACC.2001.945838.

[102] Kiss, B. ; Lévine, J. ; Müllhaupt, P., Modelling, Flatness and Simulation of a Class of Cranes, *Periodica Polytechnica Electrical Engineering*, vol. 42, no. 3, pp. 215–225, Jan. 1999.

[103] Knierim, K. L. ; Krieger, K. ; Sawodny, O., Flatness Based Control of a 3-DOF Overhead Crane with Velocity Controlled Drives, *IFAC Proceedings Volumes*, vol. 43, no. 18, pp. 363–368, 2010. DOI: 10.3182/20100913-3-US-2015.00083.

[104] Koivumaki, J. ; Mattila, J.: An energy-efficient high performance motion control of a hydraulic crane applying virtual decomposition control, in *2013 IEEE/RSJ International Conference on Intelligent Robots and Systems*, Tokyo: IEEE, Nov. 2013, pp. 4426–4433. DOI: 10.1109/IROS.2013.6696992.

[105] Kongsberg: *The Versatile Heave Compensator*, https://www.kongsberg.com/globalassets/kongsberg-discovery/inertial-solutions/mru/documents/374709e_datasheet_mruh_may24.pdf. (visited on 06/24/2024).

[106] Kongsberg Maritime: *Fibre rope cranes FRC*250*t working better deeper*, https://www.kongsberg.com/contentassets/f72504a28730416dac08f938f3109018/16.cranes_2p-10.08.17.pdf.

[107] Küchler, S. ; Mahl, T. ; Neupert, J. ; Schneider, K. ; Sawodny, O., Active Control for an Offshore Crane Using Prediction of the Vessel's Motion, *IEEE/ASME Transactions on Mechatronics*, vol. 16, no. 2, pp. 297–309, Apr. 2011. DOI: 10.1109/TMECH.2010.2041933.

[108] Küchler, S. ; Sawodny, O.: Nonlinear control of an active heave compensation system with time-delay, in *2010 IEEE International Conference on Control Applications*, Yokohama, Japan: IEEE, Sep. 2010, pp. 1313–1318. DOI: 10.1109/CCA.2010.5611119.

[109] Küchler, S. ; Sawodny, O., Beobachtergestützte Prognose der Vertikalbewegung eines Schiffes, *auto*, vol. 59, no. 8, pp. 502–511, Aug. 2011. DOI: 10.1524/auto.2011.0943.

[110] Kudva, P. ; Viswanadham, N. ; Ramakrishna, A., Observers for linear systems with unknown inputs, *IEEE Transactions on Automatic Control*, vol. 25, no. 1, pp. 113–115, Feb. 1980. DOI: 10.1109/TAC.1980.1102245.

[111] Kuhn, H. W. ; Tucker, A. W., Nonlinear Programming, *Berkeley Symposium on Mathematical Statistics and Probability*, vol. 2, pp. 481–492, 1951.

[112] Kutta, W., Beitrag zur näherungsweisen integration totaler differentialgleichungen, *Z. Math. Phys.*, vol. 46, pp. 435–453, 1901.

[113] Landsverk, R. ; Zhou, J.: Modeling and simulation of an offshore crane, in *2018 13th IEEE Conference on Industrial Electronics and Applications (ICIEA)*, Wuhan: IEEE, May 2018, pp. 713–718. DOI: 10.1109/ICIEA.2018.8397806.

[114] Lewis, E. V. ; Society of Naval Architects and Marine Engineers, Eds.: *Motions in waves and controllability* (Principles of naval architecture / Edward V. Lewis volume 3), Second Revision. Jersey City, NJ: The Society of Naval Architects and Marine Engineers, 1989.

[115] Lewis, F. L. ; Xie, L. ; Popa, D.: *Optimal and Robust Estimation, With an Introduction to Stochastic Control Theory*, 2nd ed. CRC press, 2017. DOI: https://doi.org/10.1201/9781315221656.

[116] Li, L. ; Gao, Z. ; Moan, T., Joint Distribution of Environmental Condition at Five European Offshore Sites for Design of Combined Wind and Wave Energy Devices, *Journal of Offshore Mechanics and Arctic Engineering*, vol. 137, no. 3, p. 031 901, Jun. 2015. DOI: 10.1115/1.4029842.

[117] Li, S. ; Yang, J. ; Chen, W.-H. ; Chen, X., Eds.: *Disturbance Observer-Based Control: Methods and Applications*. Boca Raton, Fla.: CRC Press, 2014.

[118] Liebherr: *Offshore crane technology*, https://www.liebherr.com/shared/media/maritime-cranes/downloads-und-brosch%C3%BCren-neu/brosch%C3%BCren/offshore-cranes/offshore-crane-technology-liebherr-heavetronic.pdf. (visited on 06/02/2024).

[119] Lu, B. ; Fang, Y. ; Sun, N. ; Wang, X., Antiswing Control of Offshore Boom Cranes With Ship Roll Disturbances, *IEEE Transactions on Control Systems Technology*, vol. 26, no. 2, pp. 740–747, Mar. 2018. DOI: 10.1109/TCST.2017.2679060.

[120] Luenberger, D. G., Observing the State of a Linear System, *IEEE Transactions on Military Electronics*, vol. 8, no. 2, pp. 74–80, 1964. DOI: 10.1109/TME.1964.4323124.

[121] MacGregor Norway AS: *Offshore ahc cranes*. [Online]. Available: https://www.macgregor.com/Products/products/offshore-and-subsea-load-handling/ahc-cranes/ (visited on 10/09/2020).

[122] MacGregor Norway AS: *Proven 3D motion compensation*, https://www.macgregor.com/globalassets/products--solutions/colibritm-crane-and-tool_march-2023.pdf. (visited on 06/02/2024).

[123] Maciejowski, J. M.: *Predictive Control: With Constraints*. Harlow, England ; New York: Prentice Hall, 2002.

[124] Martin, I. A. ; Irani, R. A., Dynamic modeling and self-tuning anti-sway control of a seven degree of freedom shipboard knuckle boom crane, *Mechanical Systems and Signal Processing*, vol. 153, p. 107 441, May 2021. DOI: 10.1016/j.ymssp.2020.107441. (visited on 06/02/2024).

[125] Moslatt, G.-A. ; Hansen, M. R.: Modeling of Friction Losses in Offshore Knuckle Boom Crane Winch System, in *2018 Global Fluid Power Society PhD Symposium (GFPS)*, Samara: IEEE, Jul. 2018, pp. 1–7. DOI: 10.1109/GFPS.2018.8472316.

[126] National Oilwell Varco *NOV*: *Anti-Sway Rotator*, https://www.nov.com/media/nov/files/products/rig/anti-sway-rotator-asr/antisway-rotator-flyer.pdf. (visited on 06/02/2024).

[127] National Oilwell Varco *NOV*: *Automatic Overload Protection Systems (AOPS) for Offshore Cranes*, https://www.nov.com/media/nov/files/products/rig/marine-and-construction/offshore-cranes/automatic-overload-protection-system-aops.pdf. (visited on 06/02/2024).

[128] Neupert, J. ; Hildebrandt, A. ; Sawodny, O. ; Schneider, K.: Trajectory Tracking For Boom Cranes Using A Flatness Based Approach, in *2006 SICE-ICASE International Joint Conference*, Busan Exhibition & Convention Center-BEXCO, Busan, Korea: IEEE, 2006, pp. 1812–1816. DOI: 10.1109/SICE.2006.315717.

[129] Neupert, J. ; Mahl, T. ; Haessig, B. ; Sawodny, O. ; Schneider, K.: A heave compensation approach for offshore cranes, in *2008 American Control Conference*, Seattle, WA: IEEE, Jun. 2008, pp. 538–543. DOI: 10.1109/ACC.2008.4586547.

[130] Neupert, J. ; Arnold, E. ; Schneider, K. ; Sawodny, O., Tracking and anti-sway control for boom cranes, *Control Engineering Practice*, vol. 18, no. 1, pp. 31–44, Jan. 2010. DOI: 10.1016/j.conengprac.2009.08.003.

[131] Nitsch, M.: *Navigation of a miniaturized autonomous underwater vehicle exploring waters under ice*. RWTH Aachen University, 2024, PhD Thesis. DOI: 10.18154/RWTH-2024-05964.

[132] Nocedal, J. ; Wright, S. J.: *Numerical optimization*, 2nd ed. Springer New York, NY, 2006. DOI: https://doi.org/10.1007/978-0-387-40065-5.

[133] Nordhammer, P. A. ; Bak, M. K. ; Hansen, M. R.: Controlling the slewing motion of hydraulically actuated cranes using sequential activation of counterbalance Valves, in *12th International Conference on Control, Automation and Systems*, Jeju Island, Korea, Oct. 2012, pp. 773–778.

[134] Organization, W. M.: *Manual on Codes International Codes* (1). Geneva: WMO, 2019, vol. 306.

[135] Ouyang, H. ; Uchiyama, N. ; Sano, S.: Anti-sway control of rotary crane only by horizontal boom motion, in *2010 IEEE International Conference on Control Applications*, Yokohama, Japan: IEEE, Sep. 2010, pp. 591–595. DOI: 10.1109/CCA.2010.5611096.

[136] Pardalos, P. M. ; Rasskazova, V. ; Vrahatis, M. N., Eds.: *Black Box Optimization, Machine Learning, and No-Free Lunch Theorems* (Springer Optimization and Its Applications). Cham: Springer International Publishing, 2021, vol. 170. DOI: 10.1007/978-3-030-66515-9.

[137] Park, K. I.: *Fundamentals of Probability and Stochastic Processes with Applications to Communications*. Cham: Springer International Publishing, 2018. DOI: 10.1007/978-3-319-68075-0.

[138] Perrault, D. E., Probability of Sea Condition for Ship Strength, Stability, and Motion Studies, *Journal of Ship Research*, vol. 65, no. 01, pp. 1–14, Mar. 2021. DOI: 10.5957/JOSR.05190024.

[139] Pierson, W. J. ; Moskowitz, L., A proposed spectral form for fully developed wind seas based on the similarity theory of S. A. Kitaigorodskii, *Journal of Geophysical Research*, vol. 69, no. 24, pp. 5181–5190, Dec. 1964. DOI: 10.1029/JZ069i024p05181.

[140] Purcell, M. J. ; Forrester, N. C.: Bobbing Crane Heave Compensation for the Deep Towed Fiber Optic Survey System, in *Society of Naval Architects and Marine Engineers*, Wood Hole, MA, USA, May 1994, p. 16.

[141] Qian, D.: *Anti-Sway Control for Cranes, Design and Implementation Using MATLAB*. Berlin Boston: De Gruyter, 2018. DOI: doi:10.1515/9783110520101.

[142] Ramli, L. ; Mohamed, Z. ; Abdullahi, A. M. ; Jaafar, H. ; Lazim, I. M., Control strategies for crane systems: A comprehensive review, *Mechanical Systems and Signal Processing*, vol. 95, pp. 1–23, Oct. 2017. DOI: 10.1016/j.ymssp.2017.03.015.

[143] Rao, C. ; Rawlings, J. ; Mayne, D., Constrained state estimation for nonlinear discrete-time systems: Stability and moving horizon approximations, *IEEE Transactions on Automatic Control*, vol. 48, no. 2, pp. 246–258, Feb. 2003. DOI: 10.1109/TAC.2002.808470.

[144] Rao, C. V. ; Rawlings, J. B., Constrained process monitoring: Moving-horizon approach, *AIChE Journal*, vol. 48, no. 1, pp. 97–109, 2002. DOI: https://doi.org/10.1002/aic.690480111.

[145] Rasmussen, C. E. ; Williams, C. K. I.: *Gaussian Processes for Machine Learning*. The MIT Press, 2005. DOI: https://doi.org/10.7551/mitpress/3206.001.0001.

[146] Rawlings, J. B. ; Mayne, D. Q. ; Diehl, M.: *Model Predictive Control: Theory, Computation and Design*, 2nd edition. Santa Barbara: Nob Hill Publishing, LLC, 2020.

[147] Richter, M.: *Modellbasierte Methoden zur Systemanalyse und Regelung für die aktive Seegangskompensation bei Tiefseekranen*, 1st ed. Düren, Germany: Shaker Verlag GmbH, 2018.

[148] Richter, M. ; Arnold, E. ; Schneider, K. ; Eberharter, J. K. ; Sawodny, O.: Model predictive trajectory planning with fallback-strategy for an active Heave Compensation system, in *2014 American Control Conference*, Portland, OR, USA: IEEE, Jun. 2014, pp. 1919–1924. DOI: 10.1109/ACC.2014.6859017.

[149] Runge, C. ; Mehmke, R., Organ für angewandte Mathematik, *Zeitschrift für Mathematik und Physik*, vol. 46, p. 141, 1901.

[150] Runge, C., Über die numerische auflösung von differentialgleichungen, *Mathematische Annalen*, vol. 46, no. 2, pp. 167–178, 1895. DOI: https://doi.org/10.1007/BF01446807.

[151] SAE International Recommended Practice: *Taxonomy and definitions for terms related to driving automation systems for on-road motor vehicles*, SAE Standard J3016_202104, Apr. 2021. DOI: https://doi.org/10.4271/J3016_202104.

[152] Sanfilippo, F. ; Hatledal, L. I. ; Pettersen, K. Y. ; Zhang, H., A benchmarking framework for control methods of maritime cranes based on the functional mockup interface, *IEEE Journal of Oceanic Engineering*, vol. 43, no. 2, pp. 468–483, 2018. DOI: 10.1109/JOE.2017.2691920.

[153] Scantrol AS: *Adaptive active heave compensation for all winches*. [Online]. Available: https://www.scantrol.com/wp-content/uploads/2013/02/AHC-Datasheet.pdf (visited on 10/09/2020).

[154] Schaper, U. ; Dittrich, C. ; Arnold, E. ; Schneider, K. ; Sawodny, O., 2-DOF skew control of boom cranes including state estimation and reference trajectory generation, *Control Engineering Practice*, vol. 33, pp. 63–75, Dec. 2014. DOI: 10.1016/j.conengprac.2014.09.009. (visited on 06/02/2024).

[155] Schlanbusch, R. ; Oland, E. ; R. Bechhoefer, E., Condition Monitoring Technologies for Steel Wire Ropes – A Review, *International Journal of Prognostics and Health Management*, vol. 8, no. 1, Nov. 2020. DOI: 10.36001/ijphm.2017.v8i1.2527.

[156] Schmitt, L. ; Nickig, N. ; Bahr, M. ; Gößling, S. ; Abel, D.: Review, evaluation and application of condensing algorithms for model predictive control based on a first-order method, in *2023 European Control Conference (ECC)*, 2023, pp. 1–7. DOI: 10.23919/ECC57647.2023.10178157.

[157] Seddigha, M. ; Brandao, L. ; Asgari, P.: Hoisting control strategy for offshore cargo lift transfer operations, in *Marine Operations Specialty Symposium*, (Singapore), IEEE, Sep. 2016.

[158] Sheridan, T. B. ; Verplank, W. L.: "Human and computer control of undersea teleoperators," Massachusetts Inst of Tech Cambridge Man-Machine Systems Lab, Tech. Rep., 1978.

[159] Siciliano, B. ; Sciavicco, L. ; Villani, L. ; Oriolo, G.: *Robotics, Modelling, Planning and Control* (Advanced Textbooks in Control and Signal Processing). Springer London, 2010.

[160] Simon, D.: *Optimal State Estimation: Kalman, H∞, and Nonlinear Approaches*, 1st ed. Wiley, May 2006. DOI: 10.1002/0470045345.

[161] Skogestad, S. ; Postlethwaite, I.: *Multivariable feedback control: analysis and design*. John Wiley & Sons, 2005.

[162] Smith, O. J., Closer control of loops with dead time, *Chemical engineering progress*, vol. 53, pp. 217–219, 1957.

[163] SMST: *3d motion compensated cranes*, https://www.smstequipment.com/media/1411/smst-motioncompensatedcranes-flyera4-2020v1.pdf. (visited on 05/01/2024).

[164] Sontag, E. D.: *Mathematical Control Theory* (Texts in Applied Mathematics), Marsden, J. E. ; Sirovich, L. ; Golubitsky, M. ; Jäger, W., Eds. New York, NY: Springer New York, 1998, vol. 6. DOI: 10.1007/978-1-4612-0577-7.

[165] Sørensen, J. K. ; Hansen, M. R. ; Ebbensen, M. K.: Boom Motion Control Using Pressure Control Valve, in *8th FPNI Ph.D Symposium on Fluid Power*, Lappeenranta, Finland: American Society of Mechanical Engineers, Jun. 2014, V001T05A009. DOI: 10.1115/FPNI2014-7853.

[166] Sørensen, J. K.: *Reduction of Oscillations in Hydraulically Actuated Knuckle Boom Cranes*, Ph.D. dissertation, University of Agder, 2016.

[167] Sørensen, J. K. ; Hansen, M. ; Ebbensen, M. K.: Load independent velocity control on boom motion using pressure control valve, in *14th Scandinavian International Conference on Fluid Power*, Tampere, Finland, 2015.

[168] Stenger, D.: *Automatic tuning of control engineering algorithms with Bayesian optimization*. RWTH Aachen University, 2023, PhD Thesis. DOI: 10.18154/RWTH-2023-09801.

[169] Stenger, D. ; Abel, D.: *Benchmark of Bayesian Optimization and Metaheuristics for Control Engineering Tuning Problems with Crash Constraints*, 2022. DOI: 10.48550/ARXIV.2211.02571.

[170] Tearle, B. ; Wabersich, K. P. ; Carron, A. ; Zeilinger, M. N., A predictive safety filter for learning-based racing control, *IEEE Robotics and Automation Letters*, vol. 6, no. 4, pp. 7635–7642, 2021. DOI: 10.1109/LRA.2021.3097073.

[171] Tenny, M. ; Rawlings, J.: Efficient moving horizon estimation and nonlinear model predictive control, in *Proceedings of the 2002 American Control Conference (IEEE Cat. No.CH37301)*, Anchorage, AK, USA: IEEE, 2002, 4475–4480 vol.6. DOI: 10.1109/ACC.2002.1025355.

[172] Torsethaugen, K., Two peak wave spectrum model, *Proceedings of the International Conference on Offshore Mechanics and Arctic Engineering - OMAE*, vol. 2, pp. 175–180, Jan. 1993.

[173] Torsethaugen, K. ; Haver, S.: Simplified double peak spectral model for ocean waves, ser. International Ocean and Polar Engineering Conference, vol. All Days, May 2004, ISOPE-I-04–289. [Online]. Available: https://onepetro.org/ISOPEIOPEC/proceedings-pdf/ISOPE04/All-ISOPE04/ISOPE-I-04-289/1852112/isope-i-04-289.pdf.

[174] Tysse, G. O. ; Cibicik, A. ; Egeland, O., Vision-based control of a knuckle boom crane with online cable length estimation, *IEEE/ASME Transactions on Mechatronics*, pp. 1–1, 2020. DOI: 10.1109/TMECH.2020.3024637.

[175] Tysse, G. O. ; Egeland, O., Dynamic Interaction of a Heavy Crane and a Ship in Wave Motion, *Modeling, Identification and Control: A Norwegian Research Bulletin*, vol. 39, no. 2, pp. 45–60, 2018. DOI: 10.4173/mic.2018.2.1. (visited on 06/02/2024).

[176] Tysse, G. O. ; Egeland, O.: Crane load position control using Lyapunov-based pendulum damping and nonlinear MPC position control, in *2019 18th European Control Conference (ECC)*, Naples, Italy: IEEE, Jun. 2019, pp. 1628–1635. DOI: 10.23919/ECC.2019.8796215.

[177] van Albada, S. B. ; van Albada, G. D. ; Hildre, H. P. ; Zhang, H.: A Novel Approach To Anti-Sway Control For Marine Shipboard Cranes, in *ECMS 2013 Proceedings Edited by: Webjorn Rekdalsbakken, Robin T. Bye, Houxiang Zhang*, ECMS, May 2013, pp. 249–256. DOI: 10.7148/2013-0249.

[178] Vaughan, J. ; Kim, D. ; Singhose, W., Control of Tower Cranes With Double-Pendulum Payload Dynamics, *IEEE Transactions on Control Systems Technology*, p. 5 422 812, Nov. 2010. DOI: 10.1109/TCST.2010.2040178.

[179] Wabersich, K. P. ; Zeilinger, M. N.: Linear model predictive safety certification for learning-based control, in *2018 IEEE Conference on Decision and Control (CDC)*, 2018, pp. 7130–7135. DOI: 10.1109/CDC.2018.8619829.

[180] Wabersich, K. P. ; Zeilinger, M. N., A predictive safety filter for learning-based control of constrained nonlinear dynamical systems, *Automatica*, vol. 129, p. 109 597, 2021. DOI: https://doi.org/10.1016/j.automatica.2021.109597.

[181] Wang, Z. ; Jegelka, S.: *Max-value Entropy Search for Efficient Bayesian Optimization*, 2017. DOI: 10.48550/ARXIV.1703.01968.

[182] Warren, C.: Global path planning using artificial potential fields, in *Proceedings, 1989 International Conference on Robotics and Automation*, 1989, 316–321 vol.1. DOI: 10.1109/ROBOT.1989.100007.

[183] Woodacre, J. ; Bauer, R. ; Irani, R., A review of vertical motion heave compensation systems, *Ocean Engineering*, vol. 104, pp. 140–154, Aug. 2015. DOI: 10.1016/j.oceaneng.2015.05.004. (visited on 06/02/2024).

[184] Wu, X. ; He, X., Control of the bridge crane by constructing a Lyapunov function: Theoretical design and experimental verification, *Transactions of the Institute of Measurement and Control*, vol. 39, no. 12, pp. 1763–1770, Dec. 2017. DOI: 10.1177/0142331216646823.

[185] Wu, X. ; He, X. ; Sun, N. ; Fang, Y.: A novel anti-swing control method for 3-D overhead cranes, in *2014 American Control Conference*, Portland, OR, USA: IEEE, Jun. 2014, pp. 2821–2826. DOI: 10.1109/ACC.2014.6858866.

[186] Yang, Z. ; Lin, Y. ; Dong, S., Weather window and efficiency assessment of offshore wind power construction in China adjacent seas using the calibrated SWAN model, *Ocean Engineering*, vol. 259, p. 111 933, Sep. 2022. DOI: 10.1016/j.oceaneng.2022.111933. (visited on 06/02/2024).

[187] Zhang, M. ; Zhang, Y. ; Ouyang, H. ; Ma, C. ; Cheng, X., Adaptive integral sliding mode control with payload sway reduction for 4-DOF tower crane systems, *Nonlinear Dynamics*, vol. 99, no. 4, pp. 2727–2741, Mar. 2020. DOI: 10.1007/s11071-020-05471-3. (visited on 06/02/2024).

[188] Zhao, W. ; Ebbesen, M. K. ; Andersen, T. O.: Comparative Analysis of Energy Efficiency: Knuckle Boom Crane Driven by Motor-Controlled Cylinders Versus Valve-Controlled Cylinders, in *2023 11th International Conference on Control, Mechatronics and Automation (ICCMA)*, Grimstad, Norway: IEEE, Nov. 2023, pp. 201–207. DOI: 10.1109/ICCMA59762.2023.10374706.

[189] Zhou Entao ; Yang Wenlin ; Lin Junzhe: Predictive control of hydraulic winch motion control, in *2009 2nd IEEE International Conference on Computer Science and Information Technology*, Beijing, China: IEEE, 2009, pp. 1–4. DOI: 10.1109/ICCSIT.2009.5234639.